Thermal And Quantum Fluctuations in Low Dimensional Frustrated Spin Systems

Thesis submitted for the degree of
Doctor of Philosophy (Science)
in
Physics (Theoretical)

by
Manodip Routh

Department of Physics
University of Calcutta
2025

Dedicated to my Mother

Acknowledgements

Science thrives on collaboration, and this thesis would not have been possible without the support and guidance of many people.

First and foremost, I express my deepest gratitude to my advisor, Prof. Manoranjan Kumar for his invaluable guidance. I have always appreciated his remarkable intuition for physics and his ability to find interesting and timely problems to work on. I am grateful to him for introducing me to the fascinating world of frustrated magnetism.

I have greatly benefited from our weekly group meetings, which provided insights into ongoing research in strongly correlated systems. I sincerely thank my past and present group members—Dr. Aslam Parvej, Dr. Sudipta Pattanyak, Dr. Debasmita Maity, Dr. Sudip Kumar Saha, Dr. Monalisa Singh Roy, Dr. Koushik Mandal, Dr. Saniur Rahaman, Dr. Jyotirmoy Sau, Monalisa Chatterjee, Dr. Joy Prakash Das, Dr. Sambunath Das, Dr. Sourav Chakraborty, Dr. Sumit Haldar, Sourabh Saha, Ayan Jana, and Dr. Dibyajyoti Saikia—for their valuable discussions, suggestions, and friendship.

I am especially grateful to my first collaborator, Prof. Zoltán G. Soos, Princeton University, for his guidance and for the enriching discussions that shaped my research. I would also like to thank Prof. Tanusri Saha-Dasgupta and my advisor for giving me the opportunity to participate in the exchange program at IFW Dresden, Germany. My time there was highly productive, thanks to collaborations with Prof. Satoshi Nishimoto and Prof. Jeroen van den Brink. I am particularly thankful to Prof. Nishimoto, who taught me how to efficiently do the numerical analysis, as the these are very much time taking in many body physics. Ever since, I enjoy working with him on Kitaev magnet. My sincere thanks also go to Grit Rötzer for her warm hospitality in Dresden. I am deeply grateful to Prof. Arun Paramekanti, University of Toronto, for his mentorship and for providing me with valuable learning opportunities. His guidance and patience have allowed me to discuss both academic and non-academic topics freely. He has played a key role in helping me connect theoretical ideas with experimental data. I would also like to acknowledge my collaborators, Prof. Tanusri Saha-Dasgupta, SNBNCBS, Prof. S. M. Yusuf, BARC, Mumbai, and Dr. Anup Kumar Bera, BARC, Mumbai. I have truly enjoyed working with Dr. Sudip Kumar Saha, Manoj Gupta, Sayan Ghosh, and Anutosh Biswas. I sincerely thank my Ph.D. thesis committee members, Prof. Punyabrata Pradhan and Prof. Thirupathaiah Setti, for their valuable feedback and suggestions, which improved my understanding.

I am indebted to my M.Sc. professors at IIT Guwahati, who laid the foundation for my Ph.D. studies—Prof. Subhaditya Bhattacharya, Prof. Sayan Chakrabarti, Prof. Charudatt Y. Kadolkar, Prof. Debaprasad Maity, Prof. Arunansu Sil, Prof. Girish Sampath Setlur, Prof. Kanhaiya Pandey, and Prof. Pankaj Kumar Mishra.

Conferences and workshops organized by Dr. Kumar have broadened my exposure to the condensed matter physics community and helped me refine my organizational and communication skills. I sincerely thank Dr. Kumar and the S. N. Bose Centre for their support.

Life at S. N. Bose National Centre has been made smoother by the dedication of many individuals. I extend my gratitude to the Academic Section, Computer Services Cell, Library, Accounts Section, Reception and Dispatch teams, and Security personnel. Special thanks to the Bhagirathi Canteen and the SNB Students' Mess for creating a warm and welcoming environment.

Being part of the SNB student community has been an enriching experience. My heartfelt thanks to Ram Krishna Patra, Samrat Sen, Dr. Anirban Mukherjee, Dr. Ananda Gopal Maity, Dr. Tanmoy Chakraborty, Dr. Premashis Kumar, Dr. Arun Maurya, Sweta Ghosh, Dr. Sayan Routh, Dr. Krishnendu Sinha, Dr. Shiladitya Karmakar, Dr. Abhik Ghosh Moulick, Dr. Sumanti Patra, Bidhan Kumbhakar, Arnab Paul for their friendship and support.

I am forever grateful to my college professors, especially Dr. Mantu Kumar Das, Dr. Tanusri Pal, Dr. Parthasarathi Das, Dr. Swapan Kumar Shee, and Dr. Makhanlal Nanda Goswami, as well as my school teachers, Mr. Soumitra Dey, Mr. Dilip Kumar Guria, Mr. Hariballav Pal, and Mr. Ashoke Sir, who have shaped my academic path.

In this challenging world, the relationships we build become our greatest support. I feel fortunate to have always been surrounded by great friends. My college years were enriched by Bratati Paul, Pritha Dutta, Prasanta Chowdhury. Special thanks to Sibnath Ghosh and Ardhendu Bera for making my college days memorable. I am especially grateful to my best friend, Anjan Pal, for always being there for me. His unwavering support and positive attitude have been a true inspiration. He is my go-to person for any problems in my life.

During my postgraduate days at IIT Guwahati, I cherished my time with Barnabha Bandopadhay, Swarup Kanti Sarkar, Ananda Gopal Maity, Modasser Hossain, Afsar Reja, Dharmendra Samota, Sandeep Nehera.

Now, I want to acknowledge the most special people in my Ph.D. journey. One of my greatest joys has been the companionship of my dearest friends—Anirban Paul, Samir Rom, Aishwaryo Ghosh (Rik), and Krishnendu Patra (Kaka). We have shared countless unforgettable memories. Their guidance, support, and friendship have made this journey truly meaningful. Our late-night *addas* will always hold a special place in my heart. I deeply admire Rik's wisdom about life, Samir's commitment to his decisions, Kaka's resilience in tough times, and Anirban's positive outlook on life. Their influence has left a lasting impression on me. I am especially thankful to Rik for his support during my time in Dresden. I wish them all success and happiness in life.

Finally, I want to thank the most important people in my life—my parents, Manindra Nath Routh and Purabi Routh, my uncle Pradip Routh, my sister Arpita Routh, my elder sister Prativa Routh Das, my brother-in-law Sourav Das, and my nephew Swarnabha Das. They mean everything to me, and words cannot express my gratitude and love for them. Their unwavering support and unconditional love have been my greatest strength. I am also thankful for the goodwill of my extended family from maternal side, especially my uncle Sudip Kumar Maity and aunt Kakali Maity. Above all, my deepest gratitude goes to the love of my life, Manika Ghosh, for standing by me during tough times and sharing my dreams and happiness.

This journey would not have been possible without these amazing people, and I extend my heartfelt gratitude to each of them.

Manodip Routh

List of Publications

To be included in the Ph.D Thesis:

1. **Spin Peierls transition of $J_1 - J_2$ and extended models with ferromagnetic J_1: Sublattice dimerization and thermodynamics of zigzag chains in β-TeVO$_4$**
   Manodip Routh, Sudip Kumar Saha, Manoranjan Kumar, Zoltán G. Soos
   Physical Review B **105** (23), 235109 (2022).

2. **Phase diagram of a spin-$\frac{1}{2}$ coupled trimer system**
   Manodip Routh, Sudip Kumar Saha, Aslam Parvej, Manoranjan Kumar
   (manuscript to be submitted).

3. **Emergent Quadrupolar order in the spin-$\frac{1}{2}$ Kitaev-Heisenberg model**
   Manodip Routh*, Sayan Ghosh*, Jeroen van den Brink, Satoshi Nishimoto, Manoranjan Kumar
   Physical Review B (letter) **109**, L220403 (2024). [*Equal contribution]

4. **Interplay of Dzyaloshinskii-Moriya and Kitaev interactions in honeycomb lattice**
   Manodip Routh, Ayushi Sinhania, Satoshi Nishimoto, Manoranjan Kumar
   (manuscript to be submitted).

Other Works:

1. **Low-temperature thermodynamics of the antiferromagnetic $J_1 - J_2$ model: Entropy, critical points, and spin gap**
   Sudip Kumar Saha, **Manodip Routh**, Manoranjan Kumar, and Zoltán G. Soos
   Physical Review B **103**, 245139 (2021).

2. **Proximate Dirac spin liquid in the honeycomb lattice $J_1 - J_3$ XXZ model: Numerical study and application to cobaltates**
   Anjishnu Bose*, **Manodip Routh***, Sreekar Voleti*, Sudip Kumar Saha, Manoranjan Kumar, Tanusri Saha-Dasgupta, and Arun Paramekanti,
   Physical Review B **108**, 174422 (2023). [*Equal contribution]

3. **Interchain interactions, multimagnon condensation, and strain effect in the chain compound** NaVOPO$_4$
   Manoj Gupta*, **Manodip Routh***, Manoranjan Kumar, Tanusri Saha-Dasgupta
   Physical Review B 110, 054441 (2024). [*Equal contribution]

4. **Emergent quasi-particles in spin-1 trimer chain**
   Manodip Routh*, Anutosh Biswas*, Manoranjan Kumar
   arXiv:2503.12565. [*Equal contribution]

5. **Exploring Quantum Phases in Frustrated Spin-1/2 Chain and Ladders: A Comprehensive Review**
   Manodip Routh*, Sayan Ghosh*, Manoranjan Kumar
   (Submitted in JPCM as an invited topical review). [*Equal contribution]

Contents

Dedication iv

Acknowledgments vii

List of Publications x

List of Figures xxiii

List of Tables xxv

1 Introduction 1

1.1 Frustrated Magnetism 4

1.2 Low-dimensional systems and frustrated magnetism 7

1.2.1 One-dimensional Chain 7

1.2.1.1 Quantum phases 7

1.2.1.2 Experimental realization of 1D chain 10

1.2.1.3 Dimerized $J_1 - J_2$ model 13

1.2.1.4 Experimental realization: Spin-Peierls materials 13

1.2.2 The Kitaev model 14

1.2.2.1 Majorana fermion representation of spin-1/2 15

1.2.2.2 Quadratic Hamiltonian 16

1.2.2.3 Experimental Realization of the Kitaev Model 20

1.3 Outline of the thesis 21

2 Numerical Methods 23

2.1 Introduction 23

2.2 Exact Diagonalization 24

2.3 Density Matrix Renormalization Group (DMRG) 26

2.3.1 Density Matrix Formalism in DMRG 28

2.3.2 DMRG for a 1D Linear Chain 29

2.3.2.1 Infinite DMRG Algorithm 30

2.3.2.2 Finite DMRG Algorithm 31

2.3.3 DMRG algorithm for PBC 33

2.3.4 Finite temperature calculation: Hybrid ED/DMRG 34

2.4 Conclusion 37

3 Spin Peierls transition of $J_1 - J_2$ and extended models with ferromagnetic J_1. 39
3.1 Introduction 39
3.2 Electronic Instability 44
3.3 Thermodynamics 48
3.4 Spin-Peierls transition 51
3.5 β-TeVO$_4$ Thermodynamics 56
3.6 Conclusion 62

4 Phase diagram of spin-1/2 coupled trimer chains 65
4.1 Introduction 65
4.2 Model Hamiltonian & method 67
4.3 Quantum phase diagram 68
4.3.1 High-spin ground state 70
4.3.1.1 Perturbation theory for spin-1/2 trimer chain 72
4.3.2 AFM (QLRO) phase 74
4.3.3 Incommensurate (IC) phase 77
4.3.4 Gapped dimer phase 79
4.3.5 Trimer-dimer transition 79
4.4 Conclusion 81

5 Emergent Quadrupolar Order in the Spin-1/2 Kitaev-Heisenberg Model 83
5.1 Introduction 83
5.2 Quadrupolar operator 84
5.3 Model Hamiltonian 85
5.4 Methods 86
5.5 Quadrupolar order in the 2-leg ladder 86
5.6 Quadrupolar order in the 2D honeycomb lattice 90
5.7 Conclusion 92

6 Impact of Dzyaloshinskii-Moriya in Kitaev-Heisenberg model on honeycomb lattices 95
6.1 Introduction 95
6.2 Model Hamiltonian 97
6.3 Numerical Method 98
6.4 Results for Two-Leg Ladder 98
6.4.1 Phase diagram for finite DMI ($D \neq 0$) 99
6.4.2 Effect of DMI on KSL phases 101
6.5 Chiral spin structure 106
6.6 Results for 2D honeycomb lattice 108
6.7 Conclusion 109

7 Conclusion **111**

Bibliography **113**

List of Figures

1.1 (a) Geometrically frustrated system on a triangular lattice. Three neighboring spins cannot be pairwise antialigned, and the system is frustrated. (b) The kagome lattice consists of corner-sharing triangles. (c) The pyrochlore lattice is a network of corner-sharing tetrahedra. This figure is adapted from Ref. [237]. . 5

1.2 (a) Exchange frustration on a 1D chain with nearest neighbor (NN) exchange J_1 and next-nearest neighbor (NNN) exchange J_2. (b) 1D chain as zigzag ladder with NN exchange J_1 and NNN exchange J_2. (c) coupled trimer chain with intra-trimer NN exchange J_1 and NNN exchange J_2 and inter-trimer NN exchange J_1' and NNN exchange J_2'. (d) two-leg ladder with rung exchange J_r, leg exchange J_l and diagonal exchange J_d. (e) 2D square lattice with NN exchange J_1 and NNN exchange J_2. (f) 2D honeycomb lattice with NN exchange J_1 and NNN exchange J_2. (g) honeycomb lattice with Kitaev exchange. Red, blue and green bonds indicate bond dependent Kitaev exchanges (K_x, K_y, K_z). 6

1.3 The quantum phase diagram of the Hamiltonian $H(J_1, J_2)$, as depicted in Eq. (1.2.1), displays the critical points for the ratio J_2/J_1 at -0.25, -0.81, 2.27, and 0.2411. The exact location of $J_2/J_1 = -0.25$ separates a gapless ferromagnetic (FM) phase from a gapped incommensurate (IC) phase. Between $J_2/J_1 = -0.81$ and $J_2/J_1 = 2.27$, a gapless decoupled phase is observed, where open and closed circles represent spins oriented in and out of the plane, respectively. The gapped IC phase continues until the Majumdar-Ghosh (MG) point, $J_1 = 2J_2$, and the dimer phase persists until $J_2/J_1 = 0.2411$, beyond which the system transitions into a gapless antiferromagnetic (AFM) phase. This figure is reproduced and modified from the ref. [335]. 8

1.4 Doubly degenerate dimerized ground states ($|\mathrm{MG1}\rangle$ and $|\mathrm{MG2}\rangle$) of the MG model are shown and solid bonds indicate the dimer singlet of two neighboring spins. . 9

1.5 3D Crystallographic structures of (a) $CuGeO_3$, (b) $LiCuSbO_4$, and (c) $LiCuVO_4$. In these compounds, edge-sharing CuO_4 octahedra organize into spin-1/2 chains oriented along the *c*-axis in $CuGeO_3$, the *a*-axis in $LiCuSbO_4$, and the *b*-axis in $LiCuVO_4$. The nearest-neighbor (J_1) and next-nearest-neighbor (J_2) spin-exchange interactions are depicted by black lines. The interaction J_1 is antiferromagnetic in $CuGeO_3$, whereas it is ferromagnetic in both $LiCuSbO_4$ and $LiCuVO_4$. 12

1.6 Schematic representation of the Kitaev model. This model features anisotropic spin-spin interactions, where the interaction type depends on the orientation of the bonds. Each bond is labeled as x, y, or z to signify the bond-dependent nature of the interactions. 14

1.7 Schematic representation of the Kitaev model on a honeycomb lattice, featuring bond-dependent interactions K_x, K_y, and K_z. The model admits an exact solution by introducing four Majorana fermions per site (depicted as yellow, blue, green, and brown circles). These fermions can be reorganized into a static $\mathbb{Z}_2$ gauge field (represented by the blue, green, and brown ovals) and a remaining itinerant Majorana fermion (yellow circle). This figure is adapted from Ref. [357]. 17

1.8 Phase diagram of the Kitaev model plotted on the plane satisfying $K_x+K_y+K_z =$ const. The blue-shaded regions represent gapped spin-liquid phases that occur when one of the three coupling strengths dominates. In contrast, a gapless spin-liquid phase emerges near the isotropic point $K_x = K_y = K_z$, marked by the red dot. This figure is adapted from Ref. [357]. 18

1.9 Formation of spin-orbit entangled $j = \frac{1}{2}$ moments in a d^5 electronic configuration, relevant for iridium ions (Ir^{4+}) and ruthenium ions (Ru^{3+}). Figure adapted from Ref. [357]. 20

2.1 **Infinite DMRG steps**. It starts with superblock of four sites as shown in (a). The renormalized system (left or right) block of one site are shown inside the square in solid blue line and the magenta square made of dashed line containing left block and new site represents the new left block for the next step (b) as shown by the magenta arrow. At each step, the superblock size grows. In (c) the targeted system size is shown. 30

2.2 **Finite DMRG steps.** It starts with left and right block of equal size and two new site block of one sites as shown in (a). The renormalized system block is shown inside the blue square made of solid line whereas the magenta square with dotted line represents the new left block for the next step (b). The left/right block increases/decreases back and forth. At the end of the sweep, left and right block are of equal size again as shown in (i). Several steps of a finite dmrg sweeps are shown in (a) - (i). 32

2.3 **DMRG steps for PBC:** At each step, two new blocks of $N = 2$ sites are added, as shown in (a). The renormalized left and right blocks are depicted inside the squares with solid blue lines. The red squares with solid lines represent the new site blocks. The magenta square with dashed lines indicates the new left block, which is formed by combining the old left block and the two new blocks. The new right block is the reflection of the new left block. These become the left and right blocks for the next step (b), as indicated by the magenta arrow. The black squares with solid lines represent the superblock at each step. In (c), the targeted system size is displayed. 35

3.1 (a)–(c) Illustrations of the J_1–J_2 spin chain as described by Eq. 3.1.1, highlighting different dimerization patterns. The exchange interactions vary as $(1+\delta)$ or $(1-\delta)$ depending on whether the associated bond length is shortened or elongated. (a) Uniform chain with evenly spaced spin sites and constant J_1 and J_2 couplings. (b) Dimerized configuration with alternating nearest-neighbor couplings $J_1(1 \pm \delta)$, while next-nearest-neighbor J_2 remains unchanged. (c) Sublattice dimerization applied to the J_2 bonds, producing an alternating $J_2(1 \pm \delta)$ pattern. (d), (e) Schematics of the extended J_1–J_2 model incorporating sublattice dimerization with two geometries: (d) collinear and (e) zigzag. In both cases, every other nearest-neighbor bond maintains $J_1(1 + \gamma)$, while the alternating bond strength follows $J_1(1-\gamma \pm \delta)$. The zigzag structure reduces to a ladder geometry for $\delta = 0$, with leg couplings J_2 and rung couplings alternating as $J_1(1 \pm \gamma)$. 42

3.2 Ground state energy per site for the ferromagnetic J_1–J_2 spin chain consisting of N sites, evaluated for frustration parameters $\alpha = 0.55$ and 0.65. The solid lines represent results obtained using Eq. 3.2.1, incorporating a dimerized chain structure with nearest-neighbor couplings of the form $-(1 \pm \delta)$ and uniform next-nearest-neighbor couplings α. Dashed lines correspond to Eq. 3.2.3, applied in the case of sublattice dimerization with $\gamma = 0$, where the next-nearest-neighbor interactions are modulated as $\alpha(1 \pm \delta)$, and nearest-neighbor couplings alternate between -1 and $-(1 \pm \delta)$. 46

3.3 Entropy per site, $S(T, \alpha, \gamma, N)$, as defined in Eq. 3.2.2, calculated for a spin chain of N sites with no explicit dimerization ($\delta = 0$) and frustration parameter $\alpha = 0.75$. Results are shown for both the standard J_1–J_2 model ($\gamma = 0$) and an extended model with $\gamma = 0.15$. Solid curves represent data obtained using exact diagonalization (ED) for systems up to $N = 24$ (for $\gamma = 0$) and $N = 20$ (for $\gamma = 0.15$), as well as converged density matrix renormalization group (DMRG) results for temperatures $T > T(N)$, indicated by discrete points. Dashed lines illustrate the behavior of $S(T, \alpha, \gamma, N)$ at temperatures below $T(N)$. In the thermodynamic limit, the presence of a finite gap $\Delta(\alpha, \gamma)$ in the extended model ($\gamma = 0.15$) leads to a lower entropy compared to the gapless case ($\gamma = 0$). 50

3.4 Temperature dependence of the magnetic susceptibility $\chi(T, \alpha, \gamma, N)$ as described by Eq. 3.1.1, evaluated for a system of N spins with $g = 2$ and fixed $\alpha = 0.75$. Two cases are shown: the standard J_1–J_2 model with $\gamma = 0$ and the extended model with $\gamma = 0.15$, where $\delta = \gamma$. Solid curves represent exact diagonalization (ED) results up to $N = 24$ for $\gamma = 0$ and up to $N = 20$ for $\gamma = 0.15$, combined with finite-temperature DMRG data (depicted as discrete points) for temperatures above a size-dependent crossover scale $T(N)$. Dashed lines correspond to $\chi(T, \alpha, \gamma, N)$ in the low-temperature regime $T < T(N)$. At zero temperature, the susceptibility vanishes due to finite-size gaps, which extrapolate to a finite excitation gap $\Delta(\alpha, \gamma)$ in the thermodynamic limit for $\gamma = 0.15$. 51

3.5 Temperature-dependent magnetic susceptibility $\chi(T, \alpha, 0)$ for the J_1–J_2 spin chain with uniform exchange interactions ($\delta = 0$ in Eq. 3.1.1), presented as discrete data points for temperatures $T > T(\alpha, 96)$, where numerical convergence is achieved. The susceptibility for the Heisenberg antiferromagnetic (HAF) limit is extended to lower temperatures via extrapolation, approaching the exact zero-temperature value of $1/\pi^2 \approx 0.10132$. 52

3.6 Temperature dependence of the converged quantity $S'(T, \alpha, 0) = C(T, \alpha, 0)/T$ for the J_1–J_2 spin chain with no dimerization ($\delta = 0$ in Eq. 3.1.1). Data points are shown for temperatures $T > T(\alpha, 96)$, where finite-size effects are negligible. . 53

3.7 The thermodynamic driving force $-A'(T, \delta, N)$ associated with sublattice dimerization δ, as described by Eq. 3.4.1, for both the standard J_1–J_2 model and its extended version with $\gamma = 0.15$. Calculations are shown for frustration parameter $\alpha = 0.79$ and a system of N spins, as specified in Eq. 3.2.2. The open circles indicate the temperature $T(N, \delta)$ at which the dimerized phase becomes energetically favorable. 54

3.8 Temperature-dependent amplitude $\delta(T)$ of the sublattice dimerization, as obtained from Eq. 3.4.2, for spin chains comprising $N = 32$ sites. The calculations are based on the model defined in Eq. 3.2.2, with parameters chosen such that the spin-Peierls transition temperature is $T_{SP} = 0.10$. 55

3.9 Temperature dependence of the normalized specific heat, $C(T)/T$, for the spin-Peierls (SP) transitions in both the standard J_1–J_2 model ($\gamma = 0$) and the extended model with $\gamma = 0.15$, evaluated at $\alpha = 0.75$ and $T_{\mathrm{SP}} = 0.10$. The continuous green curves represent the undistorted case ($\delta = 0$), extended to $T = 0$ for $\gamma = 0$, and extrapolated from $T(128)$ down to zero temperature using Eq. 3.4.3 for $\gamma = 0.15$. The solid blue and red curves depict results from Eq. 3.4.3 for system sizes $N = 24$ and $N = 32$, respectively. The dashed red curve corresponds to $C(T, \delta(T))/T$, representing the leading contribution from Eq. 3.4.3 at $N = 32$. 56

3.10 Temperature-dependent magnetic susceptibility $\chi(T, \delta(T))$ computed for the J_1–J_2 model with $\gamma = 0$ and its extended counterpart with $\gamma = 0.15$, both at $\alpha = 0.75$ and spin-Peierls transition temperature $T_{SP} = 0.10$. The green solid curves represent the converged susceptibility $\chi(T, 0)$ for the uniform chain ($\delta = 0$) and temperatures $T \geq T(128)$, where finite-size effects are negligible. The red curves show $\chi(T, \delta(T))$ calculated with the temperature-dependent equilibrium dimerization $\delta(T)$, extrapolated to the thermodynamic limit using a system size of $N = 32$. 57

3.11 Molar magnetic susceptibility $\chi(T)$ of β-TeVO$_4$, with experimental data available down to $T = 1.9$ K from Ref. [312]. All theoretical curves, except for the exact diagonalization (ED) result at $N = 20$, represent converged $\chi(T)$ calculations using the parameters indicated in the legend. The $\chi(T) - 5$ offset curves provide a direct comparison between experiment, ED at $N = 20$, and a converged model incorporating $\gamma = 0.15$. While the theoretical results show good agreement for temperatures above 8 K, discrepancies emerge at lower temperatures. Open circles mark the temperature $T(96)$ associated with J_1–J_2 models at $\gamma = 0$, and the filled square indicates $T(128)$ for both extended models. 59

3.12 Temperature dependence of the molar specific heat divided by temperature, $C(T)/T$, for β-TeVO$_4$ after subtraction of the phonon (Debye) contribution, C_{latt}. Experimental data are taken from Ref. [313]. The plotted theoretical curves represent converged results, except for the exact diagonalization (ED) data at $N = 20$. All calculated curves show good agreement above $T > 7$ K, while deviations appear at lower temperatures. For the J_1–J_2 model with $\gamma = 0$, $C(T)/T$ remains finite as $T \to 0$. In contrast, the $\gamma = 0.15$ curves for $T < T(128)$ are obtained via extrapolation using Eq. 3.4.3. 60

3.13 **Upper panel:** Experimental data for the specific heat divided by temperature, $C(T)/T$, are shown for $T < 6$ K from Refs. [273, 372] and for $T < 10$ K from Ref. [313]. Theoretical curves for $\delta = 0$ correspond to the calculated results with $\gamma = 0.15$ presented in Fig. 3.12. The red curve indicates the predicted spin-Peierls (SP) transition, obtained from Eq. 3.4.1, assuming $\gamma = 0.15$. **Lower panel:** Magnetic susceptibility $\chi(T)$ as measured in Ref. [312]. Theoretical $\chi(T)$ curves for $\delta = 0$ are again shown for $\gamma = 0.15$, consistent with Fig. 3.11. Results labeled $\chi(T, \delta(T))$ incorporate the temperature-dependent lattice distortion $\delta(T)$ from extended models with $\gamma = 0.15$. 61

4.1 Schematic diagram. (a) General structure of a spin-1/2 coupled trimer chain, where J_1 and J_1' represent the antiferromagnetic (AFM) nearest neighbor (NN) intertrimer and intertrimer couplings, respectively. J_2 denotes the AFM next nearest neighbor (NNN) intertrimer and intertrimer couplings. (b) The same coupled trimer is depicted as a zigzag chain at $J_1' = J_1$. 68

4.2 Quantum phase diagram of the Hamiltonian in Eq. (4.2.1): The blue region indicates the AFM (QLRO) phase with quasi-long-range order and gapless excitations. The green region signifies the gapped dimer phase with short-range order. The grey region denotes the incommensurate phase with spiral spin correlations, and the red region represents the trimer phase with a high spin ground state. Phase boundaries are determined based on results from level crossings, excitation gaps, and structure factors. 69

4.3 Energy difference (Γ) between the ground state (gs) in sectors with different S^z relative to $S^z = 0$ as a function of J_2/J_1 for (a) $J_1'/J_1 = 0$ and (b) $J_1'/J_1 = 0.25$, with periodic boundary conditions (PBC) and $L = 48$ spins. The inset in (a) displays a unit cell of the 3/4 skewed ladder with site numbering. 70

4.4 (a) Schematic spin configuration of the high spin ground state with weak intertrimer NN exchange coupling (J_1'), showing the spin alignment along the z-axis. Each triangle acts as an effective spin-1/2. (b) Longitudinal spin correlations ($C(r)$) in the trimer phase for $J_1'/J_1 = 0.05$, 0.15, 0.25, 0.35 with a fixed NNN exchange $J_2/J_1 = 0.5$ and a system size of $L = 48$. The correlations alternate in sign at every third site within a narrow range of $(-0.1, 0.1)$. 72

4.5 Excitation energy of Eq. (4.2.1) for $N = 24$ with PBC for $J_1'/J_1 > 0.4$. E_m represents the lowest triplet and E_σ denotes the lowest singlet with opposite inversion symmetry. The crossing points where $E_m = E_\sigma$ are indicated by solid colored circles. 75

4.6 (a) Schematic spin configuration in the AFM (QLRO) phase, illustrating antiferromagnetic spin alignment along the z-axis. (b) Longitudinal spin correlations ($C(r)$) in this phase for $(J_1'/J_1, J_2/J_1) = (0.10, 0)$, $(0.25, 0.1)$, $(0.50, 0.2)$, $(0.75, 0.2)$, and $(1.0, 0.2)$ with a system size of $L = 96$. The correlations are fitted with a power law with logarithmic correction, indicated by dashed lines. The correlation behavior for the $J_1 - J_2$ model at $J_1'/J_1 = 1$ closely follows a power law ($\sim 1/r$), as indicated by the violet line. (c) Structure factor for the same parameter values $(J_1'/J_1, J_2/J_1)$ diverges at $q = \pi$. 76

4.7 (a) Schematic spin configuration in the incommensurate (IC) phase, showing a spiral pattern of spin alignment. Longitudinal spin correlations ($C(r)$) in this phase for a fixed $J_2/J_1 = 0.8$ with a system size of $L = 96$: (a) for $J_1'/J_1 = 0.10$, 0.25, 0.45, and (b) for $J_1'/J_1 = 0.60$, 0.75, 1.0. In (a), these correlations are fitted with a sinusoidal function with exponential decay, and in (b), they are fitted with a sinusoidal function with algebraic decay, shown by solid colored lines. (d) Structure factor for the same parameter values $(J_1'/J_1, J_2/J_1)$ diverges near $q = \pi/2$ and $3\pi/2$. 78

4.8 (a) Schematic spin configuration in the gapped dimer phase, illustrating the formation of dimers between pairs of spins. (b) Structure factor for $J_1'/J_1 = 1.0$, 0.75, and 0.50 with a fixed $J_2/J_1 = 0.50$, obtained for a system size of $L = 96$, spreading near $q = \pi$. (c) Bond-bond correlations between the two most distant bonds, showing maximum values near the dimer phase and vanishing to zero in the AFM (QLRO) phase. 80

4.9 Fourier transform of bond-bond correlation for a fixed $J_2/J_1 = 0.5$ with system size of $L = 96$: (Top) $J_1'/J_1 = 1.0$, 0.75, 0.50 diverge at $q = \pi/3$ and (b) $J_1'/J_1 = 0.35$, 0.25, 0.10 diverge at $q = 2\pi/3$, $4\pi/3$. 81

5.1 Lattice structures used in our calculations: (a) KH ladder or brickwall lattice which is obtained by deforming the honeycomb-lattice KH model. (b) 2-leg KH ladder. (c) 24-site honeycomb-lattice KH cluster with periodic boundary conditions. 85

5.2 Results for 2-leg KH ladder. (a) Absolute values of the QP order parameter for leg bonds with various system sizes. The inset represents the same physical quantity but without taking absolute values. (b) Ground-state Phase diagram for magnetic order (inner) and QP order (outer). Four long-range ordered phases: rung-singlet (RS), zigzag (ZZ), ferromagnetic (FM), stripy (ST) and two QSL phases: antiferromagnetic Kitaev (AFK) and ferromagnetic Kitaev (FK). (c) Compilation of the behavior of the QP correlation functions $|P_{\mathrm{L1L1}}(r)|$ with $N = 100 \times 2$ cluster for representative parameters (see text). (d) Inter-leg and rung-rung QP correlation functions at $\phi/\pi = 0.5$, 1.2, and 1.5. Inset: Examples for the cases where the QP correlation function exhibits an exponential decay. 87

5.3 Spin nematic state expected for a KH ladder. Schematic representation of bound pairs of magnons moving in a background of polarized spins. Here, most of the spins colored as blue and magenta arrows align in $+z$ or $-z$ directions, respectively. Flipped spins (black arrows) gain energy by propagating as bound pairs along (a) same leg in QP$_1$ phase, (b) both the same leg and across the leg in QP$_2$ phase, (c) rung, same leg and across the leg in QP$_3$ phase. (d) Phase diagram for magnetic order (inner) and QP order (outer). 88

5.4 Results for honeycomb-lattice KH model. (a) Absolute values of the QP order parameter for x or y bond, calculated using the 24-site PBC cluster. For comparison, those for the 2-leg KH ladder are also plotted. The inset represents the same physical quantity but without taking absolute values. (b) Ground-state Phase diagram for magnetic order (inner) and QP order (outer). 90

5.5 DMRG results for the QP correlation functions $P_{\mathrm{L1L1}}(r)$ at representative value of ϕ for six quantum phases using 2-leg, 4-leg, and 6-leg cylinders. 91

5.6 DMRG results for the inter-leg QP correlation functions, $P_{\mathrm{L1Ln}}(r)$ for $n = 1-3$ at magnetic ordered phases, including ZZ ($\phi/\pi = 0.65$), FM ($\phi/\pi = 1.2$), ST ($\phi/\pi = 1.6$) and QSL phase ($\phi/\pi = 0.5$), using 6-leg cylinders. 92

6.1 Schematic diagram of Kitaev Heisenberg (KH) model on (a) 2D honeycomb lattice (b) ladder with second neighbor Dzyaloshinskii-Moriya interaction (DMI). Solid (dashed) lines denote the x, y, z Kitaev (Dzyaloshinskii-Moriya) bonds. The black nearest neighbor bonds are indicating Kitaev exchanges. The red, green and blue dashed second nearest neighbor bonds are indicating bond dependent DM interactions D^x, D^y, and, D^z, respectively. 96

6.2 Phase diagram for two-leg ladder around (a) AFM and (b) FM Kitaev region for two-leg ladder in $\phi/\pi - D$ parameter space. 100

6.3 Schematic representation of spin configurations for the two-leg ladder in different phases: (a) rung-singlet, (b) zigzag, (c) ferromagnetic (FM), and (d) stripy phases. Red and blue arrows denote up and down spins, respectively. Panels (e) and (f) illustrate the spin configurations at $\phi/\pi = 0.50$ and $\phi/\pi = 1.50$ for a strong DMI with $D = 0.1$, exhibiting a chiral nature reminiscent of the vortex state observed in the two-dimensional honeycomb lattice. 102

6.4 ED results for the second-order derivative of the ground-state energy per site, $-E_0''/N$, the plaquette operator, $\mathcal{W}$, and the string order parameter, $\mathcal{O}_{\mathrm{string}}$, on a two-leg ladder as a function of ϕ/π for various values of the DMI (D). Panels (a), (c), and (e) correspond to values around the antiferromagnetic (AFM) Kitaev point, while panels (b), (d), and (f) depict results near the ferromagnetic (FM) Kitaev point. 104

6.5 Correlation length as a function of ϕ/π for several values of DMI ($D = 0$, 0.02, 0.04, 0.05, 0.06, 0.07, and 0.08) with system size of $N = 2 \times 24$. Top (bottom) panel is corresponding to the ϕ/pi around the AFK (FK) points. 105

6.6 Vector chirality $|\hat{n} \cdot v_c|$, where $\hat{n} = (\hat{x} + \hat{y} + \hat{z})/\sqrt{3}$, as a function of ϕ/π for various values of the Dzyaloshinskii-Moriya interaction (DMI) in a system of size $N = 2 \times 12$. The vector chirality is computed for each plaquette and averaged over all plaquettes. A finite value is observed over a broad range of ϕ/π around the antiferromagnetic Kitaev (AFK) and ferromagnetic Kitaev (FK) phases. As the DMI strength increases, the order parameter also increases, indicating the stabilization of magnetic ordering, such as vortex-like states. 107

6.7 Zigzag order parameter as a function of ϕ/π for various DMI with a system size of $N = 2 \times 24$. 108

6.8 Static structure factor ($S(k)$) [Eq. (6.6.1)] computed from ED for 2D-honeycomb lattice with $N = 24$ periodic boundary condition. For weak DMI ($D = 0, 0.02$), we notice that the liquid-like behavior persists, as evidenced by the Bragg peaks spreading around the K-points in the AFK phase and near the Γ-point in the FM phase, while for strong DMI ($0.02 < D \leq 0.10$), the liquid-like phase disappears, and a new phase emerges, where prominent Bragg peaks appear at the K-point, suggesting a phase resembling a vortex phase. 109

6.9 Phase diagram for 2D honeycomb lattice for three representative cases: zero DMI ($D = 0$), weak DMI ($D = 0.02$), and, strong DMI ($D = 0.1$). 110

List of Tables

2.1 For a system consisting of N spins, the total number of basis states varies across different S^z sectors. Each sector corresponds to a specific total spin projection, which determines the available basis states within that subspace. 24

3.1 Size dependence of the curvature $E''(\alpha, \gamma)$ in Eq. 3.2.4 of chains with $\alpha_1 = 0.75$, $\alpha_2 = 1.0$, N spins, and $\gamma_1 = 0$, $\gamma_2 = 0.15$ in Eq. 3.1.1 with $\delta = \gamma$. 47

3.2 Size dependence of $T(\alpha, \gamma, N)$ of chains with $\alpha_1 = 0.75$, $\alpha_2 = 1.0$ and $\gamma_1 = 0$, $\gamma_2 = 0.15$ in Eq. 3.2.2 with $\delta = 0$. 49

3.3 Exchange parameters J_1 and α as reported in Refs. [312], [273], and [372], based on fits to the magnetic susceptibility $\chi(T)$ of β-TeVO$_4$ in the paramagnetic regime. The table also includes the computed values of the saturation magnetic field B_{sat} and molar entropy $S(5.5)$ at 5.5 K. Values in parentheses indicate rescaled J_1 parameters (as described in the main text), along with the corresponding B_{sat} and $S(5.5)$. The bottom two rows present results for extended J_1–J_2 models incorporating an interchain coupling $\gamma = 0.15$. 58

4.1 First and second-neighbor spin-correlation functions $C(j, k)$ of a 3/4 ladder with PBC and $N = 48$ spins. Refer to inset of Fig. 4.3(a) for site numbers. 71

4.2 Matrix elements of spin operators in the new basis. 73

4.3 Matrix elements for $S^z_{i,3/1}$. 73

4.4 Matrix elements for $S^+_{i,3/1}$. 73

4.5 Matrix elements for $S^-_{i,3/1}$. 73

4.6 Matrix elements for $S^z_{i,2}$. 73

4.7 Matrix elements for $S^+_{i,2}$. 73

4.8 Matrix elements for $S^-_{i,2}$. 73

4.9 Crossing points $g^*(J_2/J_1, L)$, where $E_m = E_\sigma$, are presented for $J_1' = 0.4$, 0.6, 0.8, and 1.0 for various system sizes $L = 12$, 18, 24. The extrapolated values of these crossing points are listed in the last row of the table. 75

5.1 Dominant coefficients of the ground state wave function in the zigzag phase at $\phi = 0.65\pi$ with $N = 8 \times 2$ and 10×2 sites ladder. 89

Chapter 1

Introduction

Fundamental particles like electrons, neutrons, and protons serve as the essential components of matter that make up the physical world around us. While the basic principles governing the interactions between electrons and atomic nuclei are well understood, accurately predicting the behavior of systems with many particles remains a complex task. For systems of non-interacting particles, their collective properties can often be determined by averaging the behavior of individual particles. Similarly, weakly interacting particles may sometimes display characteristics resembling those of non-interacting systems. However, in the presence of strong interactions, intricate and remarkable collective phenomena can emerge. Deciphering how these macroscopic behaviors arise from the dynamics of strongly interacting microscopic elements continues to be a challenging and intriguing area of study.

The ratio between the kinetic and interaction energies of microscopic particles is governed by temperature. At low temperatures, the kinetic energy of particles decreases, which enhances the effects of interactions, as seen in ferromagnetic materials. While spin degrees of freedom exhibit significant fluctuations at high temperatures, they tend to align collectively in the same direction when the system is cooled below the Curie temperature. This alignment is primarily driven by the exchange interaction between spin degrees of freedom. The transition from disorder to order in ferromagnetic systems can be understood within the framework of Landau's theory of symmetry breaking. In the disordered state, the system remains invariant under spin rotations, while in the ordered state, a preferred direction is chosen, and the symmetry is spontaneously broken. The concept of symmetry breaking provides a comprehensive explanation for many known phase transitions and constitutes a fundamental principle in condensed matter physics.

However, certain phases of matter cannot be adequately described by Landau's theory. For instance, in the context of high-temperature superconductivity in cuprates such as $\mathrm{La_2CuO_4}$ [26], the system can be effectively modeled using the Hubbard model [12]. The Hamiltonian for this model is given by:

$$\mathcal{H}_{\text{Hubbard}} = -t_{ij} \sum_{\substack{i,j \\ \sigma=\uparrow,\downarrow}} \left(c^{\dagger}_{i\sigma} c_{j\sigma} + \text{H.c.} \right) + U \sum_{i} n_{i\uparrow} n_{i\downarrow}, \tag{1.0.1}$$

where $c^{\dagger}_{i\sigma}$ and $c_{i\sigma}$ represent the electron creation and annihilation operators with spin σ at site i, respectively, and $n_{i\sigma} = c^{\dagger}_{i\sigma} c_{i\sigma}$ is the number operator for spin σ at the i-th site. The sum over i, j indicates any pairs of sites in the lattice. The first term in the Hamiltonian accounts for the hopping of electrons between nearest-neighbor sites, where t_{ij} is the hopping integral between sites i and j. The second term represents the onsite Coulomb repulsion between electrons with opposite spins at the same site, with U being the corresponding on-site Coulomb repulsion energy. Typically t is taken to be positive, and U may be either positive or negative, but is assumed to be positive when considering electronic systems. Though in some cold atom system effective electronic interaction can be negative.

The kinetic energy term, representing electron hopping, delocalize the electrons and drives the system toward metallic behavior. In contrast, the electron-electron interaction term tries to localize electrons, favoring an insulating state. The interplay between these two competing terms underlies phenomena such as the metal-insulator transition [242]. In the limit where $t \gg U$, the system can be described by a band picture of non-interacting particles. Conversely, when $U \gg t$, electrons become highly localized due to the strong Coulomb repulsion. For a fermionic system at half-filling in the strong U limit, double occupancy of lattice sites is not energetically favorable, leading to the suppression of electron hopping to avoid the double occupancy. In this regime, the electrons' spins arrange antiferromagnetically on the lattice to further reduce the system's energy. In the strong U limit, the system develops an energy gap of order U, marking the transition to an insulating state. As $U \to \infty$, the charge degrees of freedom are entirely frozen, leaving only the spin degrees of freedom to dominate the system's behavior. This transition from a metal to an insulator as a function of the ratio U/t is known as the Mott transition [93].

In the strong U limit and at arbitrary filling except half filling, the low-energy approximation of the Hubbard model is described by the $t-J$ model, which incorporates two key interactions: electron hopping and spin exchange [93]. The Hamiltonian of the $t-J$ model is given by:

$$\mathcal{H}_{\mathrm{t-J}} = -t \sum_{\substack{i,j \\ \sigma=\uparrow,\downarrow}} \left(c^{\dagger}_{i\sigma} c_{j\sigma} + \mathrm{H.c.} \right) + J \sum_{i,j} \left(\vec{S}_i \cdot \vec{S}_j - \frac{1}{4} n_i n_j \right), \tag{1.0.2}$$

where the fermionic operators $c^{\dagger}_{i\sigma}$ and $c_{i\sigma}$ have the same meaning as in Eq. (1.0.1), and $\vec{S}_i$ represents the spin vector at site i. The first term describes electron hopping, constrained to avoid double occupancy, while the second term accounts for the antiferromagnetic interaction between nearest-neighbor spins with exchange strength $J = \frac{4t^2}{U}$.

Eq. (1.0.2) indicates that electron hopping persists in a fermionic system away from half-filling even at $U \to \infty$. However, at exactly half-filling and in the large U limit, the $t-J$ model reduces to the Heisenberg antiferromagnet (HAF), where electrons are completely localized with singly occupied sites [93]. The Hamiltonian for the Heisenberg model is given by:

$$\mathcal{H}_{\mathrm{Heisenberg}} = J \sum_{i,j} \vec{S}_i \cdot \vec{S}_j. \tag{1.0.3}$$

The Heisenberg model, Eq. (1.0.3), and its various extensions have been extensively studied in the literature. The behavior of the system depends the sign of the coupling constant J. When $J < 0$, the model is called ferromagnetic (FM), as it energetically favors neighboring spins to align in the same direction. Conversely, for $J > 0$, the model is referred to as antiferromagnetic (AFM), where neighboring spins are energetically favored to align in opposite directions.

The FM Heisenberg model was first studied by W. Heisenberg in 1928 for a spin-1/2 one-dimensional (1D) chain [142]. In 1931, Bethe introduced an ansatz to solve the spin-1/2 isotropic HAF model on a 1D chain [29]. Subsequently, Hulthén derived the exact ground-state (gs) energy of the Heisenberg model [153]. The gs shows quasi long-range spin correlation with gapless continuum of spinon excitations [70, 118].

In many cases, an exact analytical solution is unavailable. For instance, the exact ground state of the two-dimensional spin-1/2 HAF on a square lattice remains unsolved to this day. However, analytical approximation methods such as spin-wave theory [154] and numerical approaches like Exact Diagonalization [252] and Quantum Monte Carlo [283] have conclusively demonstrated that the ground state of this system exhibits magnetic order.

In many cases, magnetic materials described by models such as Eq. (1.0.3) exhibit disordered states at high temperatures and ordered states at low temperatures. However, this behavior is not universal, as certain mechanisms can inhibit the development of magnetic order, even at low temperatures. Key factors that suppress magnetic ordering include the low quantum spin number of the magnetic ions, reduced dimensionality of effective interactions at low temperatures, and various forms of frustration, such as geometric or exchange frustration. The influence of these mechanisms is discussed in detail in Section 1.1.

The properties of disordered states in low-dimensional frustrated quantum magnets present a fascinating area of study. These states often differ significantly from trivial paramagnetic phases, as they lack long-range magnetic order even at absolute zero and are characterized by a low degree of quantum entanglement. Notably, some of these disordered states can possess topological order and are referred to as *Quantum Spin Liquids (QSLs)*.

Quantum spin liquids (QSLs) are extensively studied in lattices characterized by geometric frustration, where spin interactions inhibit long-range magnetic order. Examples include the triangular [362], kagome [373], and pyrochlore lattices [373], where frustration arises from the spin configurations, leading to disordered QSL states. In the Kitaev honeycomb lattice [347], bond-dependent Ising interactions give rise to the Kitaev spin liquid, featuring exotic excitations such as Majorana fermions. These diverse lattice geometries provide unique pathways for realizing QSLs.

Frustrated quantum magnets, representing strongly correlated phases of matter, are governed by intricate interactions that challenge traditional analytical approaches, such as perturbation theory in the non-interacting limit or mean-field approximations, which often fail to accurately capture their behavior. Numerical methods have thus become crucial for studying such systems. Prominent techniques include Exact Diagonalization (ED), Quantum Monte Carlo (QMC) [307], Variational Monte Carlo [45], Density Matrix Renormalization Group (DMRG) [375, 377], and tensor network algorithms [321], each with distinct strengths and limitations. In this work, ED and DMRG have been employed, and their detailed descriptions are provided in Chapter 2.

1.1 Frustrated Magnetism

Frustrated magnetism has emerged as a rich and exciting field of research in condensed matter physics, encompassing phenomena driven by the interplay of quantum mechanics, geometry, and exchange interactions. Magnetic frustration occurs when a magnetic system cannot minimize the energy of all interactions simultaneously, leading to complex and often disordered ground states. This frustration arises when competing interactions—whether geometrical or exchange interactions—prevent a simple magnetic ordering, such as ferromagnetic or antiferromagnetic alignment. Unlike conventional magnets, where spins align in a way that minimizes the system's energy, frustrated magnets are characterized by an inability to simultaneously satisfy all local interactions, often resulting in exotic phases like spin liquids, spin glasses, spiral ordering, or incommensurate phases.

Frustrated magnetism is typically categorized into two types: *geometrical frustration* and *exchange frustration*. These types of frustration differ in their origins and can lead to distinct types of behavior, depending on the dimensionality of the system. In the following sections, we will examine these two categories of frustration from a theoretical perspective, with a focus on 1D chains, quasi-1D systems like zigzag ladder, two-leg ladders, and 2D systems.

Geometrical frustration: In geometrically frustrated magnetic systems, the underlying lattice structure prevents the simultaneous minimization of all spin-spin interactions. A well-known example of this phenomenon occurs in a triangular lattice, where three spins form a fundamental frustrated unit [15, 28, 41, 58, 94]. If two spins within a triangular plaquette align antiferromagnetically to minimize their interaction energy, the third spin cannot align in a way that satisfies all pairwise interactions [see Fig. 1.1 (a)]. Consequently, the system cannot achieve a fully ordered ground state where all interactions are minimized simultaneously.

This inherent incompatibility between antiferromagnetic interactions and the symmetry of the triangular lattice is a hallmark of geometrical frustration. In frustrated magnets, the inability to establish a unique, ordered ground-state configuration at low temperatures often results in a highly degenerate ground-state manifold. As a consequence, such systems can exhibit exotic magnetic phases, including spin liquids and spin ices, where conventional magnetic ordering is suppressed due to frustration.

In 1D and quasi-1D systems, geometrical frustration is typically less pronounced because the interaction is restricted to a linear or nearly-linear arrangement. In 2D systems, geometrical frustration can be more severe. For instance, the Kagome lattice [69, 89, 179, 216, 217, 232, 246, 298, 405] consist of corner shared triangles as shown in Fig. 1.1 (b) is a famous case of geometrically frustrated lattice. In this lattice, no spin configuration can satisfy all the interaction constraints, leading to a highly degenerate ground state. As a result, such systems often exhibit disordered ground states like spin liquids, where the spins do not order even at low temperatures. A three-dimensional analogue is the pyrochlore lattice [16, 50, 97, 251, 262, 373], built from corner-sharing tetrahedra, as shown in Fig. 1.1 (c).

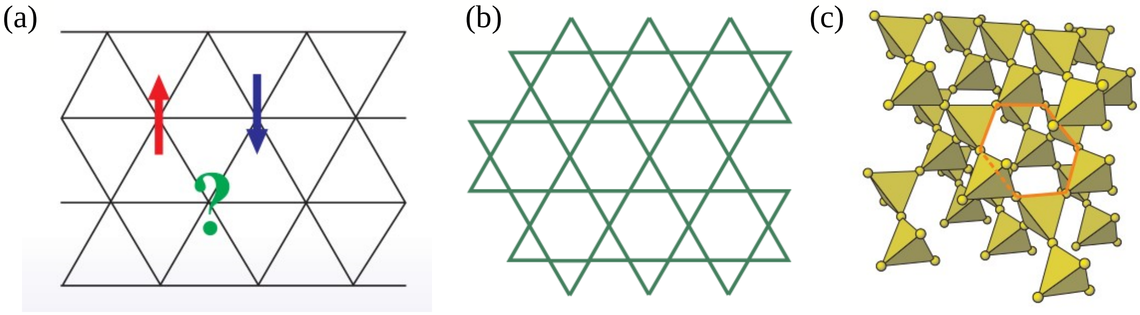

Figure 1.1: (a) Geometrically frustrated system on a triangular lattice. Three neighboring spins cannot be pairwise antialigned, and the system is frustrated. (b) The kagome lattice consists of corner-sharing triangles. (c) The pyrochlore lattice is a network of corner-sharing tetrahedra. This figure is adapted from Ref. [237].

Exchange frustration: Exchange frustration arises from competing exchange interactions between spins, which prevent the system from simultaneously satisfying all the interaction terms. In systems exhibiting exchange frustration, interactions between neighboring spins favor different types of spin alignments, leading to frustration. This form of frustration is especially relevant in systems where competing exchange interactions, such as nearest-neighbor and next-nearest-neighbor interactions, play a dominant role.

In 1D spin chains, frustration is often induced through competing nearest-neighbor (NN) and next-nearest-neighbor (NNN) interactions. For instance, the spin-1/2 Heisenberg chain with NN interaction J_1 and NNN interaction J_2, also known as the $J_1 - J_2$ model, showcases frustration for antiferromagnetic J_1 and any value of J_2 [228, 229]. Quantum fluctuations dominate, suppressing long-range magnetic order and stabilizing exotic phases like spiral, valence bond crystals [122]. This model is discussed in detail in Subsection 1.2.1.

Quasi-1D systems, such as two-leg ladders, provide another canonical example of frustration. Here, frustration arises from competition between rung (J_r) and leg (J_l) couplings. In the strong rung coupling regime ($J_r \gg J_l$), the ground state is a spin-singlet phase dominated by dimerized rung pairs [61–63]. Conversely, in the weak rung coupling regime ($J_r \ll J_l$), the system resembles a gapless spin-liquid state akin to a 1D Heisenberg chain. Introducing diagonal interactions further enhances frustration, destabilizing the singlet phase and potentially giving rise to resonating valence bond (RVB) states. Such systems are invaluable for investigating the crossover between 1D and 2D physics. Fig. 1.2 (a-d) shows the examples of exchange frustration in various 1D chain and two-leg ladder lattices.

In 2D systems, exchange frustration is typically more pronounced, often giving rise to a diverse array of exotic phases. For instance, the J_1-J_2 Heisenberg model, defined on square, triangular, or honeycomb lattices, exhibits a complex phase diagram characterized by competing antiferromagnetic orders. The frustration inherent in these systems can stabilize spiral or non-collinear magnetic ordering, depending on the relative strengths of the nearest-neighbor (J_1)

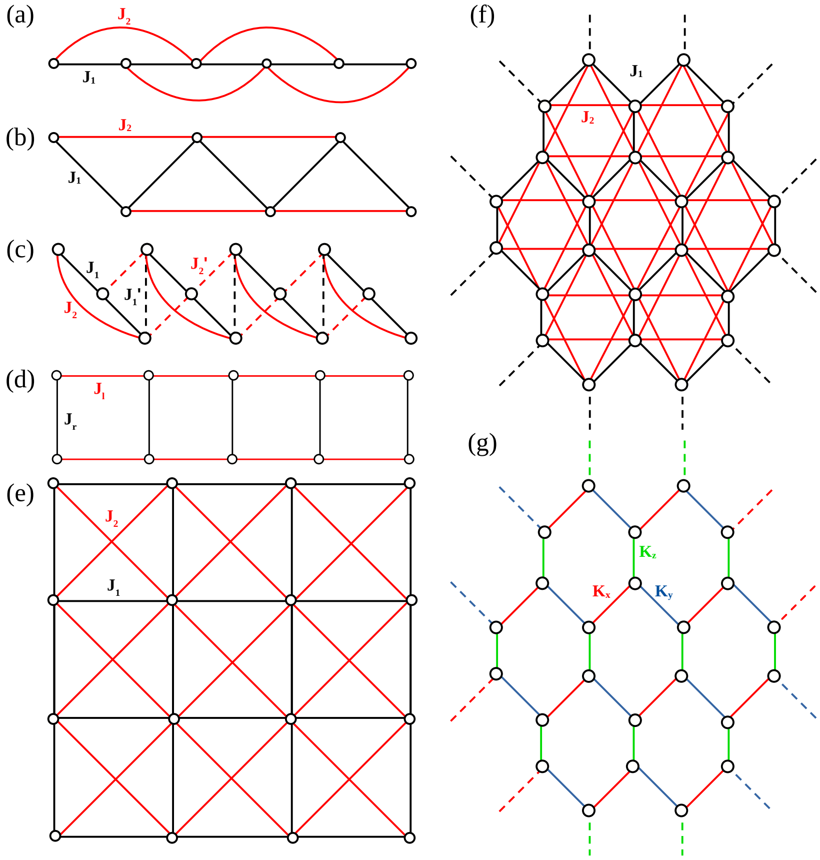

Figure 1.2: (a) Exchange frustration on a 1D chain with nearest neighbor (NN) exchange J_1 and next-nearest neighbor (NNN) exchange J_2. (b) 1D chain as zigzag ladder with NN exchange J_1 and NNN exchange J_2. (c) coupled trimer chain with intra-trimer NN exchange J_1 and NNN exchange J_2 and inter-trimer NN exchange J_1' and NNN exchange J_2'. (d) two-leg ladder with rung exchange J_r, leg exchange J_l and diagonal exchange J_d. (e) 2D square lattice with NN exchange J_1 and NNN exchange J_2. (f) 2D honeycomb lattice with NN exchange J_1 and NNN exchange J_2. (g) honeycomb lattice with Kitaev exchange. Red, blue and green bonds indicate bond dependent Kitaev exchanges (K_x, K_y, K_z).

and next-nearest-neighbor (J_2) exchange interactions [31, 77, 100, 111–113, 151, 188, 215, 235, 239, 285, 359, 383]. Fig. 1.2 (e-f) shows the examples of exchange frustration in various 2D lattices.

Another prominent example of exchange frustration is the Kitaev model on the honeycomb lattice, introduced by Alexei Kitaev in 2006 [184], which has significantly advanced the understanding of quantum magnetism by providing a concrete framework for studying quantum spin liquids (QSLs). The Kitaev model describes a system of spin-1/2 particles on a two-dimensional honeycomb lattice as shown in Fig. 1.2 (g), where the interactions are bond-dependent and anisotropic—each bond allows spin interactions along a single spin component. This unique interaction geometry induces frustration, preventing the spins from forming conventional long-range magnetic order. Instead, the system realizes a quantum spin liquid state, characterized by long-range quantum entanglement and the absence of magnetic order, even at zero temperature.

A key feature of the Kitaev model is its exact solvability in the absence of a magnetic field, which allows for a rigorous analysis of its fractionalized excitations, including Majorana fermions. Furthermore, under an applied magnetic field, the model transitions into a topological phase supporting non-Abelian anyons, with potential applications in fault-tolerant quantum computation. Experimental evidence from materials such as α-RuCl$_3$ has revealed behavior consistent with the Kitaev model, establishing its relevance for understanding quantum materials and exploring advanced technologies. A detailed discussion of the Kitaev model is provided in Subsection 1.2.2.

1.2 Low-dimensional systems and frustrated magnetism

Low-dimensional quantum spin systems, including one-dimensional (1D) chains, quasi-1D systems such as two-leg ladders, and two-dimensional (2D) lattices, provide an ideal platform for investigating the effects of frustration in magnetism. The pronounced influence of quantum fluctuations in these geometries makes them particularly interesting for theoretical and experimental studies.

1.2.1 One-dimensional Chain

A notable model incorporating both nearest-neighbor and next-nearest-neighbor interactions was introduced by Majumdar and Ghosh in 1969 [228, 229]. The Hamiltonian for this system is expressed as:

$$H(J_1, J_2) = J_1 \sum_i \vec{S}_i \cdot \vec{S}_{i+1} + J_2 \sum_i \vec{S}_i \cdot \vec{S}_{i+2}, \tag{1.2.1}$$

where the first term represents the nearest-neighbor exchange interaction, and the second term corresponds to the next-nearest-neighbor interaction. When $J_2 > 0$, the model exhibits frustration, irrespective of the sign of J_1. The degree of frustration is characterized by the parameter $\alpha = J_2/J_1$, which quantifies the competition between these exchange couplings. Since the model consists of a single spin per unit cell, the total spin $S = \sum_i S_i^z$ remains a conserved quantity. The spin exchange interactions for this system are illustrated in Fig. 1.2 (a). In the limit of large J_2/J_1, the structure effectively maps onto a zigzag chain [55].

1.2.1.1 Quantum phases

The ground-state quantum phase diagram of Eq. (1.2.1) in the $J_1 - J_2$ parameter space is shown in Fig. 1.3, revealing six primary quantum phases, including gapless QLRO (π), decoupled gapless QLRO ($\pi/2$), a gapped dimer phase, gapped spiral-I and spiral-II phases, and a ferromagnetic (FM) phase. Let us now discuss these phases in detail.

Quasi-long range order (QLRO): At $J_2 = 0$, $J_1 > 0$ limit, the model in Eq. (1.2.1) reduced to a Heisenberg antiferromagnetic (HAF) spin-1/2 chain. The ground state exhibits an antiferromagnetic spin arrangement, as illustrated in Fig. 1.2 (a). The energy spectrum is gapless

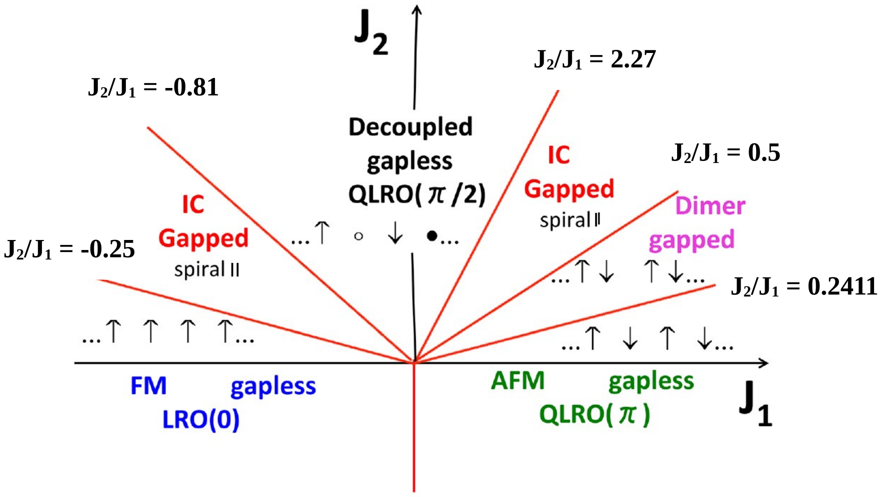

Figure 1.3: The quantum phase diagram of the Hamiltonian $H(J_1, J_2)$, as depicted in Eq. (1.2.1), displays the critical points for the ratio J_2/J_1 at -0.25, -0.81, 2.27, and 0.2411. The exact location of $J_2/J_1 = -0.25$ separates a gapless ferromagnetic (FM) phase from a gapped incommensurate (IC) phase. Between $J_2/J_1 = -0.81$ and $J_2/J_1 = 2.27$, a gapless decoupled phase is observed, where open and closed circles represent spins oriented in and out of the plane, respectively. The gapped IC phase continues until the Majumdar-Ghosh (MG) point, $J_1 = 2J_2$, and the dimer phase persists until $J_2/J_1 = 0.2411$, beyond which the system transitions into a gapless antiferromagnetic (AFM) phase. This figure is reproduced and modified from the ref. [335].

[124]. Luther and Peschel [224] first predicted the critical exponents for spin-spin power-law correlations in 1975, which agreed with Bonner and Fisher's seminal numerical results from 1964 [33]. In 1989, a multiplicative logarithmic correction to the power-law decay was introduced due to a marginally irrelevant "spin-Umklapp" process [1, 2, 107, 328], later verified numerically [9, 55, 82, 121, 125, 129, 159, 200, 201, 254, 354, 381]. The spin correlation function is given by

$$\langle S(r) \cdot S(0) \rangle \propto \frac{(-1)^r \log(r)^{1/2}}{r}. \tag{1.2.2}$$

This phase is referred QLRO (π), which signifies quasi-long-range order in the spin correlations at the wave vector $q = \pi$. Sandvik has reviewed numerical studies of the HAF and related spin chains, at $\alpha < 1$ [308]. Lecheminant addressed frustrated 1D spin system mainly from field theory perspective for $\alpha < 1$ [212]. The spectrum of this model in small α limit has been extensively studied and it is found that the lowest excitation of this model is a triplet state. [10, 11, 227].

In another extreme limit, where $J_1 \sim 0$ and $J_2 > 0$, the system can be viewed as a zigzag ladder, with all odd and all even sites forming the two legs of this ladder, connected by J_2 exchanges. The J_1 exchanges serve as the rungs between the legs, as illustrated in Fig. 1.2 (b). In absence of rung the ladder acts as two decoupled chains, with each chain behaving as a HAF spin chain exhibiting an antiferromagnetic spin configuration. The spin correlation follows the power law behavior with wave vector at $q = \pi/2$. This phase is referred to as QLRO ($\pi/2$). It persists for $-0.81 < J_2/J_1 < 2.27$ [205, 335].

Dimer phase: The doubly degenerate ground state and it's wave function was predicted by C. K. Majumdar and D. Ghosh at $J_2/J_1 = 1/2$ and it is written by

$$\begin{aligned} |\Psi_1^{\mathrm{MG}}\rangle &= \prod_{i=1}^{N/2} [2i-1, 2i] \\ |\Psi_2^{\mathrm{MG}}\rangle &= \prod_{i=1}^{N/2} [2i, 2i+1], \end{aligned} \tag{1.2.3}$$

where $[i, j]$ singlet dimer $[i, j] = \frac{1}{\sqrt{2}}(\uparrow_i\downarrow_j - \downarrow_i\uparrow_j)$. Pictorial representation of the ground states are shown in Fig. 1.4. The ground state energy is $E^{\mathrm{MG}} = -\frac{3J_1N}{8}$, and the singlet-triplet spin gap is exactly $\Delta = J_1$ [228, 229]. The gapless QLRO (π) to gapped dimer transition was first predicted in 1983 by D. Haldane at $J_2/J_1 = 0.3$ [123]. Later, it was shown numerically that the critical point is at $J_2/J_1 = 0.2411$ by Okamoto and Nomura using the level crossing method [253]. DMRG calculations also supported this claim [55, 200, 381]. For $J_2/J_1 > 0.2411$, the spin gap grows exponentially, as predicted by White and Affleck using a combination of DMRG and field theory. The spin gap is exponentially small, with the inverse correlation length. The expression for the spin gap, Δ, is given by [381]:

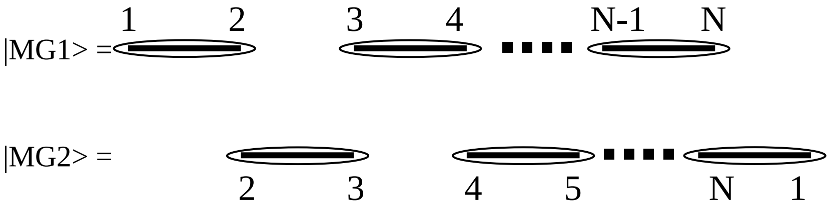

Figure 1.4: Doubly degenerate dimerized ground states ($|\mathrm{MG1}\rangle$ and $|\mathrm{MG2}\rangle$) of the MG model are shown and solid bonds indicate the dimer singlet of two neighboring spins.

$$\Delta = \frac{v_s}{\xi} \propto exp(J_1/(J_2 - J_{2c})), \tag{1.2.4}$$

where v_s and ξ are the spin wave velocity and correlation length in the system and $J_{2c} = J_2/J_1 = 0.2411$. White et al. concluded that this phase extends to $J_1 = 0$. Itoi and Qin presented a more detailed field theory for large J_2/J_1 [159] and showed that the spin correlation length diverges as:

$$\xi(J_1, J_2) \sim \exp\left[c\left(\frac{|J_1|}{J_2}\right)^{-2/3}\right] \tag{1.2.5}$$

The spin correlation function and Δ in this phase are extensively studied by various group [55, 200, 201, 381]. The dimer phase extends from $J_2/J_1 = 0.2411$ to 0.5, as shown in Fig. 1.3.

Gapped spiral I & II: In the antiferromagnetic regime ($J_1 > 0$), the gapped spiral I phase emerges at $J_2/J_1 \approx 0.55$ and persists until the decoupled phase at $J_2/J_1 = 2.27$. A similar gapped spiral phase, referred to as gapped spiral II, exists in the ferromagnetic regime ($J_1 < 0$) and spans the range $J_2/J_1 = -0.25$ to $J_2/J_1 = -0.81$. The ground state of both phases is dimerized, characterized by a finite Δ and exponentially decaying correlations [159, 335]. However, the spin gap and dimerization in the ferromagnetic regime are significantly smaller compared to their antiferromagnetic counterparts. Within these phases, the nearest-neighbor spins align with a specific pitch angle or spin wave vector q_G, determined by the J_2/J_1 ratio [38, 55, 200, 201, 353, 380].

Ferromagnetic phase: This is a trivial phase where all the spins are aligned in the same direction. However, as we increase the antiferromagnetic J_2, the frustration in the system grows, leading to a first-order transition to a singlet state at $J_2/J_1 = 1/4$. Badar et al. showed that for the ferromagnetic condition, $|J_1|/J_2 > \cos^2(\pi/N)$, where N is the system size of a one-dimensional chain [17]. Later, the transition from the ferromagnetic to the incommensurate phase at $J_2/J_1 = -0.25$ was studied by various groups [147, 196, 203, 342].

1.2.1.2 Experimental realization of 1D chain

Spin chain systems provide a vital connection between advanced concepts in many-body quantum physics and experimentally measurable properties in real materials. Furthermore, we demonstrate that frustrated magnets, characterized by a macroscopic number of quasi-degenerate states in competition, serve as an exceptional platform for exploring emergent exotic phenomena [206]. Notably, the interplay between geometric frustration and confined dimensionality facilitates the emergence of unexpected quantum phases, often associated with the spontaneous breaking of continuous or discrete symmetries, a phenomenon referred to as “order by disorder”.

In this section, we focus on the realization of the MG model in real materials. As noted earlier, low-dimensional spin-1/2 structures are commonly found in three-dimensional transition metal (TM) oxides. These materials are typically insulating in nature and exhibit localized magnetic moments. For instance, a material containing copper in the +2 oxidation state (Cu^{2+}) effectively exhibits spin-1/2. The magnetic interaction between two neighboring Cu spin-1/2 moments can arise either from direct overlap of the d-orbitals, resulting in direct exchange, or through non-magnetic ligands, leading to an indirect exchange process. Such ligands can include individual atoms such as oxygen, sulfur, or halides, or more complex molecular systems [303].

Copper oxide-based structures can be broadly classified into two categories based on the connectivity of their CuO_6 octahedra. In corner-sharing CuO_6 octahedra, each octahedron shares only a corner (vertex) with its neighbors. This arrangement facilitates significant overlap between the p-orbitals of oxygen and the 3d orbitals of adjacent Cu ions, resulting in stronger electronic interactions. Consequently, these materials exhibit stronger magnetic exchange interactions. Notable examples include Sr_2CuO_3 and $SrCuO_2$ [241].

In contrast, edge-sharing CuO_6 octahedra share one edge with neighboring octahedra, leading to a bonding environment where the orbitals of adjacent Cu ions are nearly orthogonal. This configuration limits orbital overlap and weakens direct electronic interactions, thereby reducing the dimensionality of magnetic interactions and weakening the exchange coupling.

The Goodenough-Kanamori-Anderson (GKA) rule [13, 14, 114, 173] suggests that the bond angle is also crucial in determining the nature of the exchange interaction. When the Cu-O-Cu bond angle is close to approximately 90°, it favors the superexchange mechanism, resulting in a ferromagnetic interaction. In contrast, when the bond angle is close to 180°, it leads to an antiferromagnetic exchange.

Several other transition metal (TM) atoms may also exhibit an effective spin-1/2, depending on factors such as the ionic state of the atom, crystal field splitting, and other environmental conditions. For instance, vanadium-based compounds [46, 110, 158, 191, 268, 304, 310, 312, 364, 365] can form atomic doublets or effective spin-1/2 states, exhibiting behavior analogous to the spin-1/2 state of Cu^{2+}. In many cuprates, the next-nearest-neighbor spin exchange, J_2, is finite due to possible exchange pathways such as Cu-O-O-Cu, which typically result in antiferromagnetic interactions. As previously discussed, a finite antiferromagnetic J_2 introduces frustration irrespective of the nature of the nearest-neighbor exchange, J_1. The magnitude of J_2 is influenced by the effective orbital overlaps between next-nearest-neighbor atoms.

The exchange interactions in these materials can be quantitatively determined by fitting experimental data, such as magnon dispersion obtained from neutron scattering measurements, specific heat, and magnetic susceptibility. This section focuses on spin-1/2 quasi-one-dimensional chain or zigzag ladder materials and their modeling using the MG model, emphasizing their J_1 and J_2 parameters.

There are numerous materials that exhibit antiferromagnetic J_1 and J_2 interactions, such as Sr_2CuO_3 [189, 241, 323, 333] and $SrCuO_2$ [156, 233, 241, 333, 409]. In ferromagnetic J_1 of the $J_1 - J_2$ model spin-1/2 chain are generally realized in edge-shared cupric octahedron CuO_6 and the bond angle Cu-O-Cu is generally 90^o . The exchange ratio $\alpha = J_2/|J_1|$ in these system may ranges from [80, 202] $\alpha \approx 0$ in $Ba_3Cu_3In_4O_{12}$ or $Ba_3Cu_3Sc_4O_{12}$ to $\alpha \approx 0.5$ in $(N_2H_5)CuCl_3$, [226] $LiCu_2O_2$, [263] $LiCuSbO_4$, [81] $LiCuVO_4$, [243] and $Rb_2Cu_2Mo_3O_{12}$ [134] and $LiCuVO_4$ [367] .

The compound $LiCuSbO_4$ is a well-studied spin-$\frac{1}{2}$ chain system that exhibits a ferromagnetic nearest-neighbor exchange interaction, denoted as J_1, along with a competing next-nearest-neighbor antiferromagnetic interaction. The interaction ratio is given by $J_2/J_1 = -0.45$ [81]. The crystallographic structure of $LiCuSbO_4$ is depicted in Fig. 1.5(b). Experimental investigations reveal the absence of three-dimensional magnetic ordering down to a temperature of 100 mK. Additionally, in the presence of an external magnetic field, the system stabilizes a spin-nematic phase, with weak anisotropy in the exchange interactions also being observed [117]. This behavior is in contrast to that of $LiCuVO_4$, which undergoes long-range magnetic ordering at sufficiently low temperatures, whereas $LiCuSbO_4$ remains in a disordered state down to $T_N = 0.1$ K.

The compound $LiCuVO_4$ is extensively studied for its ferroelectricity at low temperatures and spin nematicity under high magnetic fields. The crystal structure of this material is illustrated in Fig. 1.5(c). The Cu^{2+} ions form magnetic chains with spin $S = \frac{1}{2}$ along the

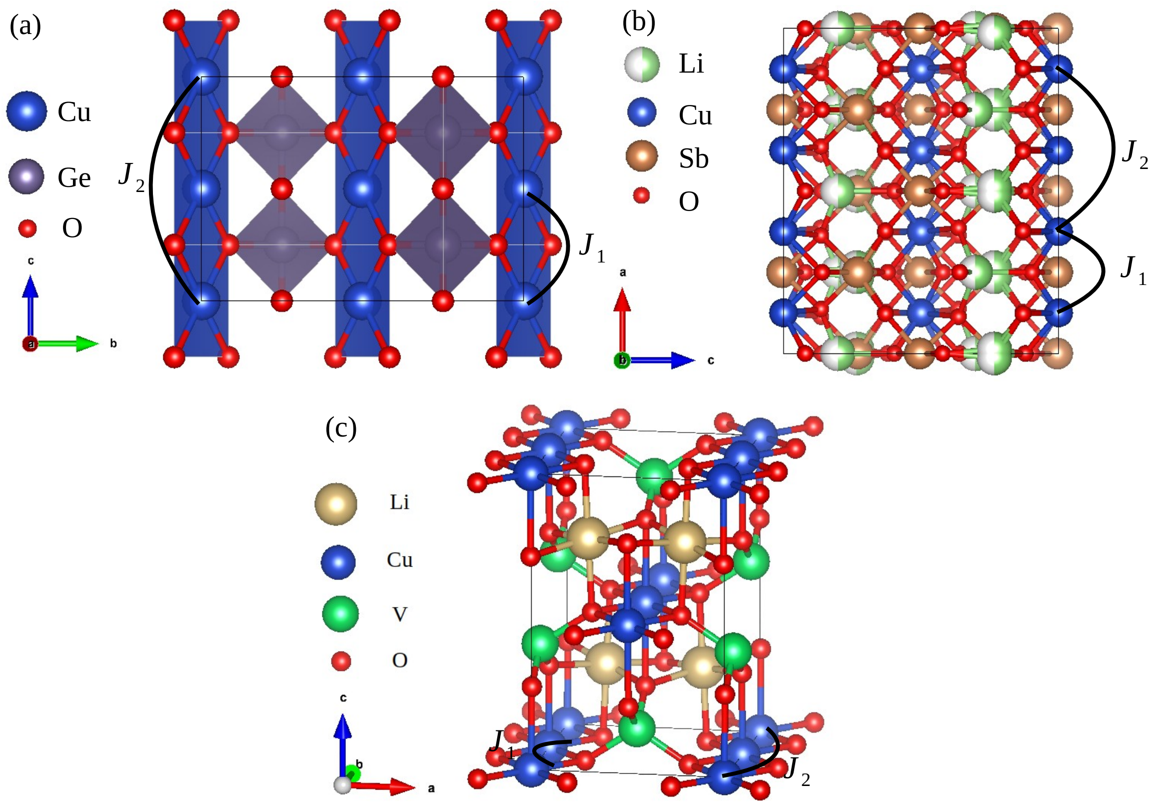

Figure 1.5: 3D Crystallographic structures of (a) $CuGeO_3$, (b) $LiCuSbO_4$, and (c) $LiCuVO_4$. In these compounds, edge-sharing CuO_4 octahedra organize into spin-1/2 chains oriented along the c-axis in $CuGeO_3$, the a-axis in $LiCuSbO_4$, and the b-axis in $LiCuVO_4$. The nearest-neighbor (J_1) and next-nearest-neighbor (J_2) spin-exchange interactions are depicted by black lines. The interaction J_1 is antiferromagnetic in $CuGeO_3$, whereas it is ferromagnetic in both $LiCuSbO_4$ and $LiCuVO_4$.

orthorhombic b axis [367]. The coupling constants are given by $J_1 = -19$ K and $J_2 = 44$ K. However, to accurately describe the long-range helical order that emerges at the Néel temperature $T_N = 2.4$ K, an interchain coupling $J_0 = -4.6$ K must be considered [87].

Another spin-1/2 chain system exhibiting diverse magnetic phases is the linarite compound $PbCuSO_4(OH)_2$. Linear spin wave theory predicts the exchange couplings to be $J_1 = -114$ K and $J_2 = 37$ K [297], although experimental observations suggest a weak interchain coupling of $J_0 = 4$ K. Density matrix renormalization group (DMRG) calculations indicate anisotropic behavior for the exchange interaction, with $J_1 = (J_{1x}, J_{1y}, J_{1z}) = (-91.1, -86.6, -88.4)$ K and $J_2 = 28.3$ K, providing a more refined description of the experimental findings. These calculations further predict an interchain coupling of $J_0 = 2.7$ K [141]. Several studies have explored the magnetic properties of this material [99, 271, 389].

The family of compounds $A_2Cu_2Mo_3O_{12}$ (A = Rb or Cs) represents another class of one-dimensional spin-1/2 Heisenberg systems. For A = Rb, the system exhibits a ferromagnetic exchange interaction with $J_1 = -138$ K and an antiferromagnetic interaction with $J_2 = 51$ K, while for A = Cs, the values of J_1 and J_2 are -93 K and 33 K, respectively [101, 136]. The compound $Rb_2Mo_3Cu_2O_{12}$ is an ideal candidate for studying systems near the critical value of

$J_2/J_1 = 0.25$ [134, 136, 139, 407]. The interaction ratio suggests that $Rb_2Mo_3Cu_2O_{12}$ hosts a spin-singlet incommensurate (IC) ground state. Thermodynamic properties such as magnetic susceptibility and specific heat, along with the field dependence of magnetization, have been computed by H. T. Lu et al. [222] using the transfer-matrix renormalization group method.

1.2.1.3 Dimerized $J_1 - J_2$ model

In certain cases, the interaction between electrons and lattice vibrations can result in lattice dimerization at low temperatures. Assuming that the dimerization affects only the nearest-neighbor exchange interactions, the modified form of the dimerized MG model can be expressed as follows:

$$H = \sum_n J_1(1 + (-1)^i \delta)(\vec{S}_i \cdot \vec{S}_{i+1}) + J_2(\vec{S}_i \cdot \vec{S}_{i+2}) \tag{1.2.6}$$

The parameter δ represents the dimerization in the nearest-neighbor exchange interactions. The ground state of the dimerized antiferromagnetic Heisenberg spin-1/2 chain is a non-degenerate singlet, and the Hamiltonian exhibits an energy gap between the singlet ground state and the lowest triplet state for any finite value of δ. This model was first studied by Bray et al. in 1975 to describe the magnetic properties of a specific material within the mean-field approximation [35]. Subsequent theoretical investigations by various groups have provided significant insights into its properties [34, 325, 345, 370]. Cross and Fisher analyzed the dimerized Heisenberg spin-1/2 chain using the mean-field random-phase approximation [59, 60]. The scaling theory predicts that the spin dimerization energy $\epsilon(\delta)$ and the spin gap $\Delta(\delta)$ scale as $\delta^{4/3}$ and $\delta^{2/3}$, respectively [59, 60]. However, experimental results have shown deviations from these scaling predictions for the spin gap [91, 170, 261].

The modeling of dimerized antiferromagnetic spin-1/2 Heisenberg chains remains a challenging problem. Recently, hybrid methods combining exact diagonalization and DMRG have emerged as accurate tools for investigating the magnetic properties of spin-Peierls and dimerized spin systems [299, 300].

1.2.1.4 Experimental realization: Spin-Peierls materials

The spin-Peierls (SP) transition in the antiferromagnetic spin-1/2 system is analogous to the Peierls transition in fermionic systems [109, 119, 265]. This transition is characterized by a lattice dimerization at low temperatures. In fermionic systems, dimerization leads to the opening of a gap at the Brillouin zone boundary in the electronic spectrum. A similar phenomenon occurs in spin chains, where dimerization stabilizes the ground state energy and opens an energy gap [36, 275].

The spin-Peierls transition was initially discovered in the organic compound TTF-$CuS_4C_4(CF_3)_4$ at $T_{SP} = 12$ K [35, 161]. The spin-1/2 chain at $T > T_{SP}$ has equally spaced TTF+ ion and is dimerized below $T < T_{SP}$. This compound is modeled by linear Heisenberg antiferromagnetic chain with equal exchange J_1 to both neighbors for $T > T_{\rm SP}$ and alternating exchange $J_1(1 \pm \delta(T))$ for lower T. Subsequently, Hase et al. found that the reduction in magnetic susceptibility, $\chi(T)$ for an inorganic compound CuGeO$_3$ [132] with $T_{\rm SP} = 14$ K. Its crystal structure is depicted in Fig. 1.5(a). By analyzing magnetic susceptibility for $T > T_{\rm SP}$, Riera and Dobry estimated $J_2/J_1 = 0.35$ with $J_1 = 160$ K [290]. However, the extensive studies of $\delta(T)$ for this compound remains inconclusive [363]. Sudip et al. utilized a hybrid ED/DMRG [299] approach, adopting the parameters $J_1 = 160$ K and $J_2/J_1 = 0.35$ [301]. They showed the scaling of $\delta(T)$ with T and scaling of singlet-triplet gap $\Delta(T)$ with T for $T < T_{\rm SP}$.

1.2.2 The Kitaev model

In this subsection, we provide a brief introduction to the Kitaev model and outline its exact solution as originally derived in Ref. [184]. This spin-1/2 model has been defined on a honeycomb lattice with a spin-1/2 at every site.

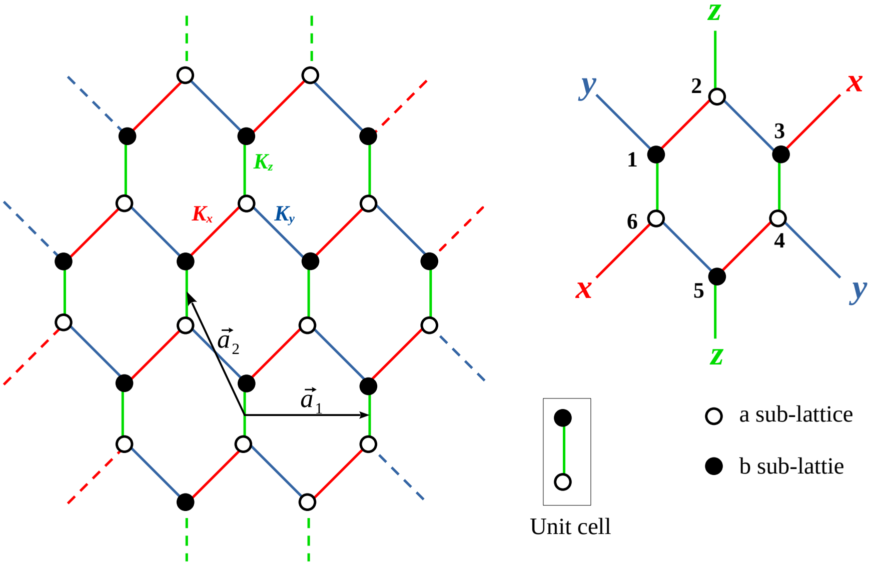

Figure 1.6: Schematic representation of the Kitaev model. This model features anisotropic spin-spin interactions, where the interaction type depends on the orientation of the bonds. Each bond is labeled as x, y, or z to signify the bond-dependent nature of the interactions.

In a honeycomb lattice, there exist three distinct types of bonds that are related by a 120° rotation symmetry. The system's Hamiltonian incorporates anisotropic nearest-neighbor spin-spin interactions, meaning that the interaction depends on the specific bond direction. Consequently, the bonds are classified into three categories: "x-links," "y-links," and "z-links," as depicted in Fig. 1.6. A pair of neighboring spins connected via an α-link ($\alpha = x, y, z$) interact through the α-component of their spin operators, contributing a term of the form $\sigma_i^\alpha \sigma_j^\alpha$ to the Hamiltonian, where the indices i and j label the lattice sites. This structure applies similarly to interactions along "y-links" and "z-links." Hence, the Hamiltonian can be written as:

$$H_{\text{Kitaev}} = -K_x \sum_{\text{x-links}} \sigma_i^x \sigma_j^x - K_y \sum_{\text{y-links}} \sigma_i^y \sigma_j^y - K_z \sum_{\text{z-links}} \sigma_i^z \sigma_j^z, \tag{1.2.7}$$

where K_x, K_y, and K_z are model parameters, and j and k label generic nearest-neighbor sites. The presence of anisotropic interactions in this spin model implies that it belongs to the class of frustrated spin systems, as a spin at any given site cannot simultaneously satisfy all three distinct interactions corresponding to the three different bond directions.

One of the fundamental characteristics of this model is the presence of multiple conserved quantities. Specifically, for each plaquette, it is possible to define an operator that commutes with the Hamiltonian. This operator, commonly referred to as the plaquette operator, is represented as $\mathcal{W}_p$, where the index p designates the corresponding plaquette. The explicit expression for the plaquette operator $\mathcal{W}_p$ is given by

$$\hat{\mathcal{W}}_p = \sigma_1^y \sigma_2^z \sigma_3^x \sigma_4^y \sigma_5^z \sigma_6^x \tag{1.2.8}$$

These plaquette operators satisfy

$$[\hat{\mathcal{W}}_p, \hat{\mathcal{W}}_q] = 0; \quad [H, \hat{\mathcal{W}}_p] = 0. \tag{1.2.9}$$

In this model, $\mathcal{W}_p$ serves as a conserved quantity. One can verify that $\mathcal{W}_p^2 = 1$, indicating that the eigenvalues of $\mathcal{W}_p$ are restricted to ± 1.

To explore the exact solution of the Kitaev model, we consider an approach that utilizes fermionization. This method, originally introduced in Ref. [184], involves expressing spin-1/2 operators in terms of Majorana fermions. The subsequent subsection provides a comprehensive discussion of this formalism.

1.2.2.1 Majorana fermion representation of spin-1/2

We begin by considering a description in which each site of the honeycomb lattice accommodates two fermionic modes, labeled as '1' and '2'. The corresponding creation and annihilation operators are denoted by $c_1^\dagger$, $c_2^\dagger$, c_1, and c_2, respectively. These operators define a four-dimensional Fock space, spanned by the basis states $|n_1, n_2\rangle = |0,0\rangle, |0,1\rangle, |1,0\rangle$, and $|1,1\rangle$, where n_1 and n_2 represent the occupation numbers of the two fermionic modes. Next, we make these fermion operators by using four Majorana fermions

$$\begin{aligned}
c &= c_1 + c_1^\dagger, \\
b^x &= \frac{1}{i}(c_1 - c_1^\dagger), \\
b^y &= c_2 + c_2^\dagger, \\
b^z &= \frac{1}{i}(c_2 - c_2^\dagger).
\end{aligned} \tag{1.2.10}$$

The operators $(\gamma_1, \gamma_2, \gamma_3, \gamma_4) = (b^x, b^y, b^z, c)$ satisfy the following relations:

$$\{\gamma_l, \gamma_m\} = \gamma_l\gamma_m + \gamma_m\gamma_l = \delta_{lm}; \quad \gamma_l = \gamma_l^\dagger. \tag{1.2.11}$$

We now introduce a representation of a spin degree of freedom using four Majorana operators. These operators act within the four-dimensional Fock space $\tilde{\mathcal{M}}$, while the physical Hilbert space corresponding to a single spin is identified as a two-dimensional subspace $\mathcal{M} \subset \tilde{\mathcal{M}}$, constrained by the following condition:

$$|\xi\rangle \in \mathcal{M} \quad \text{if and only if} \quad D\,|\xi\rangle = |\xi\rangle\,, \quad \text{where} \quad D = b^x b^y b^z c \tag{1.2.12}$$

We define $\mathcal{M}$ as the physical subspace and $\tilde{\mathcal{M}}$ as the extended space. The spin-1/2 Pauli operators, denoted by σ^x, σ^y, and σ^z, can be expressed as

$$\sigma_l^\alpha = i b_l^\alpha c_l, \quad \alpha = x, y, z \tag{1.2.13}$$

where b_l^α and c_l represent Majorana operators. It can be verified that the Pauli matrices σ^α ($\alpha = x, y, z$) commute with D, ensuring that $\mathcal{M}$ remains invariant. Additionally, they satisfy the properties $(\sigma^\alpha)^\dagger = \sigma^\alpha$, $(\sigma^\alpha)^2 = 1$, and the identity $\sigma^x\sigma^y\sigma^z = ib^x b^y b^z c = iD$. The operator D can be expressed as $D = (2c_1^\dagger c_1 - 1)(2c_2^\dagger c_2 - 1)$. This operator takes the value $+1$ in the subspace spanned by the states $|0,0\rangle$ and $|1,1\rangle$, while for the states $|0,1\rangle$ and $|1,0\rangle$, it takes the value -1. Consequently, the subspace formed by $|0,0\rangle$ and $|1,1\rangle$ is referred to as the physical subspace ($\mathcal{M}$), as the spin representation in terms of Majorana fermions is strictly valid only within this subspace.

To ensure that unphysical states are excluded, a projection operator $\mathcal{P}$ must be applied. The projection operator $\mathcal{P}_l$ at site l is defined as

$$\mathcal{P}_l = \frac{1 + D_l}{2}. \tag{1.2.14}$$

1.2.2.2 Quadratic Hamiltonian

The Kitaev Hamiltonian in the Majorana fermion representation is given by:

$$H = K_x \sum_{x\text{-link}} (ib_{x,l}^a b_{x,m}^b)(ic_l^a c_m^b) + K_y \sum_{y\text{-link}} (ib_{y,l}^a b_{y,m}^b)(ic_l^a c_m^b) + K_z \sum_{z\text{-link}} (ib_{z,l}^a b_{z,m}^b)(ic_l^a c_m^b). \tag{1.2.15}$$

The structure of this Hamiltonian is shown in Fig. 1.7. The above Hamiltonian is quartic, but remarkably the operators $u_{l,m}^\gamma = (ib_{\gamma,l}^a b_{\gamma,m}^b)$ (where $\gamma \in x, y, z$) commute with the Hamiltonian and with each other. This property reduces the Hamiltonian to a quadratic form in Majorana fermions. The u^{γ}_{lm} operators satisfy the following properties:

$$u^{\gamma}_{lm} = -u^{\gamma}_{ml}; (u^{\gamma}_{lm})^2 = 1; (u^{\gamma}_{lm})^{\dagger} = u^{\gamma}_{lm}, \tag{1.2.16}$$

and their eigenvalues are $u^{\gamma}_{l,m} = \pm 1$. Furthermore, the conserved quantity plaquette operator ($\mathcal{W}_p$) can be reformulated in terms of Majorana fermions, yielding the following expression:

$$\mathcal{W}_p = \prod_{l,m,\gamma \in \text{plaquette}} u^{\gamma}_{l,m} \tag{1.2.17}$$

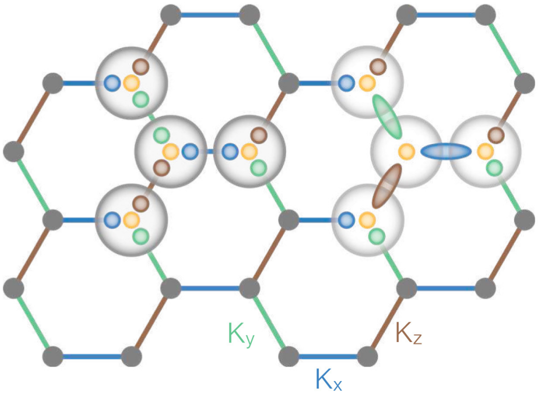

Figure 1.7: Schematic representation of the Kitaev model on a honeycomb lattice, featuring bond-dependent interactions K_x, K_y, and K_z. The model admits an exact solution by introducing four Majorana fermions per site (depicted as yellow, blue, green, and brown circles). These fermions can be reorganized into a static $\mathbb{Z}_2$ gauge field (represented by the blue, green, and brown ovals) and a remaining itinerant Majorana fermion (yellow circle). This figure is adapted from Ref. [357].

The Hamiltonian in Eq. (1.2.15) takes the form,

$$H = K_x \sum_{x\text{-link}} u^{x}_{l,m}(ic^a_l c^b_m) + K_y \sum_{y\text{-link}} u^{y}_{l,m}(ic^a_l c^b_m) + K_z \sum_{z\text{-link}} u^{z}_{l,m}(ic^a_l c^b_m). \tag{1.2.18}$$

The Hamiltonian presented in Eq. (1.2.18) represents the hopping interactions of free Majorana fermions in the presence of a $\mathbb{Z}_2$ gauge field in the background. In this framework, the $\mathbb{Z}_2$ gauge potential is denoted as $u^{\gamma}_{l,m}$.

The ground-state configuration is determined by minimizing the energy, which is achieved by setting $\mathcal{W}_p = +1$ for all plaquettes. This corresponds to fixing $u^{\gamma}_{lm} = +1$ for every bond. Now, the Hamiltonian can be exactly diagonalized to determine the ground state in the extended Hilbert space, denoted as $|\psi\rangle_{\text{ex}}$. To ensure the state resides in the physical subspace, unphysical states with $D = -1$ are projected out, yielding the physical ground state $|\psi\rangle_{\text{gs}}$, given by:

$$|\psi\rangle_{\text{gs}} = \hat{\mathcal{P}}|\psi\rangle_{\text{ex}}. \tag{1.2.19}$$

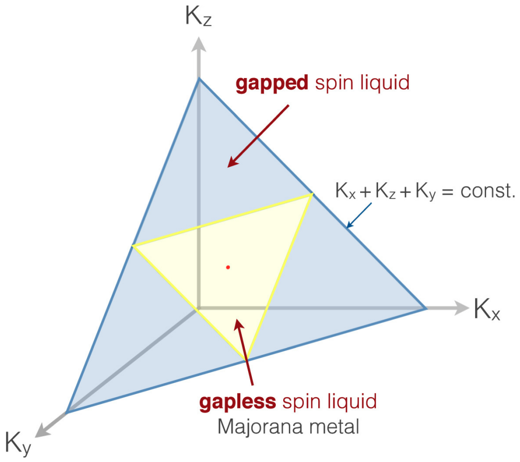

Figure 1.8: Phase diagram of the Kitaev model plotted on the plane satisfying $K_x + K_y + K_z =$ const. The blue-shaded regions represent gapped spin-liquid phases that occur when one of the three coupling strengths dominates. In contrast, a gapless spin-liquid phase emerges near the isotropic point $K_x = K_y = K_z$, marked by the red dot. This figure is adapted from Ref. [357].

Here, $\hat{\mathcal{P}}$ represents the global projection operator, defined as $\hat{\mathcal{P}} = \prod_l \frac{1+D_l}{2}$. Consequently, $|\psi\rangle_{\text{gs}}$ corresponds to the ground state within the physical Hilbert space.

Taking $\mathcal{W}_p = +1$ that contains the global minimum of energy by choosing $u^{\gamma}_{l,m} = +1$, the Hamiltonian is written as

$$\mathcal{H} = K_x \sum_{\text{x-link}} ic^a_l c^b_m + K_y \sum_{\text{y-link}} ic^a_l c^b_m + K_z \sum_{\text{z-link}} ic^a_l c^b_m, \tag{1.2.20}$$

To solve the above Hamiltonian we define the following Fourier transformations for the Majorana fermions,

$$c^{a,b}_l = \sum_k \frac{1}{\sqrt{2N}} e^{i\vec{k}\cdot\vec{r}} c^{a,b}_k, \tag{1.2.21}$$

In this framework, we consider a lattice consisting of L and N unit cells along the directions of $\mathbf{a}_1$ and $\mathbf{a}_2$, respectively [Fig. 1.6]. After performing the Fourier transformation, we get the Hamiltonian in momentum space as follow,

$$\mathcal{H} = \sum_k \begin{pmatrix} (C^a_k)^\dagger & (C^b_k)^\dagger \end{pmatrix} \begin{pmatrix} 0 & if^*_k \\ -if_k & 0 \end{pmatrix} \begin{pmatrix} C^a_k \\ C^b_k \end{pmatrix} \tag{1.2.22}$$

where,

$$f_k = \left(K_z + K_x e^{-ik\cdot a_1} + K_y e^{-ik\cdot a_2} \right). \tag{1.2.23}$$

The primitive vectors are $\mathbf{a}_1 = \left(\frac{1}{2}, \frac{\sqrt{3}}{2}\right)$ and $\mathbf{a}_2 = \left(-\frac{1}{2}, \frac{\sqrt{3}}{2}\right)$. It is easy to diagonalize the

Hamiltonian in momentum space as follows:

$$\begin{pmatrix} c_k^a \\ c_k^b \end{pmatrix} = \frac{1}{\sqrt{2}} \begin{pmatrix} v_k & -v_k \\ 1 & 1 \end{pmatrix} \begin{pmatrix} \alpha_k \\ \beta_k \end{pmatrix} \tag{1.2.24}$$

with $v_k = \frac{i f_k^*}{|f_k|}$. The diagonalized Hamiltonian is

$$\mathcal{H} = \sum_k E_k \left(\alpha_k^\dagger \alpha_k - \beta_k^\dagger \beta_k \right) \tag{1.2.25}$$

where $E_k = |f_k|$ represents the quasiparticle energy corresponding to the newly introduced field operators α_k and β_k. The ground state is determined by occupying all the quasiparticle states with negative energy, associated with β_k, and can be expressed as:

$$|\psi\rangle_{\mathrm{gs}} = \prod_{k \in \mathrm{HBZ}} \beta_k^\dagger |0\rangle, \tag{1.2.26}$$

Here, the state $|0\rangle$ denotes the vacuum, which is annihilated by the operators α_k and β_k, i.e., $\alpha_k|0\rangle = \beta_k|0\rangle = 0$. The summation runs over half of the Brillouin zone. To determine whether the spectrum is gapless, we examine the condition $f_k = 0$. It turns out that this equation has solutions if and only if the parameters $|K_x|$, $|K_y|$, and $|K_z|$ satisfy the following triangle inequalities:

$$\begin{aligned} |K_x| &\leq |K_y| + |K_z| \\ |K_y| &\leq |K_x| + |K_z| \\ |K_z| &\leq |K_x| + |K_y| \end{aligned} \tag{1.2.27}$$

The low-energy excitations in this model correspond to gapless Majorana fermions with linear dispersion. This phase is identified as the gapless-$\mathbb{Z}_2$ spin liquid phase. When the aforementioned conditions are not met, an energy gap emerges between the two bands, whose dispersion becomes parabolic, leading to the gapped-$\mathbb{Z}_2$ spin liquid phase. In the limit where $K_z \gg K_x, K_y$, the Hamiltonian effectively reduces to that of the toric code model [183, 184]. The spin-spin correlation function remains short-ranged, vanishing beyond nearest-neighbor sites [24]. Meanwhile, the dimer-dimer correlation function exhibits a power-law decay in the gapless phase, whereas it decays exponentially in the gapped phase [406].

For clarity, the ground-state phase diagram is presented in Fig. 1.8. However, this solution method does not readily provide the exact eigenstates of the Hamiltonian or those of the conserved quantities. The exact ground state of the Kitaev model can be obtained using Jordan-Wigner transformations, but a detailed discussion of this approach is beyond the scope of this thesis.

1.2.2.3 Experimental Realization of the Kitaev Model

The experimental realization of the Kitaev model and the associated spin-liquid phase remains an active area of research in condensed matter physics. The possibility of realizing the Kitaev model in real materials was first proposed by Jackeli and Khaliullin in 2009 [160]. Materials that exhibit such physics are typically found in iridium-based compounds, such as A_2IrO_3 (A = Na, Li), where iridium atoms form a honeycomb lattice [47, 155, 330].

In these compounds, the iridium ions are surrounded by oxygen octahedra, creating a crystal field that splits the Ir d-orbitals into three t_{2g} and two e_g levels, as depicted in Fig. 1.9. The five d-electrons primarily occupy the t_{2g} orbitals, forming an effective orbital angular momentum state with $l = 1$. Due to strong spin-orbit coupling, the t_{2g} levels further split into a fully filled $j = 3/2$ band and a half-filled $j = 1/2$ band. Strong electronic correlations then drive the system into a $j = 1/2$ Mott insulating state. A schematic representation of this mechanism is provided in Fig. 1.9.

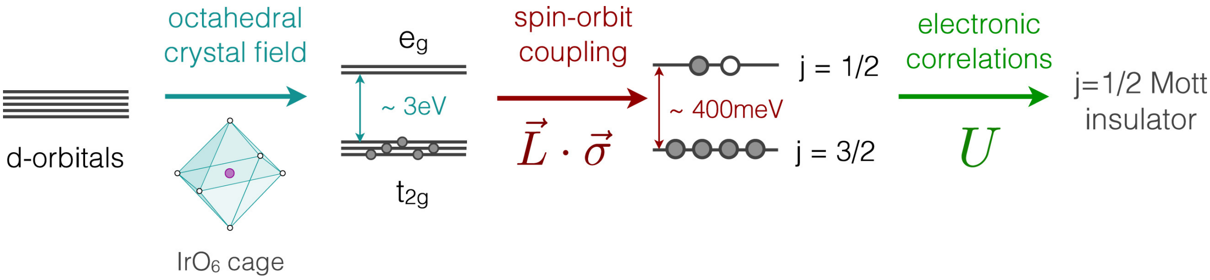

Figure 1.9: Formation of spin-orbit entangled $j = \frac{1}{2}$ moments in a d^5 electronic configuration, relevant for iridium ions (Ir^{4+}) and ruthenium ions (Ru^{3+}). Figure adapted from Ref. [357].

To gain insight into the magnetic interactions in these materials, it is important to consider the structural connectivity of IrO_6 octahedra, which can share either corners or edges. In a corner-sharing arrangement, the Ir-O-Ir bond angle is approximately 180°, facilitating an isotropic Heisenberg exchange. Conversely, in an edge-sharing configuration, the Ir-O-Ir bonds form a 90° angle, leading to two competing exchange pathways. Within a pure $j = 1/2$ picture, these interactions destructively interfere, suppressing the conventional Heisenberg exchange and giving rise to dominant anisotropic Kitaev interactions. A comprehensive multi-orbital analysis confirms that the Heisenberg term is largely reduced in favor of anisotropic bond-dependent interactions, forming the theoretical foundation of the Kitaev-Heisenberg (KH) model [160].

Several candidate materials have been identified as potential realizations of the Kitaev model, including the honeycomb iridates A_2IrO_3 (A = Na, Li) [47, 155, 330], α-$RuCl_3$ [20, 76, 162, 343, 357, 394], β-Li_2IrO_3 [162, 176, 350, 357, 394], and γ-Li_2IrO_3 [357, 358].

Despite these promising candidates, experimental studies reveal that many of these materials exhibit an antiferromagnetic (AFM) zigzag ordered phase at low temperatures under ambient conditions [167, 329]. This deviation from a spin-liquid state is attributed to additional interactions beyond the Kitaev-Heisenberg model. In particular, off-diagonal Γ interactions have been identified as a key perturbation, leading to a more generalized spin Hamiltonian:

$$\mathcal{H}_{JK\Gamma} = \sum_{\gamma-\text{bonds}} \left[J\mathbf{S}_i \cdot \mathbf{S}_j + K S_i^\gamma S_j^\gamma + \Gamma \left(S_i^\alpha S_j^\beta + S_i^\beta S_j^\alpha \right) \right] + (\text{Other interactions}). \tag{1.2.28}$$

Here, α and β refer to the two spatial directions perpendicular to $\gamma = x, y, z$. In addition, some materials also exhibit further-neighbor Heisenberg and Γ interactions.

Experimental investigations indicate that applying an external magnetic field or pressure can destabilize the AFM order, potentially driving the system toward a spin-liquid phase. However, the precise nature of this transition remains a subject of ongoing research. Since the Kitaev interaction is often regarded as the dominant term in these materials, further theoretical and experimental studies are required to clarify the conditions under which a quantum spin liquid state may emerge.

1.3 Outline of the thesis

The research presented in this thesis is structured into seven chapters, which are summarized as follows:

Chapter 1 provides a comprehensive review of relevant frustrated spin-1/2 models in one-dimensional and quasi-one-dimensional systems, along with their experimental realizations in real materials.

Chapter 2 describes the numerical techniques employed in this study, namely exact diagonalization and the density matrix renormalization group (DMRG) method. These numerical approaches are utilized to investigate the problems addressed in the thesis.

The thesis is divided into two main parts. The first part focuses on frustrated spin-1/2 models in one-dimensional and quasi-one-dimensional geometries, such as the dimerized J_1-J_2 model and the coupled trimer model with three spins per unit cell. The second part is dedicated to exchange frustration, specifically the Kitaev-Heisenberg (KH) model. The first part comprises **Chapters 3 and 4**, while the second part includes **Chapters 5 and 6**.

Chapter 3 explores the spin-$\frac{1}{2}$ J_1-J_2 chain with ferromagnetic nearest-neighbor exchange ($J_1 < 0$) and antiferromagnetic next-nearest-neighbor exchange ($J_2 > 0$). The focus is on spin-Peierls (SP) instabilities. For frustration $\alpha = J_2/|J_1| > 0.65$, the system exhibits sublattice dimerization with four spins per unit cell rather than conventional chain dimerization. Introducing asymmetric J_1 couplings ($\gamma > 0$) leads to gapped chains with conditional SP transitions and a weaker specific heat anomaly. The study demonstrates that both the J_1-J_2 and gapped models reproduce the spin susceptibility $\chi(T)$ and specific heat $C(T)$ of β-TeVO$_4$ above 8 K, but low-temperature behavior suggests that β-TeVO$_4$ is more accurately described as a gapped chain rather than a J_1-J_2 model.

Chapter 4 examines the ground state properties of a quasi-one-dimensional spin-$\frac{1}{2}$ coupled trimer model. The system is characterized by nearest-neighbor intra-trimer exchange (J_1), inter-trimer exchange (J_1'), and next-nearest-neighbor intra-trimer and inter-trimer exchange (J_2), all of which are antiferromagnetic ($J_1, J_1', J_2 > 0$). A quantum phase diagram is obtained in the $J_1'/J_1 - J_2/J_1$ space, revealing different quantum phases, including spin fluid (SF), trimer, gapless spiral, and gapped dimer phases, with phase transitions occurring as a function of inter-trimer coupling.

Chapter 5 investigates the ground state dynamics of the spin-$\frac{1}{2}$ KH model, focusing on quadrupolar (QP) order in two-leg ladder and two-dimensional honeycomb lattice geometries. The analysis reveals a robust QP order governed by the interplay between Heisenberg and Kitaev interactions. Notably, QP order is enhanced near Kitaev spin liquid (KSL) phases, despite the absence of long-range spin-spin correlations.

Chapter 6 explores the Kitaev-Heisenberg-DMI (KH-DMI) model on two-leg ladders and honeycomb lattices, investigating the influence of Dzyaloshinskii-Moriya interaction (DMI) on the Kitaev spin liquid (KSL). The study analyzes the stability of the KSL phase under varying DMI strengths and reveals distinct phase transitions, including the emergence of a vortex phase in the honeycomb lattice at strong DMI.

Finally, **Chapter 7** presents concluding remarks and discussions on the findings of this thesis.

Chapter 2

Numerical Methods

2.1 Introduction

In Chapter 1, various exotic phases in frustrated spin systems were discussed. Many of these phases can be described using quantum many-body models, where quantum interactions play a crucial role in determining the underlying physics. However, only a few quantum many-body systems can be solved analytically. For instance, in the case of the one-dimensional (1D) Heisenberg model, certain low-energy states can be determined exactly using the Bethe ansatz [29].

Solving a quantum many-body Hamiltonian is inherently challenging due to the exponential growth of the Hilbert space with system size. Specifically, for a spin-$1/2$ system with N sites, the dimension of the Hilbert space scales as 2^N. Given this rapid increase in computational complexity, exact solutions are often impractical for large systems.

To address this challenge, approximate methods—both analytical and numerical—are widely employed. Analytical techniques include spin-wave theory, field-theoretical approaches such as bosonization, and the renormalization group framework. These methods have been extensively used in the study of quantum magnetism, particularly in low-dimensional systems. However, their applicability is generally restricted to specific models, and for more complex systems, they often fail to provide reliable results.

In such cases, numerical methods serve as powerful alternatives. These methods can be broadly classified into two categories: exact numerical techniques applicable to finite systems and approximate numerical approaches. The latter includes methods such as Density Matrix Renormalization Group (DMRG), Quantum Monte Carlo (QMC), and tensor network algorithms, which have proven to be effective in exploring the physics of strongly correlated quantum systems.

The exact diagonalization (ED) numerical technique allows us to solve the many body models with small system size, i.e., with small Hilbert space dimension. For large system sizes several approximate numerical techniques have been developed, i.e., quantum monte carlo (QMC) [308], numerical renormalization group (RG) [391], density matrix renormalization group (DMRG) [375, 377], tensor network [321], etc. In this thesis all the results shown in the next chapters are mostly calculated using ED for small systems and DMRG for larger systems. In this chapter[1], we are going to discuss next the ED and conventional DMRG method.

---

[1] This chapter provieds the numerical methods employed in all the problems of this thesis.

2.2 Exact Diagonalization

The properties of model Hamiltonians can be analyzed by computing their eigenvalues and eigenstates. This is accomplished by expressing the Hamiltonian in a suitable basis and subsequently diagonalizing the resulting matrix. The Exact Diagonalization (ED) method involves considering the full Hilbert space of a finite system, enabling an exact solution within the chosen basis. A key advantage of this numerical approach is its ability to yield precise solutions for the model Hamiltonian. However, its applicability is restricted to relatively small system sizes due to the exponential growth of the Hilbert space with system size.

The Hamiltonians introduced in Chapter 1 commute with the total spin operators S and S^z, i.e., $[H, S^2] = 0$ and $[H, S^z] = 0$. Consequently, H, S^2, and S^z share a common set of eigenfunctions, with corresponding eigenvalues denoted by E, $S(S+1)$, and m_s, respectively. The conservation of S and S^z results in a block-diagonal structure of the Hamiltonian matrix within a fixed S^z sector, thereby reducing computational complexity.

For spin-1/2 systems, the z-axis is chosen as the quantization axis, with the two possible spin orientations, up ($\Uparrow$) and down ($\Downarrow$), represented as 1 and 0, respectively. The spin operators S^x and S^y can be expressed using the raising (S^+) and lowering (S^-) operators. The basis states form an orthonormal set, ensuring that the Hamiltonian matrix remains symmetric. Table 2.1 provides the total number of basis states in different S^z sectors for a system consisting of N spins.

S^z	Total number of basis states
0	$\binom{N}{N/2}$
1	$\binom{N}{N/2-1}$
2	$\binom{N}{N/2-2}$
$\vdots$	$\vdots$
$N/2$	1

Table 2.1: For a system consisting of N spins, the total number of basis states varies across different S^z sectors. Each sector corresponds to a specific total spin projection, which determines the available basis states within that subspace.

The study of ground-state properties in frustrated magnetic models presents significant challenges due to the presence of large degeneracies in low-lying energy states. This often results in slow convergence or even non-convergent energy calculations. To mitigate these issues, the Hilbert space is partitioned into different symmetry subspaces. In many models, spin-parity and inversion symmetry remain conserved, allowing for a reduction in computational complexity.

The spin-parity operator is associated with a global rotation of all spins around either the x or y axis by an angle of π, leaving the Hamiltonian invariant. However, this holds strictly within the $S^z = 0$ sector. Similarly, inversion symmetry corresponds to a reflection about an axis passing through two specific sites, labeled as 1 and $N/2 + 1$, which also preserves the Hamiltonian.

These symmetries are incorporated into the Hamiltonian matrix through unitary transformations, thereby reducing its dimensionality and improving computational efficiency. The transformed Hamiltonian takes the form $\tilde{H} = U^\dagger H U$, where U is a unitary symmetry operator of dimension $N \times m$. Upon transformation, the effective Hamiltonian $\tilde{H}$ has a reduced dimensionality of $m \times m$, where $m < N$. These symmetry reductions are implemented after performing block diagonalization using the total spin projection S^z, further decreasing the dimension of each block in a given S^z sector.

Solving a many-body model Hamiltonian via exact diagonalization involves the following steps:

1. Construction of the basis states.

2. Formation of the Hamiltonian matrix in the chosen basis.

3. Diagonalization of the Hamiltonian matrix.

The computational cost for full diagonalization of a sparse matrix of dimension $m \times m$ is m^3 , whereas cost of finding only low-lying energies of a sparse matrix goes as $m^{3/2}$. This implies that working with moderate to large system sizes would involve working with Hamiltonian matrices of dimension $\sim 10^6 - 10^7$, which is computationally expensive. There exist many algorithms like Lanczos method [207, 208], modified Lanczos algorithms [289], Davidson algorithms [67, 68] etc., that can be employed to find the low-lying eigenstates without full diagonalization of the Hamiltonian matrix. Davidson algorithm is among the most popular algorithms for calculating the low-lying eigenstates a large symmetric and sparse matrix [291]. We use a modified version of this algorithm – the Rettrup algorithm [287] for the problems in this thesis, which also works for non-symmetric matrices. We briefly discuss the Rettrup algorithm below.

Consider a large, sparse Hamiltonian matrix H of dimension $N \times N$. Retrup's algorithm begins with a set of m orthonormal vectors, denoted as $\{\vec{Q}_j\}$ for $j = 1, 2, \ldots, m$. These vectors serve as a basis for constructing a reduced Hamiltonian matrix of order $m \times m$, denoted by $\{h_{ij}\}$. The elements of this reduced matrix are determined using the relation $h_{ij} = \langle \vec{Q}_i | H | \vec{Q}_j \rangle$. The eigenvalues $E_k^{(m)}$ and eigenvectors $\vec{C}_k^{(m)}$ of the reduced matrix can then be obtained through standard exact diagonalization techniques. For convenience, the eigenvalues and their corresponding eigenvectors are typically arranged in ascending order based on energy.

If we are interested in the lth eigenvalue of the Hamiltonian matrix ($l \leq m$), then we need to consider the weighted residue vector $\vec{W}_l^{(m)}$, whose ith component, $W_l^{(m)}(i)$, is given by the coordinate relaxation method as

$$W_l^{(m)}(i) = \frac{R_l^{(m)}(i)}{(E_l^{(m)} - H_{ii})} \tag{2.2.1}$$

where $R_l^{(m)}(i)$ is the ith component of the residue vector for the lth approximate eigenvalue.

$\vec{R}_l^{(m)}$ is given by

$$\vec{R}_l^{(m)} = (H - E_l^{(m)}\mathbb{I})\vec{C}_l^{(m)} \tag{2.2.2}$$

where, $\mathbb{I}$ is the identity (unit) matrix and $\vec{C}_l^{(m)} = \sum_{i=1}^{m} c_l^{(m)}(i)\vec{Q}_i$. At this point, the space of trial vectors is augmented by adding the vector

$$\vec{Q}_{m+1} = \frac{\vec{Q}'_{m+1}}{|\vec{Q}'_{m+1}|}. \tag{2.2.3}$$

The vector $\vec{Q}'_{m+1}$ is obtained as the projection of $\vec{W}_l^{(m)}$, which is orthogonal to the m-dimensional space, and is given by the Gram-Schmidt orthogonalization procedure,

$$\vec{Q}'_{m+1} = \vec{W}_l^{(m)} - \sum_{k=1}^{m} \langle \vec{W}_l^{(m)}, \vec{Q}_k \rangle \vec{Q}_k. \tag{2.2.4}$$

The procedure is iterated until either the norm of the residue vector is below a desired threshold value, or the magnitude of no component of the residue vector exceeds a chosen threshold. If the augmented small matrix, $\{h_{ij}\}$, reaches a previously chosen maximum dimension L, above which the procedure is slow, it is possible to restart the whole calculation by choosing $\vec{Q}_1, \vec{Q}_2, \ldots, \vec{Q}_m$ to be $\vec{C}_1^{(L)}, \vec{C}_2^{(L)}, \ldots, \vec{C}_m^{(L)}$, where $\vec{C}_i^{(L)}$ is the eigenvector of the ith lowest eigenvalue of the $L \times L$ small matrix. It is usually found that Rettrup's procedure is very fast, owing to rapid convergence to the true solution, even when the initial guess space of $\{\vec{Q}_m\}$ is crudely chosen. In fact, $m = 1$ is adequate for obtaining the low-lying states.

2.3 Density Matrix Renormalization Group (DMRG)

Density Matrix Renormalization Group (DMRG) is a state-of-the-art numerical method [375] developed to systematically truncate irrelevant degrees of freedom at each iterative step. This approach reduces system complexity while retaining essential physical properties, enabling accurate descriptions of large quantum systems with manageable computational resources. Among the earliest renormalization techniques was Kadanoff's block formation method for spin clusters [171]. This method calculated scaling relations and critical exponents, providing a foundational idea for iteratively reducing the degrees of freedom without altering core physics. Another significant method was the Numerical Renormalization Group (NRG), introduced by Wilson [393], a momentum-space renormalization technique successfully applied to the Kondo model [391].

Despite its success in solving problems like transport phenomena [391, 392], real-space implementations of NRG faced challenges due to hard wall boundary conditions forming during block merging. These conditions led to inaccuracies in wavefunction calculations [267, 386]. The NRG method involves dividing a system into smaller blocks, constructing a superblock Hamiltonian, and iteratively truncating the Hilbert space. However, this method struggles with strongly correlated systems due to issues arising from the isolation of blocks. In the renormalization group (RG) procedure, consider two blocks, A and B, each with a Hilbert space of dimension m. The combined superblock has a Hilbert space dimension of m^2, with the superblock Hamiltonian including the Hamiltonians of A and B as well as their interaction terms. After diagonalizing the Hamiltonian, the lowest m eigenstates are retained, and the Hilbert space is truncated accordingly. The Hamiltonian is then projected onto this reduced basis to form a smaller, renormalized Hamiltonian for the next iteration. While this process doubles the system size at each step, it introduces significant errors because the truncated basis cannot accurately represent correlations near block boundaries. For instance, if the ground-state wavefunctions of two neighboring blocks have maxima at their centers and nodes at their boundaries, their product states should exhibit this pattern. However, when these blocks are combined into a superblock, the boundaries of the individual blocks become internal points, causing mismatches that lead to significant inaccuracies, particularly in strongly correlated systems [377].

S. R. White addressed these issues by introducing the density matrix into the RG framework [375, 386]. In this method, a superblock comprising the system and its environment is constructed. The reduced density matrix of the system block is obtained by tracing out the environment's degrees of freedom, and only the most relevant eigenstates, corresponding to the largest eigenvalues, are retained. This ensures that the truncated basis accurately represents the system's low-energy physics. The iterative process continues until the desired system size is reached, and the Hamiltonian is diagonalized in the truncated Hilbert space. This breakthrough significantly improved traditional RG methods, enabling the study of strongly correlated quantum systems with unprecedented accuracy.

The DMRG algorithm has gained widespread popularity in condensed matter physics due to its ability to handle strongly correlated systems. It has been applied to study the ground-state properties of one-dimensional (1D) and quasi-1D magnets, as well as fermionic and bosonic systems. References [43, 126, 128, 267, 319, 321, 378] provide detailed reviews of the DMRG method and its applications. DMRG has been successfully used to study the ground states and low-lying excited states of spin-1/2 Heisenberg models in 1D and ladder geometries [55, 195–199, 201, 205, 248, 257, 335]. Detailed investigations of spin correlations, spin gaps, low-energy spectra, and edge modes in spin-1 chains have been conducted using DMRG [71, 336, 337, 379, 385]. Additionally, DMRG has been applied to low-dimensional Fermi-Hubbard [65, 66, 163, 172, 249, 250, 352, 411] and Bose-Hubbard models [42, 192, 194, 260, 279, 292, 293], $t-J$ models [115, 165, 238, 382, 387, 388], and the Pariser-Parr-Pople model [92, 276]. Efforts continue to expand DMRG for calculating dynamical or spectral properties [84, 127, 163, 164, 174, 193, 277], extending to two-dimensional (2D) systems [83, 247, 327, 339, 346, 398, 403], real-time evolution [64, 120, 190, 209, 317, 318, 320, 384], and finite-temperature calculations [21, 39, 96, 299, 300, 326]. Although early DMRG algorithms were efficient for systems with open boundary conditions, recent modifications have successfully adapted the method for periodic boundary conditions (PBC) [72].

The following subsection describes the basic DMRG algorithm for a 1D chain in more detail.

2.3.1 Density Matrix Formalism in DMRG

The core of the DMRG algorithm lies in the systematic use of the density matrix to truncate the Hilbert space while preserving the essential physics of the system. This formalism ensures that the retained states are the most relevant for describing the system's low-energy properties.

Consider a system block A of length L with a Hilbert space of dimension m and an environment block B of the same length and dimension. Considering the linear growth of blocks of $N = 1$ or 2 site (new site block), the N new sites will be added to both system and environment block. The superblock, which includes these blocks and additional new sites, will be of total length $2L + 2N$. Considering $|a_i\rangle$ is a basis set of block A, $|b_i\rangle$ is a basis set of environment block B, both with Hilbert space dimension m and $|\sigma_i\rangle$ is a basis set of new site block with N local new sites with Hilbert space dimension m_σ, the basis set of the new system block (new environment block) formed with old block A (B) and new site block is the product state $\left|a'_j\right\rangle$ $\equiv |a_i\rangle\,|\sigma_i\rangle$ ($\left|b'_j\right\rangle \equiv |b_i\rangle\,|\sigma_i\rangle$) with Hilbert space dimension $m_s = m_e = mm_\sigma$.

The dimension of the superblock is $m^2{m^2}_\sigma$. The wavefunction of the superblock, $|\psi\rangle$, is expressed as a linear combination of the product states of the system and environment blocks:

$$|\psi\rangle = \sum_{ij} c_{ij}|a'_i\rangle|b'_j\rangle, \tag{2.3.1}$$

where $|a'_i\rangle$ and $|b'_j\rangle$ represent the basis states of the system and environment blocks, respectively.

Before increasing the block size by adding a new site, it is necessary to truncate the Hilbert space of the newly formed system and environment blocks. To minimize the effect of disconnected blocks on the lattice, as encountered in the RG method, these blocks are represented in the eigenspace of the density matrix. The truncation is performed in the eigenvector space corresponding to the density matrix of the block.

The density matrix for the system block is obtained by tracing out the environment's degrees of freedom:

$$\begin{aligned}
\rho &= \mathrm{Tr}_E\left(|\psi\rangle\langle\psi|\right) \\
\rho &= \sum_{ii'j} c_{ij}c^*_{i'j}|a'_i\rangle\langle a'_{i'}| \\
\langle a'_i|\rho|a'_{i'}\rangle &= \sum_j c_{ij}c^*_{i'j}
\end{aligned} \tag{2.3.2}$$

The expectation value of any operator $\hat{A}$ of system block can be written as:

$$\begin{aligned}
\langle\psi|\hat{A}|\psi\rangle &= \sum_{ii'j} c_{ij}c^{*}_{i'j}\langle a'_{i'}|\hat{A}|a'_{i}\rangle \\
&= \sum_{ii'}\langle a'_{i}|\rho|a'_{i'}\rangle\langle a'_{i'}|\hat{A}|a'_{i}\rangle \\
&= \sum_{i}\langle a'_{i}|\rho\hat{A}|a'_{i}\rangle \\
&= Tr\rho\hat{A}. \qquad (2.3.3)
\end{aligned}$$

The density matrix ρ can be diagonalized to have m_s eigenstates $|\alpha_i\rangle$ with real and positive eigenvalues α_i.

$$\rho = \sum_{i=1}^{m_s} \alpha_i \left|\alpha_i\right\rangle \left\langle\alpha_i\right| , \qquad (2.3.4)$$

where $\sum_{i=1}^{m_s} \alpha_i = 1$. The expectation value of any operator $\hat{A}$ can be written as:

$$\langle\psi|\hat{A}|\psi\rangle = Tr\rho\hat{A} = \sum_{i=1}^{m_s} \alpha_i \left\langle\alpha_i\right| \hat{A} \left|\alpha_i\right\rangle \qquad (2.3.5)$$

If we keep n_s most probable eigenvectors with largest eigenvalues out of total m_s eigenvectors, then the truncated expectation value can be expressed as a sum over only those n_s states as:

$$\langle\psi|\hat{A}|\psi\rangle_{trunc} = \sum_{i=1}^{n_s} \alpha_i \left\langle\alpha_i\right| \hat{A} \left|\alpha_i\right\rangle \qquad (2.3.6)$$

The error for $\left\langle\psi\right| \hat{A} \left|\psi\right\rangle$ in this approximation is

$$\left\langle\psi\right| \hat{A} \left|\psi\right\rangle - \left\langle\psi\right| \hat{A} \left|\psi\right\rangle_{trunc} = \sum_{i=n_s+1}^{m_s} \alpha_i\langle\alpha_i|\hat{A}|\alpha_i\rangle \qquad (2.3.7)$$

This error is minimized when the eigenvalues of the density matrix decay exponentially fast, ensuring that the neglected states in Eq. 2.3.6 have a negligible contribution to the expectation value $\langle\psi|\hat{A}|\psi\rangle$ in Eq. 2.3.3. This truncation is performed after each step in the systematic growth of the system block.

2.3.2 DMRG for a 1D Linear Chain

The DMRG algorithm comprises two main variants: the infinite-size and finite-size algorithms. The infinite-size algorithm starts with a small system and iteratively adds sites until the desired size is reached. The finite-size algorithm then optimizes the system by sweeping back and forth, refining the basis at each step.

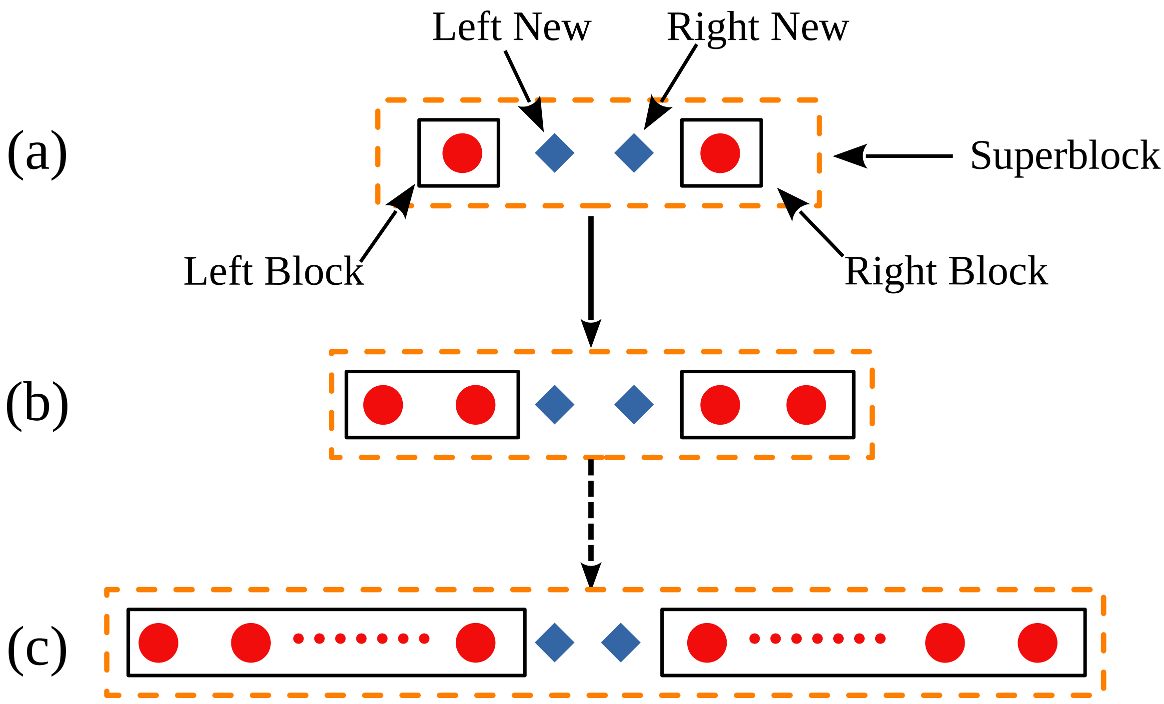

Figure 2.1: Infinite DMRG steps. It starts with superblock of four sites as shown in (a). The renormalized system (left or right) block of one site are shown inside the square in solid blue line and the magenta square made of dashed line containing left block and new site represents the new left block for the next step (b) as shown by the magenta arrow. At each step, the superblock size grows. In (c) the targeted system size is shown.

2.3.2.1 Infinite DMRG Algorithm

Let's consider a 1D system with open boundary condition (OBC). The steps of the infinite DMRG algorithm are systematically discussed below.

1. We start with a small system of four sites (Fig. 2.1) that consists of four blocks containing one site each - (from left) left block (system block) A, left new block a and right new block b, and the right block (environment block) B. The full system constituted by these four blocks is called the superblock. The initial step (a) in Fig. 2.1 depicts the initial superblock of four sites by the squares made of black dashed line and the initial system block and environment block are shown by the squares made of solid blue line at the left and the right end of the 1D chain. The left new and right new blocks are shown by the red cross.

2. The Hamiltonian of the superblock is constructed by combining the block Hamiltonians and the interactions between the blocks. The system Hamiltonian can be written as direct product of the constituent blocks as,

$$H = H_A \otimes H_a \otimes H_b \otimes H_B \tag{2.3.8}$$

The resulting superblock matrix is then diagonalized to obtain the target state $|\psi\rangle$.

3. The updated left block A' for the next step is formed by combining the current left block A with the single-site block on the left. As mentioned in the previous subsection 2.3.1, A' has a Hilbert space dimension of $m_s = mm_\sigma$, where m_σ is the Hilbert space dimension of the new-site block. Similarly, the updated right block B' is constructed in the same manner as A'. This process is illustrated in part (a) of Fig. 2.1.

4. The system block's density matrix ρ is obtained from the target states of the superblock as defined in Eq. (2.3.2). Diagonalizing this density matrix yields m_s eigenstates. Out of these, the n_s ($\leq m_s$) eigenstates with the largest eigenvalues are retained, while the others are discarded. The system block space and associated operators are then mapped onto the truncated density matrix space using a transformation matrix O, expressed as $\hat{G}' = O\hat{G}O^\dagger$. The rows of O correspond to the eigenvectors of the density matrix, with n_s rows selected for the n_s largest eigenvalues. As a result, the dimensions of O are $n_s \times m_s$.

   The operator G can represent the Hamiltonian matrix H of size $m_s \times m_s$ for the blocks A' or B', or other operators acting on these blocks. The renormalized matrix H' then has a reduced dimension of $n_s \times n_s$.

5. Next, the renormalized Hamiltonian matrices for A' and B' are treated as the left and right blocks, respectively ($A \equiv A'$ and $B \equiv B'$). This is illustrated in part (b) of Fig. 2.1, where the square outlined with a solid blue line represents the updated blocks. The newly constructed superblock is depicted by the black dashed line. The process then returns to the 2$^{\text{nd}}$ step, and the iteration is repeated until the target system size is reached.

2.3.2.2 Finite DMRG Algorithm

To get an optimized wave function and accurate system properties, we next perform finite DMRG sweeps when the desired system size $2L+2$ is reached using the infinite DMRG process, where the left and right blocks are of equal size L. The system size remains fixed at $2L+2$ in the finite DMRG algorithm, instead the left (right) block size is increased (reduced) at each step until the right block contains only one site. Then the right (left) block size is increased (reduced) at each step, until the left and right blocks are of the same size again. Now, the right (left) block size is increased (reduced) at each step until the left (right) block contains only one site. Then the left (right) block size is increased (reduced) at each step, until the left and right blocks are of the same size again. This describes one complete finite DMRG sweep.

The projection to the truncated space of the density matrix is carried out for the increasing block. The Hamiltonian matrix or the operators for the shrinking block were stored during the infinite DMRG iterations or previous steps of finite DMRG algorithm which are reused in the finite DMRG. In this procedure, both the left and right block are embedded in the total system of desired length which is required to overcome the errors appeared in case of RG technique. The finite DMRG procedure is illustrated in the schematic Fig. 2.2, and summarized below:

1. We start with the diagonalized superblock Hamiltonian obtained at the end of the infinite

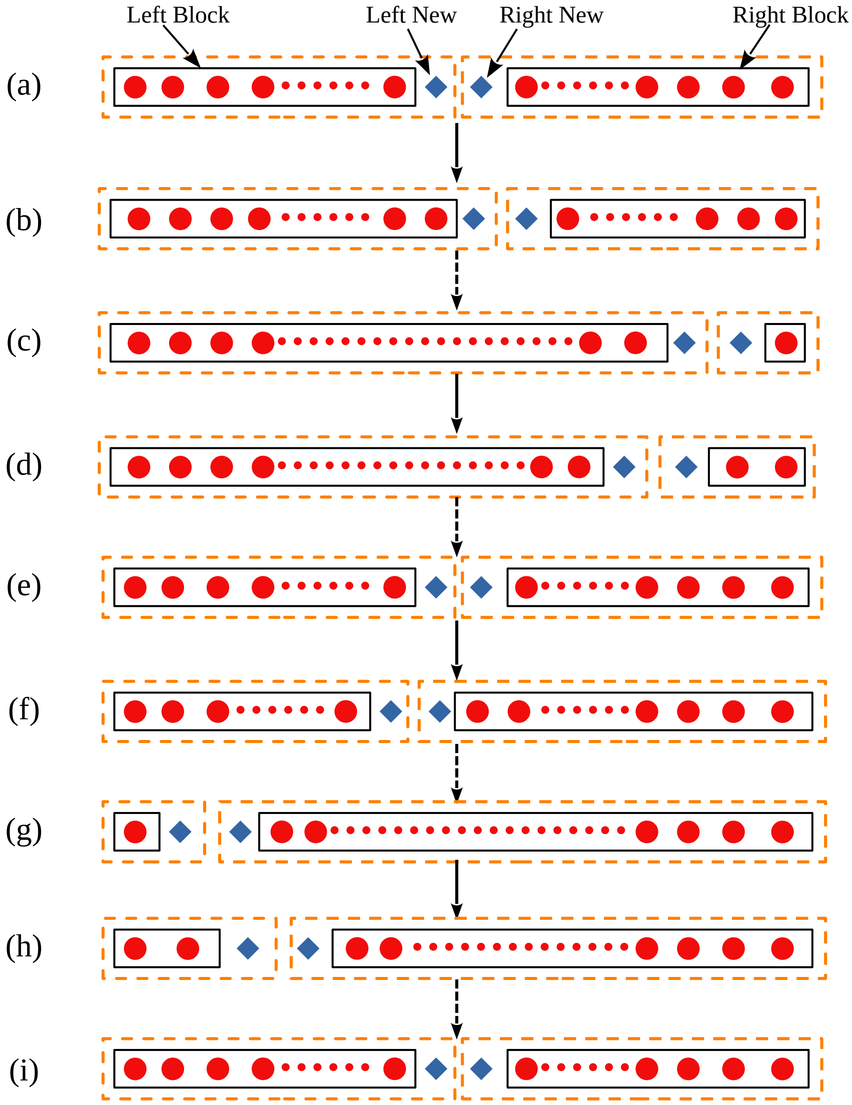

Figure 2.2: Finite DMRG steps. It starts with left and right block of equal size and two new site block of one sites as shown in (a). The renormalized system block is shown inside the blue square made of solid line whereas the magenta square with dotted line represents the new left block for the next step (b). The left/right block increases/decreases back and forth. At the end of the sweep, left and right block are of equal size again as shown in (i). Several steps of a finite dmrg sweeps are shown in (a) - (i).

DMRG algorithm discussed above. This superblock has the left and right blocks of the same size L, as shown in Fig. 2.2(a).

2. The left to right sweep starts with adding one new site to the left block $L+1$, and removing one site from the right block $L-1$ to keep the total superblock or system size $2L+2$ fixed, as shown in Fig. 2.2(b). The diagonalization of the superblock gives the target state $|\psi\rangle$.

3. The target state $|\psi\rangle$ is used to compute the density matrix ρ of the system block via Eq. (2.3.2). The density matrix is then diagonalized, and the eigenstates corresponding to the largest eigenvalues are retained as the most significant states. As in the infinite DMRG approach, the left block and its operators are renormalized using the truncated set of eigenstates of the density matrix. Meanwhile, the Hamiltonian and operators for the right block are retrieved from the saved data generated during the infinite DMRG process.

4. Let's assume that the minimum length of each block is 1. Through repeated iterations, the size of the left block gradually increases until it reaches the maximum length of $2L-1$, while the right block maintains the minimum length of 1. In this manner, the process eventually extends to an open end of the system, as illustrated in Fig. 2.2(c).

5. Once, the right block size is 1, the same process is followed in the opposite direction, i.e., the right (left) block is grown (reduced) by one site in each step until the left block is reduced to one single site as shown in Fig. 2.2 (d-g).

6. Once the left block size is 1, we again start growing the left block by one site and remove sites from the right block by one site until the left and the right block have the same size L as shown in Fig. 2.2(i).

This whole process is referred to as one finite DMRG sweep. The sweeps are repeated until accuracy up to a desired precision is reached. 5 - 10 finite DMRG sweeps are generally adequate to thermalize the 1D system.

In this thesis, we apply the conventional DMRG algorithm to 1D systems with open boundary conditions (OBC). Additionally, we employ a modified DMRG method for systems with periodic boundary conditions (PBC) [72] to mitigate the strong finite size effects at the edges. We also utilize a hybrid ED/DMRG method [299] to compute the thermodynamic properties of 1D systems. These algorithms are described in subsections 2.3.3 and 2.3.4, respectively.

2.3.3 DMRG algorithm for PBC

While conventional DMRG applied to OBC provides excellent accuracy, achieving similar precision with PBC is highly sought after in quantum many-body problems. This is because systems with OBC exhibit significant finite size effects at the edges, which can be alleviated by using PBC. Moreover, in contrast to OBC, when PBC is applied, several symmetry operators commute with the system's Hamiltonian, allowing the Hamiltonian matrix to be represented in block diagonal form. As a result, the matrix size is reduced, which lessens the computational effort.

If the conventional DMRG method for a 1D system with open boundary conditions (OBC) requires n_s most probable eigenvectors of the density matrix to form the truncated space for achieving the desired accuracy, the same method with periodic boundary conditions (PBC) requires $O(n_s^2)$ eigenvectors [322]. Consequently, the computational cost for sparse matrix diagonalization in the case of OBC scales as $O(n_s^3)$, while for PBC, the cost scales as $O(n_s^6)$ [366]. This is one of the reasons for the large errors encountered in conventional DMRG with PBC.

Additionally, it is important to note that a 1D system with periodic boundary conditions (PBC) connects the left and right ends with a long bond. The error in operators that produce off-diagonal elements, such as spin raising and lowering operators in spin models and annihilation and creation operators in fermionic models, increases with a higher number of renormalizations. The interaction between distant sites compromises the sparsity of the matrix, leading to a high numerical cost for dense matrix diagonalization, scaling as $O(n_s^4)$.

For the efficient application of DMRG to systems with periodic boundary conditions (PBC), we utilize a modified DMRG algorithm [72]. This approach avoids the repeated renormalization of operators and delivers results without compromising accuracy. The details of the algorithm are discussed below.

1. The algorithm starts with a superblock of small size, i.e., one left block, one right block and two new site blocks as shown in Fig. 2.3 (a).

2. The target state $|\psi\rangle$ is obtained from the diagonalization of the superblock. The new system (environment) block is formed by combining the left (right) block with the two-site block. The density matrix ρ of the new system block is calculated using Eq. (2.3.2).

3. The block Hamiltonian and operators are projected onto the truncated basis formed by the n_s dominant states of ρ with the largest eigenvalues.

4. Next, the two-site blocks are appended to the renormalized system and environment blocks, as illustrated in Fig. 2.3(b), and the superblock Hamiltonian is constructed. This process is then repeated from the second step until the desired superblock size is achieved.

Thus it is clear that the strategy of adding new site block in this modified algorithm avoids the long bond that occurs in the conventional DMRG method with PBC. The blocks and operators in this method are renormalized once which diminish the error in the calculation.

2.3.4 Finite temperature calculation: Hybrid ED/DMRG

The hybrid ED?DMRG technique provides an effective framework for investigating the thermodynamic properties of one-dimensional spin and fermionic chains. In this approach, the high-temperature (T) regime is typically handled through ED on small system sizes, ensuring

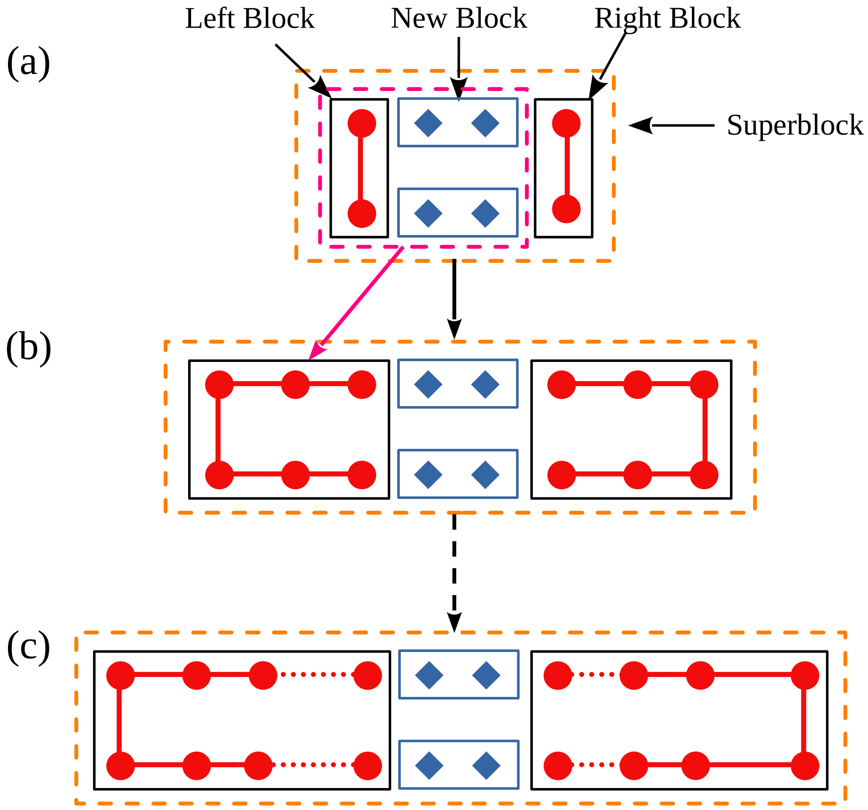

Figure 2.3: DMRG steps for PBC: At each step, two new blocks of $N = 2$ sites are added, as shown in (a). The renormalized left and right blocks are depicted inside the squares with solid blue lines. The red squares with solid lines represent the new site blocks. The magenta square with dashed lines indicates the new left block, which is formed by combining the old left block and the two new blocks. The new right block is the reflection of the new left block. These become the left and right blocks for the next step (b), as indicated by the magenta arrow. The black squares with solid lines represent the superblock at each step. In (c), the targeted system size is displayed.

an accurate description of the system's behavior at elevated temperatures. As the temperature decreases, DMRG is employed to compute low-energy excitations for progressively larger system sizes. By constructing partition functions from a limited number of states, this method enables an accurate description of low-temperature thermodynamics.

A key advantage of the hybrid ED/DMRG technique [299] is its ability to capture thermodynamic properties across a broad temperature range without requiring knowledge of the full excitation spectrum for large systems. Instead, DMRG is specifically optimized to extract low-energy states, extending its applicability beyond ground-state computations. This approach has been successfully utilized in the study of various one-dimensional spin systems [295, 299, 300] as well as fermionic models [302].

This thesis focuses on a spin-$\frac{1}{2}$ model consisting of N spins indexed by α, leading to a total of 2^N possible states. The thermodynamic properties of the system are determined using the canonical partition function:

$$Q(T,\alpha,N)=\sum_j \exp\left(-\beta E_j(\alpha,N)\right), \tag{2.3.9}$$

where $\beta=\frac{1}{k_BT}$, k_B is the Boltzmann constant, and the energy spectrum $\{E(\alpha,N)\}$ contains 2^N states for each α. The energy levels relative to the ground state are denoted as $E_j(\alpha,N)$.

We employ the efficient DMRG algorithm for periodic boundary conditions (PBC), as discussed in Section 2.3.3. Since the model incorporates second-neighbor interactions, we introduce blocks of two sites to eliminate interaction terms between pre-existing blocks. Each infinite DMRG step increases the block size by four sites.

Infinite DMRG is applied to construct systems with $N=4n$ spins. Subsequently, 5-10 sweeps of finite DMRG are performed. In most simulations, we retain $m=400$ eigenvectors corresponding to the highest eigenvalues of the system block density matrix. The superblock Hamiltonian thus has a dimension of $m^2 2^4$.

The hybrid method allows for thermodynamic calculations without requiring the full energy spectrum $\{E(\alpha,N)\}$. The DMRG approach prioritizes low-energy states $E_j(\alpha,N)$, which are significant at low temperatures. The DMRG partition function, considering l states of the superblock Hamiltonian, is given by:

$$Q_l(T,N)=\sum_{j=1}^{l}\exp\left(-\beta E_j(N)\right). \tag{2.3.10}$$

To enhance spectral accuracy, we construct system block density matrices $\rho_j(N)$ for the l levels at system size N and define an effective density matrix $\rho'(\beta',l,N)$:

$$\rho'(\beta',l,N)=\frac{\sum_{j=1}^{l}\exp(-\beta' E_j(N))}{Q_l(T,N)}. \tag{2.3.11}$$

For $l=1$, the effective density matrix simplifies to $\rho'(\beta',1)=\rho_1$, representing the ground state. Contributions for $l>1$ depend on the effective inverse temperature β'. We set $\beta'=10$ (in units of $1/|J_1|$), as the relevant temperature range is $T \sim 0.1$. Minor variations of β' (10–20%) do not significantly affect spectral accuracy. The effective density matrix plays a crucial role when low-lying excitations are closely spaced. The system block Hamiltonian and all operators are renormalized using $\rho'(\beta', l, N)$ to obtain the model Hamiltonian's energy spectrum at system size N. Initially, we take $l = 5$ or 10 to accurately determine the lowest excitations. A subsequent calculation is performed for $l > 100$. The entire spectrum experiences a uniform shift due to the inclusion of many excited states, necessitating an adjustment to align the lowest excitations with the initial calculation.

The partition function $Q(T, \alpha, N)$ in Eq. (2.3.9) is truncated using an energy cutoff $E_j(\alpha, N) \leq W_C(N)$. The cutoff $W_C(N)$ is selected to ensure the convergence of the maxima of $S_c(T, N)/T$ and $\chi_c(T, N)$, where $S(T, N)$ is the entropy per spin and $\chi(T, N)$ is the magnetic susceptibility per spin.

To reach the thermodynamic limit at system size N, we incrementally increase the cutoff energy $W_C(N)$ until the maximum of $S_C(T, N)/T$ at $T(N)$ is fully or nearly converged, typically requiring $\sim 10^3$ states. Extrapolation techniques are crucial for achieving the thermodynamic limit from finite system calculations. For quantities such as susceptibility $\chi(T)$ and specific heat $S'(T) = C(T)/T$, finite-temperature DMRG results are extrapolated using data from different system sizes.

2.4 Conclusion

This chapter has outlined the numerical methods employed in this thesis, specifically exact diagonalization and density matrix renormalization group (DMRG) techniques, which have been utilized in the analysis of various problems presented herein.

Chapter 3

Spin Peierls transition of $J_1 - J_2$ and extended models with ferromagnetic J_1.

3.1 Introduction

The one-dimensional J_1-J_2 spin chain, described by Eq. 3.1.1 with $\delta = 0$, consists of spin-$\frac{1}{2}$ moments interacting via nearest-neighbor (J_1) and next-nearest-neighbor (J_2) isotropic exchange couplings. The system has a single spin per unit cell. When the next-nearest-neighbor coupling is antiferromagnetic ($J_2 > 0$), the model exhibits frustration for both ferromagnetic and antiferromagnetic values of J_1. The degree of frustration is commonly expressed by the dimensionless ratio $\alpha = J_2/|J_1| > 0$.

Early studies of the $J_1 > 0$ sector at zero temperature ($T = 0$) revealed rich quantum behavior, including a critical point at $\alpha_c \approx 0.2411$ that separates the gapless Heisenberg antiferromagnetic (HAF) phase at $\alpha = 0$ from a gapped dimerized phase known as the Majumdar-Ghosh point at $\alpha = 1/2$ [228, 254]. This transition has been extensively investigated using both field-theoretical and numerical approaches [2, 55, 82, 195, 212, 306, 331, 335].

In the presence of an external magnetic field or additional interactions such as anisotropic or antisymmetric exchange, the J_1-J_2 model gives rise to a variety of unconventional quantum phases. These include vector chiral, multipolar, and spin-nematic phases [57, 74, 103, 104, 140, 148, 332]. Despite extensive efforts, exact thermodynamic results are available only in the unfrustrated limit where $J_2 = 0$ [169].

The thermodynamic behavior of quasi-one-dimensional magnetic materials has been shown to correlate closely, and in certain cases even semi-quantitatively, with the predictions of the J_1–J_2 spin chain model, irrespective of the sign of J_1, as discussed by Hase *et al.* [135]. This thesis primarily focuses on systems exhibiting ferromagnetic nearest-neighbor exchange interactions and their corresponding thermodynamic properties. A number of cupric oxide compounds containing spin-1/2 Cu(II) chains with ferromagnetic $J_1 < 0$ interactions have been experimentally realized. The frustration ratio $\alpha = J_2/|J_1|$ for these materials spans a wide range. For example, compounds such as $Ba_3Cu_3In_4O_{12}$ and $Ba_3Cu_3Sc_4O_{12}$ are reported to have nearly vanishing α values [80, 202], while others like $(N_2H_5)CuCl_3$ [226], $LiCu_2O_2$ [263], $LiCuSbO_4$ [81], $LiCuVO_4$ [243], and $Rb_2Cu_2Mo_3O_{12}$ [135, 402] exhibit moderate frustration with $\alpha \approx 0.5$. In these systems, the magnetic moment originates from the unpaired electron residing in the Cu^{2+} $3d_{x^2-y^2}$ orbital, which is strongly hybridized with the bridging O^{2-} ions. Although these chains are effectively one-dimensional at high temperatures, interchain couplings and additional interactions tend to become increasingly relevant as the temperature decreases, often leading to long-range magnetic order or other collective phenomena that lie beyond the scope of idealized 1D models.

The J_1–J_2 Heisenberg spin chain is composed of uniformly spaced lattice sites, as illustrated schematically in Fig. 3.1(a). When the system is coupled to lattice degrees of freedom, it becomes susceptible to a spin-Peierls (SP) distortion. Below the transition temperature T_{SP}, the chain undergoes spontaneous dimerization, leading to alternating exchange couplings of the form $J_1(1 \pm \delta)$, as depicted in Fig. 3.1(b). The distortion parameter $\delta(T)$ increases progressively as the temperature is lowered, reaching its maximum at absolute zero. Within the mean-field approximation, the spin excitation gap $\Delta(\delta(T))$ that develops in this dimerized phase exhibits behavior analogous to the energy gap in BCS superconductors, as described in Ref. [161].

In this chapter,[1] we examine the spin-Peierls (SP) transition in the context of the ferromagnetic J_1–J_2 spin chain, a scenario that exhibits notable differences from its antiferromagnetic counterpart and has received limited attention in previous studies.

The model with $J_1 < 0$ exhibits two distinct SP transitions, depending on the frustration ratio $\alpha = J_2/|J_1|$. For intermediate frustration values around $\alpha \sim 0.5$, the system undergoes a conventional dimerization of the chain at low temperatures ($T < T_{SP}$). However, for larger values of α, approximately $\alpha \sim 1$, the nature of the transition changes. In this regime, the system favors sublattice dimerization, as illustrated in Fig. 3.1(c), characterized by alternating second-neighbor couplings $J_2(1 \pm \delta)$. This pattern leads to a four-site unit cell and results in four degenerate ground states.

The mechanism behind sublattice dimerization becomes particularly transparent for $\alpha > 1$, where the ferromagnetic J_1–J_2 model effectively decouples into weakly interacting antiferromagnetic chains defined on the even and odd sublattices. A detailed discussion of the instability towards sublattice dimerization is provided in Section 3.2.

The spin Hamiltonian for the ferromagnetic J_1–J_2 chain, incorporating periodic boundary conditions, takes the form

$$H(\alpha, \delta) = \sum_r -\left(1 - \delta(-1)^r\right) \vec{S}_r \cdot \vec{S}_{r+1} + \alpha\, \vec{S}_r \cdot \vec{S}_{r+2}, \tag{3.1.1}$$

where $\alpha = J_2$ denotes the next-nearest-neighbor exchange interaction, and the nearest-neighbor coupling $|J_1|$ is chosen as the energy scale, i.e., $|J_1| = 1$. The parameter δ introduces dimerization in the *chain* geometry, as illustrated in Fig. 3.1(b).

In the absence of dimerization ($\delta = 0$), the model reduces to the well-known uniform J_1–J_2 chain with inversion symmetry about the lattice sites and a single spin-$\frac{1}{2}$ per unit cell. For this case, $H(\alpha, 0)$ exhibits a ferromagnetic ground state up to the critical frustration ratio $\alpha_c = 1/4$,

---

[1] The work reported here is based on the paper "Spin Peierls transition of $J_1 - J_2$ and extended models with ferromagnetic J_1: Sublattice dimerization and thermodynamics of zigzag chains in β-TeVO$_4$", by Manodip Routh, Sudip Kumar Saha, Manoranjan Kumar, Zoltán G. Soos in Phys. Rev. B 105 (23), 235109 (2022).

as exactly determined in Ref. [130]. Beyond this critical point ($\alpha \geq \alpha_c$), the ground state transitions into a singlet state with total spin $S = 0$—the regime of primary interest in this chapter.

Field-theoretical analyses distinguish between two regimes: gapless phases with nondegenerate ground states and gapped phases featuring a twofold ground state degeneracy [9]. In the frustrated regime $\alpha \geq \alpha_c$, the system enters an incommensurate (IC) phase characterized by a finite energy gap. Although this singlet-triplet excitation gap $\Delta(\alpha)$ is exponentially small [159], recent numerical studies have constrained it to be less than 10^{-3} [4].

At stronger frustration, specifically for $\alpha > 0.80$, the system exhibits a decoupled phase [195, 335], which becomes gapless and effectively reduces to two antiferromagnetic Heisenberg chains (HAFs) on separate sublattices as $J_1 \to 0$. Notably, the spin-$\frac{1}{2}$ HAF chain—corresponding to the special case $\alpha = \delta = 0$ in Eq. 3.1.1 with $J_1 > 0$—is one of the most thoroughly understood quantum spin models.

The J_1–J_2 spin model has found significant application in the study of quasi-one-dimensional (quasi-1D) magnetic systems, particularly those with a crystal structure comprising chains with two magnetic ions per unit cell and lacking inversion symmetry at lattice sites, even before accounting for spin-lattice interactions. An extension of this model, illustrated in Fig. 3.1(d), incorporates asymmetry in the nearest-neighbor exchange interactions. This is achieved by introducing a parameter γ, leading to exchange couplings of the form $J_1(1 \pm \gamma)$ for left and right neighbors, respectively. The resulting Hamiltonian $H(\alpha, \gamma)$, which replaces the parameter δ in Eq. 3.1.1 with γ, describes a system of reduced symmetry, explicitly breaking site-centered inversion. Within this framework, the SP transition leads to a sublattice dimerization pattern characterized by a four-site unit cell. Such a dimerized phase, depicted in Figs. 3.1(c) and 3.1(d), emerges near $\alpha \sim 1$ for both the conventional J_1–J_2 model and its asymmetric extension. At temperatures above the SP transition temperature ($T > T_{\text{SP}}$), the thermodynamic behavior of the extended model is effectively captured by Eq. 3.1.1, with the substitution $\delta = \gamma$.

The J_1–J_2 and extended models represent strongly correlated spin systems characterized by frustration α. Their ground-state ($T = 0$) properties have been extensively studied using a variety of analytical and numerical techniques. In contrast, significantly fewer methods are available for exploring their thermodynamic behavior, particularly in the low-temperature regime. For instance, Quantum Monte Carlo methods are not suitable for frustrated systems due to the sign problem. In this work, we compute the thermodynamic limit using a combination of exact diagonalization (ED) up to finite system sizes N, followed by density matrix renormalization group (DMRG) calculations for progressively larger systems, as described in Section 3.3 and previously reported in Ref. [299]. The antiferromagnetic J_1–J_2 model has been investigated using the transfer matrix renormalization group (TMRG) method [225] as well as temperature-dependent DMRG techniques [95]. These studies report the magnetic susceptibility $\chi(T)$ and specific heat $C(T)$ down to temperatures of $T/J_1 = 0.05$, with noticeable discrepancies emerging below $T/J_1 = 0.10$. Our recent work [301] demonstrated that the combined ED/DMRG

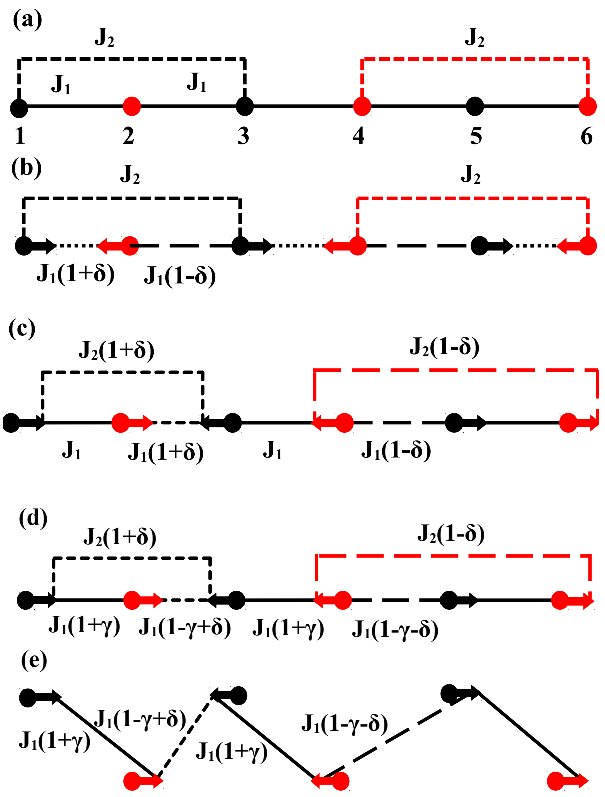

Figure 3.1: (a)–(c) Illustrations of the J_1–J_2 spin chain as described by Eq. 3.1.1, highlighting different dimerization patterns. The exchange interactions vary as $(1+\delta)$ or $(1-\delta)$ depending on whether the associated bond length is shortened or elongated. (a) Uniform chain with evenly spaced spin sites and constant J_1 and J_2 couplings. (b) Dimerized configuration with alternating nearest-neighbor couplings $J_1(1 \pm \delta)$, while next-nearest-neighbor J_2 remains unchanged. (c) Sublattice dimerization applied to the J_2 bonds, producing an alternating $J_2(1 \pm \delta)$ pattern. (d), (e) Schematics of the extended J_1–J_2 model incorporating sublattice dimerization with two geometries: (d) collinear and (e) zigzag. In both cases, every other nearest-neighbor bond maintains $J_1(1+\gamma)$, while the alternating bond strength follows $J_1(1-\gamma \pm \delta)$. The zigzag structure reduces to a ladder geometry for $\delta = 0$, with leg couplings J_2 and rung couplings alternating as $J_1(1 \pm \gamma)$.

approach provides accurate thermodynamic quantities down to $T/J_1 \sim 0.02$ for the J_1–J_2 model with antiferromagnetic $J_1 > 0$. Nevertheless, all existing approaches remain subject to further refinement and development.

Among the most extensively studied spin-Peierls (SP) systems with $J_1 > 0$ are the inorganic compound $CuGeO_3$ [131, 133], characterized by $\alpha = 0.35$ and investigated thoroughly during the 1990s, and the organic molecular crystal TTF-$CuS_4C_4(CF_3)_4$ [161], modeled earlier with $\alpha = 0$ corresponding to the Heisenberg antiferromagnet (HAF). Quantitative modeling of the magnetic susceptibility $\chi(T)$ for both systems above the SP transition temperature ($T > T_{SP}$) has been successfully performed using correlated spin states [90, 161]. The availability of large, high-quality $CuGeO_3$ crystals enabled inelastic neutron scattering experiments [223, 231, 245, 284], which exposed the shortcomings of mean-field approaches in describing the low-temperature phase ($T < T_{SP}$). Notably, the temperature dependence of the spin gap deviates from predictions of the BCS gap function, a discrepancy that remains unresolved in Uchinokura's 2002 review [363]. The SP transition and $\chi(T)$ behavior have been investigated using transfer-matrix renormalization group (TMRG) techniques [186] as well as exact diagonalization/density matrix renormalization group (ED/DMRG) methods [300], with a comparative discussion provided later in the manuscript. Correlated spin states [300] have been shown to reproduce the inelastic neutron data and successfully model both the specific heat anomaly and $\chi(T)$ in $CuGeO_3$. Moreover, they yield a self-consistent spin gap for the HAF, whose thermal evolution differs from the BCS form.

The magnetic behavior of β-$TeVO_4$ has attracted considerable attention over the past decade. [273, 312, 314, 372] This compound presents a number of unique characteristics as a quasi-one-dimensional (quasi-1D) material. Its crystallographic structure [312] reveals spin-1/2 zigzag chains running along the c axis within the bc plane, as schematically illustrated in Fig. 3.1(e). Experimental studies have reported three magnetic phase transitions occurring below 10 K, [273, 312, 372] often interpreted within the framework of the $T = 0$ phase diagram of the ferromagnetic J_1–J_2 model, which is typically applied to the system's paramagnetic regime. The magnetically active electron resides in the V^{4+} $3d_{xy}$ orbital, [185, 310] whose lobes are oriented approximately at $\pm\pi/4$ with respect to the bridging O^{2-} ions. Experimental measurements of the molar spin susceptibility $\chi(T)$ and the spin contribution to the specific heat $C(T)$ have been modeled [273, 312, 313, 372] using slightly differing estimates for the exchange constant J_1, with the frustration parameter α ranging from approximately 0.77 to 1. Notably, the transition at 4.6 K to an antiferromagnetic phase has yet to be quantitatively described within existing models. All three observed transitions have been qualitatively linked to a combination of ferromagnetic and antiferromagnetic exchange interactions between spins located on adjacent chains. [273, 312, 372] However, as discussed below, our analysis indicates that the ferromagnetic J_1–J_2 model fails to capture the low-temperature magnetic properties, which instead suggest a gapped excitation spectrum.

The extended model, described by Eq. 3.1.1 with the substitution γ for δ, features two spins per unit cell and exhibits a finite singlet–triplet energy gap, $\Delta(\alpha, \gamma) > 0$, which increases monotonically with γ. The ground state remains a nondegenerate singlet. This extended J_1–J_2 formulation offers a controlled framework for investigating gapped spin chains. We have calculated the thermodynamic properties of the one-dimensional Hamiltonian $H(\alpha, \gamma)$ with quantitative accuracy for temperatures $T > 0.03|J_1|$. The parameter choices for α and γ are guided by relevance to the material β-$TeVO_4$. A combined thermodynamic analysis indicates that $H(\alpha, \gamma)$ with $\gamma \approx 0.15$ serves as a reasonable first approximation for modeling β-$TeVO_4$.

It is important to differentiate between idealized one-dimensional spin models, such as Eq. 3.1.1, which assume rigid linear chains, and real quasi-one-dimensional materials. Models incorporating isotropic exchange and uniform spacing between spins are of fundamental theoretical interest, especially since isotropic exchange typically dominates the thermodynamic response. Nevertheless, Eq. 3.1.1 is inherently approximate and incomplete—not only due to the exclusion of interchain coupling and spin-lattice interactions, but also because it overlooks anisotropies introduced by spin–orbit coupling. These anisotropies manifest through modifications to the isotropic exchange and result in nontrivial g-tensors in external magnetic fields. Furthermore, dipolar interactions among electronic spins and hyperfine couplings with nuclear spins are also neglected. Although these terms are weak, they can play a significant role at low temperatures, both within and between chains.

This distinction between theoretical models and real materials is particularly pronounced in the case of β-TeVO$_4$. The conventional J_1–J_2 model assumes a single spin per unit cell and inversion symmetry at lattice sites. In contrast, β-TeVO$_4$ possesses a considerably lower symmetry. [312] The structure contains two inequivalent zigzag chains, each with two spins per unit cell. Notably, the inversion centers are not located on individual chains but lie between them, effectively interchanging the two chains under inversion symmetry.

The structure of this chapter is as follows. In Section 3.2, we examine the instability of the J_1–J_2 spin model within the singlet sector, where increasing the frustration parameter α induces dimerization along chains or sublattices. For the extended model with $\gamma > 0$, the onset of sublattice dimerization occurs under specific conditions. Section 3.3 presents the thermodynamic properties of the Hamiltonian $H(\alpha, \gamma)$, highlighting the strong dependence of the magnetic susceptibility $\chi(T, \alpha, \gamma)$ and specific heat $C(T, \alpha, \gamma)$ on γ at low temperatures. In Section 3.4, we model the spin-Peierls (SP) transition to a dimerized state using the conventional framework of linear spin-phonon coupling and a harmonic lattice [340], contrasting the behavior of the J_1–J_2 and extended models. Section 3.5 demonstrates that the thermodynamic response of the extended J_1–J_2 model captures key features of β-TeVO$_4$ in the paramagnetic regime, accurately reproducing experimental $\chi(T)$ and $C(T)$ data down to 2 K—well below the transition at 4.6 K. Notably, the transition manifests as a pronounced anomaly in $C(T)$ but produces only a subtle feature in $\chi(T)$. A concluding discussion is provided in Section 3.6.

3.2 Electronic Instability

Peierls first demonstrated that one-dimensional (1D) metals exhibit a ground-state instability. For a fixed electronic bandwidth of $4t$, a linear electron-phonon coupling induces a gap at the Fermi wave vector k_F in lattices characterized by harmonic potentials. A bond dimerization of the form $t(1 \pm \delta)$ reduces the ground-state energy of a half-filled band by opening a gap at $k_F = \pm\pi/2$. This electronic instability extends to correlated systems and to linear spin-phonon interactions in Heisenberg antiferromagnetic (HAF) chains and other spin systems. Modulations of exchange interactions that preserve the total values of J_1 and J_2 are permitted. Periodic boundary conditions are taken to represent a fixed system length or, equivalently, a constant 1D volume per spin. The dimerization instability in the antiferromagnetic J_1–J_2 model has been extensively analyzed as a function of the frustration parameter α.

In contrast, the focus of this study lies in the instability of the ferromagnetic J_1–J_2 model within the singlet sector for $\alpha > \alpha_c = 1/4$. At large α, where second-neighbor exchange dominates, the system favors sublattice dimerization, while at intermediate α, chain dimerization becomes energetically favorable. The corresponding electronic stabilization is evaluated using the Hamiltonian $H(\alpha, \delta)$ [Eq. 3.1.1], with exchange modulations depicted in Fig. 3.1(b) for chain dimerization and in Fig. 3.1(c) for sublattice dimerization.

Linear spin-phonon coupling modifies the exchange interaction by enhancing it in shortened bonds $[J(1 + \delta)]$ and reducing it in lengthened bonds $[J(1 - \delta)]$, with the total exchange conserved independently for first- and second-neighbor interactions. The ground state of $H(\alpha, \delta)$ is computed in the thermodynamic limit through exact diagonalization (ED) and density matrix renormalization group (DMRG) techniques applied to finite-size systems with periodic boundary conditions. The stabilization energy per spin due to chain dimerization in the J_1–J_2 model is defined as

$$\Delta E^{\text{chain}}(\alpha, \delta) = E_0(\alpha, \delta) - E_0(\alpha, 0), \tag{3.2.1}$$

where E_0 denotes the ground-state energy per spin.

The sublattice dimerization depicted in Fig. 3.1(c) results in an alternating next-nearest-neighbor exchange interaction given by $J_2 = \alpha(1 \pm \delta)$, while the nearest-neighbor couplings are fixed at $J_1 = -1$ for every left or right neighbor and alternate as $-(1 \pm \delta)$ for the other. The Hamiltonian for the sublattice-dimerized J_1–J_2 spin model in the absence of explicit bond alternation ($\gamma = 0$) is expressed as

$$\begin{aligned} H_S(\alpha, \gamma, \delta) = \sum_r - \left[1 - \gamma(-1)^r - \delta \cos\left(\frac{\pi r}{2}\right)\right] \vec{S}_r \cdot \vec{S}_{r+1} \\ + \alpha \left[1 + \sqrt{2}\delta \sin\left(\frac{\pi(2r-1)}{4}\right)\right] \vec{S}_r \cdot \vec{S}_{r+2}, \end{aligned} \tag{3.2.2}$$

where $\vec{S}_r$ denotes the spin-$\frac{1}{2}$ operator at site r. Sublattice dimerization in the extended model includes a nonzero alternation parameter $\gamma > 0$. To assess the energetic gain due to sublattice dimerization, we evaluate the Hamiltonian $H_S(\alpha, 0, \delta)$ on finite chains with periodic boundary conditions. The corresponding stabilization energy is defined as

$$\Delta E^{\text{sub}}(\alpha, 0, \delta) = E_S(\alpha, 0, \delta) - E_S(\alpha, 0, 0), \tag{3.2.3}$$

where E_S denotes the ground-state energy per site.

Each spin undergoes a displacement of $\pm\delta$ under either chain or sublattice dimerization. While the associated elastic energies are equivalent within the Einstein phonon model, this equivalence breaks down under more realistic phonon treatments. In a one-dimensional approximation, the optical phonon mode linked to chain dimerization exhibits a higher frequency—indicative of a stiffer lattice—compared to the $q = \pi/4$ mode characteristic of sublattice dimerization. Evaluating the electronic stabilization energy at fixed δ provides a qualitative measure of the energetically favored structural distortion.

We analyze the electronic stabilization energies from Eqs. 3.2.1 and 3.2.3 for $\alpha = 0.55$ and

0.65, as shown in the left and right panels of Fig. 3.2, employing ED for $N = 24$ and DMRG calculations for $N = 32$ and 48. For $\alpha \geq 0.65$, sublattice dimerization yields a greater reduction in energy, indicating its enhanced stability well before reaching the point where $J_2 = -J_1$. Specifically, increasing α from 0.55 to 0.65 leads to an 8% increase in ΔE^{chain} at $\delta = 0.1$, $N = 48$, whereas ΔE^{sub} decreases by 25%. This highlights a rapidly growing preference for sublattice dimerization as α increases.

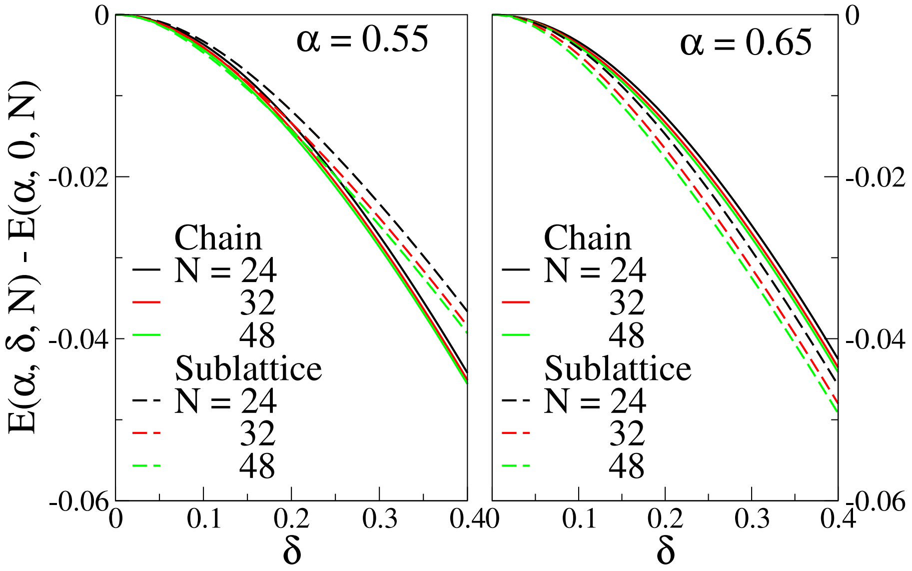

Figure 3.2: Ground state energy per site for the ferromagnetic J_1–J_2 spin chain consisting of N sites, evaluated for frustration parameters $\alpha = 0.55$ and 0.65. The solid lines represent results obtained using Eq. 3.2.1, incorporating a dimerized chain structure with nearest-neighbor couplings of the form $-(1 \pm \delta)$ and uniform next-nearest-neighbor couplings α. Dashed lines correspond to Eq. 3.2.3, applied in the case of sublattice dimerization with $\gamma = 0$, where the next-nearest-neighbor interactions are modulated as $\alpha(1 \pm \delta)$, and nearest-neighbor couplings alternate between -1 and $-(1 \pm \delta)$.

Previous studies on SP systems with $J_1 > 0$ have shown that they are inherently unstable toward chain dimerization. In contrast, the ferromagnetic J_1-J_2 model exhibits chain dimerization within the range $\alpha_c = 1/4$ to 0.55, and supports sublattice dimerization for $\alpha > 0.65$. The exact phase boundary is not determined here, as it also depends on the specific lattice geometry. Sublattice dimerization involves four spins per unit cell and remains relevant in the extended Hamiltonian $H(\alpha, \gamma)$, where $\gamma > 0$ replaces δ in Eq. 3.1.1, resulting in a system with two spins per unit cell. Without loss of generality, we consider $J_1 = -(1 \pm \gamma)$ for interactions with the left and right neighboring spins. Sublattice dimerization preserves the interaction strength with one neighbor ($J_1 = -(1 + \gamma)$), while introducing a modulation for the other. Numerical results for finite chains show that the ground state energy corresponding to a constant $J_1 = -(1 + \gamma)$ and an alternating interaction $J_1 = -(1 - \gamma \pm \delta)$ is lower than the energy for the reversed case, where $J_1 = -(1 - \gamma)$ remains unchanged and the alternation occurs in $J_1 = -(1 + \gamma \pm \delta)$, as described in Eq. 3.2.2.

The zigzag chain or two-rail ladder shown in Fig. 3.1(e) consists of rails with exchange coupling J_2 and rungs with exchange J_1. The arrows represent sublattice dimerization, which introduces alternating interactions of the form $\alpha(1 \pm \delta)$ along the rails. In the extended model, parallel arrows at neighboring sites still yield $J_1 = -(1+\gamma)$ on alternating rungs. On the remaining rungs, the J_1 values deviate from $-(1-\gamma \pm \delta)$ due to geometrical factors, as the corresponding antiparallel arrows are not aligned along the rungs. However, such details may be premature at this stage, given that exchange interactions are influenced not only by interatomic distances but also by the specific orbital pathways involved.

All subsequent calculations are carried out on systems exhibiting collinear sublattice dimerization. When $\gamma = 0$, Eq. 3.2.2 describes the J_1–J_2 model depicted in Fig. 3.1(c), where every alternate bond has a fixed interaction strength $J_1 = -1$, and the remaining J_1 couplings are modulated as $-(1 \pm \delta)$. The extended model shown in Fig. 3.1(d) corresponds to $\gamma > 0$ in Eq. 3.2.2, where the unmodulated J_1 remains at $-(1+\gamma)$, while the modulated interactions become $-(1-\gamma \pm \delta)$.

As previously noted, the singlet–triplet excitation gap $\Delta(\alpha, \gamma)$ increases with γ in the extended model. In contrast, the gap $\Delta(\alpha)$ in the ferromagnetic J_1–J_2 model vanishes in the decoupled phase and becomes exponentially small in the incommensurate (IC) phase. A finite $\Delta(\alpha, \gamma)$ enables a conditional spin-Peierls (SP) transition to a dimerized sublattice phase. The SP instability is governed by the electronic force constant, represented by the curvature of the ground state energy per site:

$$E_0''(\alpha, \gamma) = \left(\frac{\partial^2 E_0(\alpha, \gamma, \delta)}{\partial \delta^2} \right)_0 . \tag{3.2.4}$$

Here, $E_0(\alpha, \gamma, \delta)$ denotes the ground state energy per site corresponding to Eq. 3.2.2. It reduces to the J_1–J_2 model for $\gamma = 0$, and to the extended model when $\gamma > 0$. The curvature is negative because $E_0(\alpha, \gamma, \delta)$ attains a maximum at $\delta = 0$. The instability is termed conditional if $E_0''(\alpha, \gamma, N)$ remains finite in the thermodynamic limit. Table 3.1 presents the size dependence of this curvature for system sizes up to $N = 64$, evaluated at $\alpha = 0.75$ and 1, and for $\gamma = 0$ and 0.15. Since numerical derivatives are computed from small energy differences, accurate values of $E_0(\alpha, \gamma, \delta, N)$ are required. For $\gamma > 0$, the curvature values show convergence with increasing system size, while for $\gamma = 0$, they grow steadily with N, which is consistent with expectations. A much larger N would be needed to investigate $\Delta(\alpha)$ within the IC phase. To a leading approximation, the curvatures in Table 3.1 scale proportionally with α, reflecting the antiferromagnetic exchange between neighboring spins within a sublattice.

Table 3.1: Size dependence of the curvature $E''(\alpha, \gamma)$ in Eq. 3.2.4 of chains with $\alpha_1 = 0.75$, $\alpha_2 = 1.0$, N spins, and $\gamma_1 = 0$, $\gamma_2 = 0.15$ in Eq. 3.1.1 with $\delta = \gamma$.

N	$E''(\alpha_1, \gamma_1)$	$E''(\alpha_1, \gamma_2)$	$E''(\alpha_2, \gamma_1)$	$E''(\alpha_2, \gamma_2)$
24	-1.511	-1.324	-2.103	-1.968
32	-1.976	-1.498	-2.704	-2.278
48	-2.940	-1.501	-3.877	-2.298
64	-4.085	-1.504	-5.126	-2.304

In summary, Section 3.2 discusses sublattice dimerization as the SP instability occurring in the ferromagnetic J_1-J_2 model for $\alpha > 0.65$. The corresponding spin Hamiltonian is denoted as $H_S(\alpha, \gamma, \delta)$ in Eq. 3.2.2, where $\gamma = 0$ represents the J_1-J_2 model, and $\gamma > 0$ refers to its extended version. The parameter δ takes the value zero in the paramagnetic phase at temperatures above T_{SP}, and becomes nonzero when sublattice dimerization sets in. The SP instability is found to be unconditional in the J_1-J_2 model, whereas it is conditional in the extended model. The low-temperature thermodynamic properties of $H_S(\alpha, \gamma, 0)$ are analyzed in Section 3.3, and the SP transition to the dimerized sublattice phase in both models is presented in Section 3.4.

3.3 Thermodynamics

Spin chains with isotropic exchange interactions possess a total of 2^N spin states for a system of size N. In such systems, both the total spin $S \leq N/2$ and its Zeeman projection S^Z remain conserved quantities. We investigate the low-temperature thermodynamic behavior of the Hamiltonian $H_S(\alpha, \gamma, 0)$ for parameter regimes relevant to the paramagnetic phase of β-TeVO$_4$.

ED provides the complete energy spectrum $E(\alpha, \gamma, N)$ for systems up to $N = 24$ when $\gamma = 0$, and up to $N = 20$ for $\gamma > 0$, where translational symmetry is reduced. For larger system sizes, DMRG calculations are carried out using periodic boundary conditions and within fixed S^Z sectors, following the methodology outlined in Ref. [299]. In the DMRG procedure, the superblock consists of four new sites in addition to the left and right blocks. The dimension of the corresponding superblock Hamiltonian is $m^2 \cdot 4^2$, where m (typically 400) represents the number of eigenvectors associated with the largest eigenvalues of the system block's reduced density matrix. The ground state with $S^Z = 0$, denoted as $E_1(N)$, is taken as the reference with zero energy. Excited states are indexed by $j > 1$ and have excitation energies $E_j(N) > 0$. To accurately compute the low-lying excitations, we first perform a calculation targeting the lowest $l = 5$–10 eigenstates of the superblock. A second DMRG run is then performed targeting a larger number of states, typically $l > 100$ (commonly around 200). Due to contributions from multiple excited states in the reduced density matrix, the resulting energy spectrum is uniformly red-shifted. To correct for this, we apply a constant energy shift to the spectrum, and use the results from the first DMRG calculation to obtain precise values for the lowest excitations.

We introduce an energy cutoff $W(N)$ and construct the canonical partition function $Q_C(T, N)$ by including all $R(N)$ states with energies $E_j(N) \leq W(N)$. Using these $R(N)$ states, we calculate the entropy $S_C(T, N)$, magnetic susceptibility $\chi_C(T, N)$, and other thermodynamic quantities from $Q_C(T, N)$. The thermodynamic limit at system size N is approached by increasing $W(N)$ until the maximum of $S_C(T, N)/T$ at temperature $T(N)$ becomes stable or nearly stable. This typically occurs when $R(N) \sim 10^3$ states are included. At the maximum of $S(T)/T$, the derivative $S'(T_m)$ satisfies $S'(T_m) = S(T_m)/T_m$. Therefore, convergence of the size at this maximum gives the thermodynamic limit of $S'(T)$ at $T = T(N)$. Finite size effects are minimized in a narrow temperature range around $T(N)$ before the truncation starts to affect the results.

Table 3.2: Size dependence of $T(\alpha, \gamma, N)$ of chains with $\alpha_1 = 0.75$, $\alpha_2 = 1.0$ and $\gamma_1 = 0$, $\gamma_2 = 0.15$ in Eq. 3.2.2 with $\delta = 0$.

N	$T(\alpha_1, \gamma_1)$	$T(\alpha_1, \gamma_2)$	$T(\alpha_2, \gamma_1)$	$T(\alpha_2, \gamma_2)$
32	0.091	0.101	0.096	0.125
48	0.062	0.075	0.054	0.078
64	0.042	0.062	0.037	0.056
96	0.025	0.040	0.028	0.039

Table 3.2 shows the values of $T(N)$ for the specified α and γ in Eq. 3.2.2, with $\delta = 0$. Reliable thermodynamic results are obtained for $T > 0.03$ for system sizes up to $N = 96$. The $T(N)$ points are closely spaced, and more data points can be generated if needed. Larger system sizes, such as $N \sim 200$, can be reached with increased computational effort. The maximum accessible system size is limited by the density of correlated states in the model. Although extrapolation to lower T is feasible, it is generally not possible to reach $T = 0$. For instance, in the case of the HAF, there are known logarithmic corrections to $\chi(T)$ [169].

Fig. 3.3 compares $S(T, \alpha, \gamma, N)$ at $\alpha = 0.75$ for $\gamma = 0$ and 0.15 in the left and right panels, respectively. Solid and dashed lines represent ED and DMRG results, while the points correspond to $T(N)$ up to $N = 96$ for $\gamma = 0$ and $N = 128$ for $\gamma = 0.15$. The thermodynamic limit is estimated by interpolating between the $T(N)$ points and ED data for small systems. A linear extrapolation gives the $\gamma = 0$ entropy $S(T, \alpha, 0)$ and a finite value of $S'(T, \alpha, 0) = C(T, \alpha, 0)/T$ at $T = 0$; deviations from linearity at lower T are likely due to the exponentially small $\Delta(\alpha)$. For $\gamma = 0.15$, the system is clearly gapped, with $S'(T) = 0$ at $T = 0$ and reduced entropy compared to the $\gamma = 0$ case.

The size dependence of $\chi(T, \alpha, \gamma, N)$ is shown in Fig. 3.4 for $\alpha = 0.75$ chains with $\gamma = 0$ and 0.15. The logarithmic scale highlights the low T region. The susceptibilities overlap at slightly higher T than the temperatures $T(N)$ estimated from the entropy. In the left panel, the thermodynamic limit of $\chi(T, \alpha, 0)$ shows a maximum at $T_m = 0.34$, a minimum at lower T, and increases again as $T \to 0$, at least until $T \sim \Delta(\alpha)$. In the right panel, the gapped system with $\gamma = 0.15$ shows increasing susceptibility up to a maximum. The convergence of $\chi(T, \alpha, \gamma, N)$ at low T with increasing system size indicates that $\Delta(\alpha, \gamma)$ reduces finite-size effects for $N \sim 100$. The susceptibilities for $\gamma = 0$ and 0.15 become equal for $T > 0.60$ since the total exchange is independent of γ. A larger $\Delta(\alpha, \gamma)$ leads to convergence at higher T.

The thermodynamics of β-TeVO$_4$ was previously studied using the J_1-J_2 model and ED for $N < 20$ spins. [273, 312, 372] Finite size effects appear in $\chi(T)$ at $T \sim 0.15$ or $T \sim 6$ K for $-J_1 \sim 40$ K. These effects become significant in Fig. 3.4 when T is below the singlet-triplet gap corresponding to the system size N. The size dependence at $\gamma = 0.15$, where the chain is gapped, shows that results converge at $N = 128$ to $\chi(T)$ for $T > 0.03$, providing a good approximation even down to $T = 0$.

Similar $\chi(T, \alpha, \gamma)$ or $S(T, \alpha, \gamma)$ curves in the thermodynamic limit are obtained using ED for small N, DMRG at the points $T(N)$, and extrapolation to $T < T(N)$ for the largest

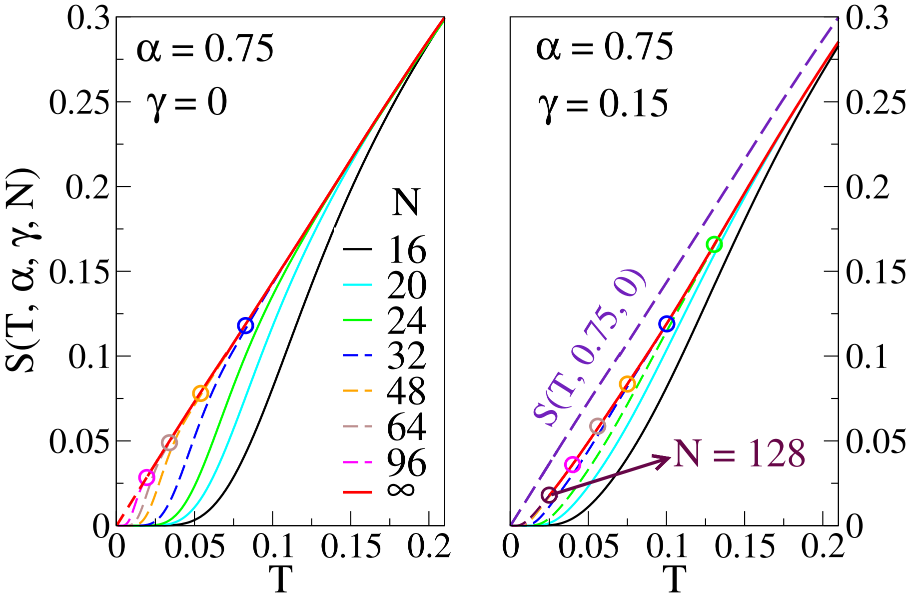

Figure 3.3: Entropy per site, $S(T, \alpha, \gamma, N)$, as defined in Eq. 3.2.2, calculated for a spin chain of N sites with no explicit dimerization ($\delta = 0$) and frustration parameter $\alpha = 0.75$. Results are shown for both the standard J_1–J_2 model ($\gamma = 0$) and an extended model with $\gamma = 0.15$. Solid curves represent data obtained using exact diagonalization (ED) for systems up to $N = 24$ (for $\gamma = 0$) and $N = 20$ (for $\gamma = 0.15$), as well as converged density matrix renormalization group (DMRG) results for temperatures $T > T(N)$, indicated by discrete points. Dashed lines illustrate the behavior of $S(T, \alpha, \gamma, N)$ at temperatures below $T(N)$. In the thermodynamic limit, the presence of a finite gap $\Delta(\alpha, \gamma)$ in the extended model ($\gamma = 0.15$) leads to a lower entropy compared to the gapless case ($\gamma = 0$).

N considered. The dependence of $\chi(T, \alpha, 0)$ on α is shown in Fig. 3.5 for the ferromagnetic J_1-J_2 model with $\alpha > 0.65$. The smallest value of susceptibility corresponds to the HAF, and its extrapolated behavior at lower T matches the exact result for $\chi(T)$ when $T \geq 0.01$; logarithmic corrections enhance [169] the exact $\chi(0) = 1/\pi^2$ by 6% at $T = 0.005$. As the antiferromagnetic exchange increases, $\chi(T, \alpha, 0)$ decreases with increasing α, as expected. The temperature dependence is monotonic for small α, and near the critical point $\alpha_c = 1/4$, it closely follows a power law [299] of the form $T^{-1.18}$. A secondary peak appears at $\alpha = 0.75$, which shifts to higher T with increasing α and becomes the only peak for $\alpha > 1$.

The thermodynamic limit of $S'(T, \alpha, 0) = C(T, \alpha, 0)/T$ is presented in Fig. 3.6 for the J_1-J_2 model at frustration values $\alpha > 0.65$. For the HAF, we find $S'(0) = 0.66$, which is close to the exact value of $2/3$. As α decreases, the density of low-energy states increases. The position of the maximum shifts toward lower T and eventually merges with the peak at $T = 0$. In the high T limit, the area under all the curves approaches $\ln 2$.

For fixed $|J_1| = 1$, the ED/DMRG technique provides the thermodynamic behavior of $H_S(\alpha, \gamma)$, Eq. 3.2.2, with $\delta = 0$ down to progressively lower temperatures $T \geq T(N)$, which depend on the system size N. Systems with $\alpha > 0.65$ exhibit instability toward sublattice dimerization. The equilibrium dimerization amplitude $\delta(T)$ decreases from its zero-temperature value $\delta(0)$ to $\delta(T_{SP}) = 0$ at the transition point. Obtaining the equilibrium $\delta(T)$ requires a

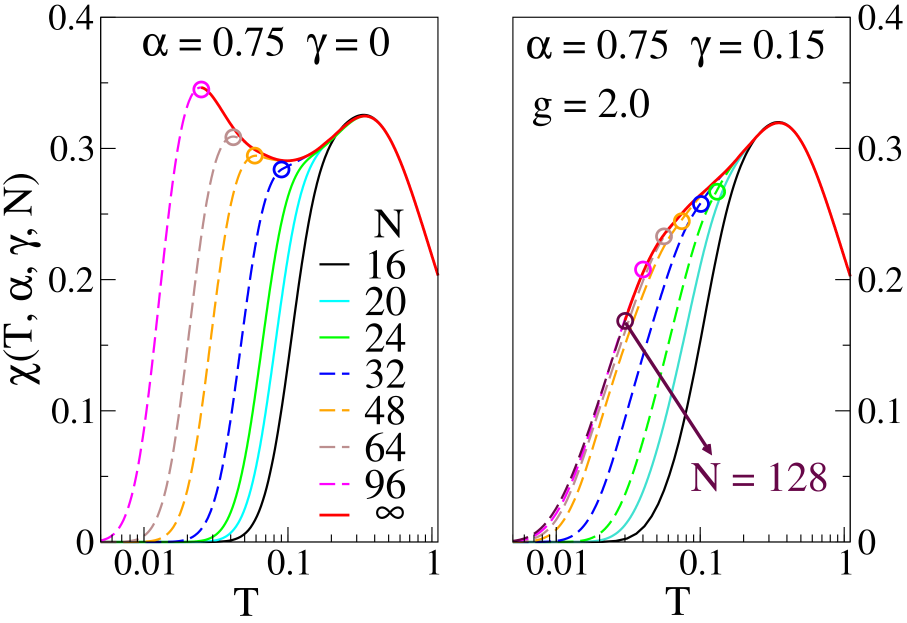

Figure 3.4: Temperature dependence of the magnetic susceptibility $\chi(T, \alpha, \gamma, N)$ as described by Eq. 3.1.1, evaluated for a system of N spins with $g = 2$ and fixed $\alpha = 0.75$. Two cases are shown: the standard J_1–J_2 model with $\gamma = 0$ and the extended model with $\gamma = 0.15$, where $\delta = \gamma$. Solid curves represent exact diagonalization (ED) results up to $N = 24$ for $\gamma = 0$ and up to $N = 20$ for $\gamma = 0.15$, combined with finite-temperature DMRG data (depicted as discrete points) for temperatures above a size-dependent crossover scale $T(N)$. Dashed lines correspond to $\chi(T, \alpha, \gamma, N)$ in the low-temperature regime $T < T(N)$. At zero temperature, the susceptibility vanishes due to finite-size gaps, which extrapolate to a finite excitation gap $\Delta(\alpha, \gamma)$ in the thermodynamic limit for $\gamma = 0.15$.

direct inclusion of the lattice degrees of freedom in order to properly account for the electronic instability.

3.4 Spin-Peierls transition

The Peierls instability in a half-filled band of noninteracting fermions arises from the filled valence band formed by bonding orbitals at $T = 0$, while the conduction band, consisting of antibonding orbitals, remains empty. The curvature of the ground state diverges as $E'' \propto \ln \delta$ [221], and the band gap is given by $4\delta(0)$ in reduced units ($t = 1$). As temperature increases, thermal excitation leads to partial occupation of antibonding orbitals and partial depletion of bonding orbitals, thereby reducing $\delta(T)$. The tendency towards dimerization is counteracted by a harmonic lattice potential of $\delta^2/2\epsilon_d$ per site, associated with an optical phonon at wave vector $q = \pm\pi/2$. In addition to assuming linear electron-phonon coupling and a harmonic lattice [340], two standard approximations are applied: the adiabatic (Born-Oppenheimer) approximation, which neglects nuclear kinetic energy, and the mean-field approximation, which assumes a uniform bond distortion amplitude $\delta(T)$. The lattice force per site that counterbalances the electronic instability is δ/ϵ_d, and these approximations are also applicable to interacting fermion

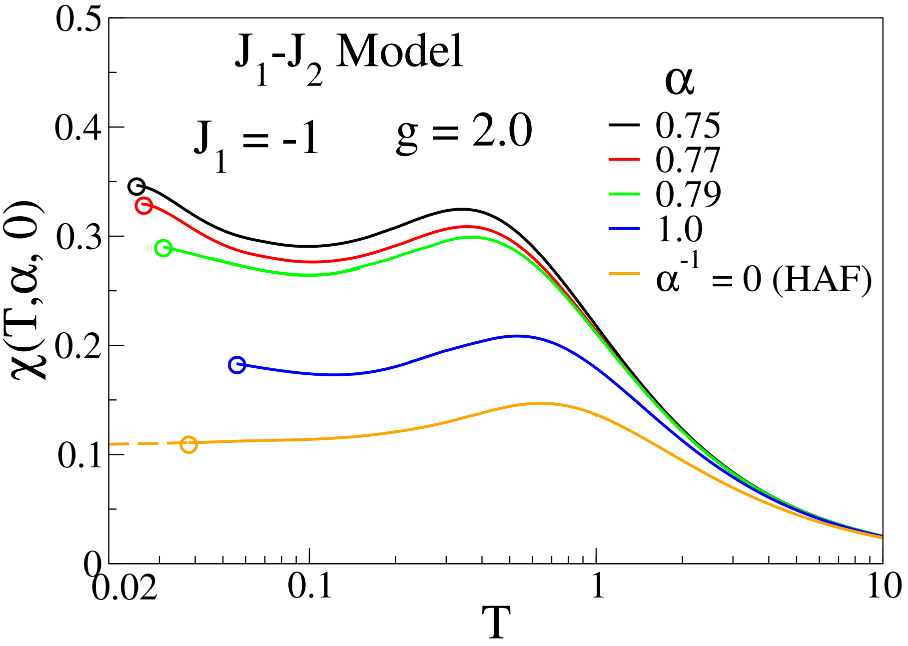

Figure 3.5: Temperature-dependent magnetic susceptibility $\chi(T, \alpha, 0)$ for the J_1–J_2 spin chain with uniform exchange interactions ($\delta = 0$ in Eq. 3.1.1), presented as discrete data points for temperatures $T > T(\alpha, 96)$, where numerical convergence is achieved. The susceptibility for the Heisenberg antiferromagnetic (HAF) limit is extended to lower temperatures via extrapolation, approaching the exact zero-temperature value of $1/\pi^2 \approx 0.10132$.

systems or correlated spin chains.

The equilibrium sublattice dimerization for $\alpha > 0.65$ in Eq. 3.2.2 is described by

$$\frac{\delta(T)}{\epsilon_d} = -\left(\frac{\partial A(T, \delta)}{\partial \delta}\right)_{\delta(T)} \qquad T \leq T_{SP} \tag{3.4.1}$$

where $A(T, \delta)$ denotes the free energy per site. While the thermodynamic limit of the derivative with respect to δ has been well established for noninteracting fermions using the grand canonical partition function, it remains unknown for correlated spin chains, including the HAF. Equation 3.4.1 serves as the SP gap equation and provides a criterion for self-consistency. Given that $\delta(T_{SP}) = 0$, the experimentally observed T_{SP} sets the value of the stiffness $1/\epsilon_d$, or vice versa, allowing determination of $\delta(T)$ down to zero temperature. Thus, the transition is controlled by a single parameter, either T_{SP} or the stiffness.

We consider $A(T, \delta, N) = -T \ln Q(T, \delta, N)$, where $Q(T, \delta, N)$ is the canonical partition function for a system of size N, and solve Eq. 3.4.1 to obtain $\delta(T, N)$ for $T \leq T_{SP}$. As discussed in Section 3.3, convergence of the derivative $A'(T, \delta, N) = \partial A(T, \delta, N)/\partial \delta$ to its thermodynamic limit occurs for $T > T(N)$. The dependence of $A'(T, \delta, N)$ on system size is illustrated in Fig. 3.7 for $\alpha = 0.79$ and $\gamma = 0$ or 0.15, shown in the left and right panels, respectively.

The sublattice dimerization driving force, $-A'(T, \delta, N)$, decreases with increasing T, as expected. Its dependence on system size becomes weaker as δ increases, since a larger δ enhances the gap $\Delta(\delta)$. For $\delta = 0.105$, the values of $A'(T, \delta, N)$ at $T = 0$ show near convergence by

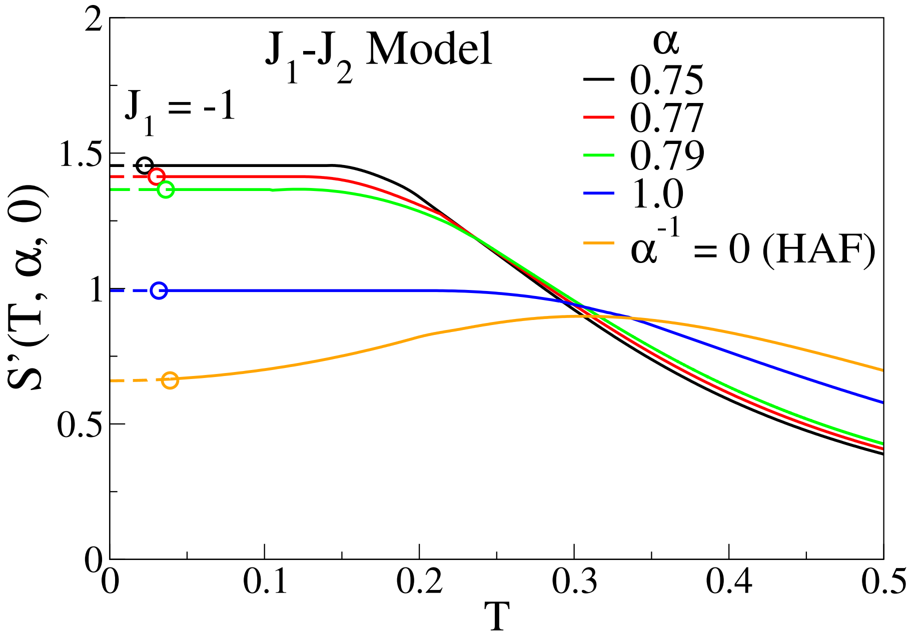

Figure 3.6: Temperature dependence of the converged quantity $S'(T, \alpha, 0) = C(T, \alpha, 0)/T$ for the J_1–J_2 spin chain with no dimerization ($\delta = 0$ in Eq. 3.1.1). Data points are shown for temperatures $T > T(\alpha, 96)$, where finite-size effects are negligible.

$N = 32$ in both panels. Near the transition temperature T_{SP}, the curves for $\delta = 0.005$ have already reached the thermodynamic limit for $T > T(32)$. The thermodynamic limit is effectively achieved at $N = 32$ around $T \sim T_{SP}$ due to the elevated temperature, and also around $T \sim 0$ because of the large value of $\Delta(\delta(0))$.

Since $\delta(T_{SP}) = 0$, the curvature $-A''(T_{SP}, 0)$ sets the stiffness parameter $1/\epsilon_d$ at a given T_{SP}. A typical value used is $T_{SP} = 0.10$. For temperatures $T \leq T_{SP}$, the value of $\delta(T)$ is obtained from Eq. 3.4.1, where $\delta(0)$ is given by $E'(\delta(0))/A''(T_{SP}, 0)$. Almost identical $\delta(T, N)$ for $N = 24$ and 32 suggests that $\delta(T)$ has converged for a system size of $N = 32$. These converged $\delta(T)$ results are presented in Fig. 3.8 for $\alpha = 0.79$ with $\gamma = 0$ and 0.15 in the upper panel, and for $\alpha = 0.75$ with $\gamma = 0$ and 0.15 in the lower panel. To calculate the temperature derivative $d\delta(T)/dT$, which is required in the following analysis, $\delta(T)$ is fitted using the expression

$$\frac{\delta(T)}{\delta(0)} = \left[1 - \left(\frac{T}{T_{SP}}\right)^a\right]^b \qquad T \leq T_{SP} \tag{3.4.2}$$

The fitting parameters are $a = 3.868$, $b = 0.354$ for $\alpha = 0.79$, $\gamma = 0$, and $a = 2.835$, $b = 0.408$ for $\alpha = 0.75$, $\gamma = 0.15$. The variation of $\delta(T)$ near T_{SP} is more gradual in the gapped chain with $\gamma > 0$ compared to the sharper drop in the gapless case.

An SP transition generates a $C(T)$ anomaly and a discontinuous $\chi(T)$ slope at T_{SP}. We evaluate the anomaly for $T \leq T_{SP}$ as

$$\frac{C(T)}{T} \equiv \frac{dS(T, \delta(T))}{dT} = \frac{\partial S(T, \delta(T))}{\partial T} + \frac{d\delta(T)}{dT}\frac{\partial S(T, \delta(T))}{\partial \delta}$$

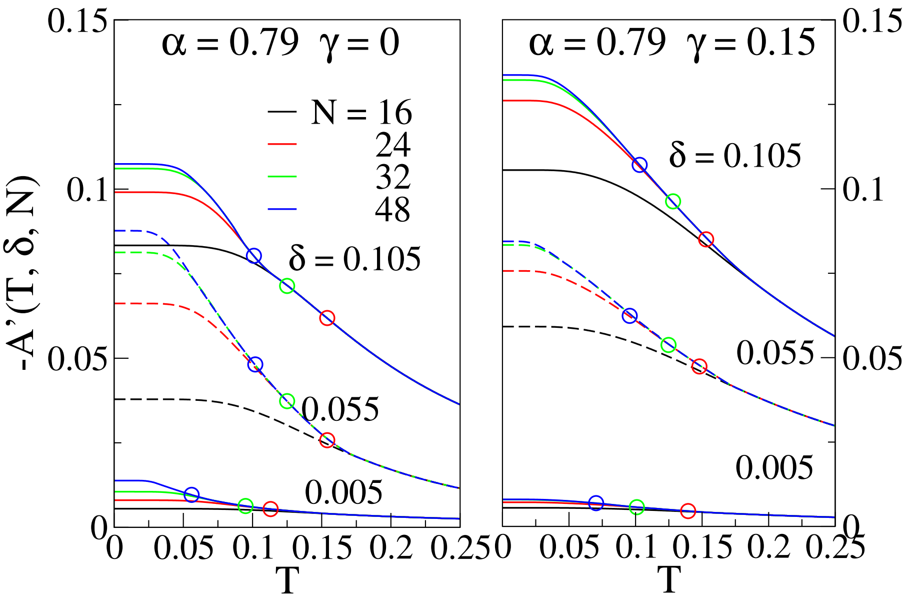

Figure 3.7: The thermodynamic driving force $-A'(T, \delta, N)$ associated with sublattice dimerization δ, as described by Eq. 3.4.1, for both the standard J_1–J_2 model and its extended version with $\gamma = 0.15$. Calculations are shown for frustration parameter $\alpha = 0.79$ and a system of N spins, as specified in Eq. 3.2.2. The open circles indicate the temperature $T(N, \delta)$ at which the dimerized phase becomes energetically favorable.

The first term, $C(T, \delta(T))/T$ is evaluated at the equilibrium $\delta(T)$. The second term shows a discontinuity at T_{SP}, where $\delta(T) = 0$ for $T \geq T_{SP}$. This abrupt change is a well-known consequence of the mean-field approximation, which entirely neglects lattice fluctuations.

Figure 3.9 presents the calculated values of $C(T)/T$ for $T_{SP} = 0.10$, $\alpha = 0.75$, and two cases: $\gamma = 0$ (left panel) and $\gamma = 0.15$ (right panel). The anomaly is computed for system size $N = 32$, which is sufficiently large to represent the thermodynamic limit for these parameters. The solid green lines corresponding to $\delta = 0$ show the converged $C(T)/T$ results for temperatures $T \geq T_{SP}$ or for cases where no phase transition occurs. In the right panel with $\gamma = 0.15$, the green line at $T < T_{SP}$ for $\delta = 0$ is obtained by extrapolating the entropy for $N = 128$ using the expression

$$S(T) = cT^{-\eta} \exp(-\Delta/T) \qquad T \leq T(128) \tag{3.4.3}$$

where Δ is the singlet-triplet energy gap $\Delta(\alpha, \gamma)$, evaluated at $N = 128$. The parameters η and c are determined by matching both the value and slope of $S(T)$ to the calculated entropy and its derivative at $T = T(128)$. The dashed red curves represent $C(T, \delta(T))/T$, which is the first term in Eq. 3.4.3, calculated for the converged $N = 32$ systems.

As discussed in Section 3.3, the total area under the curve defined by $S'(T) = C(T)/T$ approaches $ln2$ in the high-temperature limit for all parameter sets. Because $C(T)/T$ remains the same for $T \geq T_{SP}$, a consistent value of $S(T_{SP})$ directly indicates that the area up to T_{SP} under both the green $\delta = 0$ and red $\delta(T)$ curves in either panel of Fig. 3.9 is identical. These curves intersect at a temperature $T' < T_{SP}$, and the area between them up to T' is noticeably

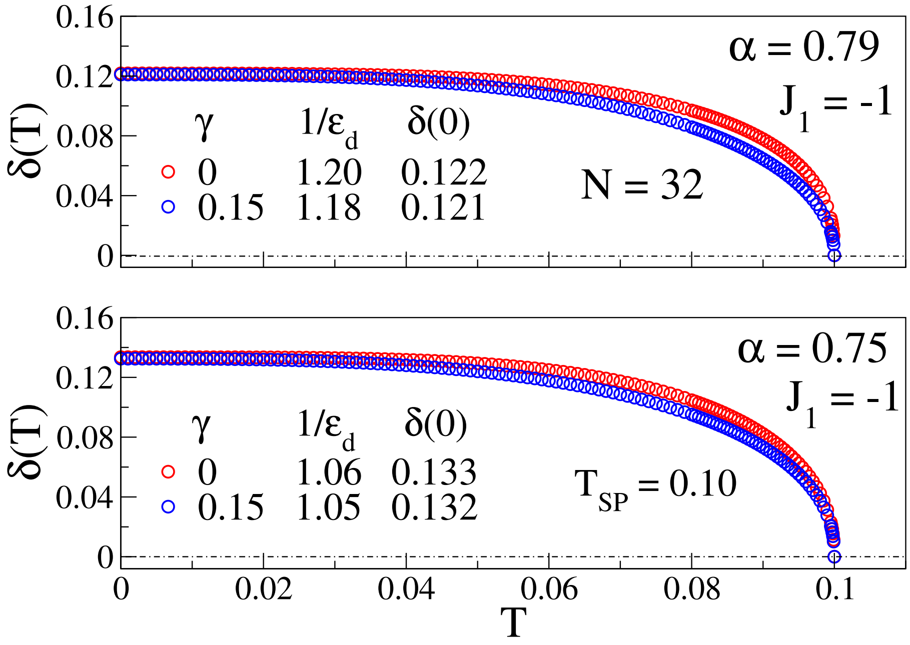

Figure 3.8: Temperature-dependent amplitude $\delta(T)$ of the sublattice dimerization, as obtained from Eq. 3.4.2, for spin chains comprising $N = 32$ sites. The calculations are based on the model defined in Eq. 3.2.2, with parameters chosen such that the spin-Peierls transition temperature is $T_{SP} = 0.10$.

smaller when $\gamma = 0.15$ compared to $\gamma = 0$. As a result, the area from T' to T_{SP} must also be smaller for the gapped system with $\gamma = 0.15$ undergoing a conditional SP transition. It is important to note that the reduced anomaly in $C(T)/T$ for $\gamma = 0.15$ mainly arises from the singlet-triplet gap $\Delta(\alpha, \gamma)$ and the entropy $S(T_{SP}, \alpha, \gamma)$. The role of lattice approximations in determining the calculated dimerization is of lesser importance, since $\delta(T)$ primarily affects the shape of the anomaly.

Fig. 3.10 presents the computed $\chi(T, \delta(T))$ for the models shown in Fig. 3.9, using parameters $T_{SP} = 0.10$, $\alpha = 0.75$, and $\gamma = 0$ (left panel) or $\gamma = 0.15$ (right panel), with $\delta = 0$ for $T > T_{SP}$. The green curves ($\delta = 0$) represent the converged susceptibilities of chains that do not undergo an SP transition. The red curves display $\chi(T, \delta(T))$ for $T \leq T_{SP}$, calculated using the equilibrium values of $\delta(T)$. At T_{SP}, the SP transition leads to a discontinuous change in the slope of $\chi(T)$. In the $\gamma = 0$ case, a prominent cusp appears, corresponding to a transition from a gapped, dimerized chain to a gapless one. For $\gamma = 0.15$, the cusp is less pronounced because the sublattice dimerization primarily enhances the existing gap at $\delta = 0$. Approximations that neglect lattice fluctuations tend to make the $\chi(T)$ cusp sharper.

We investigated additional SP transitions in chains described by Eq. 3.2.2 with $\alpha > 0.65$ and $\gamma \geq 0$, and observed similar behavior in $C(T)$ and $\chi(T)$. Systems with $\gamma > 0$ demonstrate conditional instability toward sublattice dimerization. For parameter sets that yield finite gaps $\Delta(\alpha, \gamma)$, the SP transition is characterized by a noticeable but smaller anomaly in $C(T)$ along with a moderate cusp in $\chi(T)$ at T_{SP}. It is worth mentioning that SP transitions are often identified by cusps in $\chi(T)$, frequently in the absence of specific heat measurements.

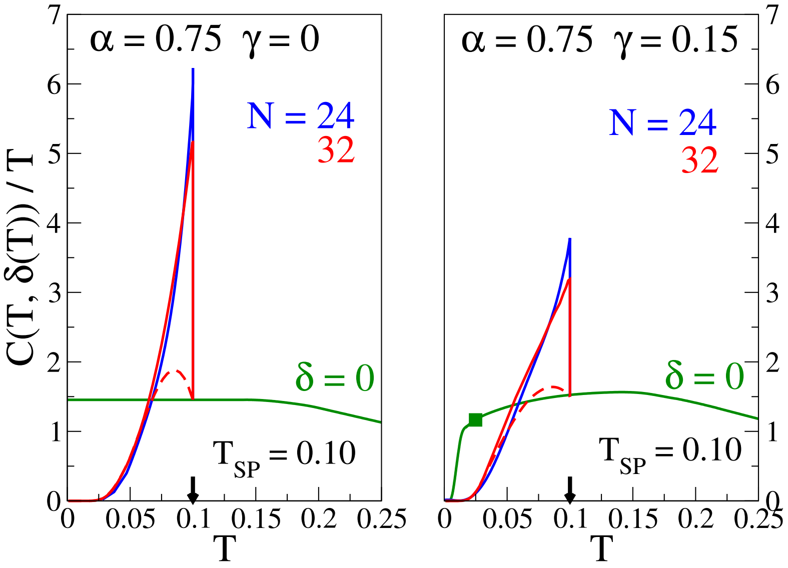

Figure 3.9: Temperature dependence of the normalized specific heat, $C(T)/T$, for the spin-Peierls (SP) transitions in both the standard J_1–J_2 model ($\gamma = 0$) and the extended model with $\gamma = 0.15$, evaluated at $\alpha = 0.75$ and $T_{\mathrm{SP}} = 0.10$. The continuous green curves represent the undistorted case ($\delta = 0$), extended to $T = 0$ for $\gamma = 0$, and extrapolated from $T(128)$ down to zero temperature using Eq. 3.4.3 for $\gamma = 0.15$. The solid blue and red curves depict results from Eq. 3.4.3 for system sizes $N = 24$ and $N = 32$, respectively. The dashed red curve corresponds to $C(T, \delta(T))/T$, representing the leading contribution from Eq. 3.4.3 at $N = 32$.

3.5 β-TeVO$_4$ Thermodynamics

We have analyzed the thermodynamic behavior of Eq. 3.2.2 for $\alpha > 0.65$, focusing on the SP transition that leads to sublattice dimerization. The extended J_1-J_2 model with isotropic exchange interactions is characterized by three main parameters: J_1, α, and γ. A fourth parameter, T_{SP}, determines the stiffness $1/\epsilon_d$ of the harmonic lattice, or alternatively, the value of $\delta(T)$ for $T \leq T_{SP}$. The model framework, including the linear spin-phonon coupling and the assumptions regarding the lattice, is clearly defined. With these four parameters, both the SP transition and the system's thermodynamics are completely described.

The quasi-1D compound β-TeVO$_4$ consists of zigzag spin chains running along the c axis. Weaker exchange interactions of either sign have been calculated [310] between spins in neighboring chains, and interchain coupling has been considered [273, 314, 372] as a possible origin of the phase transitions observed at 2.3 K, 3.3 K, and 4.6 K. Except for an early study, the magnetic susceptibility and spin-specific heat at higher temperatures have generally been interpreted using the J_1–J_2 model with $\delta = 0$ in Eq. 3.1.1.

Table 3.3 presents three reported values of J_1 and α that produce good fits to the magnetic susceptibility $\chi(T)$ and heat capacity $C(T)$ for temperatures above 8 K in the paramagnetic phase. It also includes two extended models characterized by J_1, α, and $\gamma = 0.15$. Additionally, the table provides the computed entropy $S(T)$ at $T = 5.5$ K. The energy per site in the ferromagnetic phase, where spins are fully aligned under a uniform external magnetic field B,

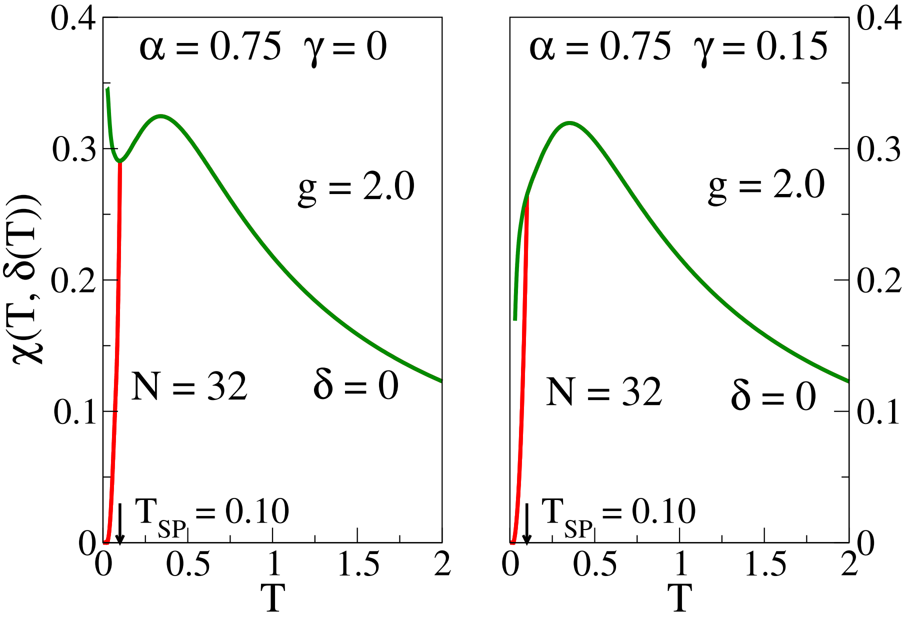

Figure 3.10: Temperature-dependent magnetic susceptibility $\chi(T,\delta(T))$ computed for the J_1–J_2 model with $\gamma = 0$ and its extended counterpart with $\gamma = 0.15$, both at $\alpha = 0.75$ and spin-Peierls transition temperature $T_{SP} = 0.10$. The green solid curves represent the converged susceptibility $\chi(T,0)$ for the uniform chain ($\delta = 0$) and temperatures $T \geq T(128)$, where finite-size effects are negligible. The red curves show $\chi(T,\delta(T))$ calculated with the temperature-dependent equilibrium dimerization $\delta(T)$, extrapolated to the thermodynamic limit using a system size of $N = 32$.

is given by

$$E_F(\alpha,\gamma,B) = -\frac{(1-\alpha)}{4} - \frac{hB}{2} \tag{3.5.1}$$

where $h = g\mu_B/|J_1|$, with $g = 2$ and μ_B denoting the Bohr magneton. The value of B_{sat} listed in Table 3.3 corresponds to the magnetic field at which the true ground state at 0 K becomes ferromagnetic. Further experimental results obtained in the paramagnetic phase offer additional uses of the Hamiltonian $H(\alpha,\gamma)$.

The reported $\chi(T)$ data are not exactly the same but vary by a few percent. We have used the $\chi(T)$ data from Savina et al. [312] as a reference, corresponding to a magnetic field applied along the a or c axis with $g = 2.0$; data in the temperature range 1.9 to 6 K are taken from Fig. 7, while data at higher temperatures are taken from Fig. 4. The measured $\chi(T)$ shown in Fig. 3.11 has been shifted downward by 5×10^{-3} and is compared to the computed curves for $\gamma = 0.15$, which have also been shifted downward and are nearly identical. We have included the exact $\chi(T,N)$ for $N = 20$, which is larger than the $N = 18$ system used in Ref. [312]; however, deviations from the experimental data at low temperatures are observed due to finite size gaps.

For the purpose of performing model-to-model comparisons and calculations, we have rescaled the data by adjusting $-J_1$ from 38.3 K to 36.6 K in Ref. [273] and from 26.6 K to 25.5 K in Ref. [372]. The rescaled values of J_1 listed in Table 3.3 result in slightly lower B_{sat} and higher

Table 3.3: Exchange parameters J_1 and α as reported in Refs. [312], [273], and [372], based on fits to the magnetic susceptibility $\chi(T)$ of β-TeVO$_4$ in the paramagnetic regime. The table also includes the computed values of the saturation magnetic field B_{sat} and molar entropy $S(5.5)$ at 5.5 K. Values in parentheses indicate rescaled J_1 parameters (as described in the main text), along with the corresponding B_{sat} and $S(5.5)$. The bottom two rows present results for extended J_1–J_2 models incorporating an interchain coupling $\gamma = 0.15$.

$-J_1$ (K)	$\alpha = J_2/\lvert J_1\rvert$	B_{sat} (T)	$S(5.5)$ (J/Kmol)
38.3[a]	0.77	22.3	1.67
38.3[b](36.6)	0.80	24.5(23.4)	1.55(1.62)
26.6[c](25.5)	1.0	24.8(23.7)	1.56(1.58)
36.0[d]	0.79	23.4	1.43
39.2[d]	0.75	23.3	1.45

[a] Ref. [312] [b] Ref. [273] [c] Ref. [372] [d] $\gamma = 0.15$

$S(5.5)$. The computed $\chi(T)$ curves shown in Fig. 3.11 agree well with each other in the paramagnetic regime. The convergence of these results for $T > 8$ K indicates that $\chi(T)$ is not very sensitive to the aligned parameters J_1, α, and γ given in Table 3.3.

At low T, the behavior is reversed, highlighting distinct variations among the calculated $\chi(T)$. The solid lines in Fig. 3.11 represent results in the thermodynamic limit for $T > T(N)$, while the marked data points correspond to $N = 96$ for the J_1-J_2 models and $N = 128$ for the extended models with $\gamma = 0.15$. The convergence of $\chi(T, N)$ toward the thermodynamic limit as N increases is illustrated in Fig. 3.4. For $\gamma = 0.15$, the gap $\Delta(\alpha, \gamma) \sim 0.05|J_1|$ has nearly reached convergence, as indicated by the $N = 96$ and 128 results. Investigating the much smaller $\Delta(\alpha)$ in the IC phase of the J_1-J_2 models requires significantly lower T. Therefore, we infer that the J_1-J_2 model with $\delta = 0$ in Eq. 3.1.1 does not adequately describe the susceptibility of β-TeVO$_4$ below 8 K.

For temperatures above $T > 15$ K, the specific heat is primarily governed by lattice phonons. In the low-temperature regime, the Debye T^3 law serves as an approximation for acoustic phonons, considering a mass M per unit cell in β-TeVO$_4$, which contains four formula units per cell. Additionally, the temperature-dependent specific heat $C(T)$ exhibits greater sensitivity to model parameters compared to the magnetic susceptibility $\chi(T)$. The $C(T)$ data for $T > 8$ K shown in Fig. 3.12 is adapted from Fig. 1 of Ref. [313], with a downward shift of 0.2, and is compared to the calculated specific heat for $\gamma = 0.15$, also shifted. The lattice contribution is given by $C_{\mathrm{latt}}(T) = 3.6 \times 10^{-4} T^3$. At low temperatures, the exact diagonalization result for $N = 20$ sites reveals finite-size gaps. Due to entropy conservation, the ratio $C(T, N)/T$ approaches the thermodynamic limit from above; this is because a reduced entropy $S(T, N)$ at low temperatures must be compensated by an increased entropy at intermediate temperatures before converging to the total entropy $S(T)$. Previous studies that modeled $C(T)$ and $\chi(T)$ in the paramagnetic regime with $N < 20$ fail to capture the low-temperature behavior accurately.

The computed molar $C(T)/T$ shown in Fig. 3.12 correspond to the same set of parameters as those in Fig. 3.11. For $\gamma = 0.15$, the data are converged for $T \geq T(128)$ and are obtained using Eq. 3.4.3 at lower temperatures. As explained in Section 3.4, the J_1–J_2 curves remain

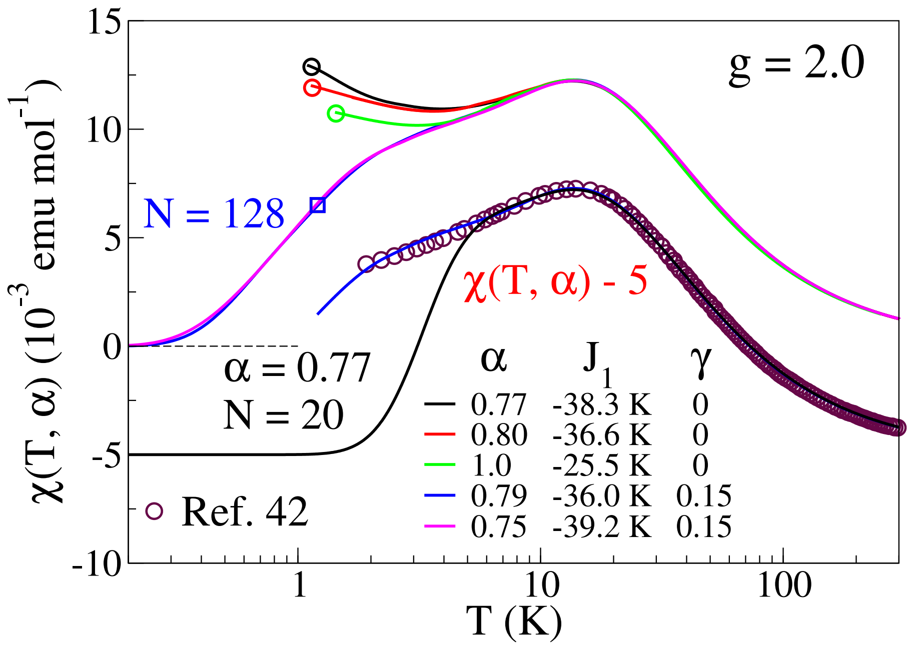

Figure 3.11: Molar magnetic susceptibility $\chi(T)$ of β-TeVO$_4$, with experimental data available down to $T = 1.9$ K from Ref. [312]. All theoretical curves, except for the exact diagonalization (ED) result at $N = 20$, represent converged $\chi(T)$ calculations using the parameters indicated in the legend. The $\chi(T) - 5$ offset curves provide a direct comparison between experiment, ED at $N = 20$, and a converged model incorporating $\gamma = 0.15$. While the theoretical results show good agreement for temperatures above 8 K, discrepancies emerge at lower temperatures. Open circles mark the temperature $T(96)$ associated with J_1–J_2 models at $\gamma = 0$, and the filled square indicates $T(128)$ for both extended models.

finite down to temperatures around $T \sim \Delta(\alpha)$, which represents the exponentially small energy gap in the IC phase. In contrast, the gapped $\gamma = 0.15$ chains satisfy $S'(0) = 0$. The results exhibit reasonable convergence for $T > 7$ K and excellent convergence for $T > 10$ K, which is comparable to the convergence observed in $\chi(T)$. Moreover, the low-temperature behavior of $C(T)$ in the thermodynamic limit differs significantly for the model parameters listed in Table 3.3.

The thermodynamic behavior of β-TeVO$_4$ described above indicates that all five models presented in Table 3.3 successfully reproduce the $\chi(T)$ and $C(T)$ data for temperatures above 8 K. Among them, the extended models with $\gamma = 0.15$ provide a significantly better agreement with the experimental $\chi(T)$ data below 8 K, as shown in Fig. 3.11. Specific heat measurements including the transition at 4.6 K have been reported by three groups [273, 313, 372], and are shown as $C(T)/T$ in the upper panel of Fig. 3.13. The anomaly associated with the transition appears broadened on the high-temperature side, which is qualitatively consistent with the influence of lattice fluctuations.

The entropy $S(5.5)$, obtained by integrating the $C(T)/T$ data up to $T = 5.5$ K, represents the measured entropy at this temperature. In this range, the Debye contribution is negligible. The integrated areas were found to be 1.35, 1.43, and 1.47 J/Kmol in Refs. [313], [372], and [273],

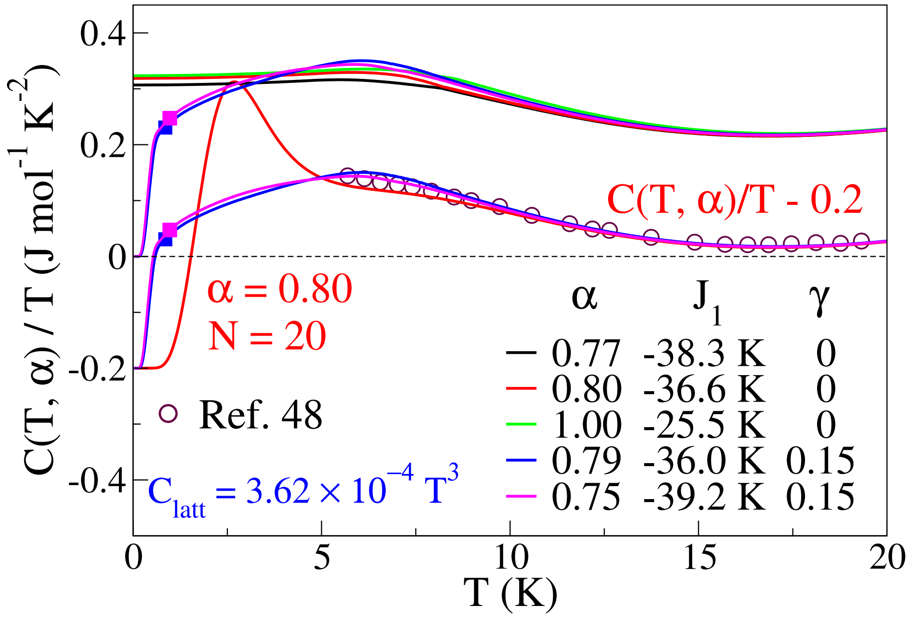

Figure 3.12: Temperature dependence of the molar specific heat divided by temperature, $C(T)/T$, for β-TeVO$_4$ after subtraction of the phonon (Debye) contribution, C_{latt}. Experimental data are taken from Ref. [313]. The plotted theoretical curves represent converged results, except for the exact diagonalization (ED) data at $N = 20$. All calculated curves show good agreement above $T > 7$ K, while deviations appear at lower temperatures. For the J_1–J_2 model with $\gamma = 0$, $C(T)/T$ remains finite as $T \to 0$. In contrast, the $\gamma = 0.15$ curves for $T < T(128)$ are obtained via extrapolation using Eq. 3.4.3.

respectively. The corresponding values of $S(5.5)$ calculated for $\gamma = 0$ in Table 3.3 exceed the measured values by approximately 10%. Adjusting J_1 as discussed in relation to $\chi(T)$ increases $S(5.5)$ by 0.07 and 0.02 J/Kmol for Refs. [273] and [372], respectively. Since entropy is a state function, $S(5.5)$ does not depend on the specific thermal path from $T = 0$ to 5.5 K. This measured entropy at 5.5 K supports the selection of the extended model with $\gamma = 0.15$.

The solid lines marked as $\delta = 0$ in the upper panel of Fig. 3.13 represent the computed values of $C(T)/T$ for the $\gamma = 0.15$ models, which are also presented in Fig. 3.12. Using the same set of parameters, the red curve corresponds to a scenario where the anomaly is interpreted as a conditional SP transition occurring at 4.6 K. A semi-quantitative fit of the absolute specific heat is achieved by assuming $T_{SP} = 4.6$ K. In comparison, the more prominent anomaly associated with gapless J_1-J_2 models exhibiting unconditional transitions is illustrated in Fig. 3.9.

The molar spin susceptibility $\chi(T)$ for temperatures below 10 K is presented in the lower panel of Fig. 3.13. The data and the curve corresponding to $\delta = 0$ are identical to those shown in Fig. 3.11. The extended models with $\gamma = 0.15$ listed in Table 3.3 provide a good description of $\chi(T)$ across the full temperature range up to 300 K. The computed $\chi(T, \delta(T))$, using the same parameters and assuming $T_{SP} = 4.6$ K, exhibits a cusp at the transition. The change in slope of $\chi(T)$ at T_{SP} is significantly more pronounced than the subtle feature observed in Fig. 7 of Ref. [312].

An intriguing aspect of the 4.6 K transition is the pronounced anomaly observed in $C(T)/T$,

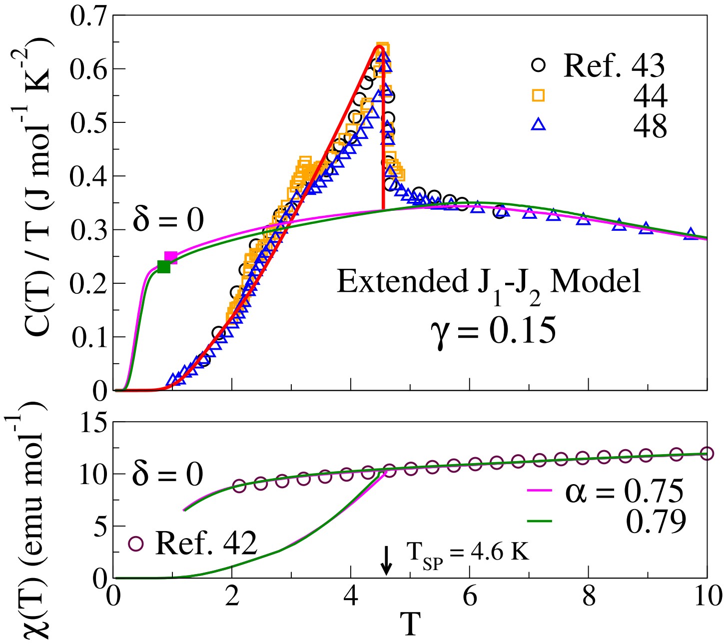

Figure 3.13: Upper panel: Experimental data for the specific heat divided by temperature, $C(T)/T$, are shown for $T < 6$ K from Refs. [273, 372] and for $T < 10$ K from Ref. [313]. Theoretical curves for $\delta = 0$ correspond to the calculated results with $\gamma = 0.15$ presented in Fig. 3.12. The red curve indicates the predicted spin-Peierls (SP) transition, obtained from Eq. 3.4.1, assuming $\gamma = 0.15$. **Lower panel:** Magnetic susceptibility $\chi(T)$ as measured in Ref. [312]. Theoretical $\chi(T)$ curves for $\delta = 0$ are again shown for $\gamma = 0.15$, consistent with Fig. 3.11. Results labeled $\chi(T, \delta(T))$ incorporate the temperature-dependent lattice distortion $\delta(T)$ from extended models with $\gamma = 0.15$.

which shows minimal correspondence in $\chi(T)$. Various other parameters have also been examined. The main challenge lies in the fact that the $C(T)/T$ data at low temperatures indicate the presence of a larger gap than that predicted by $\delta = 0$ models, which accurately describe the thermodynamic behavior at higher temperatures. However, increasing the gap leads to a decrease in $\chi(T)$. This discrepancy between the small gap implied by $\chi(T)$ and the large gap required by $C(T)$ presents a significant challenge for quantitative modeling of β-TeVO$_4$.

As mentioned in the Introduction, one-dimensional (1D) models with isotropic exchange interactions, such as Eq. 3.1.1, serve as basic approximations for understanding the magnetic behavior of quasi-1D materials. An example in the case of β-TeVO$_4$ is the saturation field B_{sat}. The g factor [273, 312] remains close to 2.0 when the magnetic field B is applied along the a or c crystallographic axis. The values of B_{sat} shown in Table 3.3 correspond to models that consider only isotropic exchange and thus represent the external magnetic field required in such idealized conditions. Experimental measurements at $T \sim 50$ mK [274, 360] yielded a saturation field of approximately 21.7 T. The discrepancy between the calculated and measured values may be reasonably explained by the presence of an internal magnetic field that contributes to the total effective field beyond the applied field B_{app}, even though the exact origin and strength of this internal field remain unclear. Additional arguments also support the possibility of such an internal field.

The modeling of β-TeVO$_4$ has already gone beyond the J_1-J_2 model at a qualitative level. Due to the low symmetry of zigzag chains, both antisymmetric and anisotropic contributions to the otherwise isotropic exchange interactions are allowed. Additionally, there are interchain couplings J', which can be either ferromagnetic or antiferromagnetic, between neighboring spins on different chains. However, specific modifications to the J_1-J_2 framework have not yet been clearly established, and performing a detailed quantitative analysis remains a difficult task.

3.6 Conclusion

The spin-Peierls (SP) instability in the ferromagnetic J_1-J_2 model, considered in the singlet sector of Eq. 3.1.1 with $J_1 < 0$ and $\delta = 0$, shows notable differences compared to SP systems with $J_1 > 0$. For values of $\alpha = J_2/|J_1| > 0.65$, the system exhibits *sublattice* dimerization, resulting in singlet ground states characterized by four spins per unit cell. When α is smaller, the system instead undergoes *chain* dimerization, which is typical for $J_1 > 0$, and leads to two spins per unit cell down to the critical point $\alpha_c = 1/4$. The treatment of SP transitions into dimerized sublattices within the J_1-J_2 model follows the usual approach: linear spin-lattice coupling, a harmonic lattice, and the use of both adiabatic and mean-field approximations for the lattice. In the singlet sector, the SP instability of the ferromagnetic J_1-J_2 model is found to be unconditional.

The extended model with $\delta = 0$ in Eq. 3.2.2 exhibits reduced symmetry, possesses a non-degenerate singlet ground state within the parameter range of interest, and features a finite singlet-triplet gap $\Delta(\alpha, \gamma)$. The spin-Peierls (SP) instability in this case is conditional, and for systems that are sufficiently soft with $\alpha > 0.65$, the transition leads to sublattice dimerization. When the SP transition is conditional, the anomaly in $C(T)/T$ and the cusp in $\chi(T)$ at T_{SP} are both diminished in magnitude, as discussed in Section 3.4.

ED/DMRG is a recent method [299] used to study the low-temperature thermodynamic properties of 1D spin chains. It has been tested against certain exact and numerical results [301], but broader acceptance of this technique as a reliable tool will require further comparative studies. The SP transition in CuGeO$_3$ has been modeled using TMRG [186] and ED/DMRG [300], both employing the same lattice approximations and parameter values: $J_1 = 160$ K, frustration $\alpha = 0.35$, and $T_{SP} = 14.4$ K. In the TMRG approach, the stiffness K (or $1/\epsilon_d$) was found to be $11J_1$ ($11.1J_1$), with $\delta(0) = 0.026$ (0.0248) and a gap $\Delta = 40$ K (38 K) at $T = 0$ K. The same $\chi(T)$ data was quantitatively fitted for $T > T_{SP}$ in Fig. 4 of [186] and across the full temperature range in Fig. 5 of [300], as required for self-consistency by Eq. 3.4.1. Achieving a quantitative TMRG fit to $\chi(T)$ below T_{SP} required [186] a slightly reduced stiffness of $K = 10.2J$, which in turn resulted in a higher $T_{SP} = 15.2$ K. The self-consistency condition was met to within 8%. For comparison, a mean-field fit to $\chi(T)$ below T_{SP} in an organic SP system with $\alpha = 0$ yielded [161] a transition temperature $T_{SP} = 9$ K, which is 25% lower than the experimentally observed value of 12 K.

The ED/DMRG approach allows the study of low-temperature (T) thermodynamic properties of correlated spin chains, including the J_1-J_2 model and its extended versions. To minimize finite-size effects, large system sizes with $N \sim 100$ or more are typically necessary. However, as spin correlations weaken at high T, smaller system sizes become adequate. For J_1-J_2 models with $N < 20$, ED has been used to analyze various combinations of J_1 and α, successfully describing the magnetic susceptibility $\chi(T)$ and spin specific heat $C(T)$ of β-TeVO$_4$ in the paramagnetic region. Nonetheless, this approach does not capture the behavior below 10 K, where the data suggest a gapped excitation spectrum. To address this discrepancy, the extended models with $\gamma = 0.15$ and the values of J_1 and α listed in Table 3.3 are required, as discussed in Section 3.5.

We were unable to successfully reproduce the $C(T)/T$ and $\chi(T)$ data shown in Fig. 3.13. The $\delta = 0$ curves in the lower panel describe $\chi(T)$ down to 2 K without indicating a spin-Peierls (SP) transition at 4.6 K. Using the same values of J_1, α, γ, and $T_{SP} = 4.6$ K, we obtain the red $\gamma = 0.15$ curves in the upper panel. However, the significant gap arising from sublattice dimerization does not agree with the observed behavior of $\chi(T)$.

The J_1–J_2 model has been previously employed to explore the quantum phases of β-TeVO$_4$ at low temperatures and under varying magnetic fields, ranging from $B = 0$ to $B > B_{\text{sat}}$. This analysis provides a consistent, though qualitative, description. The observed quantum phases correspond to the symmetry inherent in the J_1–J_2 model, which is significantly higher than the actual symmetry of the material. Measurements of $\chi(T)$ and $C(T)$ suggest the presence of gapped systems, with gap values considerably larger than $\Delta(\alpha)$, although the origin of the gap is not necessarily attributed to γ. Experimental comparisons yield precise parameters for one-dimensional models with isotropic exchange interactions, which serve as a foundation for further investigation of the magnetic behavior in complex quasi-one-dimensional materials.

Chapter 4

Phase diagram of spin-1/2 coupled trimer chains

4.1 Introduction

Low-dimensional quantum spin systems with competing interactions have become an intriguing subject in the last few decades [73, 206, 286, 368, 369]. The competition between exchange interactions in these systems leads to a diverse range of exotic phases. Alternating exchange interactions in one-dimensional (1D) or quasi-1D spin models, which imply a longer unit cell compared to uniform systems, can introduce interesting electronic and magnetic properties, leading to entirely new phases not present in models with uniform exchange. Therefore, models with non-uniform exchange are more generalized, and a thorough study of these models is relevant as they offer a broader scope to represent many low-dimensional magnetic materials that show poor agreement with uniform model systems. For instance, the spin-1/2 Heisenberg antiferromagnet (HAF) with a one spin per unit cell, whether or not it includes additional frustrated exchange, does not exhibit a magnetic plateau [30, 143]. In contrast, the spin-1/2 coupled trimers having a unit cell made of three spin spin-1/2 (trimerized nearest neighbor (NN) exchange), displays a plateau at one-third of the saturation magnetization [146, 218]. The appearance of the plateau is consistent with the theorem of Oshikawa, Yamanaka, and Affleck [258].

We notice that various types of exchange pathway arrangements are possible in trimer systems. These systems can be classified into two categories: (i) pathways that include only nearest-neighbor (NN) exchange interactions, and (ii) pathways that incorporate both nearest-neighbor and next-nearest-neighbor (NNN) exchange interactions. For instance, $3\mathrm{CuCl}_2 \cdot 2\mathrm{dx}$ (dx = dioxane) belongs to the first category and can be modeled as a spin-1/2 Heisenberg trimer chain with J_1-J_1-J_1' interactions (intratrimer J_1 and intertrimer J_1'), where $J_1 < 0$ is ferromagnetic (FM) and $J_1' > 0$ is antiferromagnetic (AFM) [7]. Hida studied this model and reported a 1/3 magnetization plateau for small J_1/J_1' [146]. Another spin-1/2 trimer chain compound, $\mathrm{Cu}_3\mathrm{P}_2\mathrm{O}_6(\mathrm{OH})_2$, with AFM interactions $J_1 > 0$ and $J_1' > 0$, also exhibits a 1/3 magnetization plateau [137].

The second category includes compounds such as $\mathrm{A}_2\mathrm{Cu}_3\mathrm{Ge}_4\mathrm{O}_{12}$ (where A = Na, K) [27, 54, 272, 338], which is an excellent realization of a coupled spin-1/2 trimer system with antiferromagnetic intratrimer exchange J_1, J_2, and intertrimer exchange J_1'. Here, J_1 and J_1' correspond to NN exchange interactions, while J_2 represents an NNN exchange interaction. Another example is the Heisenberg diamond ladder, characterized by diamond-shaped unit cells made of trimer unit, arranged along the chain, has attracted significant attention in both experimental and theoretical studies [78, 79, 102, 150, 157, 180, 181, 255, 256, 305, 309, 344, 349, 355, 404]. Compounds such as $Cu_3(CO_3)_2(OH)_2$ [180, 181], $A_3Cu_3(PO_4)_4$ [where A = Ca, Sr], and $Bi_4Cu_3V_2O_{14}$ [305] are modeled by the Heisenberg diamond chain.

Another key property of trimer system is that antiferromagnetically weakly coupled spin-1/2 trimer chains exhibit emergent composite excitations of novel quasi-particles, namely doublons and quartons, in addition to low-energy fractional spinon excitations [27, 53, 54, 213, 272]. The emergent composite quasi-particles exist only in the weak intertrimer exchange limit ($J_1'/J \ll 1$). As $J_1'/J \to 1$, these states fractionalized into conventional spinon continuum.

Motivated by the diverse range of theoretical and experimental studies in spin-1/2 trimer compounds, we consider a general quasi-1D spin-1/2 coupled trimer model and investigate its ground state (gs) properties. The model includes NN intertrimer exchange J_1 and intertrimer exchange J_1', while the NNN intertrimer and intertrimer exchange is J_2 and J_2', respectively. Often in real materials, we find the NNN exchanges fall under two categories: either $J_2 >> J_2'$ or $J_2 << J_2'$. For example, when $J_2 \sim 0$, it becomes a diamond lattice. When $J_2' \sim 0$, this becomes coupled trimer as seen in $Na_2Cu_3Ge_4O_{12}$ [27]. Therefor, in this manuscript we have considered a special case where $J_2 = J_2'$. The schematic figure of coupled trimer is shown in Fig. 4.1 (a). The model simplifies to the uniform $J_1 - J_2$ model [55, 200, 201, 381] when $J_1' = J_1$ as shown in Fig. 4.1(b). When $J_1' < J_1$, the uniform model transforms into a set of trimers connected by intertrimer NN exchange J_1' and NNN exchange J_2. Within each trimer, spins interact through NN exchange J_1 and NNN exchange J_2. Therefore, J_2 tends to make the chain uniform, while J_1' induces trimerization, introducing another form of frustration into the model. In an isolated trimer ($J_1' = 0$), two spins form a singlet pair while one spin remains unpaired, contributing to the magnetization. Consequently, a system of L spins with $\frac{L}{3}$ isolated trimers is expected to have a high spin gs ($S^z = \frac{L}{6}$) even in finite systems, unlike a uniform system where the finite system size always results in a singlet gs ($S^z = 0$). Both strong J_1' and strong J_2 tend to destabilize the high spin gs. At strong intertrimer NN interaction ($J_1' > 0.5J_1$), the system shows no signs of a high spin gs and exhibits all the exotic phases similar to the uniform $J_1 - J_2$ model, although the phase boundaries are shifted due to the weak trimerization effect. Based on the results for excitation gap, level crossing, spin correlations, structure factor, and bond-bond correlations, we construct a quantum phase diagram (QPD) in the $J_1'/J_1 - J_2/J_1$ parameter space. The QPD is divided into two regions. In the region where the intertrimer exchange is weak ($0 \leq J_1'/J_1 < 0.4$), we identify three distinct phases: AFM with quasi-long-range order (QLRO), trimer or high spin ground state, and gapless spiral. In the region where the intertrimer exchange is strong ($0.4 \leq J_1'/J_1 \leq 1.0$), the SF and spiral phases with a gap persist, and a gapped dimer phase emerges between them.

The chapter is divided into four main sections. Section 4.2 covers the model Hamiltonian and the method. Section 4.3 presents the quantum phase diagram (QPD) and provides details about the phases. Finally, section 4.4 concludes the results.

4.2 Model Hamiltonian & method

We consider a spin-1/2 antiferromagnetic (AFM) quasi-1D chain with periodic boundary conditions (PBC) in the presence of trimerized interactions. In this setup, every three consecutive spins along the chain are coupled by strong exchange interactions, forming a trimer unit. These trimer units are then connected to each other by comparatively weaker interactions. Given our interest in systems with frustration, where a variety of exotic phases are expected to emerge, we include antiferromagnetic (AFM) next-nearest neighbor (NNN) exchange interactions in addition to the nearest neighbor (NN) interactions in this model. The Hamiltonian of the spin-1/2 AFM trimer model, consisting of N trimers or L $(= 3N)$ spins with periodic boundary conditions (PBC), can be expressed as follows:

$$\mathcal{H} = \mathcal{H}_{\text{intertrimer}} + \mathcal{H}_{\text{intertrimer}} \tag{4.2.1}$$

where, the Hamiltonian for intertrimer interactions is:

$$\begin{aligned} \mathcal{H}_{\text{intertrimer}} &= \sum_{r=1}^{L/3} \Big[J_1 (\vec{S}_{r,1} \cdot \vec{S}_{r,2} + \vec{S}_{r,2} \cdot \vec{S}_{r,3}) \\ &+ J_2 \vec{S}_{r,1} \cdot \vec{S}_{r,3} \Big] \end{aligned} \tag{4.2.2}$$

and the Hamiltonian for intertrimer interactions is:

$$\begin{aligned} \mathcal{H}_{\text{intertrimer}} &= \sum_{r=1}^{L/3} [J_1' \vec{S}_{r,3} \cdot \vec{S}_{r+1,1} \\ &+ J_2 (\vec{S}_{r,2} \cdot \vec{S}_{r+1,1} + \vec{S}_{r,3} \cdot \vec{S}_{r+1,2})] \end{aligned} \tag{4.2.3}$$

Here, $S_{r,i}$ is a spin$-1/2$ operator acting on i-th site of r-th trimer. J_1 and J_2 represent the NN and NNN intertrimer interactions, respectively, within a trimer unit. Whereas the NN and NNN intertrimer couplings that connect NN trimers are denoted by J_1' and J_2, respectively. The coupled trimer is shown in Fig. 4.1(a). In this manuscript, we consider only the NN interactions to be trimerized and NNN interactions uniform along the chain. The intertrimer NN exchange $J_1 = 1$ is chosen as the unit of energy. The parameter space is confined between two parameters J_1'/J_1 and J_2/J_1 and our study is limited to $0 \leq J_2/J_1 \leq 1$.

The Hamiltonian in Eq. (4.2.1) reduces to the frustrated $J_1 - J_2$ model at $J_1' = J_1$ with uniform AFM NN and NNN couplings. In this limit, the Hamiltonian in Eq. (4.2.1) can be written as:

$$\mathcal{H} = J_1 \sum_r \vec{S}_r \cdot \vec{S}_{r+1} + J_2 \sum_r \vec{S}_r \cdot \vec{S}_{r+2} \tag{4.2.4}$$

This 1D-chain system can be visualized as a zigzag ladder, where spins along each leg interact via exchange J_2, and nearest-neighbor (NN) inter-leg spins are coupled via J_1, as shown in Fig.4.1(b). The competition between J_1 and J_2 in Eq. (4.2.4) results in a rich phase

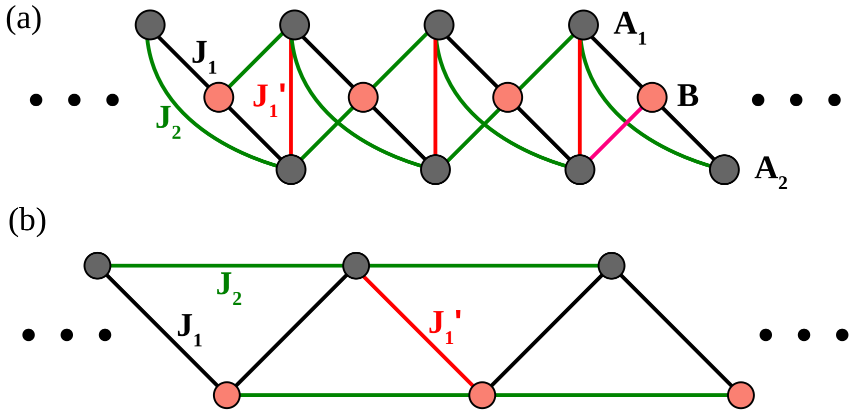

Figure 4.1: Schematic diagram. (a) General structure of a spin-1/2 coupled trimer chain, where J_1 and J_1' represent the antiferromagnetic (AFM) nearest neighbor (NN) intertrimer and intertrimer couplings, respectively. J_2 denotes the AFM next nearest neighbor (NNN) intertrimer and intertrimer couplings. (b) The same coupled trimer is depicted as a zigzag chain at $J_1' = J_1$.

diagram [334]. Trimerization in the system occurs when $J_1'/J_1 < 1$ in Eq. (4.2.1). However, J_2 uniformly connects the intertrimer and intertrimer spins, trying to preserve the characteristics of a uniform spin chain and introducing additional competition alongside frustration. The effect of trimerization in the system, along with other exotic phases, is discussed in the following sections.

We use exact diagonalization (ED) for trimer up to 24 spins. The relevant 24 spin trimer with PBC has an integral number of unit cells and sectors with inversion symmetry at some sites. For larger systems, we employed the Density Matrix Renormalization Group method (DMRG), a state-of-the-art numerical technique for accurately calculating gs and a few low-lying excited energy states of strongly interacting quantum systems [374, 376]. The DMRG scheme for building a trimer is by adding four new sites at a time, starting with a ring of four sites. The truncation error in our calculation is below 10^{-10} by keeping up to $m = 700$ eigenvectors corresponding to highest eigenvalues of the density matrix. The largest trimer studied in this manuscript is up to 100 sites.

4.3 Quantum phase diagram

We computed the quantum phase diagram (QPD) of the Hamiltonian in Eq. (4.2.1) within the J_1'/J_1 and J_2/J_1 parameter space. The resulting phase diagram in Fig. 4.2 can be divided into two regions. In the weak intertrimer exchange limit ($0 \leq J_1'/J_1 < 0.4$), as J_2 increases, we identify three distinct phases: AFM (QLRO), trimer or high spin ground state, and gapped spiral. In the strong intertrimer exchange limit ($0.4 \leq J_1'/J_1 \leq 1.0$), the SF and spiral phases persist, with a gapped dimer phase occurring in between. At $J_1' = 0$, the system transforms into a 3/4 skewed ladder, where the rungs of the 3/4 ladder define alternating fused three and four membered rings [108]. The ground state is a singlet ($S^z = 0$) for $J_2/J_1 > 0.634$, and a high

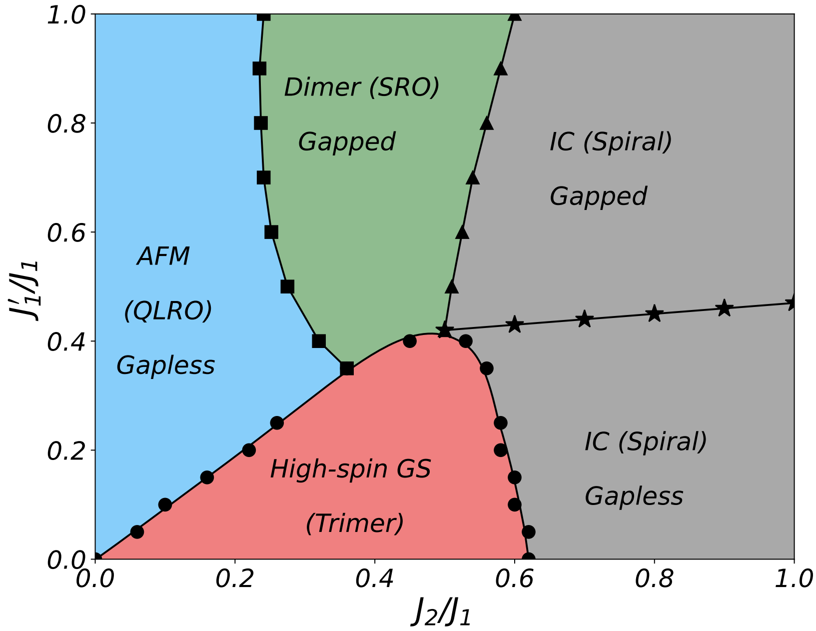

Figure 4.2: Quantum phase diagram of the Hamiltonian in Eq. (4.2.1): The blue region indicates the AFM (QLRO) phase with quasi-long-range order and gapless excitations. The green region signifies the gapped dimer phase with short-range order. The grey region denotes the incommensurate phase with spiral spin correlations, and the red region represents the trimer phase with a high spin ground state. Phase boundaries are determined based on results from level crossings, excitation gaps, and structure factors.

spin ground state with $S^z = L/6$ for $0 < J_2/J_1 < 0.634$. Each trimer has an effective spin-1/2, and the transition from $S^z = 0$ to $L/6$ indicates a ferromagnetic effective exchange between trimers.

As the NN intertrimer exchange (J_1') increases, a competition arises between the NN intertrimer exchange (J_1') and the NNN intertrimer exchange J_2. The high spin ground state (gs) persists in the weak intertrimer exchange limit ($0 \leq J_1'/J_1 < 0.4$) until these exchanges become comparable. In the regime of strong intertrimer exchange ($0.4 \leq J_1'/J_1 \leq 1.0$), the ground state is a singlet for any value of J_2, not a high spin ground state. The boundary indicated by a black solid line with filled circles in Fig. 4.2 separates the singlet gs from the high spin gs.

Level crossing in the finite system indicates the boundary between the spin liquid phase with quasi-long-range order (QLRO) and the dimer gapped phase with short-range order (SRO), as shown by the black solid line with filled squares in Fig. 4.2. The incommensurate or spiral phase stabilize for strong NNN exchange J_2 which can be characterized by a periodicity of $(2\pi/q)$ and finite-range sinusoidal spin correlations. The nature of this spiral phase, whether gapped or gapless, depends on the value of the intertrimer exchange (J_1'). For strong J_1', this phase exhibits a non-degenerate ground state with an exponentially small gap, whereas for weak J_1', it manifests as a gapless phase. The boundary between the dimer gapped phase and the spiral phase is indicated by solid black line with triangles, and the boundary between the

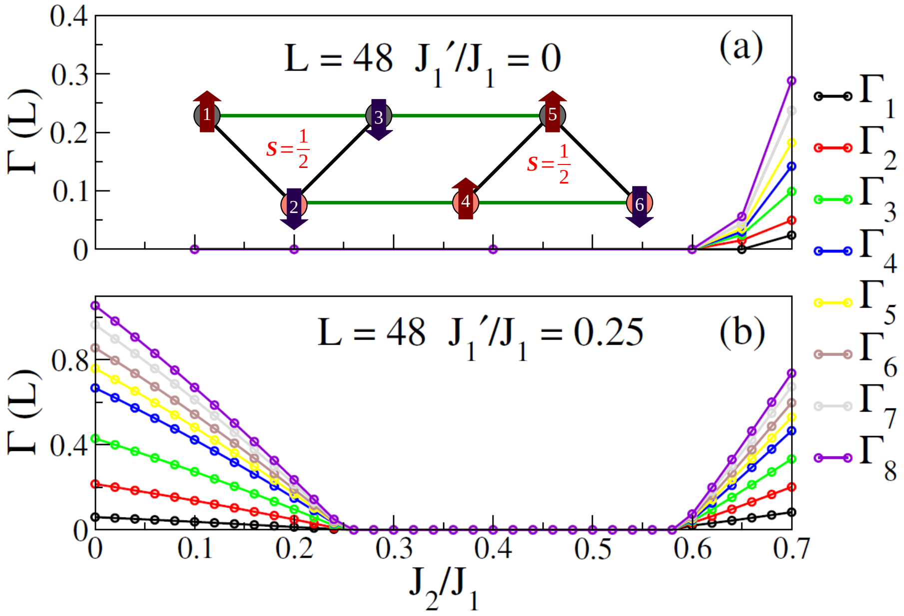

Figure 4.3: Energy difference (Γ) between the ground state (gs) in sectors with different S^z relative to $S^z = 0$ as a function of J_2/J_1 for (a) $J_1'/J_1 = 0$ and (b) $J_1'/J_1 = 0.25$, with periodic boundary conditions (PBC) and $L = 48$ spins. The inset in (a) displays a unit cell of the 3/4 skewed ladder with site numbering.

gapped and gapless spiral phase is shown by solid black line with star symbols in Fig. 4.2. These quantum phases are extensively described in the subsequent sections.

4.3.1 High-spin ground state

The $J_1 - J_2$ model features one spin per unit cell. The ground state (gs) is a singlet ($S^z = 0$)) across the parameter space where J_1 and J_2 are both positive, encompassing phases such as the AFM (QLRO) phase and the gapped dimer or incommensurate phase [204, 334]. In the conventional two-leg ladder with one J_1 rung, each unit cell accommodates two spins and exhibits inversion symmetry at the midpoint of every rung. Here, the ground state is a singlet with a finite Singlet-triplet gap for $J_1 > 0$. Ladders with skewed rungs may lack inversion symmetry at certain sites in one or both legs.

The model in Eq. (4.2.1) transform into a 3/4 skewed ladder at $J_1' = 0$. In this case the spin S^z of the absolute gs is obtained by comparing the lowest energy in sectors with different S^z,

$$\Gamma(L) = E_0(S^z, L) - E_0(0, L) \tag{4.3.1}$$

We find $S^z = 0$ when $\Gamma > 0$, level crossing when $\Gamma = 0$, and $S^z > 0$ given by the largest S^z for which $\Gamma < 0$. DMRG gives accurate results for the low-energy states of long ladders. The z component of the total spin, S^z , is conserved and exploiting this conservation is straightforward. The spin (S^z) of ground state is determined by the highest S^z value for which $E_0(S^z) - E_0(0)$ is zero. Fig. 4.3(a) shows the energy difference ($\Gamma(L)$) for a PBC ladder of $L = 6n = 48$ (n being the number of unit cell) spins which has a high spin gs with $S^z = L/6 = 8$ for $0 < J_2/J_1 < 0.634$ and a singlet gs for $J_2/J_1 > 0.634$. Each triangle has an effective spin-1/2, and the transition from $S^z = 0$ to 8 indicates a ferromagnetic effective exchange between triangles.

We calculate spin density : $\rho_j =< \psi_0|S^z_j|\psi_0 >$ and spin correlations : $C(j,k) =< \psi_0|S_j \cdot S_k|\psi_0 >$ for a system with $N = 48$ spins, where ψ_0 is the ground state wave function. First and second-neighbor spin correlations are listed in Table 4.1. One unit cell of 3/4 skewed ladder with site numbering is shown in inset of Fig. 4.3 (a). Spin densities vanish identically in singlet states. The sign of $C(1,3)$ changes near the jump from $S^z = 0$ to 8 shown in Table. 4.1. The limiting spin densities are $\rho_1 = -1/6$ at the apex and $\rho_2 = 1/3$ at each base, which gives an unpaired spin per triangle. The gs has $S^z = L/6$ and one unpaired spin per triangle for $0 < J_2/J_1 < 0.634$.

Table 4.1: First and second-neighbor spin-correlation functions $C(j,k)$ of a 3/4 ladder with PBC and $N = 48$ spins. Refer to inset of Fig. 4.3(a) for site numbers.

J_2	$C(1,2)$, $C(2,3)$	$C(3,4)$	$C(1,3)$	$C(2,4)$, $C(3,5)$
0	-0.1667	0.1111	0.0834	-0.0556
0.01	-0.1672	0.1121	0.0845	-0.0569
0.05	-0.1696	0.1163	0.0895	-0.0569
0.20	-0.1764	0.1315	0.1081	-0.0836
0.50	-0.1770	0.1551	0.1368	-0.1246
0.64	-0.1697	0.1603	0.1423	-0.1396
0.65	-0.1046	0.0638	-0.0035	-0.1148
0.68	-0.0967	0.0569	-0.0186	-0.1191
1.0	-0.04	0.0323	-0.1195	-0.1418

As the NN inter-trimer exchange (J_1') increases, there is a competition between the NN inter-trimer exchange (J_1') and the NNN intra-trimer exchange J_2. The high spin ground state (gs) persists in the weak intra-trimer exchange limit ($0 \leq J_1'/J_1 < 0.4$) until these exchanges become comparable. In the regime of strong inter-trimer exchange ($0.4 \leq J_1'/J_1 \leq 1.0$), the ground state is a singlet for any value of J_2, rather than a high spin ground state. Fig. 4.3(b) shows the energy difference (Γ_S) for $J_1' = 0.25$ with $N = 48$ spins. The high spin gs is in the range $0.25 < J_2/J_1 < 0.60$. In the phase diagram in Fig. 4.2, the high spin gs phase is shown in the red region.

A phenomenon of these quantum spin chains is analogous to the quantum Hall effect - topological quantization of a physical quantity under a changing magnetic field. This phenomenon is known as the magnetization plateau. In this phase, a 1/3 magnetization plateau, consistent with the OYA condition [259], is observed. To further look at how this magnetization plateau appears, the spatial dependence of the averaged local spin correlation $C(r) =< S^z_0.S^z_r >$ in the ground states under different couplings at zero field is presented, as shown in Fig. 4.4(b). It is seen that in absence of external field, the expectation value $C(r)$ changes its sign at every three sites within a very small range of $(-0.1, 0.1)$.

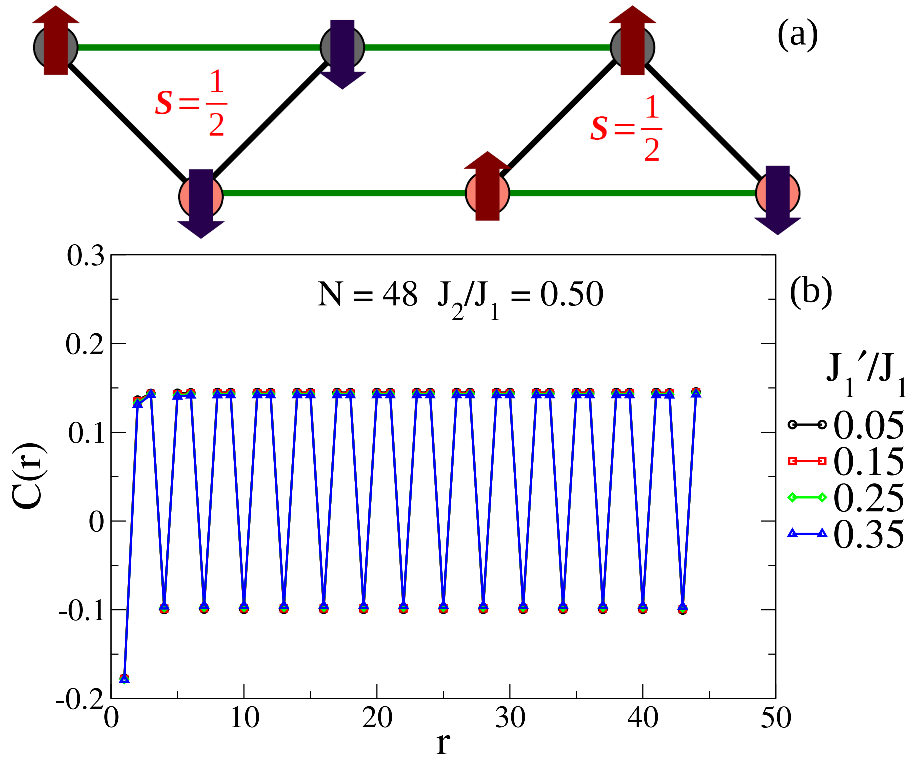

Figure 4.4: (a) Schematic spin configuration of the high spin ground state with weak intertrimer NN exchange coupling (J_1'), showing the spin alignment along the z-axis. Each triangle acts as an effective spin-1/2. (b) Longitudinal spin correlations ($C(r)$) in the trimer phase for $J_1'/J_1 = 0.05$, 0.15, 0.25, 0.35 with a fixed NNN exchange $J_2/J_1 = 0.5$ and a system size of $L = 48$. The correlations alternate in sign at every third site within a narrow range of $(-0.1, 0.1)$.

4.3.1.1 Perturbation theory for spin-1/2 trimer chain

In the limit where the intertrimer interactions are weak ($J_1' << J_1$, $J_2 << J_1$), the system can be modeled as an effective spin-1/2 Heisenberg antiferromagnetic chain. To find the effective Hamiltonian in weak intertrimer couplings limit we perform the 1st order degenerate perturbation theory. The total Hamiltonian of two trimer unit can be expressed as:

$$\mathcal{H}_{tot} = 2\mathcal{H}_0 + \mathcal{H}' \tag{4.3.2}$$

where, $\mathcal{H}_0 = J_1(\vec{S}_1.\vec{S}_2 + \vec{S}_2.\vec{S}_3) + J_2\vec{S}_1.\vec{S}_3$, and $\mathcal{H}' = J_1'\vec{S}_{i,3}.\vec{S}_{j,1} + J_2'(\vec{S}_{i,2}.\vec{S}_{j,1} + \vec{S}_{i,3}.\vec{S}_{j,2})$.

At $J_1' = J_2' = 0$, the ground state of the Hamiltonian in Eq. (4.3.2) can be written as product states of two isolated trimer units. The ground state (gs) of isolated spin-1/2 trimer is a $S = 1/2$ doublet. The wave functions can be written as:

$$\begin{aligned} |1/2\rangle &= \frac{1}{\sqrt{6}}(|\uparrow\downarrow\uparrow\rangle - 2|\downarrow\uparrow\uparrow\rangle + |\uparrow\uparrow\downarrow\rangle) \\ |-1/2\rangle &= \frac{1}{\sqrt{6}}(|\downarrow\uparrow\downarrow\rangle - 2|\uparrow\downarrow\downarrow\rangle + |\downarrow\downarrow\uparrow\rangle) \end{aligned} \tag{4.3.3}$$

Therefore, the new basis in which we write the Hamiltonian in Eq. (4.3.2), are $|1/2_i 1/2_j\rangle$, $|1/2_i - 1/2_j\rangle$, $|-1/2_i 1/2_j\rangle$, $|-1/2_i - 1/2_j\rangle$.

The perturbative part of the Hamiltonian in Eq. (4.3.2) can be written in terms of creation and annihilation operators as,

$$\begin{aligned}\mathcal{H}' &= J_1' \vec{S}_{i,3}.\vec{S}_{j,1} + J_2'(\vec{S}_{i,2}.\vec{S}_{j,1} + \vec{S}_{i,3}.\vec{S}_{j,2}) \\ &= \frac{J_1'}{2}(S^+_{i,3}S^-_{j,1} + S^-_{i,3}S^+_{j,1}) + J_1' S^z_{i,3}S^z_{j,1} \\ &+ \frac{J_2'}{2}(S^+_{i,2}S^-_{j,1} + S^-_{i,2}S^+_{j,1}) + J_2' S^z_{i,2}S^z_{j,1} \\ &+ \frac{J_2'}{2}(S^+_{i,3}S^-_{j,2} + S^-_{i,3}S^+_{j,2}) + J_2' S^z_{i,3}S^z_{j,2} \end{aligned} \tag{4.3.4}$$

The complete set of matrix elements for spin operators in Eq. (4.3.4) are provided in Table 4.2.

Table 4.2: Matrix elements of spin operators in the new basis.

Table 4.3: Matrix elements for $S^z_{i,3/1}$.

$S^z_{i,3/1}$	$\|1/2_i\rangle$	$\|-1/2_i\rangle$
$\|1/2_i\rangle$	$\frac{2}{3}$	0
$\|-1/2_i\rangle$	0	$-\frac{2}{3}$

Table 4.4: Matrix elements for $S^+_{i,3/1}$.

$S^+_{i,3/1}$	$\|1/2_i\rangle$	$\|-1/2_i\rangle$
$\|1/2_i\rangle$	0	$-\frac{2}{3}$
$\|-1/2_i\rangle$	0	0

Table 4.5: Matrix elements for $S^-_{i,3/1}$.

$S^-_{i,3/1}$	$\|1/2_i\rangle$	$\|-1/2_i\rangle$
$\|1/2_i\rangle$	0	0
$\|-1/2_i\rangle$	$-\frac{2}{3}$	0

Table 4.6: Matrix elements for $S^z_{i,2}$.

$S^z_{i,2}$	$\|1/2_i\rangle$	$\|-1/2_i\rangle$
$\|1/2_i\rangle$	$-\frac{1}{3}$	0
$\|-1/2_i\rangle$	0	$\frac{1}{3}$

Table 4.7: Matrix elements for $S^+_{i,2}$.

$S^+_{i,2}$	$\|1/2_i\rangle$	$\|-1/2_i\rangle$
$\|1/2_i\rangle$	0	$\frac{1}{3}$
$\|-1/2_i\rangle$	0	0

Table 4.8: Matrix elements for $S^-_{i,2}$.

$S^-_{i,2}$	$\|1/2_i\rangle$	$\|-1/2_i\rangle$
$\|1/2_i\rangle$	0	0
$\|-1/2_i\rangle$	$\frac{1}{3}$	0

Using these matrices, the perturbative Hamiltonian in Eq. (4.3.4) can be expressed as,

$$\begin{aligned}\mathcal{H}'_{i,j} = \frac{J_1'}{2}&\Big[\begin{pmatrix}0 & -\frac{2}{3}\\ 0 & 0\end{pmatrix}\otimes\begin{pmatrix}0 & 0\\ -\frac{2}{3} & 0\end{pmatrix} + \begin{pmatrix}0 & 0\\ -\frac{2}{3} & 0\end{pmatrix}\otimes\begin{pmatrix}0 & -\frac{2}{3}\\ 0 & 0\end{pmatrix}\Big] + \begin{pmatrix}\frac{2}{3} & 0\\ 0 & -\frac{2}{3}\end{pmatrix}\otimes\begin{pmatrix}\frac{2}{3} & 0\\ 0 & -\frac{2}{3}\end{pmatrix} \\ + \frac{J_2'}{2}&\Big[\begin{pmatrix}0 & \frac{1}{3}\\ 0 & 0\end{pmatrix}\otimes\begin{pmatrix}0 & 0\\ -\frac{2}{3} & 0\end{pmatrix} + \begin{pmatrix}0 & 0\\ \frac{1}{3} & 0\end{pmatrix}\otimes\begin{pmatrix}0 & -\frac{2}{3}\\ 0 & 0\end{pmatrix}\Big] + \begin{pmatrix}-\frac{1}{3} & 0\\ 0 & \frac{1}{3}\end{pmatrix}\otimes\begin{pmatrix}\frac{2}{3} & 0\\ 0 & -\frac{2}{3}\end{pmatrix} \\ + \frac{J_2'}{2}&\Big[\begin{pmatrix}0 & -\frac{2}{3}\\ 0 & 0\end{pmatrix}\otimes\begin{pmatrix}0 & 0\\ \frac{1}{3} & 0\end{pmatrix} + \begin{pmatrix}0 & 0\\ -\frac{2}{3} & 0\end{pmatrix}\otimes\begin{pmatrix}0 & \frac{1}{3}\\ 0 & 0\end{pmatrix}\Big] + \begin{pmatrix}\frac{2}{3} & 0\\ 0 & -\frac{2}{3}\end{pmatrix}\otimes\begin{pmatrix}-\frac{1}{3} & 0\\ 0 & \frac{1}{3}\end{pmatrix}\end{aligned} \tag{4.3.5}$$

Next, we introduce a new set of spin operators in the effective spin-1/2 basis to express $\mathcal{H}'$. Here, τ^+, τ^-, and τ^z denote the creation, annihilation, and z-component of the spin operators, respectively, for the effective spin-1/2.

$$\tau_i^+ \left|-1/2_i\right\rangle = \left|1/2_i\right\rangle,\ \tau_i^+ \left|1/2_i\right\rangle = 0$$

$$\tau_i^- \left|-1/2_i\right\rangle = 0,\ \tau_i^- \left|1/2_i\right\rangle = \left|-1/2_i\right\rangle$$

$$\tau_i^z \left|1/2_i\right\rangle = \tfrac{1}{2}\left|1/2_i\right\rangle,\ \tau_i^z \left|-1/2_i\right\rangle = -\tfrac{1}{2}\left|-1/2_i\right\rangle$$

Rearranging the terms in Eq. (4.3.5) we get the effective Hamiltonian as,

$$\begin{aligned}\mathcal{H}_{i,j}^{'} &= \frac{4J_1'}{9} \times \left(\frac{1}{2}[\begin{pmatrix}0 & 1\\ 0 & 0\end{pmatrix} \otimes \begin{pmatrix}0 & 0\\ 1 & 0\end{pmatrix} + \begin{pmatrix}0 & 0\\ 1 & 0\end{pmatrix} \otimes \begin{pmatrix}0 & 1\\ 0 & 0\end{pmatrix}] + \begin{pmatrix}1 & 0\\ 0 & -1\end{pmatrix} \otimes \begin{pmatrix}1 & 0\\ 0 & -1\end{pmatrix}\right)\\ &= \frac{4J_1'}{9} \times \left(\frac{1}{2}(\tau_i^+ \otimes \tau_j^- + \tau_i^- \otimes \tau_j^+) + \tau_i^z \otimes \tau_j^z\right) - \frac{4J_2'}{9} \times \left(\frac{1}{2}(\tau_i^+ \otimes \tau_j^- + \tau_i^- \otimes \tau_j^+) + \tau_i^z \otimes \tau_j^z\right)\\ &= \frac{4(J_1'-J_2')}{9} \sum_i \tau_i \cdot \tau_j\end{aligned} \tag{4.3.6}$$

The final form of the effective spin-1/2 Hamiltonian is given by

$$\mathcal{H}_{\text{eff}} = J_{\text{eff}} \sum_i \tau_i \cdot \tau_j, \tag{4.3.7}$$

where $J_{\text{eff}} = \frac{4(J_1'-J_2')}{9}$.

4.3.2 AFM (QLRO) phase

The Hamiltonian in Eq. (4.2.1) reduces to the frustrated $J_1 - J_2$ model at $J_1' = J_1$ with uniform AFM NN and NNN couplings. The gs degeneracy at $g_{\text{MG}} = J_2/J_1 = 0.5$ (Majumdar-Ghosh (MG) point) is between even and odd states under inversion symmetry that is broken in dimer phase [228, 229]. We define E_σ and E_m as the excitation energy to the lowest singlet and triplet, respectively. Both have finite-size contributions. Motivated by field theory, Okamoto and Nomura [253] argued that the gapped dimer phase with doubly degenerate GS must have two singlets below the lowest triplet. In finite systems, the singlet and triplet cross at $g^*(N)$ where $E_\sigma = E_m$. They found $g^*(N)$ exactly up to $N = 24$, noted the weak size dependence and extrapolated to $g_{\text{ON}} = 0.2411$, the quantum critical point at which an exponentially small gap (E_m) opens. The excitations E_m and E_σ are well known for HAF at $J_2 = 0$ in Eq. (4.2.4). To lowest order in logarithmic corrections, Woynarovich and Eckle report [396]

$$E_m(N) = \frac{\pi^2}{2N}\left(1 - \frac{1}{2lnN}\right) \tag{4.3.8}$$

Fig. 4.5 illustrates the evolution of E_m and E_σ with increasing frustration $g = J_2/J_1$ for $0.4 \leq J_1'/J_1 \leq 1.0$ with $L = 24$ spins. The singlet-triplet crossing points are listed in Table 4.9. The singlet and triplet levels intersect at $g^*(24) = 0.241$ where $E_m = E_\sigma$ for $J_1' = J_1$. As the inter-trimer exchange (J_1') decreases, the crossing point g^* increases, shifting the AFM (QLRO)-dimer transition point to a higher value. Below $J_1'/J_1 = 0.4$, the dimer phase does not appear. The colored solid circles in Fig. 4.5 indicate the crossing points at various J_1'. At lower

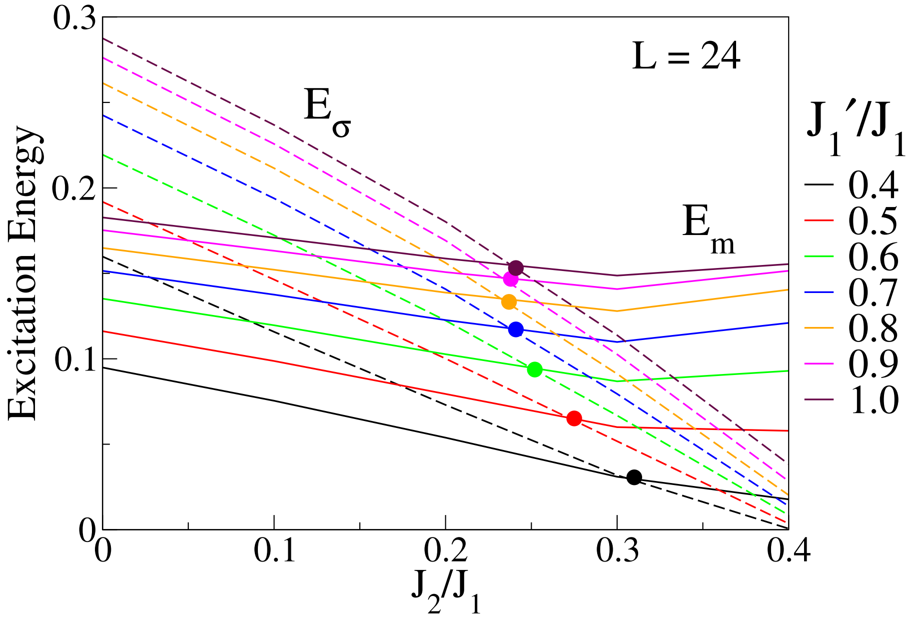

Figure 4.5: Excitation energy of Eq. (4.2.1) for $N = 24$ with PBC for $J_1'/J_1 > 0.4$. E_m represents the lowest triplet and E_σ denotes the lowest singlet with opposite inversion symmetry. The crossing points where $E_m = E_\sigma$ are indicated by solid colored circles.

Table 4.9: Crossing points $g^*(J_2/J_1, L)$, where $E_m = E_\sigma$, are presented for $J_1' = 0.4$, 0.6, 0.8, and 1.0 for various system sizes $L = 12$, 18, 24. The extrapolated values of these crossing points are listed in the last row of the table.

	$J_1'/J_1 = 0.4$	$J_1'/J_1 = 0.6$	$J_1'/J_1 = 0.8$	$J_1'/J_1 = 1.0$
	$g*(J_2/J_1)$	$g*(J_2/J_1)$	$g*(J_2/J_1)$	$g*(J_2/J_1)$
$L = 12$	0.351	0.263	0.239	0.245
$L = 18$	0.316	0.253	0.234	0.244
$L = 24$	0.303	0.248	0.233	0.242
$L \sim \infty$	0.287	0.244	0.231	0.241

inter-trimer exchange (J_1'), a stronger NNN exchange (J_2) is required to induce dimerization in the system, resulting in a small gap opening up. Extrapolation of the crossing points has been done to accurately determine $g^*(J_1', J_2)$, and the extrapolated values are listed in Table 4.9. The blue region in the phase diagram (Fig. 4.2) denotes the spin-fluid region.

In case of 1D spin$-1/2$ HAF model, spin correlations behaves as [106] :

$$C(r) \simeq \frac{C_1}{r^2} + C_2\frac{(-1)^r log(r)^\sigma}{r} \tag{4.3.9}$$

with $\sigma = 0.5$. Similarly, in the regular $J_1 - J_2$ model, spin correlations exhibit quasi long-range order (QLRO) at wave vector $q_G = \pi$ for $J_2/J_1 < 0.2411$ and short range order (SRO) at wave vector $q_G = \pi$ for $0.2411 < J_2/J_1 < 0.55$ [334]. To understand the effect of inter-trimer exchange (J_1') on these correlations in the spin-fluid region, we compute the longitudinal spin correlation $C(r) = \langle S_0^z S_r^z \rangle$ for a system size of $L = 96$, using a reference site positioned at the center of a trimer. The spin configuration is shown in Fig. 4.6(a), where the spins are aligned

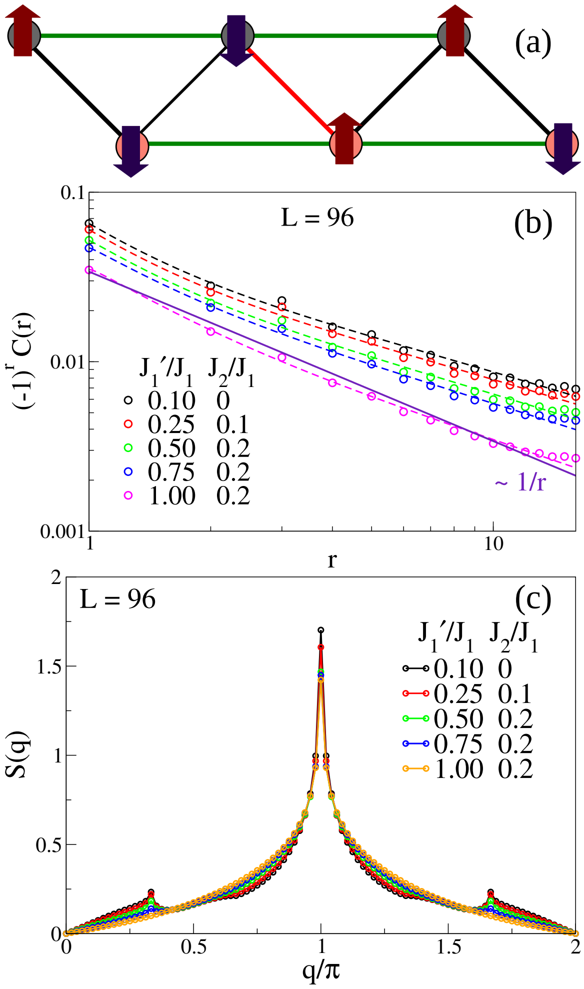

Figure 4.6: (a) Schematic spin configuration in the AFM (QLRO) phase, illustrating antiferromagnetic spin alignment along the z-axis. (b) Longitudinal spin correlations ($C(r)$) in this phase for $(J_1'/J_1, J_2/J_1) = (0.10, 0)$, $(0.25, 0.1)$, $(0.50, 0.2)$, $(0.75, 0.2)$, and $(1.0, 0.2)$ with a system size of $L = 96$. The correlations are fitted with a power law with logarithmic correction, indicated by dashed lines. The correlation behavior for the $J_1 - J_2$ model at $J_1'/J_1 = 1$ closely follows a power law ($\sim 1/r$), as indicated by the violet line. (c) Structure factor for the same parameter values $(J_1'/J_1, J_2/J_1)$ diverges at $q = \pi$.

antiferromagnetically. Fig. 4.6(b) shows the spin correlation in the spin-fluid region for several values of J_1' and J_2. We found that the spin correlations follow a power law with logarithmic correction even in the presence of inter-trimer exchange (J_1'). The power coefficient (σ) increases as J_1' decreases.

The static structure factor $S(q)$ is the Fourier transform of spin correlations in the ground state, defined as:

$$S(q) = \sum_r \left\langle \vec{S}_0 \cdot \vec{S}_r \right\rangle e^{iqr} \tag{4.3.10}$$

The wave vector in the first Brillouin zone are $q = 2\pi m/N$ with $m = 0, \pm 1, ..., N/2$; q is discrete in finite systems, continuous in infinite chain. We consider $S(q)$ with spin correlation function $C(r) =< S_0^z S_r^z >$ in Eq. (4.2.1). The sum over all spin correlations is $S(0) = S(S+1)/N$; it is zero for a singlet gs. The sum over q in the Brillouin zone and limit $L \sim \infty$ lead in general to the sum rule since $C(0) = 3/4$ for $S = 1/2$.

$$\frac{1}{L}\sum_q S(q; J_2/J_1, L) = \frac{3}{4} = \frac{1}{\pi}\int_0^\pi dqS(q) \tag{4.3.11}$$

When $C(r)$ has a finite range, $S(q)$ remains finite, and the sum in Eq. (4.3.17) becomes constant once the system size exceeds the correlation length. In a regular $J_1 - J_2$ model at $J_1' = J_1$, spin correlations are confined to neighbors at the MG point $J_2/J_1 = 1/2$, where the exact ground state for even L results in

$$S(q; 1/2) = \frac{3}{4}(1 - cosq) \tag{4.3.12}$$

The size dependence is entirely in the discrete q values. The Brillouin zone $0 \leq q < 2\pi$ conveniently displays the peak $S(q = \pi; 0, L)$, which increases with system size L and is known to diverge in the infinite chain, indicating QLRO(π) [3, 308]. The area under the curve is conserved according to Eq. (4.3.17). The peak remains at $q = \pi$ for several values of J_1' and J_2 with a system size of $N = 96$, as shown in Fig. 4.6(c), defining the QLRO(π) phase. The smaller peaks are due to the different environment of the reference site and the presence of inter-trimer interactions (J_1'). As the inter-trimer interactions (J_1') decrease, the peaks at $q = \pi/3$ and $5\pi/3$ become more prominent due to trimerization.

4.3.3 Incommensurate (IC) phase

The incommensurate (IC) phase becomes stable for strong NNN exchange, $J_2/J_1 > 0.6$. In this phase, the spins align antiferromagnetically in a spiral pattern with a wave vector between $\pi/2$ and π, as depicted in Fig. 4.7(a). This IC phase can be divided into two regions based on the value of inter-trimer NN exchange J_1'. In the region where $0.5 < J_1'/J_1 \leq 1$, spin correlations follow a spiral pattern with exponential decay, expressed as

$$C(r) \sim e^{-r/\zeta} \sin(\theta r + c), \tag{4.3.13}$$

where ζ is the correlation length and θ is the pitch angle. This is referred to as the gapped IC phase due to the presence of a gap in the excitations. In the region with weak inter-trimer NN exchange ($0 \leq J_1' < 0.5$), spin correlations exhibit a spiral nature with algebraic decay, given by

$$C(r) \sim r^{-k} \sin(\theta r + c), \tag{4.3.14}$$

where k is the coefficient of the power law and θ is the pitch angle. This is referred to as the gapless IC phase as the excitations are gapless in this phase.

Fig. 4.7(b) illustrates the correlations in this phase for various values of inter-trimer NN exchange J_1' with a fixed NNN exchange $J_2/J_1 = 0.8$. The top layer of Fig. 4.7(b) shows the spiral nature of correlations fitted with a sinusoidal function with algebraic decay for weaker J_1', while the bottom layer shows the spiral nature of correlations fitted with a sinusoidal function with exponential decay for strong inter-trimer NN exchange J_1'.

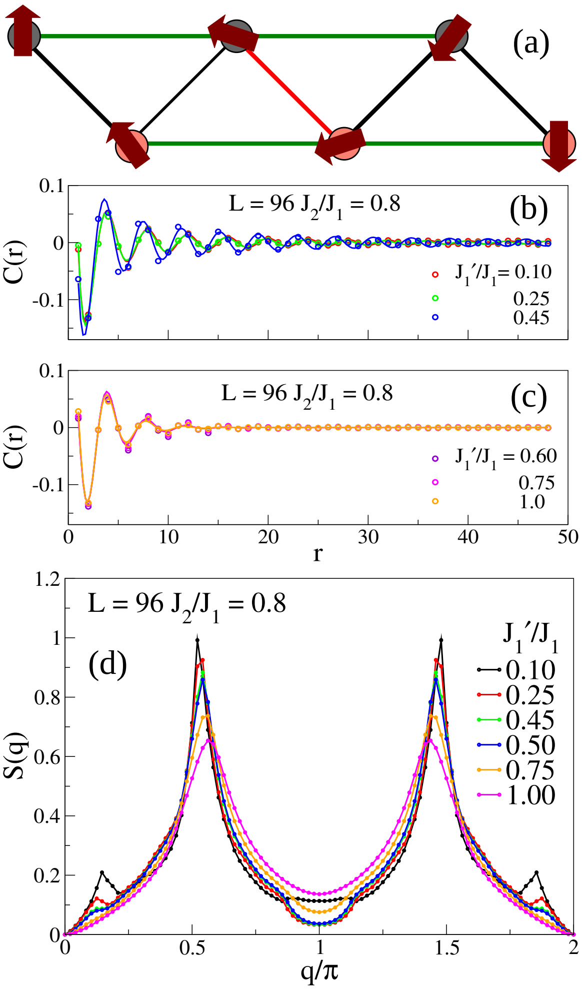

Figure 4.7: (a) Schematic spin configuration in the incommensurate (IC) phase, showing a spiral pattern of spin alignment. Longitudinal spin correlations ($C(r)$) in this phase for a fixed $J_2/J_1 = 0.8$ with a system size of $L = 96$: (a) for $J_1'/J_1 = 0.10$, 0.25, 0.45, and (b) for $J_1'/J_1 = 0.60$, 0.75, 1.0. In (a), these correlations are fitted with a sinusoidal function with exponential decay, and in (b), they are fitted with a sinusoidal function with algebraic decay, shown by solid colored lines. (d) Structure factor for the same parameter values ($J_1'/J_1, J_2/J_1$) diverges near $q = \pi/2$ and $3\pi/2$.

The structure factor in the IC phase diverges between $\pi/2 < q < \pi$. Fig. 4.7(c) shows the structure factor for several values of inter-trimer NN exchange J_1' with a fixed NNN exchange $J_2 = 0.8$ for a system of $N = 96$. In this case, the structure factor peak diverges at $q = \pi/2$. The smaller peaks are attributed to the effects of inter-trimer interactions.

4.3.4 Gapped dimer phase

In the regular $J_1 - J_2$ model described by Eq. (4.2.4), at $J_1' = J_1$, the Majumdar-Ghosh (MG) point at $J_2/J_1 = 0.5$ has exact ground states for an even number of spins L. The ground state is doubly degenerate and form singlet dimer and they are represented by the Kekulé valence bond (VB) diagrams and it's wave function is written as $|\Psi_1^{\mathrm{MG}}\rangle = \prod_{i=1}^{N/2}[2i-1,2i]$, $|\Psi_2^{\mathrm{MG}}\rangle = \prod_{i=1}^{N/2}[2i,2i+1]$, where $[i,j]$ singlet dimer $[i,j] = \frac{1}{\sqrt{2}}(\uparrow_i\downarrow_j - \downarrow_i\uparrow_j)$. At the MG point, spin correlations are confined to neighboring spins, and the structure factor follows the relation $S(q;1/2) = \frac{3}{4}(1-cosq)$.

As we reduce the intertrimer interaction (J_1'), the dimer phase still exist up to $J_1'/J_1 = 0.4$, but the ground state is no longer a doubly degenerate state. The spin configuration in this dimer phase is shown in Fig. 4.8(a), where the magenta shaded ellipse denote the singlet dimer state $(|\frac{1}{\sqrt{2}}(\uparrow\downarrow - \downarrow\uparrow))$. Fig. 4.8(b) presents the structure factor $(S(q))$ in the dimer phase for various values of intertrimer exchange J_1' with a fixed NNN exchange $J_2/J_1 = 0.5$. The structure factor spreads around $q = \pi$, but there is a deviation from $(1-\cos q)$ due to the trimerization in the system.

Bond-bond correlation— To further understand this phase we compute the four-point correlation function of the most distant bonds, $p = 2n$, at frustration J_2/J_1 in increasingly large $L = 4n$ chains

$$C_4(p, J_1'/J_1, J_2/J_1) = \langle S_1^z S_2^z S_{2n+1}^z S_{2n+2}^z \rangle \tag{4.3.15}$$

The next most distant bond has $p = 2n-1$ and correlation function $C_4(2n-1, J_1', J_2)$. The difference is

$$D_4(2n, J_1'/J_1, J_2/J_1) = C_4(2n, J_1'/J_1, J_2/J_1) - C_4(2n-1, J_1'/J_1, J_2/J_1) \tag{4.3.16}$$

Fig. 4.8(c) shows the difference in bond-bond correlations between the two most distant bonds as a function of NNN exchange J_2/J_1 $(0 < J_2/J_1 < 0.7)$ for various values of intertrimer NN exchange interactions J_1'. The amplitude of $32D_4(2n, J_1'/J_1, J_2/J_1)$ is unity at the MG point $(J_1'/J_1 = 1,\ J_2/J_1 = 1/2)$. When the intertrimer NN exchange J_1'/J_1 is reduced from 1, the peak position of J_2/J_1 where $32D_4(2n, J_1'/J_1, J_2/J_1)$ is maximized decreases, and its amplitude also decreases from unity. This dependence is strong in the gapless phase and weak in the dimer phase due to the large gap.

4.3.5 Trimer-dimer transition

A first-order phase transition occurs from the trimer to the dimer phase as the inter-trimer exchange (J_1') varies from lower to higher values. To understand this trimer-dimer transition,

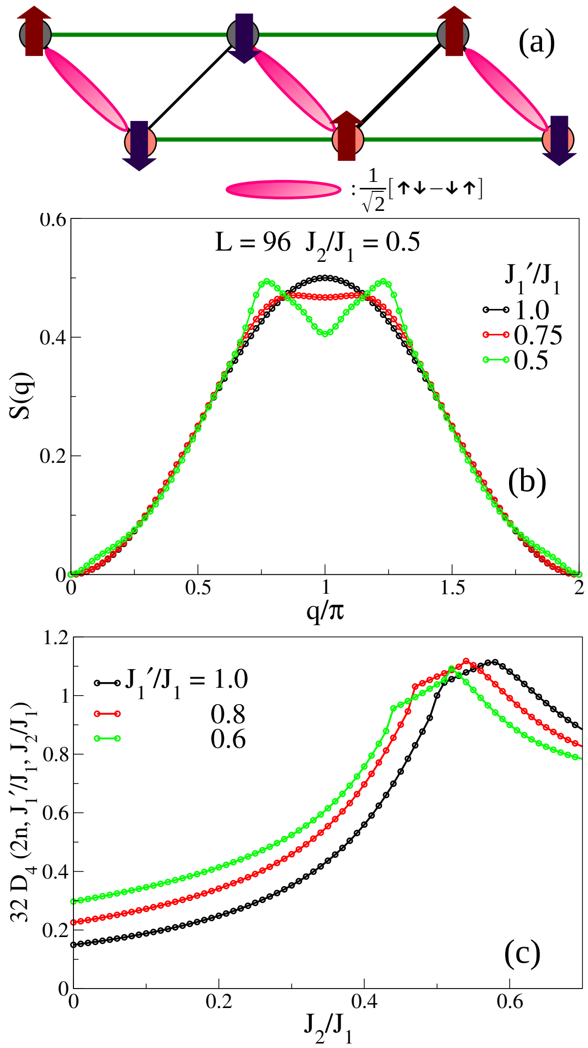

Figure 4.8: (a) Schematic spin configuration in the gapped dimer phase, illustrating the formation of dimers between pairs of spins. (b) Structure factor for $J_1'/J_1 = 1.0$, 0.75, and 0.50 with a fixed $J_2/J_1 = 0.50$, obtained for a system size of $L = 96$, spreading near $q = \pi$. (c) Bond-bond correlations between the two most distant bonds, showing maximum values near the dimer phase and vanishing to zero in the AFM (QLRO) phase.

we calculate the Fourier transform of bond-bond correlations in Eq. (4.3.15), defined as follows:

$$S'(q) = \sum_r \left\langle S_r^z S_{r+1}^z S_{r+p}^z S_{r+1+p}^z \right\rangle e^{iqp}, \tag{4.3.17}$$

where the distance between two bonds is $p = r' - r$. In the dimer phase, the unit cell consists of two spins, causing the Fourier transform of bond-bond correlations ($S'(q)$) to diverge at $q = 2\pi/2 = \pi$. Conversely, in the trimer phase, the unit cell comprises three spins, leading $S'(q)$ to diverge at $q = 2\pi/3$ and $4\pi/3$. Fig. 4.9 illustrates the Fourier transform of bond-bond correlations ($S'(q)$) for various values of inter-trimer NN exchange J_1', with a fixed NNN exchange of $J_2/J_1 = 0.5$.

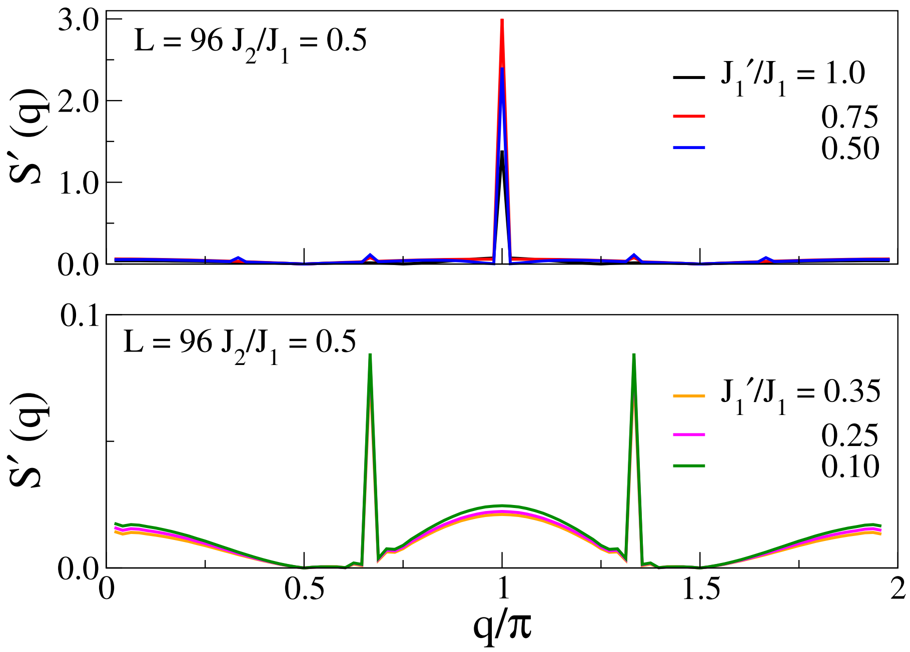

Figure 4.9: Fourier transform of bond-bond correlation for a fixed $J_2/J_1 = 0.5$ with system size of $L = 96$: (Top) $J_1'/J_1 = 1.0,\ 0.75,\ 0.50$ diverge at $q = \pi/3$ and (b) $J_1'/J_1 = 0.35,\ 0.25,\ 0.10$ diverge at $q = 2\pi/3,\ 4\pi/3$.

4.4 Conclusion

In this study, we investigate the ground state properties of a quasi-1D spin-1/2 coupled trimer model with nearest-neighbor (NN) intertrimer exchange J_1, intertrimer exchange J_1', and next-nearest-neighbor (NNN) intertrimer and intertrimer exchange J_2. The model simplifies to the uniform $J_1 - J_2$ model when $J_1' = J_1$. For $J_1' < J_1$, the uniform model transforms into trimers connected by J_1' and J_2.

Within each trimer, spins interact via J_1 and J_2, where J_2 tends to homogenize the chain, while J_1' induces trimerization, adding frustration. In isolated trimers ($J_1' = 0$), two spins form a singlet pair, leaving one spin unpaired, contributing to magnetization. Hence, a system of L spins with $\frac{L}{3}$ isolated trimers is expected to have a high spin ground state ($S^z = \frac{L}{6}$) in finite systems, unlike a uniform system with a singlet ground state ($S^z = 0$). strong J_1' and J_2 destabilize the high spin ground state. At $J_1' > 0.5J_1$, the system shows no high spin ground state and exhibits phases similar to the uniform $J_1 - J_2$ model, though phase boundaries shift due to weak trimerization.

Based on the results from excitation gaps, level crossing, spin correlations, structure factors, and bond-bond correlations, we construct a quantum phase diagram (QPD) in the $J_1'/J_1 - J_2/J_1$ parameter space. The QPD is divided into two regions: for weak intertrimer exchange ($0 \leq J_1'/J_1 < 0.4$), there are three distinct phases: spin fluid (SF), trimer or high spin ground state, and gapless spiral. For strong intertrimer exchange ($0.4 \leq J_1'/J_1 \leq 1.0$), the SF and spiral phases with a gap persist, and a gapped dimer phase emerges between them. Additionally, we notice a first-order phase transition from the trimer to the dimer phase as the intertrimer exchange (J_1') increases. In the dimer phase, where each unit cell contains two spins, the Fourier transform of bond-bond correlations ($S'(q)$) diverges at $q = \pi$. Conversely, in the trimer phase, where each unit cell consists of three spins, $S'(q)$ diverges at $q = 2\pi/3$ and $4\pi/3$.

Chapter 5

Emergent Quadrupolar Order in the Spin-$1/2$ Kitaev-Heisenberg Model

---

5.1 Introduction

Quantum spin liquids (QSLs) represent a quantum phase of matter that challenges traditional understanding by lacking magnetic long-range order (LRO), yet they may exhibit global topological order [18]. These elusive states emerge in frustrated magnetic systems, where competing spin exchange interactions not only foster the QSL state but also lead to complex entangled states such as dimer formations, fractional excitations like spinons, and Majorana excitations in the ground state (gs) [37, 75, 88, 138, 187, 311, 316, 397, 412]. A key development in understanding QSLs was the Kitaev model, which proposed spin-1/2 particles on a hexagonal lattice with direction-dependent exchange interactions, introducing frustration into the system [184]. The gs of this model is a QSL, characterized by Majorana fermions and gauge vortices as elementary excitations [22, 23, 25, 144, 211, 230].

The experimental pursuit of the Kitaev model has prominently featured Iridium-based materials such as A_2IrO_3 (A=Na, Li), where Ir atoms form a honeycomb structure [155, 330]. In these materials, the octahedral coordination of ligands induces a crystal field, splitting the Ir d-orbitals into t_{2g} and e_g levels. Strong spin-orbit coupling further splits the t_{2g} orbitals, allowing the two highest states of each to mimic effective spin-1/2 degrees of freedom. This results in orbital-dependent, directionally anisotropic spin exchanges, i.e., so-called Kitaev interactions [357]. However, the Kitaev-Heisenberg (KH) model, incorporating residual nearest-neighbor Heisenberg interactions, offers a more realistic description of the magnetic properties of these materials [47]. Similar Hamiltonians have been proposed for materials like α-$RuCl_3$ [20, 76, 162, 343, 357, 394], β-Li_2IrO_3 [162, 176, 350, 357, 394], and γ-Li_2IrO_3 [357, 358].

The gs phase diagram of the honeycomb-lattice KH model has been extensively studied, revealing four magnetic LRO phases (Néel, zigzag (ZZ), stripy (ST), and ferromagnetic (FM)) and two QSL phases; FM Kitaev (FK) and antiferromagnetic Kitaev (AFK) QSLs by tuning the Heisenberg and Kitaev interactions [47, 98, 116, 315]. However, the potential for a quantum phase involving multi-polar spin states, such as a quadrupolar (QP) or spin-nematic state, in the KH model remains largely unexplored. From an experimental perspective, third-order positive susceptibility probing a higher-order correlation such as QP has been observed at zero magnetic field in α-$RuCl_3$ [149]. Yet, the intricate mechanisms behind these observations are not fully elucidated. In addition to these experimental findings, the present study is further motivated by the inclusion of a staggered QP operator in the Hamiltonian of the KH model (see below).

The QP phase, established in liquid crystal systems [8, 177, 178, 236], manifests in magnetic systems as spin nematics, where magnetic quadrupole moments create orientational order without magnetic LRO [206, 210, 361]. Initially identified in spin-1 systems with biquadratic exchange [32], this order has been explored in various Heisenberg spin-1 models [152, 270, 351]. Extending this concept to spin-1/2 systems has spurred research, particularly in J_1-J_2 chain systems under strong magnetic fields [148, 264, 341]. In the context of Kitaev systems, a spin-nematic phase in the spin-1/2 Kitaev-Ising model has been predicted, arising from the interplay between Kitaev QSL and magnetic LRO, but lacking topological order [244]. Additionally, four-body interactions among Majorana fermions in the Kitaev QSL could induce a topological nematic phase transition, evolving from the chiral QSL phase to the toric code phase [348].

In this chapter[1], we explore the gs dynamics of the spin-$\frac{1}{2}$ KH model, focusing on the QP order. We investigate two geometries: the 2-leg ladder and the two-dimensional (2D) honeycomb lattice, using exact diagonalization (ED) and density-matrix renormalization group (DMRG) methods. Our primary contribution is a detailed exploration of the QP order parameter and correlation functions within these systems. We present a novel gs phase diagram highlighting the QP order as a function of the ratio between Heisenberg and Kitaev interactions. A striking aspect of our findings is the robust presence and stability of QP order across a wide range of the phase diagram, with a notable enhancement near the Kitaev QSL phases. This enhancement occurs despite the absence of longer-range spin-spin correlations, adding a new dimension to our understanding of the interplay between QP order and QSLs.

5.2 Quadrupolar operator

The QP state emerges as a quantum ordered phase characterized by collective bimagnon excitations. This intriguing state, while exhibiting a preference for the orientation of paired magnons, notably does not break time-reversal symmetry. Its detection hinges on the analysis of a symmetric and traceless rank-2 tensor operator [266]:

$$\hat{Q}_{ij}^{\alpha\beta} = S_i^{\alpha} S_j^{\beta} + S_j^{\alpha} S_i^{\beta} - \frac{2}{3}(S_i.S_j)\delta_{\alpha\beta} \tag{5.2.1}$$

where α and β represent the Cartesian coordinates such as x, y, z. As explained below, the Hamiltonian of the KH model can be reformulated to explicitly include a specific component of Eq. (5.2.1):

$$\hat{Q}_{ij}^{x^2-y^2} = \frac{1}{2}(S_{i,j}^{+} S_{i+1,j}^{+} + S_{i,j}^{-} S_{i+1,j}^{-}). \tag{5.2.2}$$

---

[1] The work reported here is based on the paper "Emergent Quadrupolar Order in the Spin-1/2 Kitaev-Heisenberg Model", by Manodip Routh, Sayan Ghosh, Jeroen van den Brink, Satoshi Nishimoto, Manoranjan Kumar in Phys. Rev. B 109, L220403 (2024)

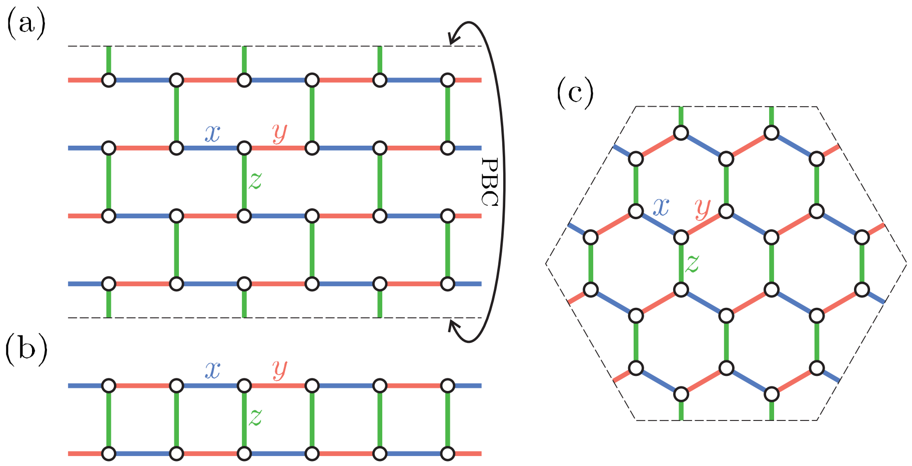

Figure 5.1: Lattice structures used in our calculations: (a) KH ladder or brickwall lattice which is obtained by deforming the honeycomb-lattice KH model. (b) 2-leg KH ladder. (c) 24-site honeycomb-lattice KH cluster with periodic boundary conditions.

5.3 Model Hamiltonian

We consider a spin-1/2 KH model on both a ladder and a honeycomb lattice [47]. The Hamiltonian is given by

$$\mathcal{H} = J\sum_{i,j}\vec{S}_i\cdot\vec{S}_j + K\sum_{\gamma}\sum_{i,j}S_i^{\gamma}S_j^{\gamma}. \tag{5.3.1}$$

Where S_i^{γ} is the γ ($= x$, y, or z) component of the spin-1/2 operator $\vec{S}_i$ at site i. Here, J and K denote the Heisenberg and Kitaev interactions, respectively. To facilitate analysis, we introduce an angular parameter ϕ ($\in [0, 2\pi]$), defining $J = \cos\phi$ and $K = \sin\phi$.

For the ladder or cylinder geometry, the Hamiltonian is adapted to include the spin-1/2 operator $\vec{S}i, j$ at site i on the j-th leg:

$$\begin{aligned}\mathcal{H}_{\text{leg}} &= \frac{2J+K}{4}\sum_{j=1}^{n}\sum_{i=1}^{L}(S_{i,j}^{+}S_{i+1,j}^{-} + S_{i,j}^{-}S_{i+1,j}^{+})\\ &+ \frac{K}{2}\sum_{j=1}^{n}\sum_{i=1}^{L}(-1)^{i+j}(\hat{Q}_{ij}^{x^2-y^2}) + J\sum_{j=1}^{n}\sum_{i=1}^{L}(S_{i,j}^{z}S_{i+1,j}^{z})\\ &\equiv \mathcal{H}_{\text{exc}} + \mathcal{H}_{\text{Q}} + \mathcal{H}_{\text{z}}. \end{aligned}\tag{5.3.2}$$

In this formulation, $\mathcal{H}_{\text{Q}}$ signifies the QP operator. Its dominance suggests the potential stabilization of QP order. The possibility of QP order arising through similar mechanisms has been previously discussed in the context of J_1-J_2 chain systems under magnetic fields [117].

Although the Kitaev model was originally proposed for the honeycomb lattice, it is recognized that any three-coordinated lattice with Kitaev interactions can exhibit similar intriguing properties. In this sense, the KH model on a 2-leg ladder [Fig. 5.1(b)], derived from a brickwall lattice analogous to the honeycomb lattice, aligns with the necessary geometry. This alignment indicates that the 2-leg KH ladder can offer vital insights into the behavior of the 2D honeycomb-lattice KH model. Notably, the gs phase diagram of the ladder model displays significant similarities with the 2D counterpart in terms of magnetic order and Kitaev QSL, with the key distinction being the replacement of the Néel phase by the rung-singlet (RS) phase [6, 44]. Therefore, initiating our investigation with the 2-leg KH ladder is a strategic choice. This setup not only allows for precise numerical calculations but also facilitates reliable extrapolations to the thermodynamic limit, essential for exploring novel phenomena in the 2D KH model. Building upon this, we extend our investigation to 4-leg and 6-leg cylinders [Fig. 5.1(a)], progressively approaching the 2D bulk limit. This systematic increase in the number of legs serves to bridge our understanding from the simpler ladder systems to the more complex dynamics inherent in the full 2D KH model.

5.4 Methods

To investigate the intricate dynamics of the KH model, we employ two complementary computational techniques. For the 2-leg ladder system [Fig. 5.1(b)], encompassing system sizes up to 12×2, and for the 24-site periodic boundary condition (PBC) cluster [Fig. 5.1(c)], we utilize the exact diagonalization (ED) method. For larger systems, specifically extended 2-leg ladders, as well as 4-leg and 6-leg cylinders [Fig. 5.1(a)], we implement the DMRG method. In our DMRG calculations, we retain up to 5000 density-matrix eigenstates during the renormalization process. This high number of kept states ensures the accuracy of our results, with the largest discarded weight being maintained at an impressively low level of approximately 2×10^{-5}.

5.5 Quadrupolar order in the 2-leg ladder

We commence our analysis with the 2-leg ladder system. To obtain a comprehensive phase diagram for QP order as a function of ϕ, we calculate the QP order parameter $\langle \hat{Q}_{ij}^{x^2-y^2} \rangle$ using ED. Our findings, focusing on a single bond along the leg, are depicted in Fig.5.2(a). We find that $\langle \hat{Q}_{ij}^{x^2-y^2} \rangle$ exhibits finite values over a broad range of ϕ ($0.48\pi \lesssim \phi \lesssim 1.56\pi$) with minimal finite-size effects. This order parameter parameter shows significant values in the AFK, FK, and ZZ phases of the magnetic phase diagram, while it rather diminishes in the FM phase [Fig.5.2(b)]. Conversely, when i and j are positioned on a rung bond, $\langle \hat{Q}_{ij}^{x^2-y^2} \rangle$ consistently equals zero.

To further substantiate these findings, using DMRG we compute leg-leg and rung-rung QP correlation functions, defined as:

$$P_{\mathrm{LmLn}}(r) = \langle S^+_{i,m} S^+_{i+1,m} S^-_{i+r,n} S^-_{i+1+r,n} \rangle \tag{5.5.1}$$

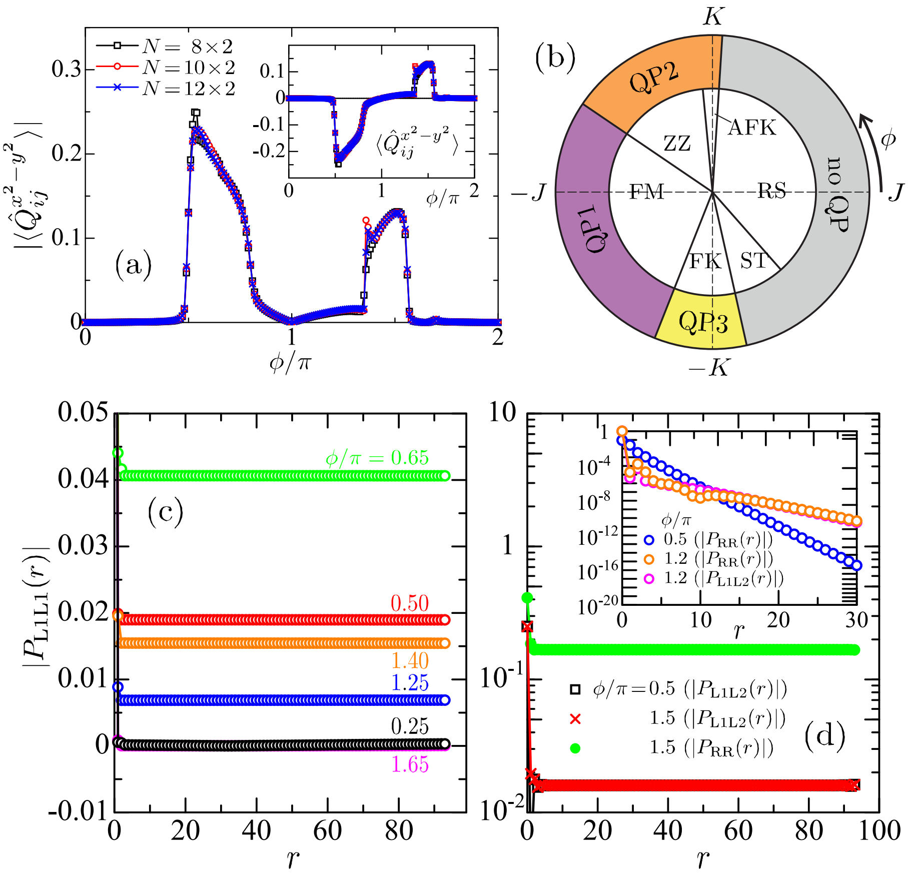

Figure 5.2: Results for 2-leg KH ladder. (a) Absolute values of the QP order parameter for leg bonds with various system sizes. The inset represents the same physical quantity but without taking absolute values. (b) Ground-state Phase diagram for magnetic order (inner) and QP order (outer). Four long-range ordered phases: rung-singlet (RS), zigzag (ZZ), ferromagnetic (FM), stripy (ST) and two QSL phases: antiferromagnetic Kitaev (AFK) and ferromagnetic Kitaev (FK). (c) Compilation of the behavior of the QP correlation functions $|P_{\mathrm{L1L1}}(r)|$ with $N = 100 \times 2$ cluster for representative parameters (see text). (d) Inter-leg and rung-rung QP correlation functions at $\phi/\pi = 0.5$, 1.2, and 1.5. Inset: Examples for the cases where the QP correlation function exhibits an exponential decay.

and

$$P_{\mathrm{RR}}(r) = \langle S^+_{i,m} S^+_{i,m+1} S^-_{i+r,m} S^-_{i+r,m+1}\rangle, \tag{5.5.2}$$

respectively. The results, summarized in Fig.5.2(c,d), reveal that the intra-leg correlation $P_{\mathrm{L1L1}}(r)$ exhibits QP LRO within the ϕ range where $\langle\hat{Q}_{ij}^{x^2-y^2}\rangle$ is finite. Note that $P_{\mathrm{L1L1}}(r)$ alternates in sign with distance. Meanwhile, near both Kitaev points $\phi = \pm\pi/2$, the inter-leg correlation $P_{\mathrm{L1L2}}(r)$, and near the FK phase, the rung-rung correlation $P_{\mathrm{RR}}(r)$, also exhibit QP LRO. Unlike $P_{\mathrm{L1L1}}(r)$, both $P_{\mathrm{L1L2}}(r)$ and $P_{\mathrm{RR}}(r)$ are always positive. Interestingly, despite the rung QP order parameter being consistently zero across all ϕ values, $P_{\mathrm{RR}}(r)$ still exhibits LRO in the FK phase. This suggests that states of QP order with broken spin-rotational symmetry are degenerate, leading to a zero local order parameter, yet detectable through correlation functions.

From these correlation function analyses, the ϕ domain for QP order can be classified into four phases: QP1 (only $P_{\mathrm{L1L1}}(r)$ shows LRO), QP2 (both $P_{\mathrm{L1L1}}(r)$ and $P_{\mathrm{L1L2}}(r)$ show LRO), QP3 (all of $P_{\mathrm{L1L1}}(r)$, $P_{\mathrm{L1L2}}(r)$, and $P_{\mathrm{RR}}(r)$ show LRO), and a phase with no QP LRO. In Fig.5.3 schematic picture of quadrupolar states is shown. Both $P_{\mathrm{L1L2}}(r)$ and $P_{\mathrm{RR}}(r)$ are always positive i.e. indicates non-staggered behaviour. The first type of phase involves the confinement of two spin flips along the leg, as depicted in Fig.5.3(a). This phase is denoted as QP_1 and exhibits long-range order along the leg ($P_{\mathrm{L1L1}}(r)$). The second type of phase is QP_2, featuring long-range pair correlation along the same leg ($P_{\mathrm{L1L1}}(r)$) and across the leg ($P_{\mathrm{L1L2}}(r)$), as illustrated in Fig. 5.3(b). The third type is QP_3, exhibits long-range pair correlation along the rung ($P_{\mathrm{RR}}(r)$), the same leg ($P_{\mathrm{L1L1}}(r)$), and across the leg ($P_{\mathrm{L1L2}}(r)$), as shown in Fig. 5.3(c).

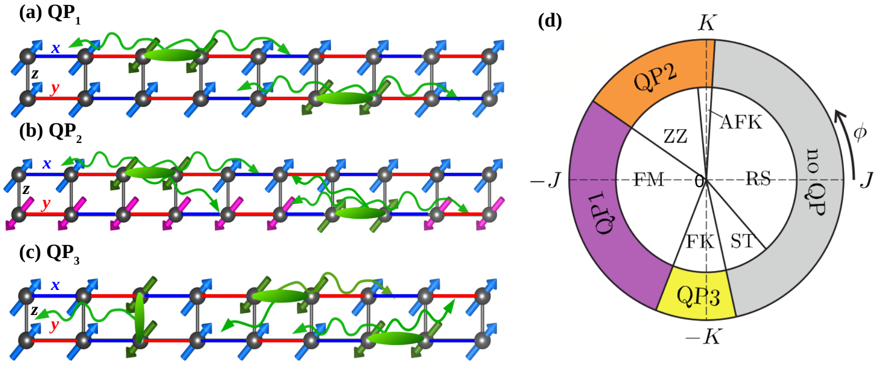

Figure 5.3: Spin nematic state expected for a KH ladder. Schematic representation of bound pairs of magnons moving in a background of polarized spins. Here, most of the spins colored as blue and magenta arrows align in $+z$ or $-z$ directions, respectively. Flipped spins (black arrows) gain energy by propagating as bound pairs along (a) same leg in QP_1 phase, (b) both the same leg and across the leg in QP_2 phase, (c) rung, same leg and across the leg in QP_3 phase. (d) Phase diagram for magnetic order (inner) and QP order (outer).

The correspondence with the magnetic order phases is shown in the phase diagram in Fig.5.2(b). The phase diagram for QP order can be reasonably explained by considering the spin structures of the corresponding magnetic phases. In the FM phase ($0.81 \lesssim \phi/\pi \lesssim 1.38$), the near-full magnetization results in smaller values of $P_{\mathrm{L1L1}}(r)$ and $|\langle \hat{Q}_{ij}^{x^2-y^2} \rangle|$, and they vanish without $\mathcal{H}_{\mathrm{Q}}$ at $\phi = \pi$. The ZZ phase ($0.53 \lesssim \phi/\pi \lesssim 0.81$) exhibits Ising-type LRO in each leg with opposite polarization between legs [6], leading to the anticipated development of $P_{\mathrm{L1L2}}(r)$. However, $P_{\mathrm{RR}}(r)$ does not show LRO due to antiparallel spin orientation on the rungs.

The ground state properties of ZZ phase can be analyzed using the wave function. The wave function at $\phi \approx 0.65\pi$ can be written as follows,

$$\begin{aligned}
\psi(\phi) \approx\ & [(C_1 + \sum_{m=1}^{N/2} C_2(-1)^m (S^+_{m,1}S^+_{m+1,1} + S^-_{m,2}S^-_{m+1,2}) + C_3 S^+_{m,1}S^-_{m,2}) \\
+\ & \sum_{m\neq n=1}^{N/2} C_4 S^+_{m,1}S^+_{m+1,1}S^+_{n,1}S^+_{n+1,1} + \cdots] \prod_{i=1}^{N/2} S^-_{i,1}\left|\Uparrow\right\rangle \\
+\ & [(C_1 + \sum_{m=1}^{N/2} C_2(-1)^m (S^-_{m,1}S^-_{m+1,1} + S^+_{m,2}S^+_{m+1,2}) + C_3 S^-_{m,1}S^+_{m,2}) \\
+\ & \sum_{m\neq n=1}^{N/2} C_4 S^-_{m,1}S^-_{m+1,1}S^-_{n,1}S^-_{n+1,1} + \cdots] \prod_{i=1}^{N/2} S^+_{i,1}\left|\Downarrow\right\rangle \\
+\ & \cdots
\end{aligned} \tag{5.5.3}$$

where, $\left|\Uparrow\right\rangle$ and $\left|\Downarrow\right\rangle$ denote spin-up and spin-down states, respectively. The largest coefficient C_1 corresponds to two configurations where spins in one leg align along the +z direction and spins in the other leg align along the −z direction. The next dominant configurations with coefficients C_2 and C_3 correspond to $2N$ and N configurations, exhibiting a simultaneous double spin flip along the leg and the rung. C_4 corresponds to $2N$ configurations with a simultaneous four-spin flip along the leg. The contributions from other configurations involving multiple spin flips are comparatively small. The system size dependence of these coefficients is shown in the Table. 5.1. Due to the large quantum fluctuations in this phase, all the configurations contribute substantially to the QP order, which accounts for the highest QP order in this phase.

Table 5.1: Dominant coefficients of the ground state wave function in the zigzag phase at $\phi = 0.65\pi$ with $N = 8 \times 2$ and 10×2 sites ladder.

Coefficients	$N = 8 \times 2$	No. of diagrams	$N = 10 \times 2$	No. of diagrams
C_1	0.43387	2	0.34001	2
C_2	0.09194	32 ($2N$)	0.07170	48 ($2N$)
C_3	0.08103	16 (N)	0.06424	16 (N)
C_4	0.02541	32 ($2N$)	0.01947	48 ($2N$)

In the RS ($-0.26 \lesssim \phi/\pi \lesssim 0.48$) and ST ($1.57 \lesssim \phi/\pi \lesssim 1.74$) phases, the each leg possesses a Néel-type LRO, precluding the dominance of the $\mathcal{H}_{\text{Q}}$ term. Thus, a QP order is absent.

In the AFK ($0.48 \lesssim \phi/\pi \lesssim 0.53$) and FK ($1.38 \lesssim \phi/\pi \lesssim 1.57$) phases, the competition between dipole fluctuations ($\mathcal{H}_{\text{exc}}$) and QP fluctuations ($\mathcal{H}_{\text{Q}}$) complicates gs determination. Nevertheless, the larger coefficient of $\mathcal{H}_{\text{Q}}$ supports the emergence of QP order along the leg, as corroborated by our numerical results. Remarkably, in the FK phase, the rung QP correlation function $P_{\text{RR}}(r)$ also exhibits LRO, with a saturation value exceeding $P_{\text{L1L1}}(r)$. This is attributed to the FM Ising character of rung interactions, conducive to bimagnon formation [324].

The gs wave function in the FK phase at $\phi \approx 1.53\pi$ can be approximated as,

$$\begin{aligned}\psi(\phi) &\approx [C_1 + \sum_{m=n=1}^{N/2} C_2 S^-_{m,1} S^-_{m+1,1} S^-_{n,2} S^-_{n+1,2} + S^-_{m,1} S^-_{m,2} S^-_{n,1} S^-_{n,2}]\,|{\Uparrow}\rangle \\ &+ [C_1 + \sum_{m=n=1}^{N/2} C_2 S^+_{m,1} S^+_{m+1,1} S^+_{n,2} S^+_{n+1,2} + S^+_{m,1} S^+_{m,2} S^+_{n,1} S^+_{n,2}\,|{\Downarrow}\rangle] + \cdots \qquad (5.5.4)\end{aligned}$$

Here, double spin flips occur only along the rung. C_1 corresponds to configurations where all the spins align along +z or −z direction. C_2 corresponds to simultaneous double-spin flips along rung. Due to strong Kitaev interaction, quantum fluctuations are very high in this phase, and coefficients are comparable. The other configurations with multiple spin flips are with small contributions. These configurations contribute significantly to the QP order parameter, which is finite in this phase.

Given these insights, we hypothesize that QP order might also be present in the 2D honeycomb KH system, akin to the 2-leg ladder scenario. To test this hypothesis, we extend our investigation to isotropic honeycomb cluster as well as 4-leg and 6-leg cylinders, in the parts that follow.

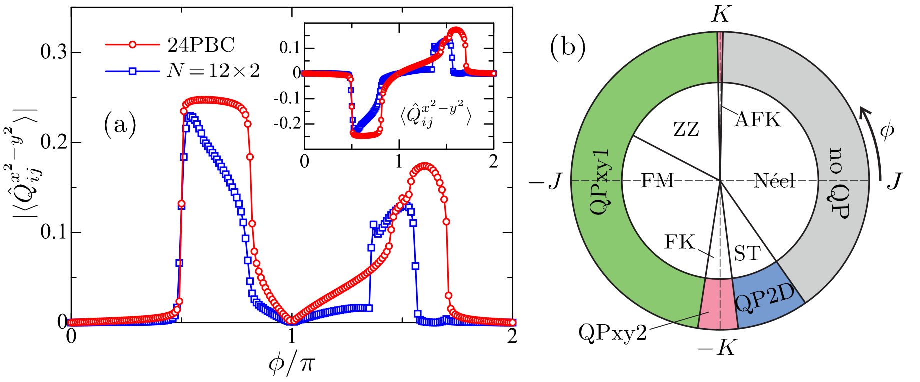

Figure 5.4: Results for honeycomb-lattice KH model. (a) Absolute values of the QP order parameter for x or y bond, calculated using the 24-site PBC cluster. For comparison, those for the 2-leg KH ladder are also plotted. The inset represents the same physical quantity but without taking absolute values. (b) Ground-state Phase diagram for magnetic order (inner) and QP order (outer).

5.6 Quadrupolar order in the 2D honeycomb lattice

Analogous to the approach for the 2-leg ladder, we first aim to grasp the overall picture of the QP order phase diagram as a function of ϕ by calculating the QP order parameter using ED on the 24-site PBC cluster.The results, illustrated in Fig. 5.4(a), are compared with those from the 2-leg ladder. In the context of magnetic order phases for the 2D honeycomb-lattice KH model, the QP order parameter is finite in the AFK ($0.494 \lesssim \phi/\pi \lesssim 0.506$), ZZ ($0.506 \lesssim \phi/\pi \lesssim 0.847$), FM ($0.847 \lesssim \phi/\pi \lesssim 1.452$), FK ($1.452 \lesssim \phi/\pi \lesssim 1.539$), and ST ($1.539 \lesssim \phi/\pi \lesssim 1.694$) phases, and it is zero only in the Néel phase ($-0.306 \lesssim \phi/\pi \lesssim 0.494$). While the results are fundamentally similar to those for the 2-leg ladder, a notable difference is that the QP order parameter remains finite even in the ST phase. For the z-bonds, similar to the rung QP in the 2-leg ladder, the QP order parameter is zero.

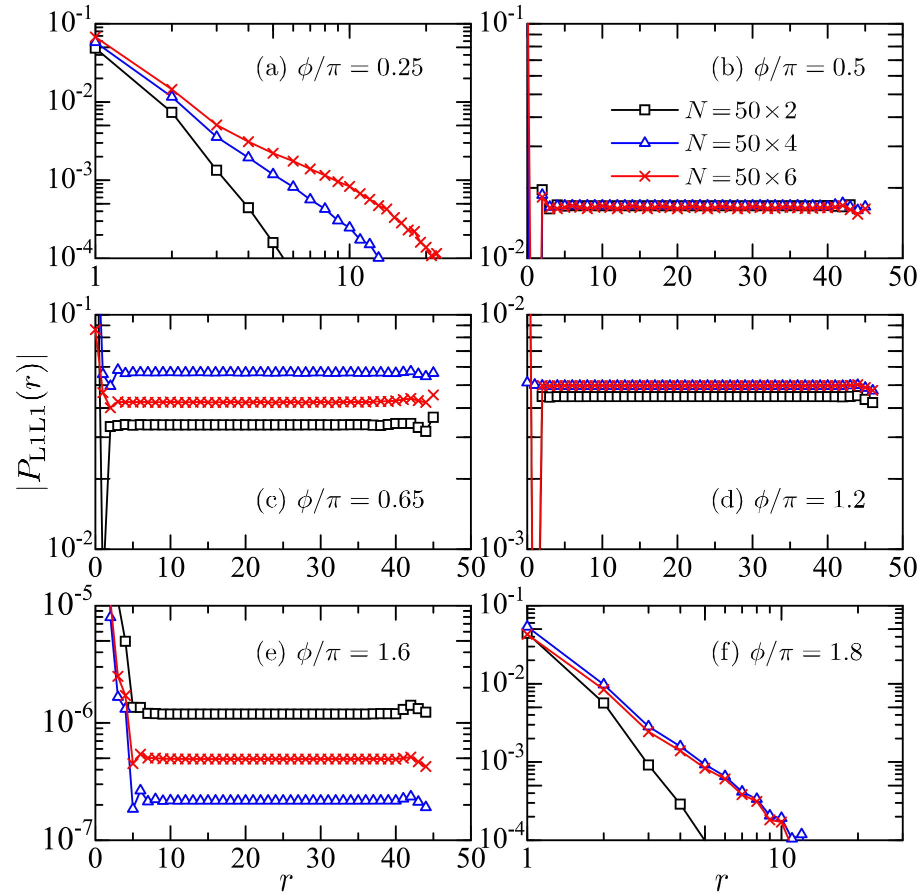

Figure 5.5: DMRG results for the QP correlation functions $P_{\mathrm{L1L1}}(r)$ at representative value of ϕ for six quantum phases using 2-leg, 4-leg, and 6-leg cylinders.

To ascertain the persistence of QP order in the bulk limit, we compute QP correlation functions using DMRG for 4-leg and 6-leg cylinders, in addition to the 2-leg ladder. Focusing on the intra-leg QP correlation function, $P_{\mathrm{L1L1}}(r)$, we observe in Fig. 5.5 that, consistent with the QP order parameter results, $P_{\mathrm{L1L1}}(r)$ converges to a finite value in the long-distance limit for all magnetic phases except the Néel phase. Importantly, this convergence value does not diminish with an increasing number of legs, suggesting its stability in the bulk limit. In the Néel phase, $P_{\mathrm{L1L1}}(r)$ exhibits a power-law decay indicating no long-range QP order.

The decay of QP correlation functions perpendicular to the leg direction, namely along the z-bond, is also of interest. We calculate the inter-leg QP correlation function, $P_{\mathrm{L1Ln}}(r)$, for various leg distances in a 50×6 system. The calculated $P_{\mathrm{L1Ln}}(r)$ for $n = 1-3$ is plotted in Fig. 5.6. In the ZZ and FM phases, the saturation value of $P_{\mathrm{L1Ln}}(r)$ at long distances follows power-law decay [Fig. 5.6(b,c)], suggesting quasi-LRO along the z-bond direction (QPxy1 phase). Near the Kitaev points (AFK and FK), a rapid decay of inter-leg correlations is observed [Fig. 5.6(a)], indicating LRO in the xy zigzag direction alone (QPxy2 phase). The ST phase

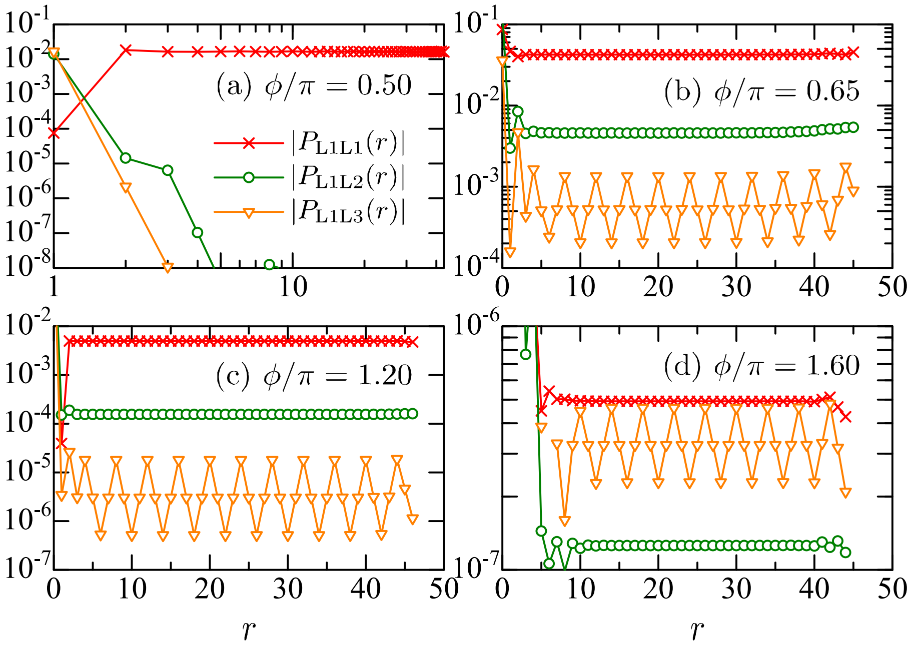

Figure 5.6: DMRG results for the inter-leg QP correlation functions, $P_{\mathrm{L1Ln}}(r)$ for $n = 1 - 3$ at magnetic ordered phases, including ZZ ($\phi/\pi = 0.65$), FM ($\phi/\pi = 1.2$), ST ($\phi/\pi = 1.6$) and QSL phase ($\phi/\pi = 0.5$), using 6-leg cylinders.

presents a unique case, where the decay along the z-bond direction does not follow a simple pattern [Fig. 5.6(d)], hinting at the potential for LRO (QP2D phase). For all ϕ values, the rung-rung QP correlation function, $P_{\mathrm{RR}}(r)$, exhibits exponential decay for both 4-leg and 6-leg cylinders. The correspondence between QP order and magnetic order is summarized in the phase diagram in Fig. 5.4(b). A notable distinction from the 2-leg ladder case is the presence of QP order in the ST phase, likely due to the unique orientation of ST order in this setting, although the magnitude of QP correlations in this phase is relatively small compared to other phases.

5.7 Conclusion

We have explored the gs dynamics of the spin-$\frac{1}{2}$ KH model, focusing particularly on the emergence and characteristics of QP order. Our study spans two distinct geometries: the 2-leg ladder and the 2D honeycomb lattice. Employing a synergistic approach combining ED and DMRG techniques, we have meticulously analyzed the QP order parameter and correlation functions in these systems. Our key contribution is the unveiling of a comprehensive gs phase diagram, which distinctly maps out the QP order in relation to the interplay between Heisenberg and Kitaev interactions. A notable discovery is the pronounced stability of QP order across a broad range of the phase diagram, underscoring its robustness in the KH model. Additionally, our findings reveal a remarkable enhancement of the QP order parameter and its correlation functions near the Kitaev QSL phases. This enhancement is particularly intriguing as it occurs in the absence of long-range spin-spin correlations, suggesting a nuanced relationship between QP order and

QSLs. In fact, the third-order positive susceptibility, indicative of a general signature of QP order, has been observed in α-RuCl$_3$ [149], where the relationship between K and J appears to be $-K \gg J > 0$ [400], suggesting a proximity to the FK QSL phase.

These insights not only advance our understanding of the KH model but also contribute significantly to the broader discourse on quantum magnetism in low-dimensional systems, highlighting the intricate interplay between different types of quantum order.

Chapter 6

Impact of Dzyaloshinskii-Moriya in Kitaev-Heisenberg model on honeycomb lattices

---

6.1 Introduction

The exploration of new quantum phases in strongly correlated systems has generated considerable interest in Kitaev materials. These materials exhibit bond-dependent interactions that can lead to quantum spin liquid (QSL) states [184]. In the ideal Kitaev model, spin-$\frac{1}{2}$ moments interact along specific bond directions on a honeycomb lattice, resulting in an exactly solvable QSL ground state. This state is characterized by fractionalized Majorana fermions and emergent $\mathbb{Z}_2$ gauge fields [160, 356]. Jackeli and Khaliullin showed that such bond-directional Kitaev interactions can be realized in d^5 transition-metal compounds with strong spin-orbit coupling [160]. This discovery led to the identification of a class of materials known as Kitaev materials [145, 282, 294, 347, 395], which are currently being extensively studied.

However, real materials are not ideal and include additional interactions such as Heisenberg terms, off-diagonal exchanges, and Dzyaloshinskii-Moriya interaction (DMI) [48, 145, 278, 280, 347, 395]. These extra terms can destabilize the Kitaev spin liquid (KSL) phase and lead to various long-range magnetic orders, such as Néel, zigzag, stripy, or ferromagnetic phases [48, 49, 49, 168, 175, 220, 269]. Among these, DMI is especially interesting because it arises from spin-orbit coupling in systems without inversion symmetry. It can induce chiral magnetic orders and topological excitations, possibly converting a gapless quantum spin liquid (QSL) into a chiral QSL with edge states [85, 86, 240].

The presence of DMI in Kitaev materials has been confirmed in compounds like α-$RuCl_3$, Li_2IrO_3, and CrI_3, where it significantly affects their magnetic properties and thermal Hall responses [19, 52, 395, 399, 401]. Recent studies show that the combined effect of Kitaev and DMI interactions can lead to new topological magnon effects, such as thermal Hall and magnon Nernst responses [105, 234, 410]. Applying a magnetic field further changes the symmetry and strongly influences the topological magnon transport [410].

Additionally, theoretical studies suggest that DMI can stabilize complex spin textures like skyrmions and vortex states, which are of great interest in the study of topological magnetism [214, 371].

Although the original Kitaev spin liquid (KSL) was introduced on a honeycomb lattice, it is now known that Kitaev interactions on any three-coordinated lattice can lead to interesting

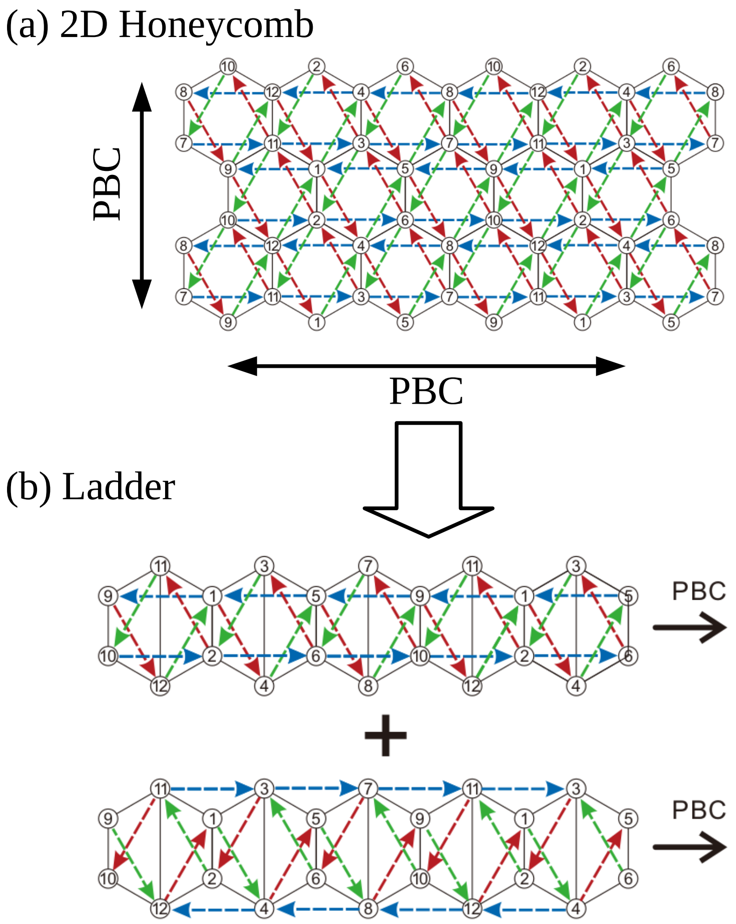

Figure 6.1: Schematic diagram of Kitaev Heisenberg (KH) model on (a) 2D honeycomb lattice (b) ladder with second neighbor Dzyaloshinskii-Moriya interaction (DMI). Solid (dashed) lines denote the x, y, z Kitaev (Dzyaloshinskii-Moriya) bonds. The black nearest neighbor bonds are indicating Kitaev exchanges. The red, green and blue dashed second nearest neighbor bonds are indicating bond dependent DM interactions D^x, D^y, and, D^z, respectively.

quantum phases. In this regard, a two-leg ladder geometry also meets the necessary geometrical conditions for realizing Kitaev interactions. Since the combined effects of Kitaev and Heisenberg interactions in two- or three-dimensional systems can be computationally demanding, it is useful to first study simpler geometries. A natural next step is to investigate quasi-one-dimensional systems. In this context, the Kitaev-Heisenberg (KH) model has recently been explored in detail on one-dimensional spin chains [5] and two-leg ladders [6, 44, 296].

Motivated by numerous experimental and theoretical studies, we investigate the Kitaev-Heisenberg-DMI (KH-DMI) model on two geometries: the two-leg ladder and the two-dimensional (2D) honeycomb lattice. We employ exact diagonalization (ED) and density-matrix renormalization group (DMRG) techniques to explore the effect of DMI on the stability of the KSL phase and the emergence of other novel magnetic phases.

In this chapter, we investigate the effect of DMI on the stability of the KSL phase in two different geometries. For the two-leg ladder, we find that the KSL phase remains stable for weak

DMI ($0 \leq D \leq 0.05$), although the phase boundary shifts noticeably. When the DMI becomes stronger ($0.05 < D \leq 0.1$), the system gradually changes from the KSL phase to a non-Kitaev spin liquid (non-KSL) phase, characterized by exponentially decaying spin correlations. This change is a crossover rather than a sharp phase transition. Interestingly, the vector chirality stays non-zero across the entire DMI range, indicating that chiral order coexists with the KSL phase.

In contrast, for the 2D honeycomb lattice, the behavior is different. The KSL phase survives only for very weak DMI ($0 \leq D \leq 0.02$). In the strong DMI regime, the system develops a vortex state. These findings underline the significant role of dimensionality in determining the nature of quantum phases.

The chapter is organized as follows. In Sec. 6.2, we introduce the KH-DMI Hamiltonian and explain how it is defined on both two-leg ladder and the honeycomb lattice. Section 6.3 describes the computational methods used in this work, including ED and DMRG. In Sec. 6.4, we present and discuss the results for two-leg ladder, focusing on spin correlations, various order parameters, and vector chirality. In Sec. 6.6, we compare the results between two-leg ladder and 2D honeycomb lattice. Finally, in Sec. 6.7, we summarize the main results of the study.

6.2 Model Hamiltonian

The magnetic order observed in Kitaev materials, such as the zigzag order in Na_2IrO_3 [56, 219, 408] and $RuCl_3$ [40, 166], can be stabilized by Heisenberg interactions (J). As a result, the minimal model that captures the zigzag order in these systems is the Kitaev-Heisenberg (KH) model.

Another Kitaev material, α-Li_2IrO_3, which is believed to be isostructural to its Na-based counterpart, also shows magnetic ordering. Resonant magnetic X-ray diffraction and powder magnetic neutron diffraction experiments on α-Li_2IrO_3 reveal incommensurate magnetic order. In this state, the magnetic moments within the iridium honeycomb layers exhibit counter-rotating behavior on nearest-neighbor sites [390].

Interestingly, a similar type of magnetic order is also found in the three-dimensional polymorphs β-Li_2IrO_3 and γ-Li_2IrO_3. Before this experimental discovery, several theoretical works [281, 288] had predicted spiral or other incommensurate magnetic states in the honeycomb lattice, although none had anticipated the counter-rotating spiral configuration. While earlier studies focusing only on nearest-neighbor terms emphasized the role of bond anisotropy [182], more recent work [395] has shown that second-neighbor Dzyaloshinskii-Moriya interaction (DMI), along with other long-range second- and third-neighbor interactions, is essential to stabilize the counter-rotating spiral order.

Motivated by these findings, we consider the Kitaev-Heisenberg (KH) model with second-nearest neighbor (2NN) DMI. The Hamiltonian is given by

$$\mathcal{H} = \sum_{\langle i,j \rangle} J_{ij} \vec{S}_i \cdot \vec{S}_j + \sum_{\langle i,j \rangle} K_{ij}^{\gamma} S_i^{\gamma} S_j^{\gamma} + \sum_{\langle i,j \rangle} \vec{D}_{ij} \cdot \left(\vec{S}_i \times \vec{S}_j \right), \tag{6.2.1}$$

where $J_{\langle i,j \rangle}$ and $K^{\gamma}_{\langle i,j \rangle}$ ($\gamma \in \{x, y, z\}$) represent the Heisenberg and Kitaev exchanges on nearest-neighbor (NN) bonds, respectively, and $\vec{D}_{\langle\langle ij \rangle\rangle} = (D^x_{\langle\langle ij \rangle\rangle}, D^y_{\langle\langle ij \rangle\rangle}, D^z_{\langle\langle ij \rangle\rangle})$ denotes the 2NN DM vector. The DM vectors are bond-dependent and specified as follows: $D^x_{\langle\langle ij \rangle\rangle} = (0, -D, -D)$, $D^y_{\langle\langle ij \rangle\rangle} = (-D, 0, -D)$, and $D^z_{\langle\langle ij \rangle\rangle} = (-D, -D, 0)$.

For convenience, we define an angular parameter $\phi \in [0, 2\pi]$, such that $J = \cos\phi$ and $K = \sin\phi$. The strength of the DMI is varied within the range $0 \leq D \leq 0.1$.

The DMI part of the Hamiltonian in Eq. (6.2.1) can be simplified as:

$$\sum_{\langle\langle ij \rangle\rangle} D_{ij} \cdot (\vec{S}_i \times \vec{S}_j) = \sum_{\langle\langle ij \rangle\rangle} \begin{bmatrix} 0 & -D & -D \\ S_i^x & S_i^y & S_i^z \\ S_j^x & S_j^y & S_j^z \end{bmatrix} + \sum_{\langle\langle ij \rangle\rangle} \begin{bmatrix} -D & 0 & -D \\ S_i^x & S_i^y & S_i^z \\ S_j^x & S_j^y & S_j^z \end{bmatrix} + \sum_{\langle\langle ij \rangle\rangle} \begin{bmatrix} -D & -D & 0 \\ S_i^x & S_i^y & S_i^z \\ S_j^x & S_j^y & S_j^z \end{bmatrix} \tag{6.2.2}$$

Figures 6.1(a) and (b) illustrate how the two-leg ladder structure can be derived from a two-dimensional honeycomb lattice. The red, green, and blue dashed lines represent second-nearest-neighbor (2NN) bonds associated with the bond-dependent DM vectors D^x, D^y, and D^z, respectively. In a ladder with N sites, there are $3N/2$ nearest neighbor (NN) bonds and $3N$ second nearest neighbor bonds.

6.3 Numerical Method

To investigate the intricate ground state (gs) properties of the KH-DMI model, we employ two complementary computational techniques. For the two-leg ladder system [Fig. 6.1(b)], encompassing system sizes up to $N = L \times 2 = 12 \times 2$, and for the 24-site periodic boundary condition (PBC) honeycomb cluster [Fig. 6.1(a)], we utilize the exact diagonalization (ED) method. For larger systems, specifically two-leg ladders, we implement the DMRG method. In our DMRG calculations, we retain up to 1000 density-matrix eigenstates during the renormalization process. This high number of kept states ensures the accuracy of our results, with the largest discarded weight being maintained at an impressively low level of approximately 10^{-10}.

6.4 Results for Two-Leg Ladder

In this section, we present the results for the KH-DMI model described in Eq. (6.2.1), considering a two-leg ladder geometry. The model is studied within the parameter space defined by ϕ and D. The main goal is to understand the effect of DMI in the KSL phase. In addition, we explore the ground state phase diagram of the KH-DMI model in detail. To identify the ground-state phase boundaries, we calculate several physical quantities, as described below.

Energy derivative: We evaluate the second derivative of the ground-state energy (E_0) per site with respect to ϕ, which is defined as

$$\frac{E_0''}{N} = \frac{1}{N}\frac{\partial^2 E_0}{\partial \phi^2}. \tag{6.4.1}$$

This quantity helps in identifying phase transitions, which appear as maxima or discontinuities in $-E_0''/N$.

Plaquette operator: We also compute the expectation value of the plaquette operator $\mathcal{W}$, given by

$$\mathcal{W} = \langle S_1^x S_2^y S_3^z S_4^x S_5^y S_6^z \rangle, \tag{6.4.2}$$

which acts as an order parameter for the KSL phases. Deviations of $\mathcal{W}$ from ±1 signal a transition out of the KSL regime.

String order parameter: For the topological properties of the system, we calculate the string order parameter (SOP) [44, 51**?**], also known as hidden or non-local order. For a two leg ladder system, it is defined as

$$\mathcal{O}_{\text{string}} = \lim_{|i-j|\to\infty} \left\langle S_{i,1}^y S_{i,2}^x \left(\prod_{k=i+1}^{j-1} S_{k,1}^z S_{k,2}^z \right) S_{j,1}^y S_{j,2}^x \right\rangle .$$

Here, we choose $i = N/4$ and $j = 3N/4$ with system size $N = 8n$ (n: integer) to obtain the SOP.

Vector chiral operator: In presence of DMI, chiral spin order are expected in set in the system. The vector chiral order parameter v_c cen be characterized by the spin chirality and defined as

$$v_c = \sum_{i=1}^{3} \vec{S}_{2i-1} \times \vec{S}_{2i+1} = \sum_{i=1}^{3} \vec{S}_{2i} \times \vec{S}_{2i+2}, \tag{6.4.3}$$

where the index i refers to sites within a plaquette, as illustrated in the inset of Figure 6.6.

6.4.1 Phase diagram for finite DMI ($D \neq 0$)

The ground state phase diagram of the KH ladder in the absence of DMI ($D = 0$) consists of four ordered phases: rung-singlet (RS), zigzag (ZZ), ferromagnetic-xy (FM-xy), and stripy (ST), along with two spin liquid phases: antiferromagnetic (AFM) Kitaev (AFK) and ferromagnetic (FM) Kitaev (FK).

The RS phase is characterized by singlet dimers forming along the rungs, with spin correlations showing exponential decay along the legs. The ZZ phase exhibits Ising-type long-range order (LRO) along each leg, with opposite polarization between the two legs. In contrast, the ST phase shows Ising-type order along the rungs. The FM-xy phase is a fully polarized phase in the xy-plane.

The AFK and FK points, at $\phi/\pi = 0.50$ and $\phi/\pi = 1.50$, respectively, represent spin liquid

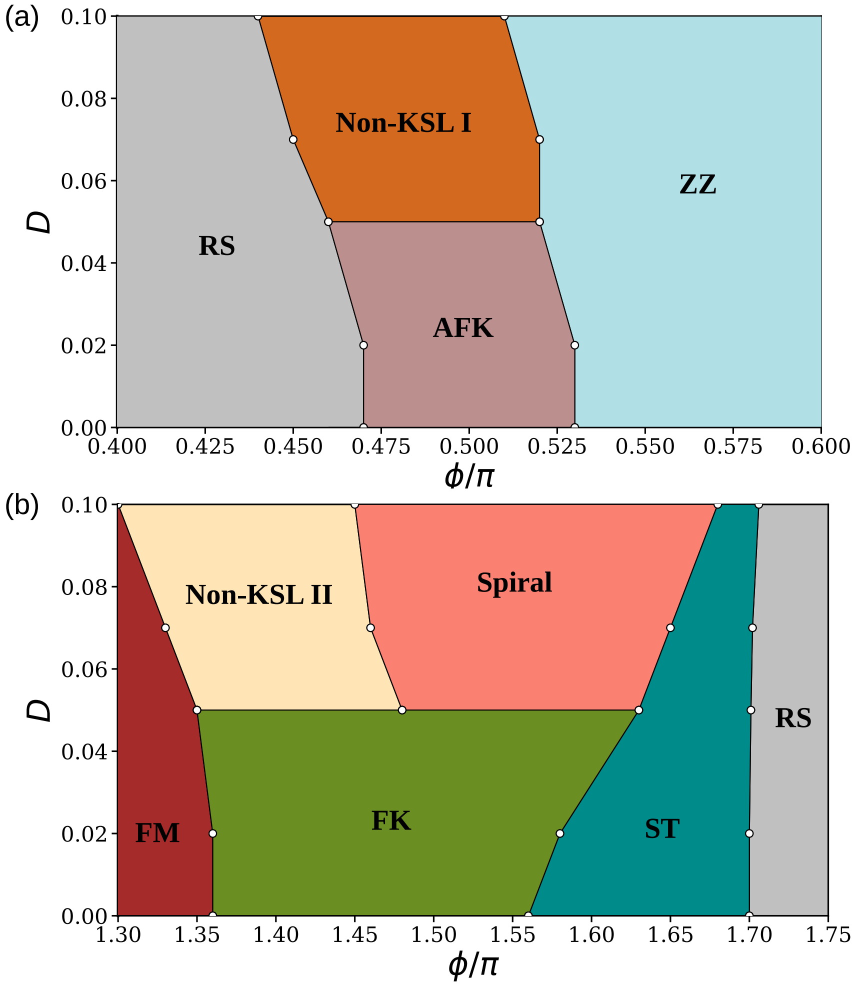

Figure 6.2: Phase diagram for two-leg ladder around (a) AFM and (b) FM Kitaev region for two-leg ladder in $\phi/\pi - D$ parameter space.

states where spin correlations are finite only between nearest neighbors, and the plaquette operator reaches its maximum value, $\mathcal{W} = 1$ [5]. These states also exhibit topological features, as indicated by a finite string order parameter ($\mathcal{O}_{\text{string}}$) [44].

Moving away from the AFK and FK points, spin correlations decay exponentially with a small correlation length. Both $\mathcal{W}$ and $\mathcal{O}_{\text{string}}$ decrease from their maximum values. Recently, we observe an enhancement of long-range quadrupolar order (QP) order near KSL phases, despite the absence of long-range spin-spin correlations [296].

Now, in the presence of DMI ($D \neq 0$), we investigate the phase diagram in the ϕ–D parameter space. Based on various order parameters and spin correlation functions, the phase boundaries are identified in the regions around the AFK and FK phases, as shown in Figures 6.2(a) and 6.2(b), respectively.

The phase diagram can be divided into two distinct regimes depending on the strength of DMI. For weak DMI ($0 \leq D \leq 0.05$), all the phases present in the standard KH ladder persist, although the phase boundaries near the AFK and FK regions shift noticeably. In contrast, for stronger DMI ($0.05 < D \leq 0.1$), the KSL phases weakens and chiral order starts dominating, we can term this phase as a non-Kitaev (conventional) spin liquid (non-KSL). In strong D limit we can call these phase as non-KSL I and non-KSL II corresponding to the AFK and FK phases, respectively. In presence of FM Kitaev a spiral phase with spiral like correlations and chiral spin texture emerges in presence of large D.

The KSL phase to non-KSL phase transition is a crossover and it is challenging to clearly identify the boundary of this crossover. In both phases, the spin correlations decay exponentially. However, the correlation length is shorter in the KSL phase compared to the non-KSL phase. Since the correlation length varies continuously with increasing DMI, we use a correlation length of $\xi(\phi/\pi) \sim 1$ as a rough indicator for the crossover from the KSL to the non-KSL phase.

The schematic spin configurations of all the robust long-range ordered phases for a finite DMI in a two-leg ladder are depicted in Fig. 6.3. Fig. 6.3(a) illustrates the formation of singlet states along the rungs of the two-leg ladder. Figs. 6.3(b), 6.3(c), and 6.3(d) display the spin configurations corresponding to the zigzag, ferromagnetic (FM), and stripy phases, respectively. The red and blue arrows represent up and down spins, respectively. Figs. 6.3(e) and 6.3(f) depict the spin configurations at $\phi/\pi = 0.50$ and $\phi/\pi = 1.50$ for a strong DMI with $D = 0.1$, revealing a chiral nature reminiscent of the vortex state observed in the two-dimensional honeycomb lattice, which is discussed in Sec. 6.6.

6.4.2 Effect of DMI on KSL phases

For the standard KH ladder ($D = 0$), the AFK phase is stable within the range $0.48 \lesssim \phi/\pi \lesssim 0.53$. Upon introducing DMI, the boundaries of the AFK phase shift, as indicated by the peak in the energy second derivative ($-E_0''/N$) shown in Fig. 6.4(a) for a two-leg ladder with system size $N = 2 \times 12$.

In the weak DMI regime ($0 \leq D \leq 0.05$), the Kitaev interaction remains dominant, and the AFK ground state persists. The second derivative of the ground-state energy shows two distinct peaks, indicating that the AFK phase boundaries shift to $0.47 \lesssim \phi/\pi \lesssim 0.52$ at $D = 0.05$. However, for stronger DMI ($0.05 < D \leq 0.10$), the DMI becomes dominant, destabilizing the AFK phase. In this regime, a non-KSL I phase with large correlation length ($\xi > 1$) emerges. Further details on spin correlations are discussed below.

While the shift in AFK phase boundaries due to DMI is relatively small, the FK phase boundaries undergo a more significant change. Without DMI ($D = 0$), the FK phase exists within $1.38 \lesssim \phi/\pi \lesssim 1.57$. For weak DMI ($0 \leq D \leq 0.05$), these boundaries shift to $1.31 \lesssim \phi/\pi \lesssim 1.62$ as D increases to 0.05. For stronger DMI ($0.05 < D \leq 0.10$), the FK phase disappears and is replaced by two distinct phases: a non-KSL II phase with large correlation length ($\xi > 1$), and a spiral phase characterized by chiral spin correlations. These correlations are analyzed in detail below.

Figures 6.4(c) and (d) show the plaquette operator $\mathcal{W}$ for a two-leg ladder with $N = 2 \times 12$

(a) Rung-Singlet

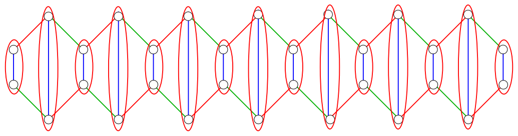

(b) Zigzag

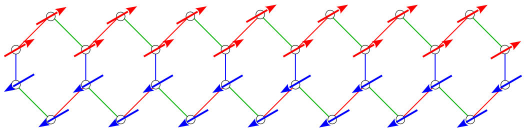

(c) FM

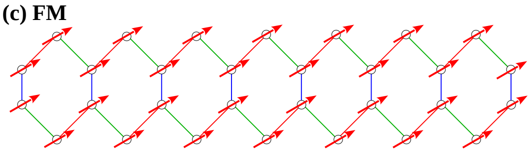

(d) Stripy

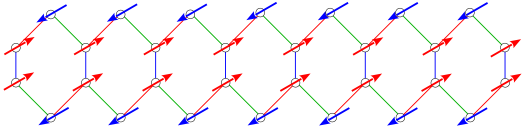

(e) φ=0.5π, D=0.1

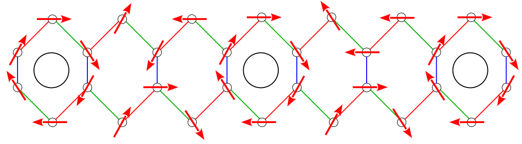

(f) φ=1.5π, D=0.1

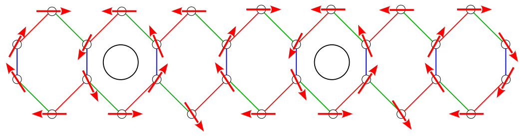

Figure 6.3: Schematic representation of spin configurations for the two-leg ladder in different phases: (a) rung-singlet, (b) zigzag, (c) ferromagnetic (FM), and (d) stripy phases. Red and blue arrows denote up and down spins, respectively. Panels (e) and (f) illustrate the spin configurations at $\phi/\pi = 0.50$ and $\phi/\pi = 1.50$ for a strong DMI with $D = 0.1$, exhibiting a chiral nature reminiscent of the vortex state observed in the two-dimensional honeycomb lattice.

as a function of ϕ/π, for various values of DMI around the AFK and FK regions. Finite-size effects appear to be negligible within the spin-liquid phases.

In the standard KH ladder with $D = 0$, the plaquette operator reaches a value of 1 at the Kitaev points $\phi = \pm\pi/2$. As the system deviates from these points, $\mathcal{W}$ decreases. For finite DMI ($D > 0$), both the maximum value of $\mathcal{W}$ and the location of this maximum shift, in a manner similar to the energy derivative. Notably, the behavior of $\mathcal{W}$ differs between FM Kitaev and AFM Kitaev interactions: $\mathcal{W}$ shows a broader peak on the FM side, suggesting that the KSL phase is more robust in the FM case than in the AFM case.

For weak DMI ($0 \leq D \leq 0.05$), $\mathcal{W}$ remains close to 1, indicating the persistence of the KSL phase. In contrast, for stronger DMI ($0.05 < D \leq 0.10$), $\mathcal{W}$ decreases to approximately 0.7 in the non-KSL I phase and to 0.85 in the non-KSL II phase. The plaquette operator remains finite in the non-KSL phases, reflecting the gradual evolution of the spin-liquid character from Kitaev-type to non-Kitaev-type with increasing DMI.

Figures 6.4(e) and (f) present the behavior of the string order parameter $\mathcal{O}_{\text{string}}$ around the AFK and FK regions for a two-leg ladder with $N = 2 \times 12$, plotted as a function of ϕ/π for different values of D. For the KH ladder at $D = 0$, the normalized $\mathcal{O}_{\text{string}}$ reaches 1 at both the FM and AFM Kitaev points, and decreases as the system moves away from the KSL region. The behavior of $\mathcal{O}_{\text{string}}$ closely follows that of the plaquette operator.

For finite DMI ($D \neq 0$), the maximum value of $\mathcal{O}_{\text{string}}$ decreases from 1, with a shift in its peak location similar to that observed in $\mathcal{W}$. In the weak DMI regime ($0 \leq D \leq 0.05$), $\mathcal{O}_{\text{string}}$ remains close to 1, whereas in the strong DMI regime ($0.05 < D \leq 0.10$), its maximum value decreases to approximately 0.6 at $D = 0.10$. As with the plaquette operator, $\mathcal{O}_{\text{string}}$ remains finite in the non-KSL phases, reflecting the gradual transition from a Kitaev-type to a non-Kitaev-type spin-liquid state.

In the pure Kitaev model on a honeycomb lattice, the spin correlations exhibit a highly anisotropic and bond-dependent nature, confined to nearest-neighbor sites. The two-spin correlation function $\langle S_i^\alpha S_j^\alpha \rangle$ ($\alpha = x,\, y,\, z$) is nonzero only for spin components matching the bond type (e.g., $\langle S_i^x S_j^x \rangle$ is finite for x-type bonds) and decays rapidly to zero. However, when perturbations such as Heisenberg exchange and DMI are introduced, the nature of spin correlations changes significantly.

The Heisenberg interaction introduces isotropic exchange coupling between spins, favoring non-Kitaev magnetic ordering. In the presence of a finite Heisenberg term, the competition between bond-dependent Kitaev interactions and isotropic exchange results in the emergence of long-range magnetic order, such as zigzag, stripy, FM, and rung singlet phases, depending on the sign and strength of the Heisenberg coupling. This ordering tendency enhances spin correlations beyond nearest neighbors, disrupting the pure KSL state.

The DMI, on the other hand, breaks inversion symmetry and induces nontrivial spin textures. In the presence of both perturbations, the competition between the KSL phase and ordered states leads to rich phase diagrams where the spin correlations evolve from being short-ranged

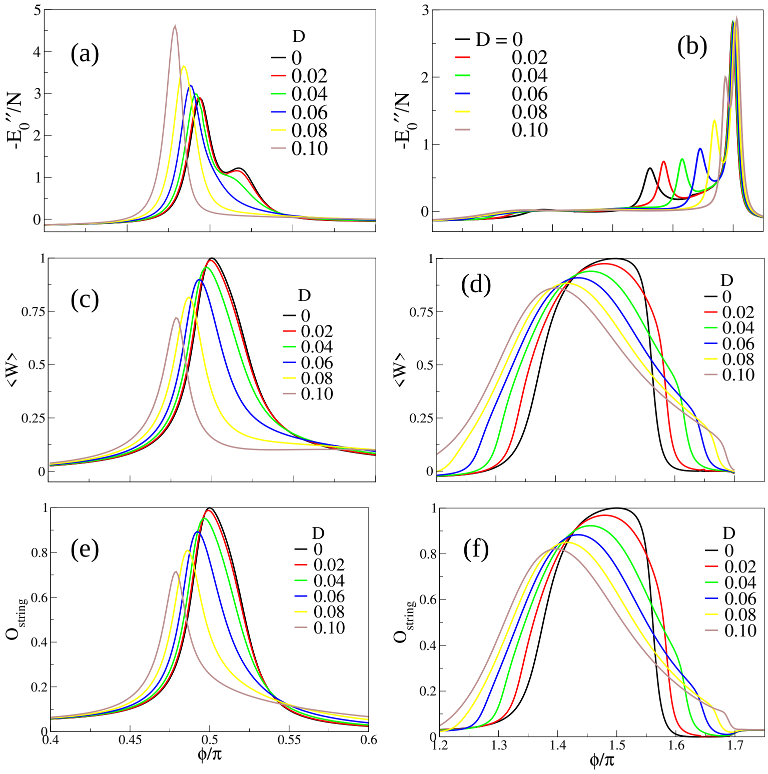

Figure 6.4: ED results for the second-order derivative of the ground-state energy per site, $-E_0''/N$, the plaquette operator, $\mathcal{W}$, and the string order parameter, $\mathcal{O}_{\text{string}}$, on a two-leg ladder as a function of ϕ/π for various values of the DMI (D). Panels (a), (c), and (e) correspond to values around the antiferromagnetic (AFM) Kitaev point, while panels (b), (d), and (f) depict results near the ferromagnetic (FM) Kitaev point.

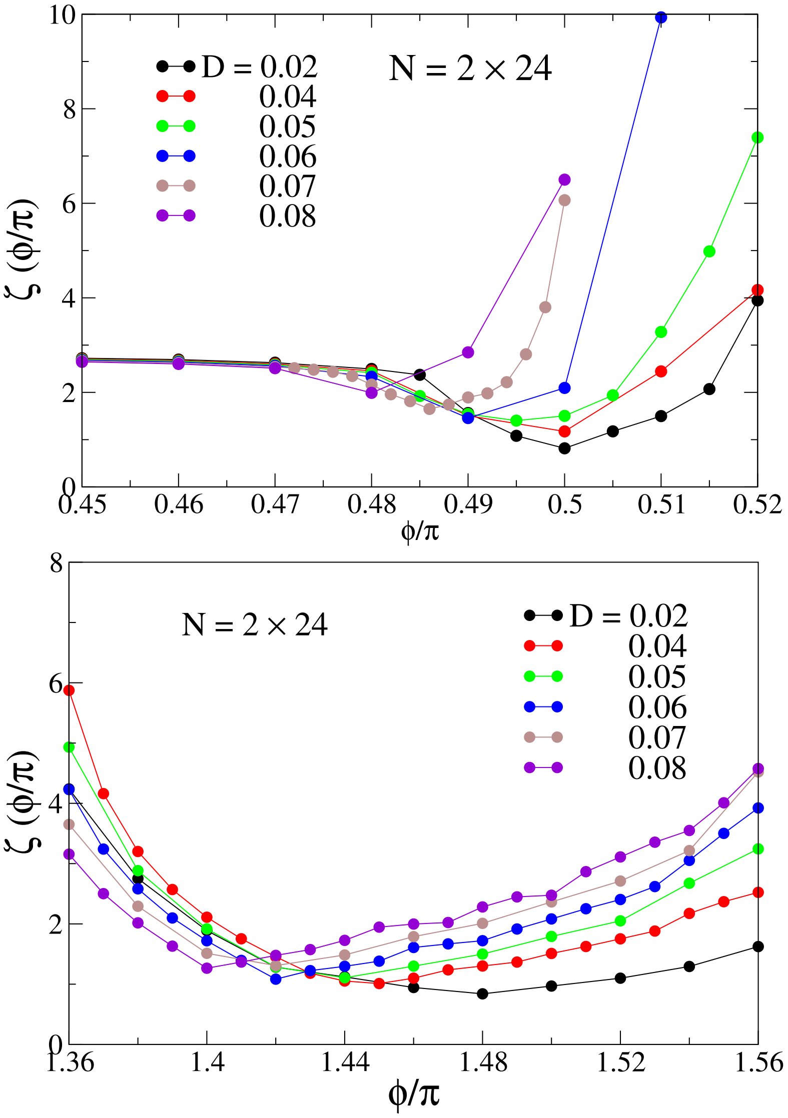

Figure 6.5: Correlation length as a function of ϕ/π for several values of DMI ($D = 0$, 0.02, 0.04, 0.05, 0.06, 0.07, and 0.08) with system size of $N = 2 \times 24$. Top (bottom) panel is corresponding to the ϕ/pi around the AFK (FK) points.

and bond-dependent in the Kitaev limit to more extended and complex patterns depending on the relative strengths of the perturbations.

We have elaborately studied the spin correlations using DMRG in all phases for various values of DMI. Our primary focus is to understand the behavior of the correlations around the KSL phases. For this purpose, we calculated the total correlation, defined as,

$$\begin{aligned} C(r) &= \langle \vec{S}_0 \cdot \vec{S}_r \rangle \\ &= \langle S_0^x S_r^x \rangle + \langle S_0^y S_r^y \rangle + \langle S_0^z S_r^z \rangle \end{aligned} \tag{6.4.4}$$

In the standard KH ladder ($D = 0$), rung singlet (RS) and zigzag (ZZ) phases exist around AFK phase. In the RS phase, spin correlations decay exponentially to zero. In the ZZ phase, spins along each leg exhibit long-range order. Specifically, the S^z component maintains long-range order, whereas the S^x and S^y components decay over short distances.

As we introduce the DMI, the spin correlations are no longer remain finite only for nearest neighbor near the AFK phase. They follow exponential decay with smaller correlation length compared to RS phase. We consider correlation length as a rough indicator for the crossover from KSL to non-KSL phases with increasing DMI. Fig. 6.5(a) shows the correlation length as a function of ϕ/π ($0.45 \leq \phi/\pi \leq 0.52$) for various values of DMI (D) around the AFK point for a ladder of system size $N = 2 \times 24$.

The DMI dependence of correlation length as seen in Fig. 6.5 (a) show that the RS phase is very much robust as the correlation lengths do not change much with increasing DMI. We also notice that the minima of the correlation length shifts to a lower value of ϕ with increasing DMI, which indicates that the liquid phase boundary shifts in presence of DMI.

The correlation length remains nearly constant up to a certain value of $\phi/\pi = 0.47$ in the RS phase at $\xi(\phi/\pi) \sim 2.30$, after which it decreases to a minimum and then begins to increase again. These minima are exactly similar to the maxima of plaquette operator, string order parameter. For weak DMI ($0 \leq D \leq 0.05$), AFK phase still persists with minimum correlation length nearly equals to one unit length ($\xi(\phi/\pi) \sim 1$). But for stronger DMI ($0.05 < D \leq 0.10$), non-KSL I phase appear with minimum correlation length is greater than one unit length ($\xi(\phi/\pi) > 1$).

In the ferromagnetic side near FK phase, spin correlations also follow exponential decay. Fig. 6.5 (b) shows the correlation length as a function of ϕ/π ($1.36 \leq \phi/\pi \leq 1.56$) for various values of DMI (D) around the FK point. Here also, for weak DMI ($0 \leq D \leq 0.05$), the FK phase is dominant with small correlation length ($\xi(\phi/\pi) \sim 1$) and for strong DMI ($0.05 < D \leq 0.10$), a non-KSL II phase appears with large correlation length ($\xi(\phi/\pi) > 1$). We have noticed that correlations decay much faster in the FM side compared to AFM side, suggesting that the liquid phase is more stable for FM Kitaev coupling.

6.5 Chiral spin structure

As the DMI is present, we expect the emergence of chiral spin structures in the system. The chiral vector, v_c, which characterizes spin chirality, is defined as:

$$v_c = \sum_{i=1}^{3} \vec{S}_{2i-1} \times \vec{S}_{2i+1} = \sum_{i=1}^{3} \vec{S}_{2i} \times \vec{S}_{2i+2}, \tag{6.5.1}$$

where the index i is defined as shown in the inset of Fig. 6.6. Since the DMI acts on second-nearest-neighbor bonds, the resulting chirality is confined to the triangular plaquettes influenced by the DMI. The chiral vector v_c serves as an indicator of vortex-like states in the honeycomb lattice. However, in the case of the two-leg ladder, the reduced dimensionality hinders the formation of vortex states.

Nevertheless, we find a finite value of $|\hat{n} \cdot v_c|$ over a range of ϕ around AFK and FK phases, indicating that the DMI induces a chiral ordering within the liquid phase. We present the plaquette averaged $|\hat{n} \cdot v_c|$, where the unit vector $\hat{n}$ is defined as $\hat{n} = (\hat{x} + \hat{y} + \hat{z})/\sqrt{3}$.

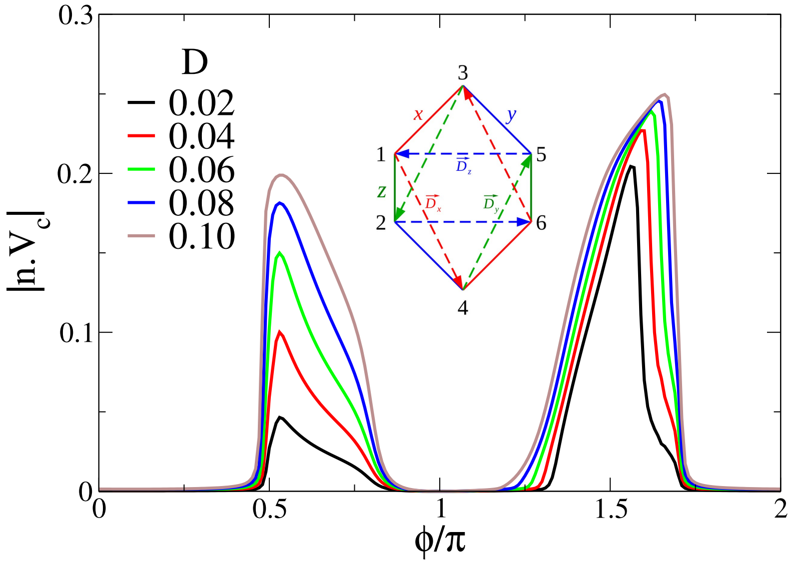

Figure 6.6: Vector chirality $|\hat{n} \cdot v_c|$, where $\hat{n} = (\hat{x} + \hat{y} + \hat{z})/\sqrt{3}$, as a function of ϕ/π for various values of the Dzyaloshinskii-Moriya interaction (DMI) in a system of size $N = 2 \times 12$. The vector chirality is computed for each plaquette and averaged over all plaquettes. A finite value is observed over a broad range of ϕ/π around the antiferromagnetic Kitaev (AFK) and ferromagnetic Kitaev (FK) phases. As the DMI strength increases, the order parameter also increases, indicating the stabilization of magnetic ordering, such as vortex-like states.

Figure 6.6 shows the vector chirality as a function of ϕ for different values of DMI with a ladder of system size $N = 2 \times 12$. The finite size effect is negligible in this case. In the absence of DMI ($D = 0$), the order parameter vanishes, whereas for finite DMI ($D \neq 0$), the order parameter $|\hat{n} \cdot v_c|$ increases with increasing DMI.

For weak DMI ($0 < D \leq 0.05$), although the vector chirality remains finite, the competition between Kitaev and DMI interactions leads to a Kitaev-dominated regime, suggesting a persistence of the liquid phase. For strong DMI ($D > 0.05$), though the DMI dominates, zigzag phase persists for moderate DMI ($0.05 < D \leq 0.08$)in the AFM Kitaev regime.

We define the following order parameter to analyze the instability of zigzag ordering:

$$\begin{aligned} \mathcal{O}_{zigzag}(N) &= \frac{1}{2}\Big(|\langle S^z_{L/2,1}\rangle + \langle S^z_{L/2+1,1}\rangle \\ &- \langle S^z_{L/2,2}\rangle - \langle S^z_{L/2+1,2}\rangle|\Big) \qquad (6.5.2) \\ \mathcal{O}_{zigzag} &= \lim_{L\to\infty} \mathcal{O}_{zigzag}(L) \qquad (6.5.3) \end{aligned}$$

The zigzag order parameter is shown in Fig. 6.7. The zigzag order parameter ($\mathcal{O}_{zigzag}$) remains finite ($\simeq 0.70$) in presence of DMI throughout most of the phase and approaches zero near the AFK-zigzag and zigzag-FM for weak DMI and non-KSL I-zigzag and zigzag-FM for strong DMI. In contrast, on the FM Kitaev side, spiral phase emerges with spiral like spin correlations.

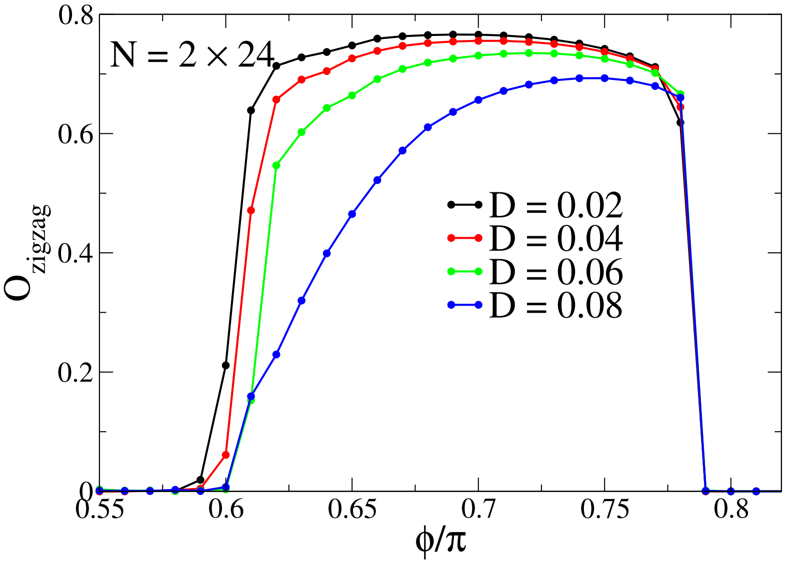

Figure 6.7: Zigzag order parameter as a function of ϕ/π for various DMI with a system size of $N = 2 \times 24$.

We compute the spin components by pinning field at $\phi = \pm\pi/2$ for very strong DMI ($D = 0.10$) and we found that in both AFM and FM Kitaev side, the spin configurations show chiral ordering as shown in Figures 6.3 (e) and (f).

6.6 Results for 2D honeycomb lattice

The gs phase diagram of the KH model on a honeycomb-lattice in absence of DMI ($D = 0$) has been extensively studied, revealing four magnetic long-range ordered phases Néel, ZZ, ST, and FM and two QSL phases; AFK and FK phases by tuning the Heisenberg and Kitaev interactions [48, 145, 278, 280, 347, 395].

In presence of DMI ($D \neq 0$), the results for the 2D honeycomb lattice differ from the two-leg ladder in many ways. In order to understand the phases we computed static spin structure factor $S(k)$, which reflects spin correlations at wave vector Q across the cluster:

$$S(k) = \frac{1}{N}\sum_{ij}\langle \vec{S}_i \cdot \vec{S}_j \rangle e^{ik\cdot(\mathbf{r}_i - \mathbf{r}_j)} \tag{6.6.1}$$

where N is the total number of lattice sites and r_i denotes the position of site i. By examining the behavior of $S(k)$, we can determine the nature of spin ordering within the various phases.

We begin by focusing on the AFK and FK phases. Fig. 6.8 shows the structure factor for various DM interaction ($D = 0$, 0.02, 0.05, and 0.10) at $\phi/\pi = 0.50$ and 1.50. For weak DMI ($D = 0, 0.02$), we notice that the liquid-like behavior still persists, as evidenced by the Bragg peaks spreading around the K-points in the AFK phase and near the Γ-point in the FM phase. However, for relatively strong DMI ($D = 0.05, 0.10$), the liquid-like phase disappears, and a new phase emerges, where prominent Bragg peaks appear at the K-point, suggesting a phase resembling a vortex phase.

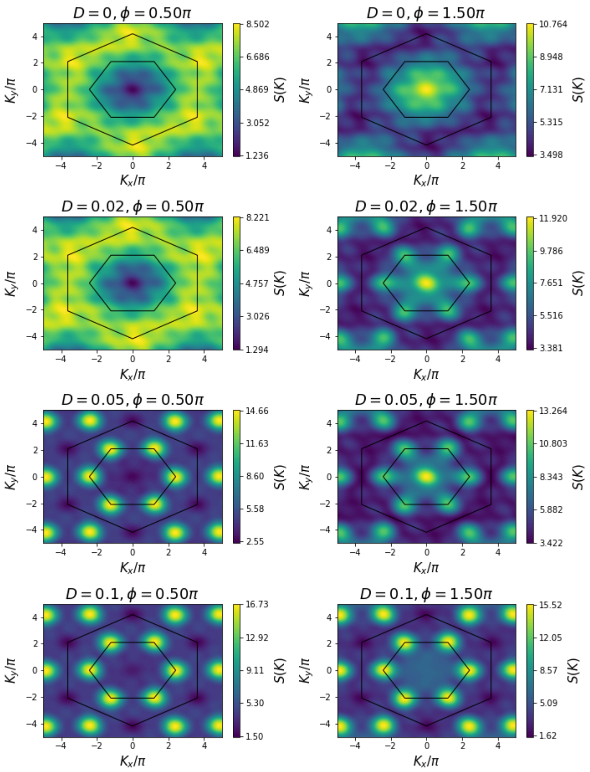

Figure 6.8: Static structure factor ($S(k)$) [Eq. (6.6.1)] computed from ED for 2D-honeycomb lattice with $N = 24$ periodic boundary condition. For weak DMI ($D = 0, 0.02$), we notice that the liquid-like behavior persists, as evidenced by the Bragg peaks spreading around the K-points in the AFK phase and near the Γ-point in the FM phase, while for strong DMI ($0.02 < D \leq 0.10$), the liquid-like phase disappears, and a new phase emerges, where prominent Bragg peaks appear at the K-point, suggesting a phase resembling a vortex phase.

To understand further we computed spin density by a pinning field in the xy-plane and it is found to be a vortex state. However, the vortex state is different for AFM Kitaev than FM Kitaev exchange. More details about the vortex state such as symmetry, topology are yet to be discovered. Using the structure factor, we construct phase diagrams for the 2D honeycomb lattice. Fig. 6.9 presents the phase diagrams for three representative cases: zero DMI ($D = 0$), weak DMI ($D = 0.02$), and, strong DMI ($D = 0.1$). This difference between the ladder and honeycomb systems arises from the effects of low dimensionality.

6.7 Conclusion

In this work, we investigate the ground-state properties of the KH model in the presence of DMI on both a two-leg ladder and a honeycomb lattice. The competition between Kitaev, Heisenberg, and DM interactions plays a crucial role in determining the stability of the underlying quantum phases. Our primary focus is to understand how DMI influences the stability of the KSL phase and facilitates the emergence of novel quantum phases.

The computed phase diagrams reveal two distinct regimes: a weak-DMI region where the KSL phase is robust, and a strong-DMI region where the system transitions into other magnetic

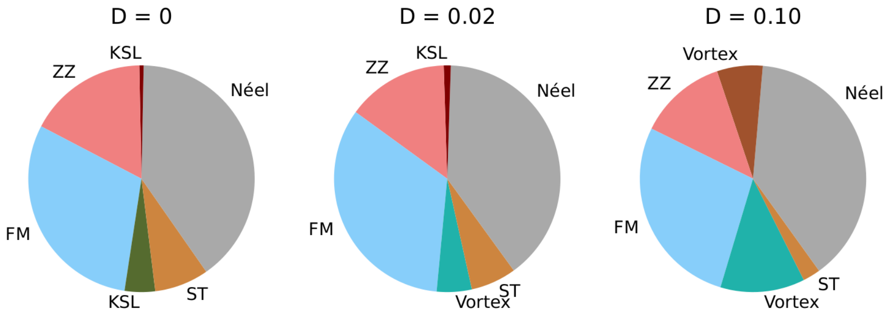

Figure 6.9: Phase diagram for 2D honeycomb lattice for three representative cases: zero DMI ($D = 0$), weak DMI ($D = 0.02$), and, strong DMI ($D = 0.1$).

phases, including non-Kitaev spin-liquid on two-leg ladder and vortex phases on a honeycomb lattice.

For the two-leg ladder, we calculate several physical quantities—including the energy derivative, plaquette operator, string order parameter, spin correlations, and vector chirality—to map out the phase diagram. In the weak DMI regime ($0 < D \leq 0.05$), the KSL phase remains stable with only a minor shift in phase boundaries. In contrast, for stronger DMI ($0.05 < D \leq 0.1$), the KSL phase becomes unstable, giving way to a non-KSL (conventional SL) phase characterized by exponentially decaying spin correlations. Notably, the vector chirality remains finite for all values of D, indicating that chiral order coexists with the KSL phase.

Additionally, in the AFM Kitaev regime, a zigzag phase persists for relatively strong DMI ($0.05 < D \leq 0.08$), whereas in the FM Kitaev regime, a spiral phase emerges, exhibiting spiral-like spin correlations.

On the honeycomb lattice, the system exhibits behavior similar to that of the ladder in the weak DMI regime. However, in the strong DMI regime, the disordered phase transitions into a vortex phase rather than a non-KSL phase, emphasizing the importance of dimensionality and connectivity in governing quantum phase stability. However, for very strong DMI the ladder shows chiral spin configurations which is analogous to vortex structure in honeycomb lattice.

In summary, our study provides valuable insights into the interplay between Kitaev and Dzyaloshinskii-Moriya interactions. We demonstrate how DMI modifies quantum spin-liquid behavior and stabilizes chiral magnetic orders. These findings may have implications for experimental realizations of Kitaev materials and the exploration of topological quantum phases in spin-orbit-coupled magnetic systems.

Chapter 7

Conclusion

In this chapter, we provide a brief summary and concluding remarks on all the problems discussed so far.

Quantum magnetism is a vast and worth of exploring field. In particular, magnetic frustration opens the door to new possible exotic phases of matter, like spin liquids, spin ices, and nematic phases. Much of what lies behind that door is yet to be completely understood. In this thesis, we focused on a special class of frustrated spin systems in one (1D) and quasi-one-dimensions (quasi 1D). Though real, effectively 1D or quasi 1D materials are not so common, there exist different classes of materials where an effective 1D or quasi 1D spin Hamiltonian is enough to capture the experimental feature, such as magnetization, specific heat, susceptibility and inelastic neutron scattering spectra, thus motivating our theoretical investigation. We have presented possible realisations of such systems exhibiting geometric frustration in chapter 1.

This thesis is devoted to study the frustrated spin models and its ground state and excited state properties. Such many-body systems are hard to solve due to large degrees of freedom in the system. Therefore, numerical studies are the main tool for investigating these models. We employed exact diagonalization (ED) and density matrix renormalization group (DMRG) techniques to study these models.

The first problem addressed in this thesis deals with the spin-Peierls (SP) instability in the ferromagnetic $J_1 - J_2$ model and its extended model. We find that for $\alpha = J_2/|J_1| > 0.65$, the system exhibits sublattice dimerization with four spins per unit cell, whereas for smaller α, conventional chain dimerization with two spins per unit cell emerges. Using ED and DMRG techniques, we study the low-temperature thermodynamics and validate the approach through comparisons with existing numerical results. Our analysis indicates that while the $J_1 - J_2$ model qualitatively describes the magnetic susceptibility $\chi(T)$ and specific heat $C(T)$ of β-TeVO$_4$. A gapped model with exchange asymmetry (γ) is necessary to explain the low-temperature behavior.

The next problem deals with quasi-1D coupled trimer model with three spins per unit cell. The competition between intra-trimer (J_1) and inter-trimer (J_1') couplings leads to frustration and distinct magnetic phases. By analyzing excitation gaps, spin correlations, and bond-bond correlations, we construct a quantum phase diagram in the $J_1'/J_1 - J_2/J_1$ space, identifying spin fluid, trimer, spiral, and gapped dimer phases. Notably, we find a first-order transition between the trimer and dimer phases, marked by a shift in bond-bond correlation divergences.

The findings presented in this thesis provide new insights into the role of frustration and exchange asymmetry in low-dimensional quantum magnets, contributing to the broader understanding of quasi-1D materials with competing interactions.

The next two problems focus on exchange frustration, arises from Kitaev model which hosts quantum spin liquid (QSLs) with complex entangled states such as fractional excitations such as spinons and Majorana fermions. The physical realization of this model in a real material has been challenging. However, the magnetic properties of a wide range of iridium- and ruthenium-based materials can provide a more realistic description of the Kitaev-Heisenberg (KH) model, incorporating residual nearest-neighbor Heisenberg interactions.

The ground state phase diagram of the honeycomb lattice KH model has been extensively studied, revealing four magnetic long-range ordered (LRO) phases (Néel, zigzag, stripy, and ferromagnetic) and two Kitaev spin liquid (KSL) phases (ferromagnetic and antiferromagnetic Kitaev) by tuning the Heisenberg and Kitaev interactions. However, the potential for a quantum phase involving higher spin states, such as a quadrupolar (QP) or nematic state, in the KH model remains largely unexplored. Given this scenario, the question arises whether there is QP order in a pure Kitaev-Heisenberg model on a spin-1/2 ladder and honeycomb lattice.

In our study, we examined the properties of the quadrupolar phase in this model on two geometries: the two-legged ladder and the two-dimensional honeycomb lattice, using ED and DMRG methods. Our analysis revealed a comprehensive ground-state phase diagram, showing the stability of quadrupolar order over a wide range of the phase diagram, particularly near the Kitaev spin liquid phases. This enhancement is particularly intriguing as it occurs in the absence of long-range spin-spin correlations, suggesting a nuanced relationship between QP order and QSLs. In fact, a positive third-order susceptibility, which is indicative of a general signature of QP order, has been observed in the vicinity of the FK QSL phase in α-RuCl$_3$. These insights not only advance our understanding of the KH model but also contribute significantly to the broader discourse on quantum magnetism in low-dimensional systems, highlighting the intricate interplay between different types of quantum order.

The last problem incorporates the Dzyaloshinskii-Moriya interaction (DMI) into the KH model (KH-DMI model), we analyzed its impact on the stability of the QSL phase and the emergence of chiral magnetic orders. Our results reveal that weak DMI ($0 < D \leq 0.05$) modifies phase boundaries while preserving the QSL phase, whereas stronger DMI ($D > 0.05$) destabilizes it, leading to new magnetic phases such as the conventional spin liquid (SL) in two-leg ladder and vortex states in honeycomb lattice.

Our findings highlight the crucial role of interaction competition in governing quantum phase stability and suggest that chiral and topological orders in Kitaev-like materials may be experimentally accessible. By providing a comprehensive phase diagram and uncovering the interplay between QSL and chiral magnetic orders, this study advances our understanding of low-dimensional quantum magnetism and its implications for future quantum materials research.

Bibliography

[1] I. Affleck. Exact correlation amplitude for the s= 1/2 heisenberg antiferromagnetic chain. *arXiv preprint cond-mat/9802045*, 1998.

[2] I. Affleck, D. Gepner, H. Schulz, and T. Ziman. Critical behaviour of spin-s heisenberg antiferromagnetic chains: analytic and numerical results. *Journal of Physics A: Mathematical and General*, 22(5):511, 1989.

[3] I. Affleck, D. Gepner, H. J. Schulz, and T. Ziman. Critical behaviour of spin-s heisenberg antiferromagnetic chains: analytic and numerical results. *Journal of Physics A: Mathematical and General*, 22(5):511, mar 1989. doi:10.1088/0305-4470/22/5/015. URL `https://dx.doi.org/10.1088/0305-4470/22/5/015`.

[4] C. E. Agrapidis, S.-L. Drechsler, J. van den Brink, and S. Nishimoto. Crossover from an incommensurate singlet spiral state with a vanishingly small spin gap to a valence-bond solid state in dimerized frustrated ferromagnetic spin chains. *Phys. Rev. B*, 95: 220404, Jun 2017. doi:10.1103/PhysRevB.95.220404. URL `https://link.aps.org/doi/10.1103/PhysRevB.95.220404`.

[5] C. E. Agrapidis, J. van den Brink, and S. Nishimoto. Ordered states in the kitaev-heisenberg model: From 1d chains to 2d honeycomb. *Scientific Reports*, 8(1):1815, 2018.

[6] C. E. Agrapidis, J. van den Brink, and S. Nishimoto. Ground state and low-energy excitations of the kitaev-heisenberg two-leg ladder. *Phys. Rev. B*, 99:224418, Jun 2019. doi:10.1103/PhysRevB.99.224418. URL `https://link.aps.org/doi/10.1103/PhysRevB.99.224418`.

[7] Y. Ajiro, T. Asano, T. Inami, H. Aruga-Katori, and T. Goto. High-field magnetization of one-dimensional s=1/2 trimer system 3cucl2·2dioxane. *Journal of the Physical Society of Japan*, 63(3):859–862, 1994. doi:10.1143/JPSJ.63.859. URL `https://doi.org/10.1143/JPSJ.63.859`.

[8] G. P. Alexander, B. G.-g. Chen, E. A. Matsumoto, and R. D. Kamien. Colloquium: Disclination loops, point defects, and all that in nematic liquid crystals. *Rev. Mod. Phys.*, 84:497–514, Apr 2012. doi:10.1103/RevModPhys.84.497. URL `https://link.aps.org/doi/10.1103/RevModPhys.84.497`.

[9] D. Allen and D. Sénéchal. Non-abelian bosonization of the frustrated antiferromagnetic spin-1/2 chain. *Physical Review B*, 55(1):299, 1997. doi:10.1103/PhysRevB.55.299. URL `https://link.aps.org/doi/10.1103/PhysRevB.55.299`.

[10] G. Ananthakrishna. Antiferromagnetic spin-wave states in a linear chain with nearest-and next-nearest-neighbour interactions. *Journal of Physics C: Solid State Physics*, 8(5):717, 1975.

[11] G. Ananthakrishna, L. Weiss, D. Foyt, and D. Klein. Properties of the linear heisenberg chain with nearest and next-nearest neighbor interactions. *Physica B+ C*, 81(2):275–284, 1976.

[12] P. W. Anderson. New approach to the theory of superexchange interactions. *Phys. Rev.*, 115:2–13, Jul 1959. doi:10.1103/PhysRev.115.2. URL `https://link.aps.org/doi/10.1103/PhysRev.115.2`.

[13] P. W. Anderson. New approach to the theory of superexchange interactions. *Phys. Rev.*, 115:2–13, Jul 1959. doi:10.1103/PhysRev.115.2. URL `https://link.aps.org/doi/10.1103/PhysRev.115.2`.

[14] P. W. Anderson. Theory of magnetic exchange interactions:exchange in insulators and semiconductors. volume 14 of *Solid State Physics*, pages 99–214. Academic Press, 1963. doi:https://doi.org/10.1016/S0081-1947(08)60260-X. URL `https://www.sciencedirect.com/science/article/pii/S008119470860260X`.

[15] P. W. Anderson. Resonating valence bonds: A new kind of insulator? *Materials Research Bulletin*, 8(2):153–160, Feb 1973. ISSN 0025-5408. URL `https://www.sciencedirect.com/science/article/pii/0025540873901670`.

[16] N. Astrakhantsev, T. Westerhout, A. Tiwari, K. Choo, A. Chen, M. H. Fischer, G. Carleo, and T. Neupert. Broken-symmetry ground states of the heisenberg model on the pyrochlore lattice. *Phys. Rev. X*, 11:041021, Oct 2021. doi:10.1103/PhysRevX.11.041021. URL `https://link.aps.org/doi/10.1103/PhysRevX.11.041021`.

[17] H. P. Bader and R. Schilling. Conditions for a ferromagnetic ground state of heisenberg hamiltonians. *Phys. Rev. B*, 19:3556–3560, Apr 1979. doi:10.1103/PhysRevB.19.3556. URL `https://link.aps.org/doi/10.1103/PhysRevB.19.3556`.

[18] L. Balents. Spin liquids in frustrated magnets. *Nature*, 464(7286):199–208, Mar 2010. ISSN 1476-4687. doi:10.1038/nature08917. URL `https://doi.org/10.1038/nature08917`.

[19] S. Bandyopadhyay, F. L. Buessen, R. Das, F. G. Utermohlen, N. Trivedi, A. Paramekanti, and I. Dasgupta. Exchange interactions and spin dynamics in the layered honeycomb ferromagnet cri$_3$. *Phys. Rev. B*, 105:184430, May 2022. doi:10.1103/PhysRevB.105.184430. URL `https://link.aps.org/doi/10.1103/PhysRevB.105.184430`.

[20] A. Banerjee, J. Yan, J. Knolle, C. A. Bridges, M. B. Stone, M. D. Lumsden, D. G. Mandrus, D. A. Tennant, R. Moessner, and S. E. Nagler. Neutron scattering in

the proximate quantum spin liquid α-rucl3. *Science*, 356(6342):1055–1059, 2017. doi:10.1126/science.aah6015. URL `https://doi.org/10.1126/science.aah6015`.

[21] T. Barthel, U. Schollwöck, and S. R. White. Spectral functions in one-dimensional quantum systems at finite temperature using the density matrix renormalization group. *Phys. Rev. B*, 79:245101, Jun 2009. doi:10.1103/PhysRevB.79.245101. URL `https://link.aps.org/doi/10.1103/PhysRevB.79.245101`.

[22] G. Baskaran. Metastable kitaev spin liquids in isotropic quantum heisenberg magnets. *arXiv preprint arXiv:2309.07119*, 2023.

[23] G. Baskaran, S. Mandal, and R. Shankar. Exact results for spin dynamics and fractionalization in the kitaev model. *Phys. Rev. Lett.*, 98:247201, Jun 2007. doi:10.1103/PhysRevLett.98.247201. URL `https://link.aps.org/doi/10.1103/PhysRevLett.98.247201`.

[24] G. Baskaran, S. Mandal, and R. Shankar. Exact results for spin dynamics and fractionalization in the kitaev model. *Phys. Rev. Lett.*, 98:247201, Jun 2007. doi:10.1103/PhysRevLett.98.247201. URL `https://link.aps.org/doi/10.1103/PhysRevLett.98.247201`.

[25] G. Baskaran, D. Sen, and R. Shankar. Spin-s kitaev model: Classical ground states, order from disorder, and exact correlation functions. *Phys. Rev. B*, 78:115116, Sep 2008. doi:10.1103/PhysRevB.78.115116. URL `https://link.aps.org/doi/10.1103/PhysRevB.78.115116`.

[26] J. G. Bednorz and K. A. Müller. Possible hightc superconductivity in the balacuo system. *Zeitschrift für Physik B Condensed Matter*, 64(2):189–193, Jun 1986. ISSN 1431-584X. doi:10.1007/BF01303701. URL `https://doi.org/10.1007/BF01303701`.

[27] A. K. Bera, S. Yusuf, S. K. Saha, M. Kumar, D. Voneshen, Y. Skourski, and S. A. Zvyagin. Emergent many-body composite excitations of interacting spin-1/2 trimers. *Nature Communications*, 13(1):6888, 2022. URL `https://doi.org/10.1038/s41467-022-34342-1`.

[28] B. Bernu, P. Lecheminant, C. Lhuillier, and L. Pierre. Exact spectra, spin susceptibilities, and order parameter of the quantum heisenberg antiferromagnet on the triangular lattice. *Phys. Rev. B*, 50:10048–10062, Oct 1994. doi:10.1103/PhysRevB.50.10048. URL `https://link.aps.org/doi/10.1103/PhysRevB.50.10048`.

[29] H. Bethe. Zur theorie der metalle. *Zeitschrift für Physik*, 71(3):205–226, Mar 1931. doi:10.1007/BF01341708. URL `https://doi.org/10.1007/BF01341708`.

[30] H. Bethe. On the theory of metals, i. eigenvalues and eigenfunctions of a linear chain of atoms. In *Selected Works Of Hans A Bethe: (With Commentary)*, pages 155–183. World Scientific, 1997.

[31] R. F. Bishop, P. H. Y. Li, O. Götze, J. Richter, and C. E. Campbell. Frustrated heisenberg antiferromagnet on the honeycomb lattice: Spin gap and low-energy parameters. *Phys. Rev. B*, 92:224434, Dec 2015. doi:10.1103/PhysRevB.92.224434. URL `https://link.aps.org/doi/10.1103/PhysRevB.92.224434`.

[32] M. Blume and Y. Hsieh. Biquadratic exchange and quadrupolar ordering. *Journal of Applied Physics*, 40(3):1249–1249, 1969. URL `https://doi.org/10.1063/1.1657616`.

[33] J. C. Bonner and M. E. Fisher. Linear magnetic chains with anisotropic coupling. *Physical Review*, 135(3A):A640, 1964.

[34] G. Bouzerar, A. P. Kampf, and G. I. Japaridze. Elementary excitations in dimerized and frustrated heisenberg chains. *Phys. Rev. B*, 58:3117–3123, Aug 1998. doi:10.1103/PhysRevB.58.3117. URL `https://link.aps.org/doi/10.1103/PhysRevB.58.3117`.

[35] J. W. Bray, H. R. Hart, L. V. Interrante, I. S. Jacobs, J. S. Kasper, G. D. Watkins, S. H. Wee, and J. C. Bonner. Observation of a spin-peierls transition in a heisenberg antiferromagnetic linear-chain system. *Phys. Rev. Lett.*, 35:744–747, Sep 1975. doi:10.1103/PhysRevLett.35.744. URL `https://link.aps.org/doi/10.1103/PhysRevLett.35.744`.

[36] J. W. Bray, L. V. Interrante, I. S. Jacobs, and J. C. Bonner. *The Spin-Peierls Transition*, pages 353–415. Springer US, Boston, MA, 1983. ISBN 978-1-4684-4175-8. doi:10.1007/978-1-4684-4175-8_7. URL `https://doi.org/10.1007/978-1-4684-4175-8_7`.

[37] C. Broholm, R. J. Cava, S. A. Kivelson, D. G. Nocera, M. R. Norman, and T. Senthil. Quantum spin liquids. *Science*, 367(6475):eaay0668, 2020. doi:10.1126/science.aay0668. URL `https://www.science.org/doi/abs/10.1126/science.aay0668`.

[38] R. Bursill, G. A. Gehring, D. J. J. Farnell, J. B. Parkinson, T. Xiang, and C. Zeng. Numerical and approximate analytical results for the frustrated spin- 1/2 quantum spin chain. *Journal of Physics: Condensed Matter*, 7(45):8605, nov 1995. doi:10.1088/0953-8984/7/45/016. URL `https://dx.doi.org/10.1088/0953-8984/7/45/016`.

[39] R. J. Bursill, T. Xiang, and G. A. Gehring. The density matrix renormalization group for a quantum spin chain at non-zero temperature. *Journal of Physics: Condensed Matter*, 8(40):L583, sep 1996. doi:10.1088/0953-8984/8/40/003. URL `https://dx.doi.org/10.1088/0953-8984/8/40/003`.

[40] H. B. Cao, A. Banerjee, J.-Q. Yan, C. A. Bridges, M. D. Lumsden, D. G. Mandrus, D. A. Tennant, B. C. Chakoumakos, and S. E. Nagler. Low-temperature crystal and magnetic structure of $\alpha-\mathrm{rucl}_3$. *Phys. Rev. B*, 93:134423, Apr

2016. doi:10.1103/PhysRevB.93.134423. URL https://link.aps.org/doi/10.1103/PhysRevB.93.134423.

[41] L. Capriotti, A. E. Trumper, and S. Sorella. Long-range néel order in the triangular heisenberg model. *Phys. Rev. Lett.*, 82:3899–3902, May 1999. doi:10.1103/PhysRevLett.82.3899. URL https://link.aps.org/doi/10.1103/PhysRevLett.82.3899.

[42] J. Carrasquilla, S. R. Manmana, and M. Rigol. Scaling of the gap, fidelity susceptibility, and bloch oscillations across the superfluid-to-mott-insulator transition in the one-dimensional bose-hubbard model. *Phys. Rev. A*, 87:043606, Apr 2013. doi:10.1103/PhysRevA.87.043606. URL https://link.aps.org/doi/10.1103/PhysRevA.87.043606.

[43] G. Catarina and B. Murta. Density-matrix renormalization group: a pedagogical introduction. *The European Physical Journal B*, 96(8):111, Aug 2023. doi:10.1140/epjb/s10051-023-00575-2. URL https://doi.org/10.1140/epjb/s10051-023-00575-2.

[44] A. Catuneanu, E. S. Sørensen, and H.-Y. Kee. Nonlocal string order parameter in the $s = \frac{1}{2}$ kitaev-heisenberg ladder. *Phys. Rev. B*, 99:195112, May 2019. doi:10.1103/PhysRevB.99.195112. URL https://link.aps.org/doi/10.1103/PhysRevB.99.195112.

[45] D. Ceperley, G. V. Chester, and M. H. Kalos. Monte carlo simulation of a many-fermion study. *Phys. Rev. B*, 16:3081–3099, Oct 1977. doi:10.1103/PhysRevB.16.3081. URL https://link.aps.org/doi/10.1103/PhysRevB.16.3081.

[46] T. Chakrabarty, A. V. Mahajan, A. A. Gippius, A. V. Tkachev, N. Büttgen, and W. Kraetschmer. Bav$_3$o$_8$: A possible majumdar-ghosh system with $s = \frac{1}{2}$. *Phys. Rev. B*, 88:014433, Jul 2013. doi:10.1103/PhysRevB.88.014433. URL https://link.aps.org/doi/10.1103/PhysRevB.88.014433.

[47] J. c. v. Chaloupka, G. Jackeli, and G. Khaliullin. Kitaev-heisenberg model on a honeycomb lattice: Possible exotic phases in iridium oxides A_2iro$_3$. *Phys. Rev. Lett.*, 105:027204, Jul 2010. doi:10.1103/PhysRevLett.105.027204. URL https://link.aps.org/doi/10.1103/PhysRevLett.105.027204.

[48] J. c. v. Chaloupka, G. Jackeli, and G. Khaliullin. Kitaev-heisenberg model on a honeycomb lattice: Possible exotic phases in iridium oxides A_2iro$_3$. *Phys. Rev. Lett.*, 105:027204, Jul 2010. doi:10.1103/PhysRevLett.105.027204. URL https://link.aps.org/doi/10.1103/PhysRevLett.105.027204.

[49] J. c. v. Chaloupka, G. Jackeli, and G. Khaliullin. Zigzag magnetic order in the iridium oxide na$_2$iro$_3$. *Phys. Rev. Lett.*, 110:097204, Feb 2013. doi:10.1103/PhysRevLett.110.097204. URL https://link.aps.org/doi/10.1103/PhysRevLett.110.097204.

[50] V. R. Chandra and J. Sahoo. Spin-$\frac{1}{2}$ heisenberg antiferromagnet on the pyrochlore lattice: An exact diagonalization study. *Phys. Rev. B*, 97:144407, Apr 2018. doi:10.1103/PhysRevB.97.144407. URL `https://link.aps.org/doi/10.1103/PhysRevB.97.144407`.

[51] H.-D. Chen and Z. Nussinov. Exact results of the kitaev model on a hexagonal lattice: spin states, string and brane correlators, and anyonic excitations. *Journal of Physics A: Mathematical and Theoretical*, 41(7):075001, feb 2008. doi:10.1088/1751-8113/41/7/075001. URL `https://dx.doi.org/10.1088/1751-8113/41/7/075001`.

[52] L. Chen, J.-H. Chung, T. Chen, C. Duan, A. Schneidewind, I. Radelytskyi, D. J. Voneshen, R. A. Ewings, M. B. Stone, A. I. Kolesnikov, B. Winn, S. Chi, R. A. Mole, D. H. Yu, B. Gao, and P. Dai. Magnetic anisotropy in ferromagnetic cri$_3$. *Phys. Rev. B*, 101:134418, Apr 2020. doi:10.1103/PhysRevB.101.134418. URL `https://link.aps.org/doi/10.1103/PhysRevB.101.134418`.

[53] J.-Q. Cheng, J. Li, Z. Xiong, H.-Q. Wu, A. W. Sandvik, and D.-X. Yao. Fractional and composite excitations of antiferromagnetic quantum spin trimer chains. *npj Quantum Materials*, 7(1):3, 2022. URL `https://doi.org/10.1038/s41535-021-00416-4`.

[54] J.-Q. Cheng, Z.-Y. Ning, H.-Q. Wu, and D.-X. Yao. Quantum phase transition and composite excitations of antiferromagnetic spin trimer chains in a magnetic field. *npj Quantum Materials*, 9(1):96, Nov 2024. ISSN 2397-4648. doi:10.1038/s41535-024-00705-8. URL `https://doi.org/10.1038/s41535-024-00705-8`.

[55] R. Chitra, S. Pati, H. Krishnamurthy, D. Sen, and S. Ramasesha. Density-matrix renormalization-group studies of the spin-1/2 heisenberg system with dimerization and frustration. *Physical Review B*, 52(9):6581, 1995. doi:10.1103/PhysRevB.52.6581. URL `https://link.aps.org/doi/10.1103/PhysRevB.52.6581`.

[56] S. K. Choi, R. Coldea, A. N. Kolmogorov, T. Lancaster, I. I. Mazin, S. J. Blundell, P. G. Radaelli, Y. Singh, P. Gegenwart, K. R. Choi, S.-W. Cheong, P. J. Baker, C. Stock, and J. Taylor. Spin waves and revised crystal structure of honeycomb iridate na$_2$iro$_3$. *Phys. Rev. Lett.*, 108:127204, Mar 2012. doi:10.1103/PhysRevLett.108.127204. URL `https://link.aps.org/doi/10.1103/PhysRevLett.108.127204`.

[57] A. V. Chubukov. Chiral, nematic, and dimer states in quantum spin chains. *Physical Review B*, 44(9):4693, 1991. doi:10.1103/PhysRevB.44.4693. URL `https://link.aps.org/doi/10.1103/PhysRevB.44.4693`.

[58] A. V. Chubukov, S. Sachdev, and T. Senthil. Large-s expansion for quantum antiferromagnets on a triangular lattice. *Journal of Physics: Condensed Matter*, 6(42):8891, oct 1994. doi:10.1088/0953-8984/6/42/019. URL `https://dx.doi.org/10.1088/0953-8984/6/42/019`.

[59] M. C. Cross. Effect of magnetic fields on a spin-peierls transition. *Phys. Rev. B*, 20:4606–4611, Dec 1979. doi:10.1103/PhysRevB.20.4606. URL `https://link.aps.org/doi/10.1103/PhysRevB.20.4606`.

[60] M. C. Cross and D. S. Fisher. A new theory of the spin-peierls transition with special relevance to the experiments on ttfcubdt. *Phys. Rev. B*, 19:402–419, Jan 1979. doi:10.1103/PhysRevB.19.402. URL `https://link.aps.org/doi/10.1103/PhysRevB.19.402`.

[61] E. Dagotto and A. Moreo. Zero-temperature properties of the two-dimensional heisenberg antiferromagnet: A numerical study. *Physical Review B*, 38(7):5087, 1988.

[62] E. Dagotto and T. Rice. Surprises on the way from one-to two-dimensional quantum magnets: The ladder materials. *Science*, 271(5249):618–623, 1996.

[63] E. Dagotto, J. Riera, and D. Scalapino. Superconductivity in ladders and coupled planes. *Physical Review B*, 45(10):5744, 1992.

[64] A. J. Daley, C. Kollath, U. Schollwöck, and G. Vidal. Time-dependent density-matrix renormalization-group using adaptive effective hilbert spaces. *Journal of Statistical Mechanics: Theory and Experiment*, 2004(04):P04005, apr 2004. doi:10.1088/1742-5468/2004/04/P04005. URL `https://dx.doi.org/10.1088/1742-5468/2004/04/P04005`.

[65] S. Daul and R. M. Noack. Ferromagnetic transition and phase diagram of the one-dimensional hubbard model with next-nearest-neighbor hopping. *Phys. Rev. B*, 58:2635–2650, Aug 1998. doi:10.1103/PhysRevB.58.2635. URL `https://link.aps.org/doi/10.1103/PhysRevB.58.2635`.

[66] S. Daul and R. M. Noack. Phase diagram of the half-filled hubbard chain with next-nearest-neighbor hopping. *Phys. Rev. B*, 61:1646–1649, Jan 2000. doi:10.1103/PhysRevB.61.1646. URL `https://link.aps.org/doi/10.1103/PhysRevB.61.1646`.

[67] E. R. Davidson. The iterative calculation of a few of the lowest eigenvalues and corresponding eigenvectors of large real-symmetric matrices. *Journal of Computational Physics*, 17(1):87–94, 1975. ISSN 0021-9991. doi:https://doi.org/10.1016/0021-9991(75)90065-0. URL `https://www.sciencedirect.com/science/article/pii/0021999175900650`.

[68] E. R. Davidson and W. J. Thompson. Monster matrices: Their eigenvalues and eigenvectors. *Computer in Physics*, 7(5):519–522, 09 1993. ISSN 0894-1866. doi:10.1063/1.4823212. URL `https://doi.org/10.1063/1.4823212`.

[69] S. Depenbrock, I. P. McCulloch, and U. Schollwöck. Nature of the spin-liquid ground state of the $s = 1/2$ heisenberg model on the kagome lattice. *Phys. Rev. Lett.*, 109:

067201, Aug 2012. doi:10.1103/PhysRevLett.109.067201. URL `https://link.aps.org/doi/10.1103/PhysRevLett.109.067201`.

[70] J. des Cloizeaux and J. J. Pearson. Spin-wave spectrum of the antiferromagnetic linear chain. *Phys. Rev.*, 128:2131–2135, Dec 1962. doi:10.1103/PhysRev.128.2131. URL `https://link.aps.org/doi/10.1103/PhysRev.128.2131`.

[71] D. Dey, M. Kumar, and Z. G. Soos. Boundary-induced spin-density waves in linear heisenberg antiferromagnetic spin chains with $s \geq 1$. *Phys. Rev. B*, 94:144417, Oct 2016. doi:10.1103/PhysRevB.94.144417. URL `https://link.aps.org/doi/10.1103/PhysRevB.94.144417`.

[72] D. Dey, D. Maiti, and M. Kumar. An efficient density matrix renormalization group algorithm for chains with periodic boundary condition. *Papers in Physics*, 8: 080006, Nov. 2016. doi:10.4279/pip.080006. URL `https://www.papersinphysics.org/papersinphysics/article/view/341`.

[73] H. T. Diep. *Magnetic systems with competing interactions: frustrated spin systems*. World Scientific, 1994.

[74] D. Dmitriev and V. Y. Krivnov. Weakly anisotropic frustrated zigzag spin chain. *Physical Review B*, 77(2):024401, 2008. doi:10.1103/PhysRevB.77.024401. URL `https://link.aps.org/doi/10.1103/PhysRevB.77.024401`.

[75] S.-H. Do, S.-Y. Park, J. Yoshitake, J. Nasu, Y. Motome, Y. S. Kwon, D. Adroja, D. Voneshen, K. Kim, T.-H. Jang, et al. Incarnation of majorana fermions in kitaev quantum spin lattice. *arXiv preprint arXiv:1703.01081*, 2017. doi:10.48550/arXiv.1703.01081. URL `https://doi.org/10.48550/arXiv.1703.01081`.

[76] S.-H. Do, S.-Y. Park, J. Yoshitake, J. Nasu, Y. Motome, Y. S. Kwon, D. Adroja, D. Voneshen, K. Kim, T.-H. Jang, et al. Majorana fermions in the kitaev quantum spin system α-rucl3. *Nature Physics*, 13(11):1079–1084, 2017. doi:10.1038/nphys4264. URL `https://doi.org/10.1038/nphys4264`.

[77] R. L. Doretto. Plaquette valence-bond solid in the square-lattice J_1-J_2 antiferromagnet heisenberg model: A bond operator approach. *Phys. Rev. B*, 89:104415, Mar 2014. doi:10.1103/PhysRevB.89.104415. URL `https://link.aps.org/doi/10.1103/PhysRevB.89.104415`.

[78] M. Drillon, E. Coronado, M. Belaiche, and R. Carlin. Low-dimensional magnetic systems; from 1d to 3d ferrimagnets. *Journal of Applied Physics*, 63(8):3551–3553, 1988.

[79] M. Drillon, M. Belaiche, P. Legoll, J. Aride, A. Boukhari, and A. Moqine. 1d ferrimagnetism in copper (ii) trimetric chains: Specific heat and magnetic behavior of a3cu3 (po4) 4 with a= ca, sr. *Journal of magnetism and magnetic materials*, 128(1-2):83–92, 1993.

[80] S. Dutton, M. Kumar, Z. Soos, C. Broholm, and R. Cava. Dominant ferromagnetism in the spin-1/2 half-twist ladder 334 compounds, ba3cu3in4o12 and ba3cu3sc4o12. *Journal of Physics: Condensed Matter*, 24(16):166001, 2012. doi:10.1088/0953-8984/24/16/166001. URL `https://doi.org/10.1088/0953-8984/24/16/166001`.

[81] S. E. Dutton, M. Kumar, M. Mourigal, Z. G. Soos, J.-J. Wen, C. L. Broholm, N. H. Andersen, Q. Huang, M. Zbiri, R. Toft-Petersen, and R. J. Cava. Quantum spin liquid in frustrated one-dimensional licusbo$_4$. *Phys. Rev. Lett.*, 108:187206, May 2012. doi:10.1103/PhysRevLett.108.187206. URL `https://link.aps.org/doi/10.1103/PhysRevLett.108.187206`.

[82] S. Eggert. Numerical evidence for multiplicative logarithmic corrections from marginal operators. *Physical Review B*, 54(14):R9612, 1996.

[83] G. Ehlers, S. R. White, and R. M. Noack. Hybrid-space density matrix renormalization group study of the doped two-dimensional hubbard model. *Phys. Rev. B*, 95:125125, Mar 2017. doi:10.1103/PhysRevB.95.125125. URL `https://link.aps.org/doi/10.1103/PhysRevB.95.125125`.

[84] S. Ejima, H. Fehske, and F. Gebhard. Dynamic properties of the one-dimensional bose-hubbard model. *Europhysics Letters*, 93(3):30002, feb 2011. doi:10.1209/0295-5075/93/30002. URL `https://dx.doi.org/10.1209/0295-5075/93/30002`.

[85] M. Elhajal, B. Canals, and C. Lacroix. Symmetry breaking due to dzyaloshinsky-moriya interactions in the kagomé lattice. *Phys. Rev. B*, 66:014422, Jul 2002. doi:10.1103/PhysRevB.66.014422. URL `https://link.aps.org/doi/10.1103/PhysRevB.66.014422`.

[86] M. Elhajal, B. Canals, R. Sunyer, and C. Lacroix. Ordering in the pyrochlore antiferromagnet due to dzyaloshinsky-moriya interactions. *Phys. Rev. B*, 71:094420, Mar 2005. doi:10.1103/PhysRevB.71.094420. URL `https://link.aps.org/doi/10.1103/PhysRevB.71.094420`.

[87] M. Enderle, C. Mukherjee, B. Fåk, R. Kremer, J.-M. Broto, H. Rosner, S.-L. Drechsler, J. Richter, J. Malek, A. Prokofiev, et al. Quantum helimagnetism of the frustrated spin-1/2 chain licuvo4. *Europhysics Letters*, 70(2):237, 2005.

[88] M. Enderle, B. Fåk, H.-J. Mikeska, R. Kremer, A. Prokofiev, and W. Assmus. Two-spinon and four-spinon continuum in a frustrated ferromagnetic spin-1/2 chain. *Physical review letters*, 104(23):237207, 2010. doi:10.1103/PhysRevLett.104.237207. URL `https://link.aps.org/doi/10.1103/PhysRevLett.104.237207`.

[89] G. Evenbly and G. Vidal. Frustrated antiferromagnets with entanglement renormalization: Ground state of the spin-$\frac{1}{2}$ heisenberg model on a kagome lattice. *Phys. Rev. Lett.*, 104:

187203, May 2010. doi:10.1103/PhysRevLett.104.187203. URL `https://link.aps.org/doi/10.1103/PhysRevLett.104.187203`.

[90] K. Fabricius, A. Klümper, U. Löw, B. Büchner, T. Lorenz, G. Dhalenne, and A. Revcolevschi. Reexamination of the microscopic couplings of the quasi-one-dimensional antiferromagnet cugeo$_3$. *Phys. Rev. B*, 57:1102–1107, Jan 1998. doi:10.1103/PhysRevB.57.1102. URL `https://link.aps.org/doi/10.1103/PhysRevB.57.1102`.

[91] K. Fabricius, A. Klümper, U. Löw, B. Büchner, T. Lorenz, G. Dhalenne, and A. Revcolevschi. Reexamination of the microscopic couplings of the quasi-one-dimensional antiferromagnet cugeo$_3$. *Phys. Rev. B*, 57:1102–1107, Jan 1998. doi:10.1103/PhysRevB.57.1102. URL `https://link.aps.org/doi/10.1103/PhysRevB.57.1102`.

[92] G. Fano, F. Ortolani, and L. Ziosi. The density matrix renormalization group method: Application to the ppp model of a cyclic polyene chain. *The Journal of Chemical Physics*, 108(22):9246–9252, 06 1998. ISSN 0021-9606. doi:10.1063/1.476379. URL `https://doi.org/10.1063/1.476379`.

[93] P. Fazekas. *Lecture Notes on Electron Correlation and Magnetism*. WORLD SCIENTIFIC, 1999. doi:10.1142/2945. URL `https://www.worldscientific.com/doi/abs/10.1142/2945`.

[94] P. Fazekas and P. W. Anderson. On the ground state properties of the anisotropic triangular antiferromagnet. *The Philosophical Magazine: A Journal of Theoretical Experimental and Applied Physics*, 30(2):423–440, 1974. doi:10.1080/14786439808206568. URL `https://doi.org/10.1080/14786439808206568`.

[95] A. E. Feiguin and S. R. White. Finite-temperature density matrix renormalization using an enlarged hilbert space. *Phys. Rev. B*, 72:220401, Dec 2005. doi:10.1103/PhysRevB.72.220401. URL `https://link.aps.org/doi/10.1103/PhysRevB.72.220401`.

[96] A. E. Feiguin and S. R. White. Finite-temperature density matrix renormalization using an enlarged hilbert space. *Phys. Rev. B*, 72:220401, Dec 2005. doi:10.1103/PhysRevB.72.220401. URL `https://link.aps.org/doi/10.1103/PhysRevB.72.220401`.

[97] C. Feng, A. Wietek, E. M. Stoudenmire, and R. R. P. Singh. Order, disorder, and monopole confinement in the spin-$\frac{1}{2}$ xxz model on a pyrochlore tube. *Phys. Rev. B*, 106:075135, Aug 2022. doi:10.1103/PhysRevB.106.075135. URL `https://link.aps.org/doi/10.1103/PhysRevB.106.075135`.

[98] X.-Y. Feng, G.-M. Zhang, and T. Xiang. Topological characterization of quantum phase transitions in a spin-1/2 model. *Phys. Rev. Lett.*, 98:087204, Feb 2007. doi:10.1103/PhysRevLett.98.087204. URL `https://link.aps.org/doi/10.1103/PhysRevLett.98.087204`.

[99] Y. Feng, K. Y. Povarov, and A. Zheludev. Magnetic phase diagram of the strongly frustrated quantum spin chain system pbcuso$_4$(OH)$_2$ in tilted magnetic fields. *Phys. Rev. B*, 98:054419, Aug 2018. doi:10.1103/PhysRevB.98.054419. URL `https://link.aps.org/doi/10.1103/PhysRevB.98.054419`.

[100] F. Ferrari and F. Becca. Dynamical properties of néel and valence-bond phases in the j1–j2 model on the honeycomb lattice. *Journal of Physics: Condensed Matter*, 32(27): 274003, apr 2020. doi:10.1088/1361-648X/ab7f6e. URL `https://dx.doi.org/10.1088/1361-648X/ab7f6e`.

[101] A. Fujimura, Y. Yasui, Y. Yanagisawa, I. Terasaki, Y. Kono, S. Kittaka, and T. Sakakibara. Comparison with ground states of frustrated quantum spin chain systems a2cu2mo3o12 (a = rb and cs). *IEEE Transactions on Magnetics*, 52(7):1–3, 2016. doi:10.1109/TMAG.2016.2517091.

[102] M. Fujisawa, J.-I. Yamaura, H. Tanaka, H. Kageyama, Y. Narumi, and K. Kindo. Crystal structure and magnetic properties of the quasi-one-dimensional quantum spin system cu2cl4· h8c4so2. *Journal of the Physical Society of Japan*, 72(3):694–697, 2003.

[103] S. Furukawa, M. Sato, and A. Furusaki. Unconventional néel and dimer orders in a spin-1 2 frustrated ferromagnetic chain with easy-plane anisotropy. *Physical Review B*, 81(9): 094430, 2010. doi:10.1103/PhysRevB.81.094430. URL `https://link.aps.org/doi/10.1103/PhysRevB.81.094430`.

[104] S. Furukawa, M. Sato, S. Onoda, and A. Furusaki. Ground-state phase diagram of a spin-1 2 frustrated ferromagnetic xxz chain: Haldane dimer phase and gapped/gapless chiral phases. *Physical Review B*, 86(9):094417, 2012. doi:10.1103/PhysRevB.86.094417. URL `https://link.aps.org/doi/10.1103/PhysRevB.86.094417`.

[105] Y. H. Gao, C. Hickey, T. Xiang, S. Trebst, and G. Chen. Thermal hall signatures of non-kitaev spin liquids in honeycomb kitaev materials. *Phys. Rev. Res.*, 1:013014, Aug 2019. doi:10.1103/PhysRevResearch.1.013014. URL `https://link.aps.org/doi/10.1103/PhysRevResearch.1.013014`.

[106] T. Giamarchi. *Quantum Physics in One Dimension*. Oxford University Press, 12 2003. ISBN 9780198525004. doi:10.1093/acprof:oso/9780198525004.001.0001. URL `https://doi.org/10.1093/acprof:oso/9780198525004.001.0001`.

[107] T. Giamarchi and H. Schulz. Correlation functions of one-dimensional quantum systems. *Physical Review B*, 39(7):4620, 1989.

[108] G. Giri, D. Dey, M. Kumar, S. Ramasesha, and Z. G. Soos. Quantum phases of frustrated two-leg spin-$\frac{1}{2}$ ladders with skewed rungs. *Phys. Rev. B*, 95:224408, Jun 2017. doi:10.1103/PhysRevB.95.224408. URL `https://link.aps.org/doi/10.1103/PhysRevB.95.224408`.

[109] F. Giustino. Electron-phonon interactions from first principles. *Rev. Mod. Phys.*, 89:015003, Feb 2017. doi:10.1103/RevModPhys.89.015003. URL `https://link.aps.org/doi/10.1103/RevModPhys.89.015003`.

[110] V. Gnezdilov, P. Lemmens, A. A. Zvyagin, V. O. Cheranovskii, K. Lamonova, Y. G. Pashkevich, R. K. Kremer, and H. Berger. Magnetic crossover and complex excitation spectrum of the ferromagnetic/antiferromagnetic spin-$\frac{1}{2}$ chain system α-tevo$_4$. *Phys. Rev. B*, 78:184407, Nov 2008. doi:10.1103/PhysRevB.78.184407. URL `https://link.aps.org/doi/10.1103/PhysRevB.78.184407`.

[111] S.-S. Gong, D. N. Sheng, O. I. Motrunich, and M. P. A. Fisher. Phase diagram of the spin-$\frac{1}{2}$ J_1-J_2 heisenberg model on a honeycomb lattice. *Phys. Rev. B*, 88:165138, Oct 2013. doi:10.1103/PhysRevB.88.165138. URL `https://link.aps.org/doi/10.1103/PhysRevB.88.165138`.

[112] S.-S. Gong, W. Zhu, D. N. Sheng, O. I. Motrunich, and M. P. A. Fisher. Plaquette ordered phase and quantum phase diagram in the spin-$\frac{1}{2}$ $J_1{-}J_2$ square heisenberg model. *Phys. Rev. Lett.*, 113:027201, Jul 2014. doi:10.1103/PhysRevLett.113.027201. URL `https://link.aps.org/doi/10.1103/PhysRevLett.113.027201`.

[113] S.-S. Gong, W. Zhu, and D. N. Sheng. Quantum phase diagram of the spin-1 $J_1 - J_2$ heisenberg model on the honeycomb lattice. *Phys. Rev. B*, 92:195110, Nov 2015. doi:10.1103/PhysRevB.92.195110. URL `https://link.aps.org/doi/10.1103/PhysRevB.92.195110`.

[114] J. B. Goodenough. Theory of the role of covalence in the perovskite-type manganites $[\mathrm{La}, m(\mathrm{II})]\mathrm{Mno}_3$. *Phys. Rev.*, 100:564–573, Oct 1955. doi:10.1103/PhysRev.100.564. URL `https://link.aps.org/doi/10.1103/PhysRev.100.564`.

[115] A. V. Gorshkov, S. R. Manmana, G. Chen, J. Ye, E. Demler, M. D. Lukin, and A. M. Rey. Tunable superfluidity and quantum magnetism with ultracold polar molecules. *Phys. Rev. Lett.*, 107:115301, Sep 2011. doi:10.1103/PhysRevLett.107.115301. URL `https://link.aps.org/doi/10.1103/PhysRevLett.107.115301`.

[116] D. Gotfryd, J. Rusnačko, K. Wohlfeld, G. Jackeli, J. Chaloupka, and A. M. Oleś. Phase diagram and spin correlations of the kitaev-heisenberg model: Importance of quantum effects. *Physical Review B*, 95(2):024426, 2017. doi:10.1103/PhysRevB.95.024426. URL `https://link.aps.org/doi/10.1103/PhysRevB.95.024426`.

[117] H.-J. Grafe, S. Nishimoto, M. Iakovleva, E. Vavilova, L. Spillecke, A. Alfonsov, M.-I. Sturza, S. Wurmehl, H. Nojiri, H. Rosner, J. Richter, U. K. Rößler, S.-L. Drechsler, V. Kataev, and B. Büchner. Signatures of a magnetic field-induced unconventional nematic liquid in the frustrated and anisotropic spin-chain cuprate licusbo4. *Scientific Reports*, 7(1):6720, Jul 2017. ISSN 2045-2322. doi:10.1038/s41598-017-06525-0. URL `https://doi.org/10.1038/s41598-017-06525-0`.

[118] R. B. Griffiths. Magnetization curve at zero temperature for the antiferromagnetic heisenberg linear chain. *Physical Review*, 133(3A):A768, 1964.

[119] G. Grüner. The dynamics of charge-density waves. *Rev. Mod. Phys.*, 60:1129–1181, Oct 1988. doi:10.1103/RevModPhys.60.1129. URL `https://link.aps.org/doi/10.1103/RevModPhys.60.1129`.

[120] F. Grusdt, M. Höning, and M. Fleischhauer. Topological edge states in the one-dimensional superlattice bose-hubbard model. *Phys. Rev. Lett.*, 110:260405, Jun 2013. doi:10.1103/PhysRevLett.110.260405. URL `https://link.aps.org/doi/10.1103/PhysRevLett.110.260405`.

[121] F. Haldane. Spontaneous dimerization in the s= 1 2 heisenberg antiferromagnetic chain with competing interactions. *Physical Review B*, 25(7):4925, 1982.

[122] F. Haldane. Continuum dynamics of the 1-d heisenberg antiferromagnet: Identification with the o(3) nonlinear sigma model. *Physics Letters A*, 93(9):464–468, 1983. ISSN 0375-9601. doi:https://doi.org/10.1016/0375-9601(83)90631-X. URL `https://www.sciencedirect.com/science/article/pii/037596018390631X`.

[123] F. D. M. Haldane. Nonlinear field theory of large-spin heisenberg antiferromagnets: Semiclassically quantized solitons of the one-dimensional easy-axis néel state. *Phys. Rev. Lett.*, 50:1153–1156, Apr 1983. doi:10.1103/PhysRevLett.50.1153. URL `https://link.aps.org/doi/10.1103/PhysRevLett.50.1153`.

[124] F. D. M. Haldane. Nonlinear field theory of large-spin heisenberg antiferromagnets: Semiclassically quantized solitons of the one-dimensional easy-axis néel state. *Phys. Rev. Lett.*, 50:1153–1156, Apr 1983. doi:10.1103/PhysRevLett.50.1153. URL `https://link.aps.org/doi/10.1103/PhysRevLett.50.1153`.

[125] F. D. M. Haldane. Nonlinear field theory of large-spin heisenberg antiferromagnets: semiclassically quantized solitons of the one-dimensional easy-axis néel state. *Physical review letters*, 50(15):1153, 1983.

[126] K. Hallberg. Density matrix renormalization: A review of the method and its applications, 2003. URL `https://arxiv.org/abs/cond-mat/0303557`.

[127] K. A. Hallberg. Density-matrix algorithm for the calculation of dynamical properties of low-dimensional systems. *Phys. Rev. B*, 52:R9827–R9830, Oct 1995. doi:10.1103/PhysRevB.52.R9827. URL `https://link.aps.org/doi/10.1103/PhysRevB.52.R9827`.

[128] K. A. Hallberg. New trends in density matrix renormalization. *Advances in Physics*, 55 (5-6):477–526, 2006. doi:10.1080/00018730600766432. URL `https://doi.org/10.1080/00018730600766432`.

[129] K. A. Hallberg, P. Horsch, and G. Martínez. Numerical renormalization-group study of the correlation functions of the antiferromagnetic spin-1/2 heisenberg chain. *Physical Review B*, 52(2):R719, 1995.

[130] T. Hamada, J.-i. Kane, S.-i. Nakagawa, and Y. Natsume. Exact solution of ground state for uniformly distributed rvb in one-dimensional spin-1/2 heisenberg systems with frustration. *Journal of the Physical Society of Japan*, 57(6):1891–1894, 1988. URL `https://doi.org/10.1143/JPSJ.57.1891`.

[131] M. Hase, I. Terasaki, and K. Uchinokura. Observation of the spin-peierls transition in linear cu^{2+} (spin-1/2) chains in an inorganic compound cugeo$_3$. *Phys. Rev. Lett.*, 70: 3651–3654, Jun 1993. doi:10.1103/PhysRevLett.70.3651. URL `https://link.aps.org/doi/10.1103/PhysRevLett.70.3651`.

[132] M. Hase, I. Terasaki, and K. Uchinokura. Observation of the spin-peierls transition in linear cu^{2+} (spin-1/2) chains in an inorganic compound cugeo$_3$. *Phys. Rev. Lett.*, 70: 3651–3654, Jun 1993. doi:10.1103/PhysRevLett.70.3651. URL `https://link.aps.org/doi/10.1103/PhysRevLett.70.3651`.

[133] M. Hase, I. Terasaki, K. Uchinokura, M. Tokunaga, N. Miura, and H. Obara. Magnetic phase diagram of the spin-peierls cuprate cugeo$_3$. *Phys. Rev. B*, 48:9616–9619, Oct 1993. doi:10.1103/PhysRevB.48.9616. URL `https://link.aps.org/doi/10.1103/PhysRevB.48.9616`.

[134] M. Hase, H. Kuroe, K. Ozawa, O. Suzuki, H. Kitazawa, G. Kido, and T. Sekine. Magnetic properties of rb$_2$cu$_2$mo$_3$o$_{12}$ including a one-dimensional spin-12 heisenberg system with ferromagnetic first-nearest-neighbor and antiferromagnetic second-nearest-neighbor exchange interactions. *Phys. Rev. B*, 70:104426, Sep 2004. doi:10.1103/PhysRevB.70.104426. URL `https://link.aps.org/doi/10.1103/PhysRevB.70.104426`.

[135] M. Hase, H. Kuroe, K. Ozawa, O. Suzuki, H. Kitazawa, G. Kido, and T. Sekine. Magnetic properties of rb$_2$cu$_2$mo$_3$o$_{12}$ including a one-dimensional spin-12 heisenberg system with ferromagnetic first-nearest-neighbor and antiferromagnetic second-nearest-neighbor exchange interactions. *Phys. Rev. B*, 70:104426, Sep 2004. doi:10.1103/PhysRevB.70.104426. URL `https://link.aps.org/doi/10.1103/PhysRevB.70.104426`.

[136] M. Hase, K. Ozawa, O. Suzuki, H. Kitazawa, G. Kido, H. Kuroe, and T. Sekine. Magnetism of a2cu2mo3o12 (a= rb or cs): Model compounds of a one-dimensional spin-1/ 2 heisenberg system with ferromagnetic first-nearest-neighbor and antiferromagnetic second-nearest-neighbor interactions. *Journal of applied physics*, 97(10), 2005.

[137] M. Hase, M. Kohno, H. Kitazawa, N. Tsujii, O. Suzuki, K. Ozawa, G. Kido, M. Imai, and X. Hu. 13 magnetization plateau observed in the spin-12 trimer chain compound $\mathrm{cu}_3(\mathrm{P}_2\mathrm{O}_6\mathrm{OH})_2$. *Phys. Rev. B*, 73:104419, Mar 2006. doi:10.1103/PhysRevB.73.104419. URL `https://link.aps.org/doi/10.1103/PhysRevB.73.104419`.

[138] A. Hashimoto, Y. Murakami, and A. Koga. Majorana excitations in the anisotropic kitaev model with an ordered-flux structure. In *Journal of Physics: Conference Series*, volume 2164, page 012028. IOP Publishing, 2022. doi:10.1088/1742-6596/2164/1/012028. URL `https://dx.doi.org/10.1088/1742-6596/2164/1/012028`.

[139] S. Hayashida, D. Blosser, K. Y. Povarov, Z. Yan, S. Gvasaliya, A. N. Ponomaryov, S. A. Zvyagin, and A. Zheludev. One- and three-dimensional quantum phase transitions and anisotropy in $\mathrm{rb}_2\mathrm{cu}_2\mathrm{mo}_3\mathrm{o}_{12}$. *Phys. Rev. B*, 100:134427, Oct 2019. doi:10.1103/PhysRevB.100.134427. URL `https://link.aps.org/doi/10.1103/PhysRevB.100.134427`.

[140] F. Heidrich-Meisner, A. Honecker, and T. Vekua. Frustrated ferromagnetic spin-1 2 chain in a magnetic field: The phase diagram and thermodynamic properties. *Physical Review B*, 74(2):020403, 2006. doi:10.1103/PhysRevB.74.020403. URL `https://link.aps.org/doi/10.1103/PhysRevB.74.020403`.

[141] L. Heinze, G. Bastien, B. Ryll, J.-U. Hoffmann, M. Reehuis, B. Ouladdiaf, F. Bert, E. Kermarrec, P. Mendels, S. Nishimoto, S.-L. Drechsler, U. K. Rößler, H. Rosner, B. Büchner, A. J. Studer, K. C. Rule, S. Süllow, and A. U. B. Wolter. Magnetic phase diagram of the frustrated spin chain compound linarite $\mathrm{pbcuso}_4(\mathrm{OH})_2$ as seen by neutron diffraction and ^{1}H-nmr. *Phys. Rev. B*, 99:094436, Mar 2019. doi:10.1103/PhysRevB.99.094436. URL `https://link.aps.org/doi/10.1103/PhysRevB.99.094436`.

[142] W. Heisenberg. Zur theorie des ferromagnetismus. *Zeitschrift für Physik*, 49(9):619–636, Sep 1928. ISSN 0044-3328. doi:10.1007/BF01328601. URL `https://doi.org/10.1007/BF01328601`.

[143] W. Heisenberg. *Zur theorie des ferromagnetismus.* Springer, 1985.

[144] M. Hermanns, K. O'Brien, and S. Trebst. Weyl spin liquids. *Physical Review Letters*, 114 (15):157202, 2015. doi:10.1103/PhysRevLett.114.157202. URL `https://link.aps.org/doi/10.1103/PhysRevLett.114.157202`.

[145] M. Hermanns, I. Kimchi, and J. Knolle. Physics of the kitaev model: Fractionalization, dynamic correlations, and material connections. *Annual Review of Condensed Matter Physics*, 9(1):17–33, 2018. doi:https://doi.org/10.1146/annurev-conmatphys-033117-053934.

[146] K. Hida. Magnetic properties of the spin-1/2 ferromagnetic-ferromagnetic-antiferromagnetic trimerized heisenberg chain. *Journal of the Physical Society of Japan*, 63 (6):2359–2364, 1994. doi:10.1143/JPSJ.63.2359. URL `https://doi.org/10.1143/JPSJ.63.2359`.

[147] K. Hida, K. Takano, and H. Suzuki. Topological phases of the spin-1/2 ferromagnetic–antiferromagnetic alternating heisenberg chain with frustrated next-nearest-neighbour interaction. *Journal of the Physical Society of Japan*, 82(6):064703, 2013. doi:10.7566/JPSJ.82.064703. URL `https://doi.org/10.7566/JPSJ.82.064703`.

[148] T. Hikihara, L. Kecke, T. Momoi, and A. Furusaki. Vector chiral and multipolar orders in the spin-$\frac{1}{2}$ frustrated ferromagnetic chain in magnetic field. *Phys. Rev. B*, 78:144404, Oct 2008. doi:10.1103/PhysRevB.78.144404. URL `https://link.aps.org/doi/10.1103/PhysRevB.78.144404`.

[149] L. Holleis, J. C. Prestigiacomo, Z. Fan, S. Nishimoto, M. Osofsky, G.-W. Chern, J. van den Brink, and B. S. Shivaram. Anomalous and anisotropic nonlinear susceptibility in the proximate kitaev magnet α-rucl3. *npj Quantum Materials*, 6(1):66, Jul 2021. ISSN 2397-4648. doi:10.1038/s41535-021-00364-z. URL `https://doi.org/10.1038/s41535-021-00364-z`.

[150] A. Honecker and A. Läuchli. Frustrated trimer chain model and cu 3 cl 6 (h 2 o) 2 2 h 8 c 4 so 2 in a magnetic field. *Physical Review B*, 63(17):174407, 2001.

[151] W.-J. Hu, S.-S. Gong, W. Zhu, and D. N. Sheng. Competing spin-liquid states in the spin-$\frac{1}{2}$ heisenberg model on the triangular lattice. *Phys. Rev. B*, 92:140403, Oct 2015. doi:10.1103/PhysRevB.92.140403. URL `https://link.aps.org/doi/10.1103/PhysRevB.92.140403`.

[152] W.-J. Hu, S.-S. Gong, H.-H. Lai, H. Hu, Q. Si, and A. H. Nevidomskyy. Nematic spin liquid phase in a frustrated spin-1 system on the square lattice. *Phys. Rev. B*, 100:165142, Oct 2019. doi:10.1103/PhysRevB.100.165142. URL `https://link.aps.org/doi/10.1103/PhysRevB.100.165142`.

[153] L. Hulthén. Über das austauschproblem eines kristalles. *Journal Name*, Volume Number: Page Numbers, 1938.

[154] D. A. Huse. Ground-state staggered magnetization of two-dimensional quantum heisenberg antiferromagnets. *Phys. Rev. B*, 37:2380–2382, Feb 1988.

doi:10.1103/PhysRevB.37.2380. URL `https://link.aps.org/doi/10.1103/PhysRevB.37.2380`.

[155] S. Hwan Chun, J.-W. Kim, J. Kim, H. Zheng, C. C. Stoumpos, C. Malliakas, J. Mitchell, K. Mehlawat, Y. Singh, Y. Choi, et al. Direct evidence for dominant bond-directional interactions in a honeycomb lattice iridate na 2 iro 3. *Nature Physics*, 11(6):462–466, 2015. doi:10.1038/nphys3322. URL `https://doi.org/10.1038/nphys3322`.

[156] K. Ishida, Y. Kitaoka, Y. Tokunaga, S. Matsumoto, K. Asayama, M. Azuma, Z. Hiroi, and M. Takano. Spin correlation and spin gap in quasi-one-dimensional spin-1/2 cuprate oxides: A ^{63}Cu nmr study. *Phys. Rev. B*, 53:2827–2834, Feb 1996. doi:10.1103/PhysRevB.53.2827. URL `https://link.aps.org/doi/10.1103/PhysRevB.53.2827`.

[157] M. Ishii, H. Tanaka, M. Hori, H. Uekusa, Y. Ohashi, K. Tatani, Y. Narumi, and K. Kindo. Gapped ground state in the spin-\bf1\bf2 trimer chain system cu 3 cl 6 (h 2 o) 2· 2h 8 c 4 so 2. *Journal of the Physical Society of Japan*, 69(2):340–343, 2000.

[158] M. Isobe and Y. Ueda. Magnetic susceptibility of quasi-one-dimensional compound α'-n a v 2 o 5–possible spin-peierls compound with high critical temperature of 34 k–. *Journal of the Physical Society of Japan*, 65(5):1178–1181, 1996.

[159] C. Itoi and S. Qin. Strongly reduced gap in the zigzag spin chain with a ferromagnetic interchain coupling. *Physical Review B*, 63(22):224423, 2001. doi:10.1103/PhysRevB.63.224423. URL `https://link.aps.org/doi/10.1103/PhysRevB.63.224423`.

[160] G. Jackeli and G. Khaliullin. Mott insulators in the strong spin-orbit coupling limit: From heisenberg to a quantum compass and kitaev models. *Phys. Rev. Lett.*, 102:017205, Jan 2009. doi:10.1103/PhysRevLett.102.017205. URL `https://link.aps.org/doi/10.1103/PhysRevLett.102.017205`.

[161] I. S. Jacobs, J. W. Bray, H. R. Hart, L. V. Interrante, J. S. Kasper, G. D. Watkins, D. E. Prober, and J. C. Bonner. Spin-peierls transitions in magnetic donor-acceptor compounds of tetrathiafulvalene (ttf) with bisdithiolene metal complexes. *Phys. Rev. B*, 14:3036–3051, Oct 1976. doi:10.1103/PhysRevB.14.3036. URL `https://link.aps.org/doi/10.1103/PhysRevB.14.3036`.

[162] L. Janssen, E. C. Andrade, and M. Vojta. Honeycomb-lattice heisenberg-kitaev model in a magnetic field: Spin canting, metamagnetism, and vortex crystals. *Phys. Rev. Lett.*, 117:277202, Dec 2016. doi:10.1103/PhysRevLett.117.277202.

[163] E. Jeckelmann. Ground-state phase diagram of a half-filled one-dimensional extended hubbard model. *Phys. Rev. Lett.*, 89:236401, Nov 2002. doi:10.1103/PhysRevLett.89.236401. URL `https://link.aps.org/doi/10.1103/PhysRevLett.89.236401`.

[164] E. Jeckelmann. Density-matrix renormalization group methods for momentum- and frequency-resolved dynamical correlation functions. *Progress of Theoretical Physics Supplement*, 176:143–164, 06 2008. ISSN 0375-9687. doi:10.1143/PTPS.176.143. URL `https://doi.org/10.1143/PTPS.176.143`.

[165] H.-C. Jiang and T. P. Devereaux. Superconductivity in the doped hubbard model and its interplay with next-nearest hopping ¡i¿t¡/i¿′. *Science*, 365(6460):1424–1428, 2019. doi:10.1126/science.aal5304. URL `https://www.science.org/doi/abs/10.1126/science.aal5304`.

[166] R. D. Johnson, S. C. Williams, A. A. Haghighirad, J. Singleton, V. Zapf, P. Manuel, I. I. Mazin, Y. Li, H. O. Jeschke, R. Valentí, and R. Coldea. Monoclinic crystal structure of $\alpha-\mathrm{rucl}_3$ and the zigzag antiferromagnetic ground state. *Phys. Rev. B*, 92:235119, Dec 2015. doi:10.1103/PhysRevB.92.235119. URL `https://link.aps.org/doi/10.1103/PhysRevB.92.235119`.

[167] R. D. Johnson, S. C. Williams, A. A. Haghighirad, J. Singleton, V. Zapf, P. Manuel, I. I. Mazin, Y. Li, H. O. Jeschke, R. Valentí, and R. Coldea. Monoclinic crystal structure of $\alpha-\mathrm{rucl}_3$ and the zigzag antiferromagnetic ground state. *Phys. Rev. B*, 92:235119, Dec 2015. doi:10.1103/PhysRevB.92.235119. URL `https://link.aps.org/doi/10.1103/PhysRevB.92.235119`.

[168] R. D. Johnson, S. C. Williams, A. A. Haghighirad, J. Singleton, V. Zapf, P. Manuel, I. I. Mazin, Y. Li, H. O. Jeschke, R. Valentí, and R. Coldea. Monoclinic crystal structure of $\alpha-\mathrm{rucl}_3$ and the zigzag antiferromagnetic ground state. *Phys. Rev. B*, 92:235119, Dec 2015. doi:10.1103/PhysRevB.92.235119. URL `https://link.aps.org/doi/10.1103/PhysRevB.92.235119`.

[169] D. Johnston, R. Kremer, M. Troyer, X. Wang, A. Klümper, S. Bud'ko, A. Panchula, and P. Canfield. Thermodynamics of spin s= 1/2 antiferromagnetic uniform and alternating-exchange heisenberg chains. *Physical Review B*, 61(14):9558, 2000. doi:10.1103/PhysRevB.61.9558. URL `https://link.aps.org/doi/10.1103/PhysRevB.61.9558`.

[170] D. C. Johnston, R. K. Kremer, M. Troyer, X. Wang, A. Klümper, S. L. Bud'ko, A. F. Panchula, and P. C. Canfield. Thermodynamics of spin $s = 1/2$ antiferromagnetic uniform and alternating-exchange heisenberg chains. *Phys. Rev. B*, 61:9558–9606, Apr 2000. doi:10.1103/PhysRevB.61.9558. URL `https://link.aps.org/doi/10.1103/PhysRevB.61.9558`.

[171] L. P. Kadanoff. Scaling laws for ising models near T_c. *Physics Physique Fizika*, 2:263–272, Jun 1966. doi:10.1103/PhysicsPhysiqueFizika.2.263. URL `https://link.aps.org/doi/10.1103/PhysicsPhysiqueFizika.2.263`.

[172] A. P. Kampf, M. Sekania, G. I. Japaridze, and P. Brune. Nature of the insulating phases in the half-filled ionic hubbard model. *Journal of Physics: Condensed Matter*, 15(34): 5895, aug 2003. doi:10.1088/0953-8984/15/34/319. URL `https://dx.doi.org/10.1088/0953-8984/15/34/319`.

[173] J. Kanamori. Superexchange interaction and symmetry properties of electron orbitals. *Journal of Physics and Chemistry of Solids*, 10(2):87–98, 1959. ISSN 0022-3697. doi:https://doi.org/10.1016/0022-3697(59)90061-7. URL `https://www.sciencedirect.com/science/article/pii/0022369759900617`.

[174] C. Karrasch, J. H. Bardarson, and J. E. Moore. Finite-temperature dynamical density matrix renormalization group and the drude weight of spin-1/2 chains. *Phys. Rev. Lett.*, 108:227206, May 2012. doi:10.1103/PhysRevLett.108.227206. URL `https://link.aps.org/doi/10.1103/PhysRevLett.108.227206`.

[175] Y. Kasahara, T. Ohnishi, Y. Mizukami, O. Tanaka, S. Ma, K. Sugii, N. Kurita, H. Tanaka, J. Nasu, Y. Motome, T. Shibauchi, and Y. Matsuda. Majorana quantization and half-integer thermal quantum hall effect in a kitaev spin liquid. *Nature*, 559(7713):227–231, Jul 2018. ISSN 1476-4687. doi:10.1038/s41586-018-0274-0. URL `https://doi.org/10.1038/s41586-018-0274-0`.

[176] V. M. Katukuri, R. Yadav, L. Hozoi, S. Nishimoto, and J. van den Brink. The vicinity of hyper-honeycomb β-li2iro3 to a three-dimensional kitaev spin liquid state. *Scientific reports*, 6(1):29585, 2016. doi:10.1038/srep29585. URL `https://doi.org/10.1038/srep29585`.

[177] H. Kelker. History of liquid crystals. *Molecular Crystals and Liquid Crystals*, 21 (1-2):1–48, 1973. doi:10.1080/15421407308083312. URL `https://doi.org/10.1080/15421407308083312`.

[178] H. Kelker. Survey of the early history of liquid crystals. *Molecular Crystals and Liquid Crystals Incorporating Nonlinear Optics*, 165(1):1–43, 1988. doi:10.1080/00268948808082195. URL `https://doi.org/10.1080/00268948808082195`.

[179] P. Khuntia, M. Velazquez, Q. Barthélemy, F. Bert, E. Kermarrec, A. Legros, B. Bernu, L. Messio, A. Zorko, and P. Mendels. Gapless ground state in the archetypal quantum kagome antiferromagnet zncu3(oh)6cl2. *Nature Physics*, 16(4):469–474, Apr 2020. ISSN 1745-2481. doi:10.1038/s41567-020-0792-1. URL `https://doi.org/10.1038/s41567-020-0792-1`.

[180] H. Kikuchi, Y. Fujii, M. Chiba, S. Mitsudo, and T. Idehara. Magnetic properties of the frustrated diamond chain compound cu3 (co3) 2 (oh) 2. *Physica B: Condensed Matter*, 329:967–968, 2003.

[181] H. Kikuchi, Y. Fujii, M. Chiba, S. Mitsudo, T. Idehara, T. Tonegawa, K. Okamoto, . f. T. Sakai, T. Kuwai, and H. Ohta. Experimental observation of the 1/3 magnetization plateau¡? format?¿ in the diamond-chain compound cu 3 (co 3) 2 (oh) 2. *Physical review letters*, 94(22):227201, 2005.

[182] I. Kimchi, R. Coldea, and A. Vishwanath. Unified theory of spiral magnetism in the harmonic-honeycomb iridates α, β, and $\gamma\,\mathrm{li_2iro_3}$. *Phys. Rev. B*, 91:245134, Jun 2015. doi:10.1103/PhysRevB.91.245134. URL `https://link.aps.org/doi/10.1103/PhysRevB.91.245134`.

[183] A. Kitaev. Fault-tolerant quantum computation by anyons. *Annals of Physics*, 303(1): 2–30, 2003. ISSN 0003-4916. doi:https://doi.org/10.1016/S0003-4916(02)00018-0. URL `https://www.sciencedirect.com/science/article/pii/S0003491602000180`.

[184] A. Kitaev. Anyons in an exactly solved model and beyond. *Annals of Physics*, 321(1):2–111, 2006. ISSN 0003-4916. doi:https://doi.org/10.1016/j.aop.2005.10.005. URL `https://www.sciencedirect.com/science/article/pii/S0003491605002381`. January Special Issue.

[185] D. Kivelson and S.-K. Lee. Esr studies and the electronic structure of vanadyl ion complexes. *The Journal of Chemical Physics*, 41(7):1896–1903, 1964.

[186] A. Klümper, R. Raupach, and F. Schönfeld. Finite temperature density-matrix-renormalization-group investigation of the spin-peierls transition in $\mathrm{cugeo_3}$. *Phys. Rev. B*, 59:3612–3616, Feb 1999. doi:10.1103/PhysRevB.59.3612. URL `https://link.aps.org/doi/10.1103/PhysRevB.59.3612`.

[187] A. Koga, Y. Murakami, and J. Nasu. Majorana correlations in the kitaev model with ordered-flux structures. *Physical Review B*, 103(21):214421, 2021. doi:10.1103/PhysRevB.103.214421. URL `https://link.aps.org/doi/10.1103/PhysRevB.103.214421`.

[188] T. Koga, N. Kurita, M. Avdeev, S. Danilkin, T. J. Sato, and H. Tanaka. Magnetic structure of the $s = \frac{1}{2}$ quasi-two-dimensional square-lattice heisenberg antiferromagnet $\mathrm{sr_2cuteo_6}$. *Phys. Rev. B*, 93:054426, Feb 2016. doi:10.1103/PhysRevB.93.054426. URL `https://link.aps.org/doi/10.1103/PhysRevB.93.054426`.

[189] K. M. Kojima, Y. Fudamoto, M. Larkin, G. M. Luke, J. Merrin, B. Nachumi, Y. J. Uemura, N. Motoyama, H. Eisaki, S. Uchida, K. Yamada, Y. Endoh, S. Hosoya, B. J. Sternlieb, and G. Shirane. Reduction of ordered moment and néel temperature of quasi-one-dimensional antiferromagnets $\mathrm{sr_2cuo_3}$ and $\mathrm{ca_2cuo_3}$. *Phys. Rev. Lett.*, 78:1787–1790, Mar 1997. doi:10.1103/PhysRevLett.78.1787. URL `https://link.aps.org/doi/10.1103/PhysRevLett.78.1787`.

[190] C. Kollath, U. Schollwöck, and W. Zwerger. Spin-charge separation in cold fermi gases: A real time analysis. *Phys. Rev. Lett.*, 95:176401, Oct 2005. doi:10.1103/PhysRevLett.95.176401. URL `https://link.aps.org/doi/10.1103/PhysRevLett.95.176401`.

[191] M. A. Korotin, I. S. Elfimov, V. I. Anisimov, M. Troyer, and D. I. Khomskii. Exchange interactions and magnetic properties of the layered vanadates $\mathrm{cav_2o_5}$, $\mathrm{mgv_2o_5}$, $\mathrm{cav_3o_7}$, and $\mathrm{cav_4o_9}$. *Phys. Rev. Lett.*, 83:1387–1390, Aug 1999. doi:10.1103/PhysRevLett.83.1387. URL `https://link.aps.org/doi/10.1103/PhysRevLett.83.1387`.

[192] T. D. Kühner and H. Monien. Phases of the one-dimensional bose-hubbard model. *Phys. Rev. B*, 58:R14741–R14744, Dec 1998. doi:10.1103/PhysRevB.58.R14741. URL `https://link.aps.org/doi/10.1103/PhysRevB.58.R14741`.

[193] T. D. Kühner and S. R. White. Dynamical correlation functions using the density matrix renormalization group. *Phys. Rev. B*, 60:335–343, Jul 1999. doi:10.1103/PhysRevB.60.335. URL `https://link.aps.org/doi/10.1103/PhysRevB.60.335`.

[194] T. D. Kühner, S. R. White, and H. Monien. One-dimensional bose-hubbard model with nearest-neighbor interaction. *Phys. Rev. B*, 61:12474–12489, May 2000. doi:10.1103/PhysRevB.61.12474. URL `https://link.aps.org/doi/10.1103/PhysRevB.61.12474`.

[195] M. Kumar and Z. Soos. Decoupled phase of frustrated spin-1 2 antiferromagnetic chains with and without long-range order in the ground state. *Physical Review B*, 88(13):134412, 2013. doi:10.1103/PhysRevB.88.134412. URL `https://link.aps.org/doi/10.1103/PhysRevB.88.134412`.

[196] M. Kumar and Z. G. Soos. Spin-parity and broken symmetry in finite spin-$\frac{1}{2}$ chains with frustrated exchange: Quantum transition from high to low spin. *Phys. Rev. B*, 85: 144415, Apr 2012. doi:10.1103/PhysRevB.85.144415. URL `https://link.aps.org/doi/10.1103/PhysRevB.85.144415`.

[197] M. Kumar and Z. G. Soos. Spin-parity and broken symmetry in finite spin-1 2 chains with frustrated exchange: Quantum transition from high to low spin. *Physical Review B—Condensed Matter and Materials Physics*, 85(14):144415, 2012.

[198] M. Kumar, S. Ramasesha, D. Sen, and Z. G. Soos. Scaling exponents in spin-$\frac{1}{2}$ heisenberg chains with dimerization and frustration studied with the density-matrix renormalization group. *Phys. Rev. B*, 75:052404, Feb 2007. doi:10.1103/PhysRevB.75.052404. URL `https://link.aps.org/doi/10.1103/PhysRevB.75.052404`.

[199] M. Kumar, S. Ramasesha, and Z. G. Soos. Bond-order wave phase, spin solitons, and thermodynamics of a frustrated linear spin-$\frac{1}{2}$ heisenberg antiferromagnet. *Phys. Rev. B*,

81:054413, Feb 2010. doi:10.1103/PhysRevB.81.054413. URL `https://link.aps.org/doi/10.1103/PhysRevB.81.054413`.

[200] M. Kumar, S. Ramasesha, and Z. G. Soos. Bond-order wave phase, spin solitons, and thermodynamics of a frustrated linear spin-$\frac{1}{2}$ heisenberg antiferromagnet. *Phys. Rev. B*, 81:054413, Feb 2010. doi:10.1103/PhysRevB.81.054413. URL `https://link.aps.org/doi/10.1103/PhysRevB.81.054413`.

[201] M. Kumar, Z. G. Soos, D. Sen, and S. Ramasesha. Modified density matrix renormalization group algorithm for the zigzag spin-$\frac{1}{2}$ chain with frustrated antiferromagnetic exchange: Comparison with field theory at large J_2/J_1. *Phys. Rev. B*, 81:104406, Mar 2010. doi:10.1103/PhysRevB.81.104406. URL `https://link.aps.org/doi/10.1103/PhysRevB.81.104406`.

[202] M. Kumar, S. Dutton, R. Cava, and Z. Soos. Spin-flop and antiferromagnetic phases of the ferromagnetic half-twist ladder compounds ba3cu3in4o12 and ba3cu3sc4o12. *Journal of Physics: Condensed Matter*, 25(13):136004, 2013. doi:10.1088/0953-8984/25/13/136004. URL `https://doi.org/10.1088/0953-8984/25/13/136004`.

[203] M. Kumar, A. Parvej, and Z. G. Soos. Level crossing, spin structure factor and quantum phases of the frustrated spin-1/2 chain with first and second neighbor exchange. *Journal of Physics: Condensed Matter*, 27(31):316001, Jul 2015. ISSN 0953-8984. doi:10.1088/0953-8984/27/31/316001. URL `https://dx.doi.org/10.1088/0953-8984/27/31/316001`.

[204] M. Kumar, A. Parvej, and Z. G. Soos. Level crossing, spin structure factor and quantum phases of the frustrated spin-1/2 chain with first and second neighbor exchange. *Journal of Physics: Condensed Matter*, 27(31):316001, jul 2015. doi:10.1088/0953-8984/27/31/316001. URL `https://dx.doi.org/10.1088/0953-8984/27/31/316001`.

[205] M. Kumar, A. Parvej, and Z. G. Soos. Level crossing, spin structure factor and quantum phases of the frustrated spin-1/2 chain with first and second neighbor exchange. *Journal of Physics: Condensed Matter*, 27(31):316001, jul 2015. doi:10.1088/0953-8984/27/31/316001. URL `https://dx.doi.org/10.1088/0953-8984/27/31/316001`.

[206] C. Lacroix, P. Mendels, and F. Mila. *Introduction to frustrated magnetism: materials, experiments, theory*, volume 164. Springer Science & Business Media, 2011.

[207] C. Lanczos. An iteration method for the solution of the eigenvalue problem of linear differential and integral operators. 1950.

[208] C. Lanczos. Solution of systems of linear equations by minimized iterations. *J. Res. Nat. Bur. Standards*, 49(1):33–53, 1952.

[209] S. Langer, F. Heidrich-Meisner, J. Gemmer, I. P. McCulloch, and U. Schollwöck. Real-time study of diffusive and ballistic transport in spin-$\frac{1}{2}$ chains using the adaptive time-dependent density matrix renormalization group method. *Phys. Rev. B*, 79:214409, Jun

2009. doi:10.1103/PhysRevB.79.214409. URL https://link.aps.org/doi/10.1103/PhysRevB.79.214409.

[210] A. Läuchli, F. Mila, and K. Penc. Quadrupolar phases of the $s = 1$ bilinear-biquadratic heisenberg model on the triangular lattice. *Phys. Rev. Lett.*, 97:087205, Aug 2006. doi:10.1103/PhysRevLett.97.087205. URL https://link.aps.org/doi/10.1103/PhysRevLett.97.087205.

[211] K. Le Hur, A. Soret, and F. Yang. Majorana spin liquids, topology, and superconductivity in ladders. *Physical Review B*, 96(20):205109, 2017. doi:10.1103/PhysRevB.96.205109. URL https://link.aps.org/doi/10.1103/PhysRevB.96.205109.

[212] P. Lecheminant. One-dimensional spin liquids. In *Frustrated Spin Systems*, pages 307–366. World Scientific, 2004.

[213] J. Li, J.-Q. Cheng, T. Datta, and D.-X. Yao. Resonant inelastic x-ray scattering spectra of spinon, doublon, and quarton excitations of a spin-$\frac{1}{2}$ antiferromagnetic heisenberg trimer chain. *Phys. Rev. B*, 111:024404, Jan 2025. doi:10.1103/PhysRevB.111.024404. URL https://link.aps.org/doi/10.1103/PhysRevB.111.024404.

[214] K. Li. Topological magnons in kitaev magnets with finite dzyaloshinskii-moriya interaction at high field. *Chinese Physics Letters*, 40(2):027502, feb 2023. doi:10.1088/0256-307X/40/2/027502. URL https://dx.doi.org/10.1088/0256-307X/40/2/027502.

[215] P. H. Y. Li and R. F. Bishop. Ground-state phases of the spin-1J_1−J_2 heisenberg antiferromagnet on the honeycomb lattice. *Phys. Rev. B*, 93:214438, Jun 2016. doi:10.1103/PhysRevB.93.214438. URL https://link.aps.org/doi/10.1103/PhysRevB.93.214438.

[216] H. J. Liao, Z. Y. Xie, J. Chen, Z. Y. Liu, H. D. Xie, R. Z. Huang, B. Normand, and T. Xiang. Gapless spin-liquid ground state in the $s = 1/2$ kagome antiferromagnet. *Phys. Rev. Lett.*, 118:137202, Mar 2017. doi:10.1103/PhysRevLett.118.137202. URL https://link.aps.org/doi/10.1103/PhysRevLett.118.137202.

[217] C. D. Ling, M. C. Allison, S. Schmid, M. Avdeev, J. S. Gardner, C.-W. Wang, D. H. Ryan, M. Zbiri, and T. Söhnel. Striped magnetic ground state of the kagome lattice in $fe_4si_2sn_7o_{16}$. *Phys. Rev. B*, 96:180410, Nov 2017. doi:10.1103/PhysRevB.96.180410. URL https://link.aps.org/doi/10.1103/PhysRevB.96.180410.

[218] G.-H. Liu, W. Li, W.-L. You, G. Su, and G.-S. Tian. Quantum phase transitions and the 1/3 magnetization plateau in the spin-1/2 ferromagnetic–ferromagnetic–antiferromagnetic chain. *Journal of Magnetism and Magnetic Materials*, 377:12–18, 2015. ISSN 0304-8853. URL https://doi.org/10.1016/j.jmmm.2014.10.016.

[219] X. Liu, T. Berlijn, W.-G. Yin, W. Ku, A. Tsvelik, Y.-J. Kim, H. Gretarsson, Y. Singh, P. Gegenwart, and J. P. Hill. Long-range magnetic ordering in na$_2$iro$_3$. *Phys. Rev. B*, 83: 220403, Jun 2011. doi:10.1103/PhysRevB.83.220403. URL `https://link.aps.org/doi/10.1103/PhysRevB.83.220403`.

[220] X. Liu, T. Berlijn, W.-G. Yin, W. Ku, A. Tsvelik, Y.-J. Kim, H. Gretarsson, Y. Singh, P. Gegenwart, and J. P. Hill. Long-range magnetic ordering in na$_2$iro$_3$. *Phys. Rev. B*, 83: 220403, Jun 2011. doi:10.1103/PhysRevB.83.220403. URL `https://link.aps.org/doi/10.1103/PhysRevB.83.220403`.

[221] H. C. Longuet-Higgins and L. Salem. The alternation of bond lengths in long conjugated chain molecules. *Proceedings of the Royal Society of London. Series A. Mathematical and Physical Sciences*, 251(1265):172–185, 1959. URL `https://doi.org/10.1098/rspa.1959.0100`.

[222] H. T. Lu, Y. J. Wang, S. Qin, and T. Xiang. Zigzag spin chains with antiferromagnetic-ferromagnetic interactions: Transfer-matrix renormalization group study. *Phys. Rev. B*, 74:134425, Oct 2006. doi:10.1103/PhysRevB.74.134425. URL `https://link.aps.org/doi/10.1103/PhysRevB.74.134425`.

[223] J.-G. Lussier, S. M. Coad, D. F. McMorrow, and D. M. Paul. The temperature dependence of the spin - peierls energy gap in. *Journal of Physics: Condensed Matter*, 8(4):L59, jan 1996. doi:10.1088/0953-8984/8/4/003. URL `https://dx.doi.org/10.1088/0953-8984/8/4/003`.

[224] A. Luther and I. Peschel. Calculation of critical exponents in two dimensions from quantum field theory in one dimension. *Physical Review B*, 12(9):3908, 1975.

[225] N. Maeshima and K. Okunishi. Antiferromagnetic zigzag spin chain in magnetic fields at finite temperatures. *Phys. Rev. B*, 62:934–939, Jul 2000. doi:10.1103/PhysRevB.62.934. URL `https://link.aps.org/doi/10.1103/PhysRevB.62.934`.

[226] N. Maeshima, M. Hagiwara, Y. Narumi, K. Kindo, T. Kobayashi, and K. Okunishi. Magnetic properties of a s= 1/2 zigzag spin chain compound (n2h5) cucl3. *Journal of Physics: Condensed Matter*, 15(21):3607, 2003.

[227] C. K. Majumdar. Antiferromagnetic model with known ground state. *Journal of Physics C: Solid State Physics*, 3(4):911, 1970.

[228] C. K. Majumdar and D. K. Ghosh. On next-nearest-neighbor interaction in linear chain. i. *Journal of Mathematical Physics*, 10(8):1388–1398, 1969.

[229] C. K. Majumdar and D. K. Ghosh. On next-nearest-neighbor interaction in linear chain. ii. *Journal of Mathematical Physics*, 10(8):1399–1402, 1969.

[230] S. Mandal, S. Bhattacharjee, K. Sengupta, R. Shankar, and G. Baskaran. Confinement-deconfinement transition and spin correlations in a generalized kitaev model. *Physical Review B*, 84(15):155121, 2011. doi:10.1103/PhysRevB.84.155121. URL `https://link.aps.org/doi/10.1103/PhysRevB.84.155121`.

[231] M. C. Martin, G. Shirane, Y. Fujii, M. Nishi, O. Fujita, J. Akimitsu, M. Hase, and K. Uchinokura. Temperature dependence of the spin-peierls energy gap and anomalous line shapes in cugeo$_3$. *Phys. Rev. B*, 53:R14713–R14716, Jun 1996. doi:10.1103/PhysRevB.53.R14713. URL `https://link.aps.org/doi/10.1103/PhysRevB.53.R14713`.

[232] K. Matan, T. Ono, Y. Fukumoto, T. J. Sato, J. Yamaura, M. Yano, K. Morita, and H. Tanaka. Pinwheel valence-bond solid and triplet excitations in the two-dimensional deformed kagome lattice. *Nature Physics*, 6(11):865–869, Nov 2010. ISSN 1745-2481. doi:10.1038/nphys1761. URL `https://doi.org/10.1038/nphys1761`.

[233] M. Matsuda and K. Katsumata. Magnetic properties of a quasi-one-dimensional magnet with competing interactions: Srcuo2. *Journal of magnetism and magnetic materials*, 140: 1671–1672, 1995.

[234] P. A. McClarty, X.-Y. Dong, M. Gohlke, J. G. Rau, F. Pollmann, R. Moessner, and K. Penc. Topological magnons in kitaev magnets at high fields. *Phys. Rev. B*, 98: 060404, Aug 2018. doi:10.1103/PhysRevB.98.060404. URL `https://link.aps.org/doi/10.1103/PhysRevB.98.060404`.

[235] R. Melzi, P. Carretta, A. Lascialfari, M. Mambrini, M. Troyer, P. Millet, and F. Mila. li$_2$VO$(si, ge)O_4$, a prototype of a two-dimensional frustrated quantum heisenberg antiferromagnet. *Phys. Rev. Lett.*, 85:1318–1321, Aug 2000. doi:10.1103/PhysRevLett.85.1318. URL `https://link.aps.org/doi/10.1103/PhysRevLett.85.1318`.

[236] N. D. Mermin and H. Wagner. Absence of ferromagnetism or antiferromagnetism in one- or two-dimensional isotropic heisenberg models. *Phys. Rev. Lett.*, 17:1133–1136, Nov 1966. doi:10.1103/PhysRevLett.17.1133. URL `https://link.aps.org/doi/10.1103/PhysRevLett.17.1133`.

[237] R. Moessner and A. P. Ramirez. Geometrical frustration. *Physics Today*, 59(2):24–29, 02 2006. ISSN 0031-9228. doi:10.1063/1.2186278. URL `https://doi.org/10.1063/1.2186278`.

[238] A. Moreno, A. Muramatsu, and S. R. Manmana. Ground-state phase diagram of the one-dimensional t-j model. *Phys. Rev. B*, 83:205113, May 2011. doi:10.1103/PhysRevB.83.205113. URL `https://link.aps.org/doi/10.1103/PhysRevB.83.205113`.

[239] K. Morita and N. Shibata. Field-induced quantum phase transitions in s = 1/2 j1–j2 heisenberg model on square lattice. *Journal of the Physical Society of Japan*, 85(9):094708, 2016. doi:10.7566/JPSJ.85.094708. URL `https://doi.org/10.7566/JPSJ.85.094708`.

[240] T. Moriya. Anisotropic superexchange interaction and weak ferromagnetism. *Phys. Rev.*, 120:91–98, Oct 1960. doi:10.1103/PhysRev.120.91. URL `https://link.aps.org/doi/10.1103/PhysRev.120.91`.

[241] N. Motoyama, H. Eisaki, and S. Uchida. Magnetic susceptibility of ideal spin 1 /2 heisenberg antiferromagnetic chain systems, $\mathrm{sr_2cuo_3}$ and $\mathrm{srcuo_2}$. *Phys. Rev. Lett.*, 76:3212–3215, Apr 1996. doi:10.1103/PhysRevLett.76.3212. URL `https://link.aps.org/doi/10.1103/PhysRevLett.76.3212`.

[242] N. F. MOTT. Metal-insulator transition. *Rev. Mod. Phys.*, 40:677–683, Oct 1968. doi:10.1103/RevModPhys.40.677. URL `https://link.aps.org/doi/10.1103/RevModPhys.40.677`.

[243] M. Mourigal, M. Enderle, B. Fåk, R. Kremer, J. Law, A. Schneidewind, A. Hiess, and A. Prokofiev. Evidence of a bond-nematic phase in licuvo 4. *Physical review letters*, 109 (2):027203, 2012. doi:10.1103/PhysRevLett.109.027203. URL `https://link.aps.org/doi/10.1103/PhysRevLett.109.027203`.

[244] J. Nasu, Y. Kato, J. Yoshitake, Y. Kamiya, and Y. Motome. Spin-liquid–to–spin-liquid transition in kitaev magnets driven by fractionalization. *Phys. Rev. Lett.*, 118:137203, Mar 2017. doi:10.1103/PhysRevLett.118.137203. URL `https://link.aps.org/doi/10.1103/PhysRevLett.118.137203`.

[245] M. Nishi, O. Fujita, and J. Akimitsu. Neutron-scattering study on the spin-peierls transition in a quasi-one-dimensional magnet $\mathrm{cugeo_3}$. *Phys. Rev. B*, 50:6508–6510, Sep 1994. doi:10.1103/PhysRevB.50.6508. URL `https://link.aps.org/doi/10.1103/PhysRevB.50.6508`.

[246] S. Nishimoto and M. Nakamura. Non-symmetry-breaking ground state of the $s = 1$ heisenberg model on the kagome lattice. *Phys. Rev. B*, 92:140412, Oct 2015. doi:10.1103/PhysRevB.92.140412. URL `https://link.aps.org/doi/10.1103/PhysRevB.92.140412`.

[247] T. Nishino. Density matrix renormalization group method for 2d classical models. *Journal of the Physical Society of Japan*, 64(10):3598–3601, 1995. doi:10.1143/JPSJ.64.3598. URL `https://doi.org/10.1143/JPSJ.64.3598`.

[248] R. Noack, S. White, and D. Scalapino. The ground state of the two-leg hubbard ladder a density-matrix renormalization group study. *Physica C: Superconductivity*, 270(3):281–296, 1996. ISSN 0921-4534. doi:https://doi.org/10.1016/S0921-4534(96)00515-1. URL `https://www.sciencedirect.com/science/article/pii/S0921453496005151`.

[249] R. M. Noack, S. R. White, and D. J. Scalapino. Correlations in a two-chain hubbard model. *Phys. Rev. Lett.*, 73:882–885, Aug 1994. doi:10.1103/PhysRevLett.73.882. URL `https://link.aps.org/doi/10.1103/PhysRevLett.73.882`.

[250] R. M. Noack, S. R. White, and D. J. Scalapino. The doped two-chain hubbard model. *Europhysics Letters*, 30(3):163, apr 1995. doi:10.1209/0295-5075/30/3/007. URL `https://dx.doi.org/10.1209/0295-5075/30/3/007`.

[251] V. Noculak, D. Lozano-Gómez, J. Oitmaa, R. R. P. Singh, Y. Iqbal, M. J. P. Gingras, and J. Reuther. Classical and quantum phases of the pyrochlore $s = \frac{1}{2}$ magnet with heisenberg and dzyaloshinskii-moriya interactions. *Phys. Rev. B*, 107:214414, Jun 2023. doi:10.1103/PhysRevB.107.214414. URL `https://link.aps.org/doi/10.1103/PhysRevB.107.214414`.

[252] J. Oitmaa and D. D. Betts. The ground state of two quantum models of magnetism. *Canadian Journal of Physics*, 56(7):897–901, 1978. doi:10.1139/p78-120. URL `https://doi.org/10.1139/p78-120`.

[253] K. Okamoto and K. Nomura. Fluid-dimer critical point in s = 12 antiferromagnetic heisenberg chain with next nearest neighbor interactions. *Physics Letters A*, 169(6):433–437, 1992. ISSN 0375-9601. doi:https://doi.org/10.1016/0375-9601(92)90823-5. URL `https://www.sciencedirect.com/science/article/pii/0375960192908235`.

[254] K. Okamoto and K. Nomura. Fluid-dimer critical point in s = 12 antiferromagnetic heisenberg chain with next nearest neighbor interactions. *Physics Letters A*, 169(6):433–437, 1992. ISSN 0375-9601. doi:https://doi.org/10.1016/0375-9601(92)90823-5. URL `https://www.sciencedirect.com/science/article/pii/0375960192908235`.

[255] K. Okamoto, T. Tonegawa, Y. Takahashi, and M. Kaburagi. The ground state of an s= 1/2 distorted diamond chain-a model of cu3cl6 (h2o) 2· 2h8c4so2. *Journal of Physics: Condensed Matter*, 11(50):10485, 1999.

[256] K. Okamoto, T. Tonegawa, and M. Kaburagi. Magnetic properties of the s= 1/2 distorted diamond chain at t= 0. *Journal of Physics: Condensed Matter*, 15(35):5979, 2003.

[257] K. Okunishi and T. Tonegawa. Magnetic phase diagram of the s=1/2 antiferromagnetic zigzag spin chain in the strongly frustrated region: Cusp and plateau. *Journal of the Physical Society of Japan*, 72(3):479–482, 2003. doi:10.1143/JPSJ.72.479. URL `https://doi.org/10.1143/JPSJ.72.479`.

[258] M. Oshikawa, M. Yamanaka, and I. Affleck. Magnetization plateaus in spin chains: "haldane gap" for half-integer spins. *Phys. Rev. Lett.*, 78:1984–1987, Mar 1997. doi:10.1103/PhysRevLett.78.1984. URL `https://link.aps.org/doi/10.1103/PhysRevLett.78.1984`.

[259] M. Oshikawa, M. Yamanaka, and I. Affleck. Magnetization plateaus in spin chains: "haldane gap" for half-integer spins. *Phys. Rev. Lett.*, 78:1984–1987, Mar 1997. doi:10.1103/PhysRevLett.78.1984. URL `https://link.aps.org/doi/10.1103/PhysRevLett.78.1984`.

[260] R. V. Pai, R. Pandit, H. R. Krishnamurthy, and S. Ramasesha. One-dimensional disordered bosonic hubbard model: A density-matrix renormalization group study. *Phys. Rev. Lett.*, 76:2937–2940, Apr 1996. doi:10.1103/PhysRevLett.76.2937. URL `https://link.aps.org/doi/10.1103/PhysRevLett.76.2937`.

[261] T. Papenbrock, T. Barnes, D. J. Dean, M. V. Stoitsov, and M. R. Strayer. Density matrix renormalization group study of critical behavior of the spin $-\frac{1}{2}$ alternating heisenberg chain. *Phys. Rev. B*, 68:024416, Jul 2003. doi:10.1103/PhysRevB.68.024416. URL `https://link.aps.org/doi/10.1103/PhysRevB.68.024416`.

[262] T. Pardini, A. Menon, S. P. Hau-Riege, and R. R. P. Singh. Local entanglement and confinement transitions in the random transverse-field ising model on the pyrochlore lattice. *Phys. Rev. B*, 100:144437, Oct 2019. doi:10.1103/PhysRevB.100.144437. URL `https://link.aps.org/doi/10.1103/PhysRevB.100.144437`.

[263] S. Park, Y. Choi, C. Zhang, and S.-W. Cheong. Ferroelectricity in an s= 1/2 chain cuprate. *Physical review letters*, 98(5):057601, 2007. doi:10.1103/PhysRevLett.98.057601. URL `https://link.aps.org/doi/10.1103/PhysRevLett.98.057601`.

[264] A. Parvej and M. Kumar. Multipolar phase in frustrated spin-1/2 and spin-1 chains. *Phys. Rev. B*, 96:054413, Aug 2017. doi:10.1103/PhysRevB.96.054413. URL `https://link.aps.org/doi/10.1103/PhysRevB.96.054413`.

[265] R. E. Peierls. *Quantum Theory of Solids*. Clarendon Press, 1996.

[266] K. Penc and A. M. Läuchli. *Spin Nematic Phases in Quantum Spin Systems*, pages 331–362. Springer Berlin Heidelberg, Berlin, Heidelberg, 2011. ISBN 978-3-642-10589-0. doi:10.1007/978-3-642-10589-0_13. URL `https://doi.org/10.1007/978-3-642-10589-0_13`.

[267] I. Peschel and V. Eisler. *The Conceptual Background of Density-Matrix Renormalization*, pages 581–596. Springer Berlin Heidelberg, Berlin, Heidelberg, 2008. ISBN 978-3-540-74686-7. doi:10.1007/978-3-540-74686-7_20. URL `https://doi.org/10.1007/978-3-540-74686-7_20`.

[268] W. E. Pickett. Impact of structure on magnetic coupling in cav$_4$o$_9$. *Phys. Rev. Lett.*, 79: 1746–1749, Sep 1997. doi:10.1103/PhysRevLett.79.1746. URL `https://link.aps.org/doi/10.1103/PhysRevLett.79.1746`.

[269] K. W. Plumb, J. P. Clancy, L. J. Sandilands, V. V. Shankar, Y. F. Hu, K. S. Burch, H.-Y. Kee, and Y.-J. Kim. $\alpha - \text{rucl}_3$: A spin-orbit assisted mott insulator on a honeycomb lattice. *Phys. Rev. B*, 90:041112, Jul 2014. doi:10.1103/PhysRevB.90.041112. URL `https://link.aps.org/doi/10.1103/PhysRevB.90.041112`.

[270] D. Podolsky and E. Demler. Properties and detection of spin nematic order in strongly correlated electron systems. *New Journal of Physics*, 7(1):59, feb 2005. doi:10.1088/1367-2630/7/1/059. URL `https://dx.doi.org/10.1088/1367-2630/7/1/059`.

[271] K. Y. Povarov, Y. Feng, and A. Zheludev. Multiferroic phases of the frustrated quantum spin-chain compound linarite. *Phys. Rev. B*, 94:214409, Dec 2016. doi:10.1103/PhysRevB.94.214409. URL `https://link.aps.org/doi/10.1103/PhysRevB.94.214409`.

[272] Prabhakar, S. Pal, U. Kumar, M. Kumar, and A. Mukherjee. Predicting fractionalized multi-spin excitations in resonant inelastic x-ray spectra of frustrated spin-1/2 trimer chains, 2024. URL `https://arxiv.org/abs/2410.15082`.

[273] M. Pregelj, A. Zorko, O. Zaharko, H. Nojiri, H. Berger, L. Chapon, and D. Arčon. Spin-stripe phase in a frustrated zigzag spin-1/2 chain. *Nature communications*, 6(1):7255, 2015.

[274] M. Pregelj, A. Zorko, D. Arčon, M. Klanjšek, O. Zaharko, S. Krämer, M. Horvatić, and A. Prokofiev. Thermal effects versus spin nematicity in a frustrated spin-1 2 chain. *Physical Review B*, 102(8):081104, 2020. doi:10.1103/PhysRevB.102.081104. URL `https://link.aps.org/doi/10.1103/PhysRevB.102.081104`.

[275] E. Pytte. Peierls instability in heisenberg chains. *Phys. Rev. B*, 10:4637–4642, Dec 1974. doi:10.1103/PhysRevB.10.4637. URL `https://link.aps.org/doi/10.1103/PhysRevB.10.4637`.

[276] C. Raghu, Y. Anusooya Pati, and S. Ramasesha. Density-matrix renormalization-group study of low-lying excitations of polyacene within a pariser-parr-pople model. *Phys. Rev. B*, 66:035116, Jul 2002. doi:10.1103/PhysRevB.66.035116. URL `https://link.aps.org/doi/10.1103/PhysRevB.66.035116`.

[277] S. Ramasesha, S. K. Pati, H. R. Krishnamurthy, Z. Shuai, and J. L. Brédas. Symmetrized density-matrix renormalization-group method for excited states of hubbard models. *Phys. Rev. B*, 54:7598–7601, Sep 1996. doi:10.1103/PhysRevB.54.7598. URL `https://link.aps.org/doi/10.1103/PhysRevB.54.7598`.

[278] K. Ran, J. Wang, W. Wang, Z.-Y. Dong, X. Ren, S. Bao, S. Li, Z. Ma, Y. Gan, Y. Zhang, J. T. Park, G. Deng, S. Danilkin, S.-L. Yu, J.-X. Li, and J. Wen. Spin-wave excitations evidencing the kitaev interaction in single crystalline $\alpha{-}\text{rucl}_3$. *Phys. Rev. Lett.*, 118:

107203, Mar 2017. doi:10.1103/PhysRevLett.118.107203. URL https://link.aps.org/doi/10.1103/PhysRevLett.118.107203.

[279] S. Rapsch, U. Schollwöck, and W. Zwerger. Density matrix renormalization group for disordered bosons in one dimension. *Europhysics Letters*, 46(5):559, jun 1999. doi:10.1209/epl/i1999-00302-7. URL https://dx.doi.org/10.1209/epl/i1999-00302-7.

[280] J. G. Rau, E. K.-H. Lee, and H.-Y. Kee. Generic spin model for the honeycomb iridates beyond the kitaev limit. *Phys. Rev. Lett.*, 112:077204, Feb 2014. doi:10.1103/PhysRevLett.112.077204. URL https://link.aps.org/doi/10.1103/PhysRevLett.112.077204.

[281] J. G. Rau, E. K.-H. Lee, and H.-Y. Kee. Generic spin model for the honeycomb iridates beyond the kitaev limit. *Phys. Rev. Lett.*, 112:077204, Feb 2014. doi:10.1103/PhysRevLett.112.077204. URL https://link.aps.org/doi/10.1103/PhysRevLett.112.077204.

[282] J. G. Rau, E. K.-H. Lee, and H.-Y. Kee. Spin-orbit physics giving rise to novel phases in correlated systems: Iridates and related materials. *Annual Review of Condensed Matter Physics*, 7(1):195–221, 2016. doi:https://doi.org/10.1146/annurev-conmatphys-031115-011319.

[283] J. D. Reger and A. P. Young. Monte carlo simulations of the spin-(1/2 heisenberg antiferromagnet on a square lattice. *Phys. Rev. B*, 37:5978–5981, Apr 1988. doi:10.1103/PhysRevB.37.5978. URL https://link.aps.org/doi/10.1103/PhysRevB.37.5978.

[284] L. P. Regnault, M. Aïn, B. Hennion, G. Dhalenne, and A. Revcolevschi. Inelastic-neutron-scattering investigation of the spin-peierls system cugeo$_3$. *Phys. Rev. B*, 53:5579–5597, Mar 1996. doi:10.1103/PhysRevB.53.5579. URL https://link.aps.org/doi/10.1103/PhysRevB.53.5579.

[285] Y.-Z. Ren, N.-H. Tong, and X.-C. Xie. Cluster mean-field theory study of j1j2 heisenberg model on a square lattice. *Journal of Physics: Condensed Matter*, 26(11):115601, mar 2014. doi:10.1088/0953-8984/26/11/115601. URL https://dx.doi.org/10.1088/0953-8984/26/11/115601.

[286] J.-P. Renard. *Magnetic Phase Transitions in Low-Dimensional Systems*, pages 125–140. Springer US, New York, NY, 1987. ISBN 978-1-4899-2091-1. doi:10.1007/978-1-4899-2091-1_9. URL https://doi.org/10.1007/978-1-4899-2091-1_9.

[287] S. Rettrup. An iterative method for calculating several of the extreme eigensolutions of large real non-symmetric matrices. *Journal of Computational Physics*, 45(1):100–107,

1982. ISSN 0021-9991. doi:https://doi.org/10.1016/0021-9991(82)90104-8. URL `https://www.sciencedirect.com/science/article/pii/0021999182901048`.

[288] J. Reuther, R. Thomale, and S. Rachel. Spiral order in the honeycomb iridate li$_2$iro$_3$. *Phys. Rev. B*, 90:100405, Sep 2014. doi:10.1103/PhysRevB.90.100405. URL `https://link.aps.org/doi/10.1103/PhysRevB.90.100405`.

[289] R. Riedinger and M. Benard. Quantum chemistry without diagonalization: An extension of the lanczos method to molecules and solids. *The Journal of Chemical Physics*, 94(2): 1222–1228, 01 1991. ISSN 0021-9606. doi:10.1063/1.460030. URL `https://doi.org/10.1063/1.460030`.

[290] J. Riera and A. Dobry. Magnetic susceptibility in the spin-peierls system cugeo$_3$. *Phys. Rev. B*, 51:16098–16102, Jun 1995. doi:10.1103/PhysRevB.51.16098. URL `https://link.aps.org/doi/10.1103/PhysRevB.51.16098`.

[291] K. F. Riley, M. P. Hobson, and S. J. Bence. *Mathematical methods for physics and engineering: a comprehensive guide.* Cambridge university press, 2006.

[292] M. Rizzi, D. Rossini, G. De Chiara, S. Montangero, and R. Fazio. Phase diagram of spin-1 bosons on one-dimensional lattices. *Phys. Rev. Lett.*, 95:240404, Dec 2005. doi:10.1103/PhysRevLett.95.240404. URL `https://link.aps.org/doi/10.1103/PhysRevLett.95.240404`.

[293] D. Rossini and R. Fazio. Phase diagram of the extended bose–hubbard model. *New Journal of Physics*, 14(6):065012, jun 2012. doi:10.1088/1367-2630/14/6/065012. URL `https://dx.doi.org/10.1088/1367-2630/14/6/065012`.

[294] I. Rousochatzakis, N. B. Perkins, Q. Luo, and H.-Y. Kee. Beyond kitaev physics in strong spin-orbit coupled magnets. *Reports on Progress in Physics*, 87(2):026502, feb 2024. doi:10.1088/1361-6633/ad208d. URL `https://dx.doi.org/10.1088/1361-6633/ad208d`.

[295] M. Routh, S. K. Saha, M. Kumar, and Z. G. Soos. Spin-peierls transition of $J_1 - J_2$ and extended models with ferromagnetic J_1: Sublattice dimerization and thermodynamics of zigzag chains in $\beta-$tevo$_4$. *Phys. Rev. B*, 105:235109, Jun 2022. doi:10.1103/PhysRevB.105.235109. URL `https://link.aps.org/doi/10.1103/PhysRevB.105.235109`.

[296] M. Routh, S. Ghosh, J. van den Brink, S. Nishimoto, and M. Kumar. Emergent quadrupolar order in the spin-$\frac{1}{2}$ kitaev-heisenberg model. *Phys. Rev. B*, 109:L220403, Jun 2024. doi:10.1103/PhysRevB.109.L220403. URL `https://link.aps.org/doi/10.1103/PhysRevB.109.L220403`.

[297] K. Rule, B. Willenberg, M. Schäpers, A. Wolter, B. Büchner, S.-L. Drechsler, G. Ehlers, D. Tennant, R. Mole, J. Gardner, et al. Dynamics of linarite: Observations of magnetic excitations. *Physical Review B*, 95(2):024430, 2017.

[298] S. Sachdev. Kagome- and triangular-lattice heisenberg antiferromagnets: Ordering from quantum fluctuations and quantum-disordered ground states with unconfined bosonic spinons. *Phys. Rev. B*, 45:12377–12396, Jun 1992. doi:10.1103/PhysRevB.45.12377. URL `https://link.aps.org/doi/10.1103/PhysRevB.45.12377`.

[299] S. K. Saha, D. Dey, M. Kumar, and Z. G. Soos. Hybrid exact diagonalization and density matrix renormalization group approach to the thermodynamics of one-dimensional quantum models. *Phys. Rev. B*, 99:195144, May 2019. doi:10.1103/PhysRevB.99.195144. URL `https://link.aps.org/doi/10.1103/PhysRevB.99.195144`.

[300] S. K. Saha, M. S. Roy, M. Kumar, and Z. G. Soos. Modeling the spin-peierls transition of spin-$\frac{1}{2}$ chains with correlated states: $J_1 - J_2$ model, cugeo$_3$, and TTF$--$cus$_4$c$_4$(CF$_3$)$_4$. *Phys. Rev. B*, 101:054411, Feb 2020. doi:10.1103/PhysRevB.101.054411. URL `https://link.aps.org/doi/10.1103/PhysRevB.101.054411`.

[301] S. K. Saha, M. Routh, M. Kumar, and Z. G. Soos. Low-temperature thermodynamics of the antiferromagnetic $J_1 - J_2$ model: Entropy, critical points, and spin gap. *Phys. Rev. B*, 103:245139, Jun 2021. doi:10.1103/PhysRevB.103.245139. URL `https://link.aps.org/doi/10.1103/PhysRevB.103.245139`.

[302] S. K. Saha, D. Maiti, M. Kumar, and Z. G. Soos. Density matrix renormalization group approach to the low temperature thermodynamics of correlated 1d fermionic models. *Journal of Magnetism and Magnetic Materials*, 552:169150, 2022. ISSN 0304-8853. doi:https://doi.org/10.1016/j.jmmm.2022.169150. URL `https://www.sciencedirect.com/science/article/pii/S0304885322001160`.

[303] T. Saha-Dasgupta. The fascinating world of low-dimensional quantum spin systems: Ab initio modeling. *Molecules*, 26(6), 2021. ISSN 1420-3049. doi:10.3390/molecules26061522. URL `https://www.mdpi.com/1420-3049/26/6/1522`.

[304] T. Saha-Dasgupta, R. Valentí, F. Capraro, and C. Gros. na$_2$v$_3$o$_7$: A frustrated nanotubular system with spin-1/2 diamond ring geometry. *Phys. Rev. Lett.*, 95:107201, Sep 2005. doi:10.1103/PhysRevLett.95.107201. URL `https://link.aps.org/doi/10.1103/PhysRevLett.95.107201`.

[305] H. Sakurai, K. Yoshimura, K. Kosuge, N. Tsujii, H. Abe, H. Kitazawa, G. Kido, H. Michor, and G. Hilscher. Antiferromagnetic order in bi 4 cu 3 v 2 o 14 with novel spin chain. *Journal of the Physical Society of Japan*, 71(4):1161–1165, 2002.

[306] A. W. Sandvik. Computational studies of quantum spin systems. *AIP Conference Proceedings*, 1297(1):135–338, 2010. doi:10.1063/1.3518900.

[307] A. W. Sandvik. Computational studies of quantum spin systems. *AIP Conference Proceedings*, 1297(1):135–338, 2010. doi:10.1063/1.3518900.

[308] A. W. Sandvik. Computational studies of quantum spin systems. In *AIP Conference Proceedings*, volume 1297, pages 135–338. American Institute of Physics, 2010. URL `https://doi.org/10.1063/1.3518900`.

[309] K. Sano and K. Takano. Spin gap of s= 1/2 heisenberg model on distorted diamond chain. *Journal of the Physical Society of Japan*, 69(8):2710–2711, 2000.

[310] A. Saúl and G. Radtke. Density functional approach for the magnetism of β-tevo$_4$. *Phys. Rev. B*, 89:104414, Mar 2014. doi:10.1103/PhysRevB.89.104414. URL `https://link.aps.org/doi/10.1103/PhysRevB.89.104414`.

[311] L. Savary and L. Balents. Quantum spin liquids: a review. *Reports on Progress in Physics*, 80(1):016502, nov 2016. doi:10.1088/0034-4885/80/1/016502. URL `https://dx.doi.org/10.1088/0034-4885/80/1/016502`.

[312] Y. Savina, O. Bludov, V. Pashchenko, S. L. Gnatchenko, P. Lemmens, and H. Berger. Magnetic properties of the antiferromagnetic spin-$\frac{1}{2}$ chain system β-tevo$_4$. *Phys. Rev. B*, 84:104447, Sep 2011. doi:10.1103/PhysRevB.84.104447. URL `https://link.aps.org/doi/10.1103/PhysRevB.84.104447`.

[313] Y. A. Savina, A. Bludov, V. Pashchenko, S. Gnatchenko, T. Zajarniuk, M. Gutowska, A. Szewczyk, P. Lemmens, and H. Berger. Heat capacity properties of quasi-one-dimensional magnet β-tevo4. *Low Temperature Physics*, 41(11):909–910, 2015.

[314] Y. O. Savina, O. Bludov, V. Pashchenko, S. Gnatchenko, P. Lemmens, and H. Berger. Features of the magnetic properties of quasi-one-dimensional β-tevo4 magnets at low temperatures. *Low Temperature Physics*, 41(4):283–286, 2015.

[315] R. Schaffer, S. Bhattacharjee, and Y. B. Kim. Quantum phase transition in heisenberg-kitaev model. *Physical Review B*, 86(22):224417, 2012. doi:10.1103/PhysRevB.86.224417. URL `https://link.aps.org/doi/10.1103/PhysRevB.86.224417`.

[316] J. Schlappa, U. Kumar, K. Zhou, S. Singh, M. Mourigal, V. Strocov, A. Revcolevschi, L. Patthey, H. Rønnow, S. Johnston, et al. Probing multi-spinon excitations outside of the two-spinon continuum in the antiferromagnetic spin chain cuprate sr2cuo3. *Nature Communications*, 9(1):5394, 2018. doi:10.1038/s41467-018-07838-y. URL `https://doi.org/10.1038/s41467-018-07838-y`.

[317] N. Schlünzen, J.-P. Joost, F. Heidrich-Meisner, and M. Bonitz. Nonequilibrium dynamics in the one-dimensional fermi-hubbard model: Comparison of the nonequilibrium green-functions approach and the density matrix renormalization group method. *Phys. Rev. B*,

95:165139, Apr 2017. doi:10.1103/PhysRevB.95.165139. URL `https://link.aps.org/doi/10.1103/PhysRevB.95.165139`.

[318] P. Schmitteckert. Nonequilibrium electron transport using the density matrix renormalization group method. *Phys. Rev. B*, 70:121302, Sep 2004. doi:10.1103/PhysRevB.70.121302. URL `https://link.aps.org/doi/10.1103/PhysRevB.70.121302`.

[319] U. Schollwöck. The density-matrix renormalization group. *Rev. Mod. Phys.*, 77:259–315, Apr 2005. doi:10.1103/RevModPhys.77.259. URL `https://link.aps.org/doi/10.1103/RevModPhys.77.259`.

[320] U. Schollwöck. Time-dependent density-matrix renormalization-group methods. *Journal of the Physical Society of Japan*, 74(Suppl):246–255, 2005. doi:10.1143/JPSJS.74S.246. URL `https://doi.org/10.1143/JPSJS.74S.246`.

[321] U. Schollwöck. The density-matrix renormalization group in the age of matrix product states. *Annals of Physics*, 326(1):96–192, 2011. ISSN 0003-4916. doi:https://doi.org/10.1016/j.aop.2010.09.012. URL `https://www.sciencedirect.com/science/article/pii/S0003491610001752`. January 2011 Special Issue.

[322] U. Schollwöck. The density-matrix renormalization group in the age of matrix product states. *Annals of Physics*, 326(1):96–192, 2011. ISSN 0003-4916. doi:https://doi.org/10.1016/j.aop.2010.09.012. URL `https://www.sciencedirect.com/science/article/pii/S0003491610001752`. January 2011 Special Issue.

[323] H. J. Schulz. Dynamics of coupled quantum spin chains. *Phys. Rev. Lett.*, 77:2790–2793, Sep 1996. doi:10.1103/PhysRevLett.77.2790. URL `https://link.aps.org/doi/10.1103/PhysRevLett.77.2790`.

[324] N. Shannon, T. Momoi, and P. Sindzingre. Nematic order in square lattice frustrated ferromagnets. *Phys. Rev. Lett.*, 96:027213, Jan 2006. doi:10.1103/PhysRevLett.96.027213. URL `https://link.aps.org/doi/10.1103/PhysRevLett.96.027213`.

[325] P. V. Shevchenko, V. N. Kotov, and O. P. Sushkov. Spectrum of elementary and collective excitations in the dimerized $s = 1/2$ heisenberg chain with frustration. *Phys. Rev. B*, 60: 3305–3315, Aug 1999. doi:10.1103/PhysRevB.60.3305. URL `https://link.aps.org/doi/10.1103/PhysRevB.60.3305`.

[326] N. Shibata. Thermodynamics of the anisotropic heisenberg chain calculated by the density matrix renormalization group method. *Journal of the Physical Society of Japan*, 66(8): 2221–2223, 1997. doi:10.1143/JPSJ.66.2221. URL `https://doi.org/10.1143/JPSJ.66.2221`.

[327] T. Shirakawa, T. Tohyama, J. Kokalj, S. Sota, and S. Yunoki. Ground-state phase diagram of the triangular lattice hubbard model by the density-matrix renormalization

group method. *Phys. Rev. B*, 96:205130, Nov 2017. doi:10.1103/PhysRevB.96.205130. URL `https://link.aps.org/doi/10.1103/PhysRevB.96.205130`.

[328] R. R. Singh, M. E. Fisher, and R. Shankar. Spin-(1/2 antiferromagnetic xxz chain: New results and insights. *Physical Review B*, 39(4):2562, 1989.

[329] Y. Singh and P. Gegenwart. Antiferromagnetic mott insulating state in single crystals of the honeycomb lattice material na_2iro_3. *Phys. Rev. B*, 82:064412, Aug 2010. doi:10.1103/PhysRevB.82.064412. URL `https://link.aps.org/doi/10.1103/PhysRevB.82.064412`.

[330] Y. Singh, S. Manni, J. Reuther, T. Berlijn, R. Thomale, W. Ku, S. Trebst, and P. Gegenwart. Relevance of the heisenberg-kitaev model for the honeycomb lattice iridates a 2 iro 3. *Physical review letters*, 108(12):127203, 2012. doi:10.1103/PhysRevLett.108.127203. URL `https://link.aps.org/doi/10.1103/PhysRevLett.108.127203`.

[331] J. Sirker. Thermodynamics of multiferroic spin chains. *Physical Review B*, 81(1):014419, 2010. doi:10.1103/PhysRevB.81.014419. URL `https://link.aps.org/doi/10.1103/PhysRevB.81.014419`.

[332] J. Sirker, V. Y. Krivnov, D. Dmitriev, A. Herzog, O. Janson, S. Nishimoto, S.-L. Drechsler, and J. Richter. J 1- j 2 heisenberg model at and close to its z= 4 quantum critical point. *Physical Review B*, 84(14):144403, 2011. doi:10.1103/PhysRevB.84.144403. URL `https://link.aps.org/doi/10.1103/PhysRevB.84.144403`.

[333] A. V. Sologubenko, K. Giannò, H. R. Ott, A. Vietkine, and A. Revcolevschi. Heat transport by lattice and spin excitations in the spin-chain compounds $srcuo_2$ and sr_2cuo_3. *Phys. Rev. B*, 64:054412, Jul 2001. doi:10.1103/PhysRevB.64.054412. URL `https://link.aps.org/doi/10.1103/PhysRevB.64.054412`.

[334] Z. G. Soos, A. Parvej, and M. Kumar. Numerical study of incommensurate and decoupled phases of spin-1/2 chains with isotropic exchange j1, j2 between first and second neighbors. *Journal of Physics: Condensed Matter*, 28(17):175603, mar 2016. doi:10.1088/0953-8984/28/17/175603. URL `https://dx.doi.org/10.1088/0953-8984/28/17/175603`.

[335] Z. G. Soos, A. Parvej, and M. Kumar. Numerical study of incommensurate and decoupled phases of spin-1/2 chains with isotropic exchange j1, j2 between first and second neighbors. *Journal of Physics: Condensed Matter*, 28(17):175603, mar 2016. doi:10.1088/0953-8984/28/17/175603. URL `https://dx.doi.org/10.1088/0953-8984/28/17/175603`.

[336] E. S. So/rensen and I. Affleck. S(k) for haldane-gap antiferromagnets: Large-scale numerical results versus field theory and experiment. *Phys. Rev. B*, 49:13235–13238, May 1994. doi:10.1103/PhysRevB.49.13235. URL `https://link.aps.org/doi/10.1103/PhysRevB.49.13235`.

[337] E. S. So/rensen and I. Affleck. Equal-time correlations in haldane-gap antiferromagnets. *Phys. Rev. B*, 49:15771–15788, Jun 1994. doi:10.1103/PhysRevB.49.15771. URL `https://link.aps.org/doi/10.1103/PhysRevB.49.15771`.

[338] C. Stoll, O. Janka, R. Pöttgen, M. Seibald, D. Baumann, K. Wurst, and H. Huppertz. Short-range antiferromagnetic ordering of netlike s = 1/2 linear trimeric units in the copper germanate $K_2Cu_3Ge_4O_{12}$. *Inorganic Chemistry*, 57(22):14421–14426, Nov 2018. ISSN 0020-1669. doi:10.1021/acs.inorgchem.8b02594. URL `https://doi.org/10.1021/acs.inorgchem.8b02594`.

[339] E. Stoudenmire and S. R. White. Studying two-dimensional systems with the density matrix renormalization group. *Annual Review of Condensed Matter Physics*, 3(Volume 3, 2012):111–128, 2012. ISSN 1947-5462. doi:https://doi.org/10.1146/annurev-conmatphys-020911-125018. URL `https://www.annualreviews.org/content/journals/10.1146/annurev-conmatphys-020911-125018`.

[340] W.-P. Su, J. Schrieffer, and A. Heeger. Soliton excitations in polyacetylene. *Physical Review B*, 22(4):2099, 1980. doi:10.1103/PhysRevB.22.2099. URL `https://link.aps.org/doi/10.1103/PhysRevB.22.2099`.

[341] J. Sudan, A. Lüscher, and A. M. Läuchli. Emergent multipolar spin correlations in a fluctuating spiral: The frustrated ferromagnetic spin-$\frac{1}{2}$ heisenberg chain in a magnetic field. *Phys. Rev. B*, 80:140402, Oct 2009. doi:10.1103/PhysRevB.80.140402. URL `https://link.aps.org/doi/10.1103/PhysRevB.80.140402`.

[342] H. Suzuki and K. Takano. Scaling property of the f–af spin chain near the exactly solvable point. *Journal of the Physical Society of Japan*, 79(4):044002, 2010. doi:10.1143/JPSJ.79.044002. URL `https://journals.jps.jp/doi/abs/10.1143/JPSJ.79.044002`.

[343] H. Suzuki, H. Liu, J. Bertinshaw, K. Ueda, H. Kim, S. Laha, D. Weber, Z. Yang, L. Wang, H. Takahashi, et al. Proximate ferromagnetic state in the kitaev model material α-rucl3. *Nature communications*, 12(1):4512, 2021. doi:10.1038/s41467-021-24722-4. URL `https://doi.org/10.1038/s41467-021-24722-4`.

[344] D. t. Swank and R. Willett. The crystal structure of cu3cl6 (h2o) 2· 2h8c4so2, trans tetra-μ-[chlorodichlorodiaquocopper (ii)] copper (ii) bis (tetramethylene sulfone), and the molecular structure of the cu3cl6 (h2o) 2 trimer. *Inorganica Chimica Acta*, 8:143–148, 1974.

[345] S. Sykora, A. Hübsch, and K. W. Becker. Computer-aided perturbation theory by cumulants: Dimerized and frustrated spin-$\frac{1}{2}$ chain. *Phys. Rev. B*, 70:054408, Aug 2004. doi:10.1103/PhysRevB.70.054408. URL `https://link.aps.org/doi/10.1103/PhysRevB.70.054408`.

[346] A. Szasz, J. Motruk, M. P. Zaletel, and J. E. Moore. Chiral spin liquid phase of the triangular lattice hubbard model: A density matrix renormalization group study. *Phys. Rev. X*, 10:021042, May 2020. doi:10.1103/PhysRevX.10.021042. URL `https://link.aps.org/doi/10.1103/PhysRevX.10.021042`.

[347] H. Takagi, T. Takayama, G. Jackeli, G. Khaliullin, and S. E. Nagler. Concept and realization of kitaev quantum spin liquids. *Nature Reviews Physics*, 1(4):264–280, Apr 2019. ISSN 2522-5820. doi:10.1038/s42254-019-0038-2. URL `https://doi.org/10.1038/s42254-019-0038-2`.

[348] M. O. Takahashi, M. G. Yamada, D. Takikawa, T. Mizushima, and S. Fujimoto. Topological nematic phase transition in kitaev magnets under applied magnetic fields. *Phys. Rev. Res.*, 3:023189, Jun 2021. doi:10.1103/PhysRevResearch.3.023189. URL `https://link.aps.org/doi/10.1103/PhysRevResearch.3.023189`.

[349] K. Takano, K. Kubo, and H. Sakamoto. Ground states with cluster structures in a frustrated heisenberg chain. *Journal of Physics: Condensed Matter*, 8(35):6405, 1996.

[350] T. Takayama, A. Kato, R. Dinnebier, J. Nuss, H. Kono, L. Veiga, G. Fabbris, D. Haskel, and H. Takagi. Hyperhoneycomb iridate β- li 2 iro 3 as a platform for kitaev magnetism. *Physical review letters*, 114(7):077202, 2015. doi:10.1103/PhysRevLett.114.077202. URL `https://link.aps.org/doi/10.1103/PhysRevLett.114.077202`.

[351] K. Tanaka and C. Hotta. Multiple quadrupolar or nematic phases driven by the heisenberg interactions in a spin-1 dimer system forming a bilayer. *Phys. Rev. B*, 101:094422, Mar 2020. doi:10.1103/PhysRevB.101.094422. URL `https://link.aps.org/doi/10.1103/PhysRevB.101.094422`.

[352] M. Tezuka, R. Arita, and H. Aoki. Phase diagram for the one-dimensional hubbard-holstein model: A density-matrix renormalization group study. *Phys. Rev. B*, 76:155114, Oct 2007. doi:10.1103/PhysRevB.76.155114. URL `https://link.aps.org/doi/10.1103/PhysRevB.76.155114`.

[353] T. Tonegawa and I. Harada. Ground-state properties of the one-dimensional isotropic spin-1/2 heisenberg antiferromagnet with competing interactions. *Journal of the Physical Society of Japan*, 56(6):2153–2167, 1987. doi:10.1143/JPSJ.56.2153. URL `https://doi.org/10.1143/JPSJ.56.2153`.

[354] T. Tonegawa and I. Harada. Ground-state properties of the one-dimensional isotropic spin-1/2 heisenberg antiferromagnet with competing interactions. *Journal of the Physical Society of Japan*, 56(6):2153–2167, 1987.

[355] T. Tonegawa, K. Okamoto, T. Hikihara, Y. Takahashi, and M. Kaburagi. Ground state of an s= 1/2 distorted diamond chain in a finite magnetic field. *Journal of Physics and Chemistry of Solids*, 62(1-2):125–128, 2001.

[356] S. Trebst and C. Hickey. Kitaev materials. *Physics Reports*, 950:1–37, 2022. ISSN 0370-1573. doi:https://doi.org/10.1016/j.physrep.2021.11.003. URL `https://www.sciencedirect.com/science/article/pii/S0370157321004051`. Kitaev materials.

[357] S. Trebst and C. Hickey. Kitaev materials. *Physics Reports*, 950:1–37, 2022. ISSN 0370-1573. doi:https://doi.org/10.1016/j.physrep.2021.11.003. URL `https://www.sciencedirect.com/science/article/pii/S0370157321004051`. Kitaev materials.

[358] A. A. Tsirlin and P. Gegenwart. Kitaev magnetism through the prism of lithium iridate. *physica status solidi (b)*, 259(5):2100146, 2022. doi:10.1002/pssb.202100146. URL `https://doi.org/10.1002/pssb.202100146`.

[359] A. A. Tsirlin, A. A. Belik, R. V. Shpanchenko, E. V. Antipov, E. Takayama-Muromachi, and H. Rosner. Frustrated spin-12 square lattice in the layered perovskite PbVo$_3$. *Phys. Rev. B*, 77:092402, Mar 2008. doi:10.1103/PhysRevB.77.092402. URL `https://link.aps.org/doi/10.1103/PhysRevB.77.092402`.

[360] A. A. Tsirlin, D. F. Weickert, N. Harrison, M. Jaime, and R. Stern. P11530-e005-pf: Magnetization measurements on single crystals -tevo4. 3 2017. doi:10.2172/1345914. URL `https://www.osti.gov/biblio/1345914`.

[361] H. Tsunetsugu and M. Arikawa. Spin nematic phase in s=1 triangular antiferromagnets. *Journal of the Physical Society of Japan*, 75(8):083701, 2006. doi:10.1143/JPSJ.75.083701. URL `https://doi.org/10.1143/JPSJ.75.083701`.

[362] C. P. Tu, Z. Ma, H. R. Wang, Y. H. Jiao, D. Z. Dai, and S. Y. Li. Gapped quantum spin liquid in a triangular-lattice ising-type antiferromagnet prmgal$_{11}$o$_{19}$. *Phys. Rev. Res.*, 6:043147, Nov 2024. doi:10.1103/PhysRevResearch.6.043147. URL `https://link.aps.org/doi/10.1103/PhysRevResearch.6.043147`.

[363] K. Uchinokura. Spin-peierls transition in cugeo3 and impurity-induced ordered phases in low-dimensional spin-gap systems. *Journal of Physics: Condensed Matter*, 14(10): R195, feb 2002. doi:10.1088/0953-8984/14/10/201. URL `https://dx.doi.org/10.1088/0953-8984/14/10/201`.

[364] Y. Ueda. Vanadate family as spin-gap systems. *Chemistry of Materials*, 10(10):2653–2664, Oct 1998. ISSN 0897-4756. doi:10.1021/cm980215w. URL `https://doi.org/10.1021/cm980215w`.

[365] R. Valentí, T. Saha-Dasgupta, J. V. Alvarez, K. Požgajčić, and C. Gros. Modeling the electronic behavior of $\gamma-$liv$_2O_5$: A microscopic study. *Phys. Rev. Lett.*, 86:5381–5384, Jun 2001. doi:10.1103/PhysRevLett.86.5381. URL `https://link.aps.org/doi/10.1103/PhysRevLett.86.5381`.

[366] M. Van Damme, R. Vanhove, J. Haegeman, F. Verstraete, and L. Vanderstraeten. Efficient matrix product state methods for extracting spectral information on rings and cylinders. *Phys. Rev. B*, 104:115142, Sep 2021. doi:10.1103/PhysRevB.104.115142. URL `https://link.aps.org/doi/10.1103/PhysRevB.104.115142`.

[367] A. N. Vasil'ev, L. A. Ponomarenko, H. Manaka, I. Yamada, M. Isobe, and Y. Ueda. Magnetic and resonant properties of quasi-one-dimensional antiferromagnet licuvo$_4$. *Phys. Rev. B*, 64:024419, Jun 2001. doi:10.1103/PhysRevB.64.024419. URL `https://link.aps.org/doi/10.1103/PhysRevB.64.024419`.

[368] A. Vasiliev, O. Volkova, E. Zvereva, and M. Markina. Milestones of low-d quantum magnetism. *npj Quantum Materials*, 3(1):18, 2018. URL `https://doi.org/10.1038/s41535-018-0090-7`.

[369] A. N. Vasiliev, O. S. Volkova, E. A. Zvereva, and M. Markina. *Low-dimensional magnetism*. CRC Press, 2019. URL `https://doi.org/10.1201/9780429288319`.

[370] T. Verkholyak, A. Honecker, and W. Brenig. Jordan-wigner approach to the frustrated spin one-half xxz chain. *The European Physical Journal B-Condensed Matter and Complex Systems*, 49:283–287, 2006.

[371] J. Wang, J. W. Li, P. Chen, and B. Tang. Interacting topological magnons in the kitaev-heisenberg honeycomb ferromagnet with the dzyaloshinskii-moriya interaction, 2025. URL `https://arxiv.org/abs/2501.02689`.

[372] F. Weickert, N. Harrison, B. L. Scott, M. Jaime, A. Leitmäe, I. Heinmaa, R. Stern, O. Janson, H. Berger, H. Rosner, and A. A. Tsirlin. Magnetic anisotropy in the frustrated spin-chain compound $\beta -$ tevo$_4$. *Phys. Rev. B*, 94:064403, Aug 2016. doi:10.1103/PhysRevB.94.064403. URL `https://link.aps.org/doi/10.1103/PhysRevB.94.064403`.

[373] J. Wen, S.-L. Yu, S. Li, W. Yu, and J.-X. Li. Experimental identification of quantum spin liquids. *npj Quantum Materials*, 4(1):12, Apr 2019. ISSN 2397-4648. doi:10.1038/s41535-019-0151-6. URL `https://doi.org/10.1038/s41535-019-0151-6`.

[374] S. R. White. Density matrix formulation for quantum renormalization groups. *Phys. Rev. Lett.*, 69:2863–2866, Nov 1992. doi:10.1103/PhysRevLett.69.2863. URL `https://link.aps.org/doi/10.1103/PhysRevLett.69.2863`.

[375] S. R. White. Density matrix formulation for quantum renormalization groups. *Phys. Rev. Lett.*, 69:2863–2866, Nov 1992. doi:10.1103/PhysRevLett.69.2863. URL `https://link.aps.org/doi/10.1103/PhysRevLett.69.2863`.

[376] S. R. White. Density-matrix algorithms for quantum renormalization groups. *Phys. Rev. B*, 48:10345–10356, Oct 1993. doi:10.1103/PhysRevB.48.10345. URL `https://link.aps.org/doi/10.1103/PhysRevB.48.10345`.

[377] S. R. White. Density-matrix algorithms for quantum renormalization groups. *Phys. Rev. B*, 48:10345–10356, Oct 1993. doi:10.1103/PhysRevB.48.10345. URL `https://link.aps.org/doi/10.1103/PhysRevB.48.10345`.

[378] S. R. White. Strongly correlated electron systems and the density matrix renormalization group. *Physics Reports*, 301(1):187–204, 1998. ISSN 0370-1573. doi:https://doi.org/10.1016/S0370-1573(98)00010-6. URL `https://www.sciencedirect.com/science/article/pii/S0370157398000106`.

[379] S. R. White. Density matrix renormalization group algorithms with a single center site. *Phys. Rev. B*, 72:180403, Nov 2005. doi:10.1103/PhysRevB.72.180403. URL `https://link.aps.org/doi/10.1103/PhysRevB.72.180403`.

[380] S. R. White and I. Affleck. Dimerization and incommensurate spiral spin correlations in the zigzag spin chain: Analogies to the kondo lattice. *Phys. Rev. B*, 54:9862–9869, Oct 1996. doi:10.1103/PhysRevB.54.9862. URL `https://link.aps.org/doi/10.1103/PhysRevB.54.9862`.

[381] S. R. White and I. Affleck. Dimerization and incommensurate spiral spin correlations in the zigzag spin chain: Analogies to the kondo lattice. *Physical Review B*, 54(14):9862, 1996.

[382] S. R. White and I. Affleck. Density matrix renormalization group analysis of the nagaoka polaron in the two-dimensional $t-j$ model. *Phys. Rev. B*, 64:024411, Jun 2001. doi:10.1103/PhysRevB.64.024411. URL `https://link.aps.org/doi/10.1103/PhysRevB.64.024411`.

[383] S. R. White and A. L. Chernyshev. Neél order in square and triangular lattice heisenberg models. *Phys. Rev. Lett.*, 99:127004, Sep 2007. doi:10.1103/PhysRevLett.99.127004. URL `https://link.aps.org/doi/10.1103/PhysRevLett.99.127004`.

[384] S. R. White and A. E. Feiguin. Real-time evolution using the density matrix renormalization group. *Phys. Rev. Lett.*, 93:076401, Aug 2004. doi:10.1103/PhysRevLett.93.076401. URL `https://link.aps.org/doi/10.1103/PhysRevLett.93.076401`.

[385] S. R. White and D. A. Huse. Numerical renormalization-group study of low-lying eigenstates of the antiferromagnetic s=1 heisenberg chain. *Phys. Rev. B*, 48:3844–3852, Aug 1993. doi:10.1103/PhysRevB.48.3844. URL `https://link.aps.org/doi/10.1103/PhysRevB.48.3844`.

[386] S. R. White and R. M. Noack. Real-space quantum renormalization groups. *Phys. Rev. Lett.*, 68:3487–3490, Jun 1992. doi:10.1103/PhysRevLett.68.3487. URL `https://link.aps.org/doi/10.1103/PhysRevLett.68.3487`.

[387] S. R. White and D. J. Scalapino. Competition between stripes and pairing in a $t - t' - j$ model. *Phys. Rev. B*, 60:R753–R756, Jul 1999. doi:10.1103/PhysRevB.60.R753. URL `https://link.aps.org/doi/10.1103/PhysRevB.60.R753`.

[388] S. R. White and D. J. Scalapino. Pairing on striped $t{-}t'{-}j$ lattices. *Phys. Rev. B*, 79:220504, Jun 2009. doi:10.1103/PhysRevB.79.220504. URL `https://link.aps.org/doi/10.1103/PhysRevB.79.220504`.

[389] B. Willenberg, M. Schäpers, A. U. B. Wolter, S.-L. Drechsler, M. Reehuis, J.-U. Hoffmann, B. Büchner, A. J. Studer, K. C. Rule, B. Ouladdiaf, S. Süllow, and S. Nishimoto. Complex field-induced states in linarite pbcuso$_4$(OH)$_2$ with a variety of high-order exotic spin-density wave states. *Phys. Rev. Lett.*, 116:047202, Jan 2016. doi:10.1103/PhysRevLett.116.047202. URL `https://link.aps.org/doi/10.1103/PhysRevLett.116.047202`.

[390] S. C. Williams, R. D. Johnson, F. Freund, S. Choi, A. Jesche, I. Kimchi, S. Manni, A. Bombardi, P. Manuel, P. Gegenwart, and R. Coldea. Incommensurate counterrotating magnetic order stabilized by kitaev interactions in the layered honeycomb $\alpha-$li$_2$iro$_3$. *Phys. Rev. B*, 93:195158, May 2016. doi:10.1103/PhysRevB.93.195158. URL `https://link.aps.org/doi/10.1103/PhysRevB.93.195158`.

[391] K. G. Wilson. The renormalization group: Critical phenomena and the kondo problem. *Rev. Mod. Phys.*, 47:773–840, Oct 1975. doi:10.1103/RevModPhys.47.773. URL `https://link.aps.org/doi/10.1103/RevModPhys.47.773`.

[392] K. G. Wilson. The renormalization group and critical phenomena. *Rev. Mod. Phys.*, 55:583–600, Jul 1983. doi:10.1103/RevModPhys.55.583. URL `https://link.aps.org/doi/10.1103/RevModPhys.55.583`.

[393] K. G. Wilson and J. Kogut. The renormalization group and the expansion. *Physics Reports*, 12(2):75–199, 1974. ISSN 0370-1573. doi:https://doi.org/10.1016/0370-1573(74)90023-4. URL `https://www.sciencedirect.com/science/article/pii/0370157374900234`.

[394] S. M. Winter, Y. Li, H. O. Jeschke, and R. Valentí. Challenges in design of kitaev materials: Magnetic interactions from competing energy scales. *Physical Review B*, 93(21):214431, 2016. doi:10.1103/PhysRevB.93.214431. URL `https://link.aps.org/doi/10.1103/PhysRevB.93.214431`.

[395] S. M. Winter, A. A. Tsirlin, M. Daghofer, J. van den Brink, Y. Singh, P. Gegenwart, and R. Valentí. Models and materials for generalized kitaev magnetism. *Journal of Physics: Condensed Matter*, 29(49):493002, nov 2017. doi:10.1088/1361-648X/aa8cf5. URL `https://dx.doi.org/10.1088/1361-648X/aa8cf5`.

[396] F. Woynarovich and H. P. Eckle. Finite-size corrections and numerical calculations for long spin 1/2 heisenberg chains in the critical region. *Journal of Physics A: Mathematical and General*, 20(2):L97, feb 1987. doi:10.1088/0305-4470/20/2/010. URL `https://dx.doi.org/10.1088/0305-4470/20/2/010`.

[397] D. Wulferding, Y. Choi, S.-H. Do, C. H. Lee, P. Lemmens, C. Faugeras, Y. Gallais, and K.-Y. Choi. Magnon bound states versus anyonic majorana excitations in the kitaev honeycomb magnet α-rucl3. *Nature communications*, 11(1):1603, 2020. doi:10.1038/s41467-020-15370-1. URL `https://doi.org/10.1038/s41467-020-15370-1`.

[398] T. Xiang, J. Lou, and Z. Su. Two-dimensional algorithm of the density-matrix renormalization group. *Phys. Rev. B*, 64:104414, Aug 2001. doi:10.1103/PhysRevB.64.104414. URL `https://link.aps.org/doi/10.1103/PhysRevB.64.104414`.

[399] R. Yadav, N. A. Bogdanov, V. M. Katukuri, S. Nishimoto, J. van den Brink, and L. Hozoi. Kitaev exchange and field-induced quantum spin-liquid states in honeycomb α-rucl3. *Scientific Reports*, 6(1):37925, Nov 2016. ISSN 2045-2322. doi:10.1038/srep37925. URL `https://doi.org/10.1038/srep37925`.

[400] R. Yadav, N. A. Bogdanov, V. M. Katukuri, S. Nishimoto, J. van den Brink, and L. Hozoi. Kitaev exchange and field-induced quantum spin-liquid states in honeycomb α-rucl3. *Scientific Reports*, 6(1):37925, Nov 2016. ISSN 2045-2322. doi:10.1038/srep37925. URL `https://doi.org/10.1038/srep37925`.

[401] R. Yadav, R. Ray, M. S. Eldeeb, S. Nishimoto, L. Hozoi, and J. van den Brink. Strong effect of hydrogen order on magnetic kitaev interactions in $h_3liir_2o_6$. *Phys. Rev. Lett.*, 121:197203, Nov 2018. doi:10.1103/PhysRevLett.121.197203. URL `https://link.aps.org/doi/10.1103/PhysRevLett.121.197203`.

[402] A. Yagi, K. Matsui, T. Goto, M. Hase, and T. Sasaki. Nmr study on the competing spin chain rb2cu2mo3o12. In *Journal of Physics: Conference Series*, volume 828, page 012016. IOP Publishing, 2017. doi:10.1088/1742-6596/828/1/012016. URL `https://doi.org/10.1088/1742-6596/828/1/012016`.

[403] S. Yamada, M. Okumura, and M. Machida. Direct extension of density-matrix renormalization group to two-dimensional quantum lattice systems: Studies of parallel algorithm, accuracy, and performance. *Journal of the Physical Society of Japan*, 78(9):094004, 2009. doi:10.1143/JPSJ.78.094004. URL `https://doi.org/10.1143/JPSJ.78.094004`.

[404] H. Yamase and H. Kohno. Possible quasi-one-dimensional fermi surface in la 2-x sr x cuo 4. *Journal of the Physical Society of Japan*, 69(2):332–335, 2000.

[405] S. Yan, D. Huse, and S. White. Spin-liquid ground state of the $s = 1/2$ kagome heisenberg antiferromagnet. *Science*, 332:1173 – 1176, 2010. doi:10.1126/science.1201080.

[406] S. Yang, S.-J. Gu, C.-P. Sun, and H.-Q. Lin. Fidelity susceptibility and long-range correlation in the kitaev honeycomb model. *Phys. Rev. A*, 78:012304, Jul 2008. doi:10.1103/PhysRevA.78.012304. URL `https://link.aps.org/doi/10.1103/PhysRevA.78.012304`.

[407] Y. Yasui, Y. Yanagisawa, R. Okazaki, I. Terasaki, Y. Yamaguchi, and T. Kimura. Magnetic field induced ferroelectric transition of quasi one-dimensional frustrated quantum spin chain system rb¡sub¿2¡/sub¿cu¡sub¿2¡/sub¿mo¡sub¿3¡/sub¿o¡sub¿12¡/sub¿. *JOURNAL OF APPLIED PHYSICS*, 113(17), MAY 7 2013. ISSN 0021-8979. doi:10.1063/1.4795844. 12th Joint MMM-Intermag Conference, Chicago, IL, JAN 14-18, 2013.

[408] F. Ye, S. Chi, H. Cao, B. C. Chakoumakos, J. A. Fernandez-Baca, R. Custelcean, T. F. Qi, O. B. Korneta, and G. Cao. Direct evidence of a zigzag spin-chain structure in the honeycomb lattice: A neutron and x-ray diffraction investigation of single-crystal $\mathrm{na_2iro_3}$. *Phys. Rev. B*, 85:180403, May 2012. doi:10.1103/PhysRevB.85.180403. URL `https://link.aps.org/doi/10.1103/PhysRevB.85.180403`.

[409] I. A. Zaliznyak, C. Broholm, M. Kibune, M. Nohara, and H. Takagi. Anisotropic spin freezing in the $S = 1/2$ zigzag chain compound $\mathrm{srcuo_2}$. *Phys. Rev. Lett.*, 83:5370–5373, Dec 1999. doi:10.1103/PhysRevLett.83.5370. URL `https://link.aps.org/doi/10.1103/PhysRevLett.83.5370`.

[410] L.-C. Zhang, F. Zhu, D. Go, F. R. Lux, F. J. dos Santos, S. Lounis, Y. Su, S. Blügel, and Y. Mokrousov. Interplay of dzyaloshinskii-moriya and kitaev interactions for magnonic properties of heisenberg-kitaev honeycomb ferromagnets. *Phys. Rev. B*, 103:134414, Apr 2021. doi:10.1103/PhysRevB.103.134414. URL `https://link.aps.org/doi/10.1103/PhysRevB.103.134414`.

[411] Y. Z. Zhang. Dimerization in a half-filled one-dimensional extended hubbard model. *Phys. Rev. Lett.*, 92:246404, Jun 2004. doi:10.1103/PhysRevLett.92.246404. URL `https://link.aps.org/doi/10.1103/PhysRevLett.92.246404`.

[412] Y. Zhou, K. Kanoda, and T.-K. Ng. Quantum spin liquid states. *Rev. Mod. Phys.*, 89:025003, Apr 2017. doi:10.1103/RevModPhys.89.025003. URL `https://link.aps.org/doi/10.1103/RevModPhys.89.025003`.